

PREDICTION OF TURBULENT BUOYANT

JETS IN CO-FLOWING STREAMS

by

James Joseph McGuirk B.Sc.(Eng),D.I.C.,M.Sc.

Thesis submitted for the Degree of Doctor of Philosophy  
in the Faculty of Engineering, University of London.

Mechanical Engineering Department,  
Imperial College  
London, S.W.7.

May 1975.

ABSTRACT

Turbulent buoyant jets in co-flowing streams have been studied both theoretically and experimentally. The theoretical study utilises a general numerical method for solving the partial differential equations which govern the transport of mass, momentum and energy in three-dimensional parabolic flows. An extension of this procedure is described to enable flows contained within irregular shaped boundaries to be treated. The method is validated by predicting laminar and turbulent duct flows and comparisons with experimental data for both hydrodynamics and heat transfer show good agreement.

A review of available turbulence models is given, and a choice is made for the predictions presented here of a model involving the solution of two additional differential equations, one for  $k$ , the turbulence kinetic energy and one for  $\epsilon$  the rate of dissipation of  $k$ . The reasons for the choice of the  $k$ - $\epsilon$  model are outlined.

The experimental investigation reports measurements made on a turbulent buoyant jet discharged into a flowing stream close to the water surface. Vertical temperature profiles are presented for a range of jet Froude numbers from 5 to 30, for jet velocity ratios of 2 to 6, and for two submergence depths. For a few cases, temperature contours over the complete cross-section of the jet are also presented.

The mathematical and turbulence models are applied to the prediction of a range of laboratory data for buoyant co-flowing jets, including the present data. In general the agreement is very good and, for the present measurements, predictions reproduce the transition from a jet-like flow to a warm water layer spreading on the water surface very well. Finally, the model for buoyant jet discharge and the method for irregular boundaries are combined to illustrate how river flow thermal-discharge problems may be predicted.

### ACKNOWLEDGEMENTS

The author wishes to express his gratitude to all those who provided help, in many different ways, during the period of the Ph.D. research.

Firstly I would like to thank my supervisor, Professor D.B. Spalding, who initiated the work and who was throughout a constant source of advice, guidance and inspiration. I should also like to thank Mr. P. Brazier and Dr. F.C. Lockwood for the advice which they gave me as members of my thesis committee.

The experimental programme was greatly assisted by the academic and technical staff of the Civil Engineering Department at Imperial College, and I am indebted to Professor J.R.D. Francis who allowed me unlimited use of facilities in the Hydraulics laboratory of that department.

Thanks are also due to many of my colleagues in the Heat Transfer Section and the librarians, technical and computing staff of the Mechanical Engineering Department who contributed at various times to the successful completion of this work, in particular I would like to thank Charles Noad for his help in taking and developing the photographs. Finally I should like to thank Mrs. Elaine Barker for her expert typing of the thesis.

CONTENTS

	<u>Page</u>
ABSTRACT	2
ACKNOWLEDGEMENTS	4
<u>CHAPTER 1</u> <u>INTRODUCTION</u>	
1.1 Thermal Pollution and its Practical Importance	8
1.2 The Aspect of the Problem Dealt With in This Thesis	9
1.3 Previous Work	11
1.3.1 Non-Buoyant Jets	
1.3.2 Buoyant Jets	
1.3.3 River Flow Discharge	
1.4 Objectives of the Present Work	22
1.5 Outline of the Thesis	24
<u>CHAPTER 2</u> <u>THE MATHEMATICAL MODEL</u>	
2.1 Introduction	25
2.2 The Governing Differential Equations	26
2.2.1 Three-dimensional Parabolic Flows	
2.2.2 Statement of the Differential Equations	
2.3 Auxiliary Information	31
2.4 The Solution Algorithm	33
2.4.1 Reduction of Equations to Finite-Difference Form	
2.4.2 The Computational Algorithm	
2.5 Initial and Boundary Conditions	46
2.6 Stability, Accuracy and Convergence	47

	<u>Page</u>
<u>CHAPTER 3      MATHEMATICAL MODELLING OF TURBULENCE</u>	
3.1 The Turbulence Model Approach and Its Historical Background	50
3.2 The k- $\epsilon$ Turbulence Model	55
3.3 Initial and Boundary Conditions in Turbulent Flow	59
<u>CHAPTER 4      A PROCEDURE FOR HANDLING IRREGULAR BOUNDARIES</u>	
4.1 Outline of the Problem	65
4.2 A Method for Irregular Boundaries	66
4.2.1 Grid Node Identification	
4.2.2 Handling of External Nodes	
4.2.3 Handling of Near-Wall Nodes	
4.3 Testing in Laminar Flows	76
4.3.1 Introduction	
4.3.2 Application to Laminar Circular Pipe Flow	
4.3.3 Application to Laminar Elliptic Duct Flow	
4.4 Testing in Turbulent Flows	85
4.4.1 Introduction	
4.4.2 Application to Turbulent Flow in a Circular Duct	
4.4.3 Application to Turbulent Flow in an Elliptic Duct	
4.5 Summary	91
<u>CHAPTER 5      EXPERIMENTAL INVESTIGATION</u>	
5.1 Objectives of Present Experiments	92
5.2 Experimental Apparatus	93
5.3 Discussion of Measurements Made	103

	<u>Page</u>
<u>CHAPTER 6</u> <u>PREDICTION OF TURBULENT BUOYANT JETS IN</u> <u>CO-FLOWING STREAMS</u>	
6.1 Introduction	108
6.2 Validation of Mathematical Model in Non-Buoyant Flows	109
6.3 Prediction of Laboratory Data	115
6.3.1 Inlet Conditions for Jet Discharge into Co-Flowing Streams	
6.3.2 Prediction of Winiarski and Chasse Data	
6.3.3 Prediction of Shirazi et al. Data	
6.3.4 Prediction of Ayoub Data	
6.3.5 Prediction of Present Experimental Data	
6.4 Summary	140
<u>CHAPTER 7</u> <u>FURTHER PREDICTIONS - A RIVER DISCHARGE PROBLEM</u>	
7.1 Introduction	141
7.2 Some Sample Calculations	142
7.2.1 The Problem Considered	
7.2.2 Results	
7.3 Summary	147
<u>CHAPTER 8</u> <u>CONCLUSIONS AND SUMMARY</u>	
8.1 Review of Work Presented	148
8.2 Suggestions for Future Work	150
<u>REFERENCES</u>	153
<u>NOMENCLATURE</u>	161
<u>APPENDIX 1</u> Some Computational Details	165
<u>APPENDIX 2</u> A Literature Review of Elliptic Duct Flow	171
<u>APPENDIX 3</u> Tabulated Experimental Data	182
<u>FIGURES</u>	192

CHAPTER 1

INTRODUCTION

1.1 Thermal Pollution and its Practical Importance

Modern society is increasingly dependent on the generation of electrical energy to fulfil its everyday needs; unfortunately, an integral part of the generation process is the rejection of large amounts of waste heat from the steam condensers which form part of the heat cycle. A simple and convenient method of disposing of this waste heat is to reject it directly into natural water bodies such as seas, lakes and rivers from which the heat is ultimately lost to the atmosphere. In recent years however, there has been a growing awareness of the detrimental effects caused by the heat on the ecology of the receiving water; the phrase 'thermal pollution' has therefore been coined.

There is agreement that to increase the water temperature may be considered as pollution since the warmer the water, the less it is able to hold dissolved oxygen; this can adversely affect fish and plant life in the water body. Secondly, a higher water temperature decreases the ability of the water to absorb safely waste products such as industrial and domestic sewage; the water may thus become polluted by these discharges more readily if it has first been polluted with thermal energy.

The problem of thermal pollution has been highlighted by recent studies showing the exponential growth of the electricity generating industry (doubling every decade in the U.S.A., see Harleman and Stolzenbach [1]) and also by the advent of nuclear



power stations which reject even more waste heat than fossil-fueled stations (approximately 2 KW for every KW of electrical energy produced). These facts have led researchers in all countries to seek reliable methods of predicting thermal-pollution processes as the laboratory modelling of these processes is both difficult and costly. An added incentive to produce prediction procedures is the way in which certain countries have worded legislation intended to combat thermal pollution; the legal requirements make use of such parameters as the maximum surface water temperature rise above ambient outside a given area or "mixing zone"; calculation procedures could easily provide such information. Having emphasised its practical importance and the pressing need for prediction procedures, it is the purpose of this thesis to contribute to the methods available for the calculation of thermal-pollution problems.

## 1.2 The Aspect of the Problem Dealt With in This Thesis

The particular form of thermal-pollution problem studied in this thesis falls into a category known as "once-through" cooling. The water is withdrawn from the lake or river and passed through the condensers where it absorbs the waste heat and its temperature is raised (typically 10-15°C rise for a 1000 megawatt unit); the water is then discharged back into the receiving body as a jet. Two methods of discharge are used, surface and submerged; the former is used to minimise the impact of the thermal effluent

along the bottom of the receiving water, but submerged discharge is often preferred because of the high dilutions which can be achieved; attention is focussed on this mode of discharge here.

Submerged discharge may itself be divided into two categories: multi-port discharge where the effluent is ejected through many holes drilled in the discharge structure, and single-port discharge. The former class is more usual in practice but since the latter is not yet fully understood and is more amenable to modelling, it is this class which is studied here.

Most discharges take place in natural-water bodies with currents in the receiving water (particularly river discharges); in addition, although most previous studies have been of discharge into infinite water bodies, practically interesting flows often interfere with the flow boundaries (either the bed of the river or the water surface where buoyancy forces lift the hot water jet). The jet itself is sometimes angled with respect to the currents in the environment, but here only parallel discharge is considered, with the jet axis horizontal. Finally, the effect of a thermal-pollution source may be viewed as taking place in two regions; firstly the 'near-field' where the flow is strongly influenced by the discharge characteristics, secondly the 'far-field' in which the mixing is dominated by the characteristics of the ambient flow; it is in the far-field where most of the injected heat is lost to the atmosphere. In this thesis only the near-field region will be studied.

To summarise therefore, the particular thermal-pollution application which is of relevance here is the near-field of a single-port submerged discharge ejected horizontally into a parallel

flowing river; the discharge may possibly be affected by the solid boundaries of the river, or by the presence of the water surface. This situation is illustrated in FIG. 1.1; it is the prediction of the flow and mixing of this turbulent buoyant jet with its environment which forms the basis of this thesis.

### 1.3 Previous Work

#### Limitations of Review

This section contains a review of previous work on turbulent buoyant jets in co-flowing streams, and also on related topics such as non-buoyant jets in flowing and stagnant surroundings. The volume of such work is so large that attention is focussed on to that which is more recent; in addition only constant density horizontal round jets are reviewed, and, where a surrounding stream is present, only parallel flow is included. Reviews of other jet flow situations and of earlier work have been given by Abramovich [2], Forstall and Shapiro [3], and Ayoub [4].

#### 1.3.1 Non-Buoyant Jets

When a round turbulent jet is discharged into still or moving surroundings, the flow pattern is as shown in FIG. 1.2. The lips of the nozzle generate mixing layers which spread inwards until they meet the axis. This marks the end of the potential core region when the central portion of the jet travelling at the original velocity has just disappeared. At the same time

the jet entrains fluid from the surroundings and the overall jet width increases. A transition zone follows where the flow adjusts to the presence of the axis of symmetry; finally there is the region of established flow in which the profiles assume similar forms (i.e. when velocity and radial distance are non-dimensionalised by suitably chosen scales, the profiles have a common shape, independent of downstream distance).

For non-buoyant jets in still surroundings, the above description has been confirmed experimentally by many authors. In the established flow region the jet is found to spread linearly and the centre-line velocity is inversely proportional to downstream distance. The length of the potential core region is dependent on conditions at the jet exit (turbulence level, boundary layers on nozzle lips, see for example Rodi [5]); but, for low exit turbulence, it is approximately five jet diameters. Sami, Carmody and Rouse [6] paid particular attention to the inlet region and have made detailed measurements in the first ten jet diameters. The measurement of turbulence quantities has confirmed that these too attain a self-similar state, although later than the mean flow field, see for example Wygnanski and Fiedler [7] and Rodi [5].

The transfer of heat and matter in a round jet has been investigated by Hinze and Zijnen [8], Corrsin and Uberoi [9], and Becker, Hottel and Williams [10]. The first of these measured radial and axial distributions of time-mean velocities, temperatures and concentrations in a gas jet and showed that the

scalar quantities also achieved self-preserving profiles. The results indicated that the rates of spread of heat and matter were mutually equal, but greater than that of velocity; the same behaviour was noted by Corrsin for a hot air jet; this work also contained measurements of turbulence quantities including temperature fluctuations and velocity-temperature correlations. Reference [10] performed similar measurements of turbulence quantities, but for concentration as opposed to temperature fluctuations.

The theoretical investigations of jets in still air are also numerous. Rodi [5] has recently presented a comprehensive treatment of the hydrodynamic problem using the computational procedure of Patankar and Spalding [11] and several advanced turbulence models; finally, Spalding [12] has demonstrated that the prediction of scalar turbulence fluctuations such as measured in [10] is also possible, using the same calculation procedure.

One of the earliest experimental investigations for jets in a moving stream was that of Forstall and Shapiro [3]. The main conclusions were: non-dimensional velocity and concentration profiles achieved self-preserving states, the profile shape being independent of jet to surrounding stream velocity ratio; material diffused more rapidly than momentum, the controlling parameter for the shape of the mixing region being the velocity ratio; this affects the length of the potential core (L) and Forstall and Shapiro derived the following empirical formula:-

$$L = 4 + \frac{12}{K} \quad , \quad K = \frac{U_{\text{Jet}}}{U_{\text{Ambient}}} \quad (1.3.1)$$

Finally, outside the potential core, centre-line values of velocity and concentration decreased in inverse proportion to  $x$  irrespective of velocity ratio. Landis and Shapiro [13] confirmed that these findings applied also to the transfer of heat in co-flowing jets.

The prediction of jets in moving streams achieved considerable attention recently at a conference on the computation of free shear flows [16]; most of the calculation procedures were of the finite-difference variety and the level of turbulence model used varied from simple (mixing length) to very advanced (solution of differential equations for the Reynolds stresses), see for example Launder et al [17].

### 1.3.2 Buoyant Jets

FIG. 1.3 indicates how the flow pattern changes when buoyancy forces exert an influence (for jet fluid lighter than ambient). The jet behaves in a similar manner to that described above but is deflected from its original axis by the buoyancy forces; the velocity ratio is still an important parameter as the ambient stream tends to bend the jet in the downstream direction. The influence of buoyancy is characterised by defining a densimetric Froude number as shown below:-

$$FR \equiv \frac{u_J}{\sqrt{\frac{\Delta\rho}{\rho_a} g d_J}} \quad (1.3.2)$$

$\Delta\rho$  is the differential density between the ambient and jet fluids; hence for small values of FR buoyancy is important and its effect decreases with increasing FR.

### Stagnant Surroundings

Buoyant jets in a still ambient environment have been investigated by Frankel and Cumming [18], Abraham [19], Anwar [20], and Fan and Brooks [21]. The first was an experimental investigation; amongst the parameters examined were the jet Froude number and submergence depth to jet diameter ratio. The results confirmed that similarity of the concentration profile was achieved and the profile was closely approximated by a Gaussian distribution. The other studies have presented theoretical treatments of the buoyant jet problem, all three using an "integral-profile" method; the assumptions involved are examined in more detail below. As an illustration, the method of Anwar is summarised here.

The flow was assumed incompressible and fully turbulent. Further, the variations in density through the flow field were considered small and hence were ignored except when considering the buoyancy force (Boussinesq approximation). To describe the distributions of velocity and density difference, the problem was assumed symmetrical about the jet axis and Gaussian profiles utilised i.e.:-

$$U = U_m e^{- (r/b)^2} \quad (1.3.3)$$

$$(\rho_a - \rho) = (\rho_a - \rho_m) e^{-(r/\lambda b)^2} \quad (1.3.4)$$

( $r$  is the radial co-ordinate in the 'natural' co-ordinate system used ( $s, r, \theta$ ) see FIG. 1.3). Here  $U_m$  and  $\rho_m$  are the values on the axis and  $\rho_a$  is the ambient density;  $\lambda$  is a spreading coefficient (supplied from experiments) to allow for matter diffusing more rapidly than velocity. These profiles were substituted into equations for mass conservation, density deficiency conservation and transport equations for vertical and horizontal momentum. The equations were integrated over the jet area to produce first order ordinary differential equations with distance along the jet axis ( $s$ ) as the independent variable. Two kinematic equations were added to relate the 'natural' and cartesian co-ordinate systems:-

$$\frac{dx}{ds} = \cos \theta \quad \frac{dy}{ds} = \sin \theta \quad (1.3.5)$$

$\theta$  is the angle between the jet axis and the horizontal plane.

Hence there results six first order equations for the six dependent variables  $U_m, \Delta\rho_m, b, x, y, \theta$ .

Before this equation set is closed, an assumption has to be made about the entrainment of ambient fluid into the jet; for example, the mass conservation equation which results from the above analysis is of the form:-

$$\frac{d}{ds} \left( \int_A \rho u dA \right) = \dot{m}'_{ent} \quad (1.3.6)$$

where  $\dot{m}'_{ent}$  is the rate of mass entrainment from the ambient per unit length along the jet axis. The assumption made was based on



an approach first introduced by Morton, Taylor and Turner [22] who proposed the equation:-

$$\dot{m}'_{ent} = \alpha . 2\pi b . \rho U_{char} \quad (1.3.7)$$

i.e. the rate of entrainment is proportional to a local characteristic velocity which is usually taken to be the velocity difference between the axis and the surroundings.  $\alpha$  is the turbulent entrainment coefficient which must be specified before predictions can be made. Usually it has been assumed a constant ( $\approx 0.1$ ) and this has produced reasonable agreement with experiment for jet trajectories and dilution rates [20, 21].

#### Co-Flowing Surroundings

Only recently have investigations included the possibility of co-flowing ambient surroundings, the investigations are thus comparatively few in number; Table 1 below gives details of the various studies. Ayoub [4] has studied the dispersion of horizontally injected dense salt jets in a co-flowing water stream; as in all the other investigations, the experimental configuration was a round jet injected into a straight rectangular open channel (see FIG. 1.4). The dimensions were such that the ambient stream could be considered infinite in extent. The experiments demonstrated that the dimensionless parameters FR and K were the only important ones by performing many experiments for different jet and stream velocities, various nozzle diameters, and various

density differences; when compared on the basis of identical FR and K values, the results for plume trajectory and dilution rate coincided. A theoretical treatment was also given based on an extension of the integral-profile method of Fan and Brooks similar to the one described above and the entrainment concept of Morton, Taylor and Turner [22]. Good agreement was obtained with the experimental results, but only when the entrainment coefficient  $\alpha$  was made a function of Froude number and 'local' velocity ratio (i.e. local maximum jet velocity divided by ambient velocity). The spreading coefficient  $\lambda$  was initially given a value 1.16 but this resulted in poor agreement with experiments; accordingly this too was altered although the value which gave the best results (0.75) did not accord with the known fact that concentration spreads faster than velocity; no explanation was given for this contradiction.

Hirst [26], [27] also used an integral profile method similar to the above but generalised to allow for jet discharge at arbitrary angles to the ambient flow (Hirst's method was used by Shirazi and Davis [30] to generate a comprehensive set of predictions for a wide range of submerged discharge problems). Again a complex entrainment function was specified depending on jet width, Froude number, jet angle  $\theta$  and velocity ratio; four constants appear in the function which are determined by fitting predictions to experimental data. The first paper applied the method to the prediction of the potential core and transition regions of buoyant and non-buoyant jets, the second extended the application to the established

flow region for jets discharged horizontally and at angles to the free stream.

Hot water jets have been studied by Shirazi et al [23], [24], [25] and Winiarski and Chasse [28], [29]; the first investigation included an attempt to study the effect of ambient turbulence by altering the roughness of the channel bed material. The results were correlated [24] in terms of jet Froude number and velocity ratio and for the smooth channel bed the following equation for dilution rate resulted:-

$$\frac{\Delta T}{\Delta T_o} = \frac{T_{\max} - T_a}{(T_{\max} - T_a)_{\text{inlet}}} = e^{4.98} \cdot \eta^{-1.024} \cdot K^{2.308} \cdot FR^{-1.581} \quad (1.3.8)$$

Here  $e = 2.713$  and  $\eta = x/d_j$  i.e. downstream distance non-dimensionalised by the nozzle diameter, the ranges of values of the various parameters studied in the experiments is given in Table 1. It was discovered that an increase in ambient turbulence level increased the exponent of  $\eta$  in eqn. 1.3.8, i.e. the dilution was quicker; the rate of plume spread was increased only slightly with increased ambient turbulence. In reference [25] an attempt was made to use the prediction procedure of Hirst [27] with allowance for ambient turbulence terms to predict the data of [23]. It was found that the measured ambient turbulence quantities had to be reduced before agreement was obtained; the author explained this inconsistency by pointing to the crudeness of the entrainment coefficient concept.

A report by Winiarski and Chasse [29] also dealt with discharge into an infinite ambient; empirical correlations were again deduced

Authors	Exptl	Theoretical	Channel + discharge Geometry (FIG. 1.4)	FR values	K values	$x/d_J$ range	Comments																
Ayoub [4]	✓	✓	<table border="1"> <thead> <tr> <th>H</th> <th>B</th> <th>h</th> <th><math>d_J</math>(m)</th> </tr> </thead> <tbody> <tr> <td>.37</td> <td>.76</td> <td>.3</td> <td>.01</td> </tr> <tr> <td></td> <td></td> <td></td> <td>.0075</td> </tr> <tr> <td></td> <td></td> <td></td> <td>.005</td> </tr> </tbody> </table>	H	B	h	$d_J$ (m)	.37	.76	.3	.01				.0075				.005	15 - 90	5 - 20	10 - 120	dense jet, effectively into infinite environment theory-integral-profile method
H	B	h	$d_J$ (m)																				
.37	.76	.3	.01																				
			.0075																				
			.005																				
Shirazi [23]	✓		.28 .59 .14 .019	6 - 200	.44 - 7.2	16 - 300	hot jet, expts. run with different channel bed material to produce different ambient turbulence levels. Empirical correlations for jet dilution, jet width etc.																
et al [24]	✓	✓	as above																				
[25]			-																				
Hirst [26]		✓		-	-	-	Integral Profile method, entrainment coefficient function of local jet Froude number, velocity ratio etc.																
[27]		✓																					
Winiarski [28]	✓		.13 .3 0 .014	12, 37	3, 8	10 - 90	[28] with jet injected along bottom, [29] for deeply submerged discharge. Empirical correlations for jet trajectory, dilution rate, jet width.																
and Chasse [29]	✓		0.3 .3 - .014	5 - 100	2 - 15	10 - 90																	

TABLE 1 DATA FOR CO-FLOW DISCHARGE

and the equations for dilution rate, plume trajectory and plume width are given below:-

$$\frac{\Delta T}{\Delta T_0} = e^{\begin{matrix} +1.47 & -1.04 & 0.1 & 0 \\ \eta & & K & FR \end{matrix}} \quad (1.3.9)$$

$$\frac{y}{d_J} = e^{\begin{matrix} -1.22 & 1.33 & 0.99 & -1.72 \\ \eta & & K & FR \end{matrix}} \quad (1.3.10)$$

$$\frac{W}{d_J} = e^{\begin{matrix} -0.29 & 0.5 & 0.28 & 0 \\ \eta & & K & FR \end{matrix}} \quad (1.3.11)$$

Again the ranges of the parameters investigated in the experiments is given in Table 1.

It is noticeable that the only similarity between eqn. (1.3.8) and (1.3.9) is in the hyperbolic rate of dilution with downstream distance, otherwise no similarity is present.

The same authors also investigated a co-flowing jet situation in which the jet was discharged along the bottom of the channel [28], various Froude numbers, velocity ratios and angles of discharges were considered and correlations were derived for the results [29]. The effect of ambient turbulence was also introduced by including a grid of turbulence generating rods upstream of the discharge, the authors state however that the results were inconclusive.

The above experiments are the sole example known to the writer of buoyant jet discharge in which the flow boundaries (in this case the solid channel bottom) affect the flow. Two

papers on jets whose development is affected by the presence of the water surface have been presented by Maxwell and Pazwash [31] and Narain [32], both however dealt with non-buoyant jets and into still ambients. Both studies used the same analytical method; the former was applied to submerged jets with a small angle of inclination to the horizontal and it was shown that the flow pattern was strongly affected by this inclination; good agreement was obtained with the experiments of the authors [33]. The latter study extended the analysis to allow for swirl in the discharged jet.

### 1.3.3 River-Flow Discharge

Calculations of the thermal-pollution of river flows such as sketched in FIG. 1.1 have been very scarce because of the complexity of the problem. Recently Zelazny and Baker [34] presented a finite-element method for calculating a realistic river pollution problem but used a very simple turbulence model. Spalding [35] also recently demonstrated a general finite-difference approach which is capable of providing predictions of river flow thermal pollution problems.

## 1.4 Objectives of the Present Work

The review of work relevant to turbulent buoyant jets in co-flowing streams presented in the previous section has outlined several areas where improvements can be made and also areas where there are gaps in available knowledge. This thesis reports work contributing to making these improvements and filling the gaps;

the main objectives are as follows:-

- To apply a mathematical model based on a finite-difference scheme and an advanced turbulence model to the problem of buoyant jets in co-flowing ambients; the nature of the model is such that the specification of the entrainment constant which was necessary in the integral-profile method is no longer required.
- To develop a method (to be used in the above finite-difference scheme) for the treatment of irregular boundaries of the flow domain; this is needed for the calculation of real river flows since the beds of rivers are usually of irregular shape. The method is to be tested by predicting laminar and turbulent duct flows whose boundaries are irregular.
- The review in section 1.3 revealed a lack of experimental data for buoyant jets discharged close to a water surface; an experimental investigation is to be conducted to provide such data.
- To validate the mathematical model by predicting the available laboratory data on turbulent buoyant jets.
- To demonstrate how a real thermal discharge into river problem may be calculated.

## 1.5 Outline of the Thesis

The thesis consists of eight chapters of which this is the first. Chapter 2 outlines the mathematical problem including details of the governing differential equations, the reduction of these to finite-difference form, and the solution algorithm used. Chapter 3 gives details of the turbulence model and why this particular version has been chosen. This is followed by a chapter describing the method of handling irregular boundaries and its validation in the calculation of duct flows. Chapter 5 contains information on the experimental investigation and the results obtained are predicted in Chapter 6 together with the results of other experimenters. Chapter 7 ties together the mathematical model for buoyant jets and the irregular boundary procedure by providing sample calculations of a river thermal pollution problem. Finally, in Chapter 8 a summary is made of the work performed; conclusions are drawn and suggestions are made for future work; details which do not fit well into the main body of the thesis are given in the appendices.



CHAPTER 2

THE MATHEMATICAL MODEL

2.1 Introduction

This chapter describes the formulation of the buoyant jet in river problem in mathematical terms; the description begins with a classification of the problem into a category known as steady three-dimensional parabolic flows; the meaning of this phrase is given below. The partial differential equations which govern the distribution of mass, momentum, energy and other scalar dependent variables are set out in full; a cartesian co-ordinate system is used and, for the moment, attention is restricted to laminar flows, although some remarks are made about the handling of turbulence which is described in detail in the following chapter. A discussion is then given of the additional information required before the mathematical problem is completely closed, again this links with the turbulence model section to follow. Next is described the particular solution procedure utilised in this thesis; the numerical scheme has been previously reported by Patankar and Spalding [36] and details are restricted to those necessary for clarity. Topics covered include:- the reduction of the differential equations to finite-difference form, including all assumptions used in the discretization procedure; the method of solving the resulting algebraic set of equations; and remarks on such computational details as accuracy, stability and convergence. The manner in which initial and boundary conditions are incorporated into the solution algorithm is also dealt with.

## 2.2 The Governing Differential Equations

### 2.2.1 Three-Dimensional Parabolic Flows

The phrase "three-dimensional parabolic (or boundary layer) flow" has most often been used in the field of external boundary layers; for example to describe the flow over an infinite swept wing or yawed cylinder (see Schlichting [37]). Patankar and Spalding [36] generalised the term to include all flows which are parabolic in one distance co-ordinate\*; flows which may be so classified have the following three important characteristics:-

- i) There is a predominant direction of flow; this direction identifies the parabolic co-ordinate and all flow reversal in this direction is absent.
- ii) The diffusion fluxes of heat, mass, momentum etc. are negligible in this direction.
- iii) Along the predominant flow direction, the downstream pressure field has little influence on the upstream flow conditions.

The first two characteristics are familiar since they also occur in two-dimensional boundary layers; the presence of the third may be more difficult to grasp but the necessity for its presence if the equation set is to be truly parabolic will become clearer later in the chapter.

---

\*Because there is a parabolic co-ordinate direction, Patankar and Spalding noted that solution procedures may take advantage of this and employ "marching integration" type methods, as described below.

It may be mentioned here that to fit into this category, certain restrictions must be imposed on the jet discharging into river situation. In order to retain a predominant direction of flow, the river must have no regions of recirculation;\* thus the parabolic direction is aligned with the river flow direction; in this thesis, in addition, only straight rivers are considered, although the solution algorithm used here has been employed successfully for the prediction of flow in curved ducts (see Patankar et al. [38]) and hence could be applied to curved rivers also. Finally, the buoyancy force which lifts the warm water to the surface must not be so dominant that the curvature of the plume is very steep; for, in this situation, the vertical velocities would be as large (or larger) than the horizontal velocities and the predominant direction of flow would have altered. In what follows the parabolic direction is always considered to be along the horizontal co-ordinate in the downstream river direction, the flow may then be treated as a three-dimensional parabolic flow.

### 2.2.2 Statement of Differential Equations

Written out in full below are the equations which govern steady, laminar three-dimensional parabolic flows; the equations are written in terms of a cartesian co-ordinate system disposed as shown in FIG. 2.1 (a rectangular river has been sketched for simplicity). The equations have been reduced from the full

---

\*Hence tidal stretches of rivers cannot be included here.

three-dimensional equations applicable to steady, constant property laminar flow (see for example Bird, Stewart and Lightfoot [39]) by invoking the mathematical consequences of the parabolic nature of the flow; in particular, the diffusion fluxes have been neglected in the predominant flow direction so that only second order differentials with respect to the lateral co-ordinates (y and z) appear. Also the pressure gradient in the axial momentum equation has been 'de-coupled' from the pressure gradients in the lateral momentum equations; this is a consequence of the third characteristic of parabolic flows given above; it is shown below that this de-coupling renders the axial direction truly one-way. For further details of the treatment of pressure, or of the terms neglected in the full equations, the reader should consult Patankar and Spalding [36] or Sharma [40].

Continuity equation

$$\frac{\partial}{\partial x} (\rho u) + \frac{\partial}{\partial y} (\rho v) + \frac{\partial}{\partial z} (\rho w) = 0 \quad (2.2.1)$$

Axial momentum equation

$$\frac{\partial}{\partial x} (\rho u^2) + \frac{\partial}{\partial y} (\rho v u) + \frac{\partial}{\partial z} (\rho w u) = \frac{\partial}{\partial y} \left( \mu \frac{\partial u}{\partial y} \right) + \frac{\partial}{\partial z} \left( \mu \frac{\partial u}{\partial z} \right) - \frac{\partial \bar{p}}{\partial x} \quad (2.2.2)$$

Vertical lateral momentum equation

$$\frac{\partial}{\partial x} (\rho u v) + \frac{\partial}{\partial y} (\rho v^2) + \frac{\partial}{\partial z} (\rho w v) = \frac{\partial}{\partial y} \left( \mu \frac{\partial v}{\partial y} \right) + \frac{\partial}{\partial z} \left( \mu \frac{\partial v}{\partial z} \right) - \frac{\partial \bar{p}}{\partial y} + \rho \beta g (T - T_{\text{ref}}) \quad (2.2.3)$$

Horizontal lateral momentum equation

$$\frac{\partial}{\partial x}(\rho uw) + \frac{\partial}{\partial y}(\rho vw) + \frac{\partial}{\partial z}(\rho w^2) = \frac{\partial}{\partial y}(\mu \frac{\partial w}{\partial y}) + \frac{\partial}{\partial z}(\mu \frac{\partial w}{\partial z}) - \frac{\partial p}{\partial z} \quad (2.2.4)$$

Temperature equation

$$\frac{\partial}{\partial x}(\rho uT) + \frac{\partial}{\partial y}(\rho vT) + \frac{\partial}{\partial z}(\rho wT) = \frac{\partial}{\partial y}(\Gamma_T \frac{\partial T}{\partial y}) + \frac{\partial}{\partial z}(\Gamma_T \frac{\partial T}{\partial z}) \quad (2.2.5)$$

It is pointed out here that these equations all fall into a common form written below for a general scalar fluid property  $\phi$ :-

$$\frac{\partial}{\partial x}(\rho u\phi) + \frac{\partial}{\partial y}(\rho v\phi) + \frac{\partial}{\partial z}(\rho w\phi) = \frac{\partial}{\partial y}(\Gamma_\phi \frac{\partial \phi}{\partial y}) + \frac{\partial}{\partial z}(\Gamma_\phi \frac{\partial \phi}{\partial z}) + S_\phi \quad (2.2.6)$$

The symbols are defined as follows:-

- |               |  |
|---------------|--|
| $u, v, w$     | velocity components in the x,y,z direction   |
| $x, y, z$     | cartesian co-ordinate system (see FIG. 2.1)  |
| $\rho$        | fluid density  |
| $\mu$         | fluid laminar viscosity  |
| $\Gamma_\phi$ | diffusion coefficient in general scalar equation<br>defined as $\Gamma_\phi = \frac{\mu}{\sigma_\phi}$ |
| $\Gamma_T$    | diffusion coefficient for temperature defined as:-<br>$\Gamma_T = \frac{\mu}{Pr}$                      |
| $Pr$          | Prandtl Number   |
| $\sigma_\phi$ | Prandtl/Schmidt Number appropriate to the<br>transport of $\phi$                                       |

$\phi$	general fluid property (scalar)
$S_{\phi}$	Source (or sink) term in $\phi$ transport equation
$\bar{p}$	Pressure appearing in axial momentum equation
$p$	Pressure in lateral momentum equations

It can be seen that an extra term has been included in the vertical momentum equation, this is a source of momentum due to buoyancy. The Boussinesq approximation (see Boussinesq [60], Turner [41]) is used here so that the differences in density of the fluid which arise due to different fluid temperatures are assumed negligible in all terms other than this source term; if the density used in all other terms in the equation is taken as the reference level then the buoyancy source may be written:-

$$S_{\text{buoy}} = -(\rho_{\text{ref}} + \Delta\rho).g \quad (2.2.7)$$

where

$$\Delta\rho = (\rho_{\text{local}} - \rho_{\text{ref}}) \quad (2.2.8)$$

(the minus sign appears because  $g$ , the gravitational acceleration, is in the negative  $y$  direction).

The first term in eqn. (2.2.7) may be ignored as this is merely the gravity force which induces a hydrostatic pressure gradient; the pressure gradients in the momentum equations then become those which drive the fluid motions alone. Equation (2.2.8) is re-written using the definition of  $\beta$ , the volumetric expansion coefficient:-

$$\beta = -\frac{1}{\rho} \frac{\partial\rho}{\partial T} \quad (2.2.9)$$

hence:-

$$S_{\text{buoy}} = \rho_{\text{ref}} \beta g (T_{\text{local}} - T_{\text{ref}}) \quad (2.2.10)$$

and this is the additional source appearing in the  $v$  momentum equation.

Summarising therefore equations (2.2.1) to (2.2.6) describe the flow of a steady three-dimensional buoyant jet discharged in a river; the equations have been given for laminar flows but it can be mentioned here that for turbulent flows, if the transport properties  $\mu$  and  $\Gamma_{\theta}$  are given 'effective' turbulent values, the same equations can be used and the dependent variables are then time-averaged values. How the effective transport properties are prescribed is left until the next chapter. Finally, the effects of buoyancy forces have been included by the presence of an extra source term in the vertical momentum equation.

### 2.3 Auxiliary Information

The differential equations themselves are an insufficient description of the problem; to complete the specification requires three further kinds of information:-

- a) Initial conditions - i.e. values of all dependent variables ( $u, v, w, p, T, \theta$ ) at the initial cross-section at which calculations are to be begun.

- b) Boundary conditions - the calculation domain sketched in FIG. 2.1 is bounded on three sides by the river walls and bed and on the fourth by the water surface; all dependent variables must be prescribed boundary values (or other conditions such as zero gradient normal to the boundary) along all four sides.
- c) Auxiliary conditions - the density, transport coefficients for  $\phi$ 's, value of  $\beta$  must be prescribed over all the solution domain. In the calculations presented in this thesis the density is assumed constant and may be found from tables; for laminar flow calculations the viscosity too is constant and well known, the turbulence model presented later allows the transport properties to be calculated in terms of other dependent variables over the whole flow domain.

When these conditions are supplied, the mathematical model is closed and attention must be turned to the solution of the equations. These are second-order, non-linear, interlinked partial differential equations; this precludes analytical solution and recourse must be made to numerical methods; this is the subject of the next section.



## 2.4 The Solution Algorithm

A review of available calculation procedures for three-dimensional parabolic equations has been given by Patankar [42]; the methods reviewed are all of the finite-difference variety, but are mostly directly suited to external boundary layers. This means that they assume the axial pressure gradient is known from the details of the flow outside the boundary layer. For general confined flows this assumption is unsuitable and Patankar and Spalding [36] developed a general calculation procedure for the equations which appeared in the previous section. The numerical scheme has been given the mnemonic SIMPLE, which stands for Semi-Implicit Method for Pressure Linked Equations; the details of the scheme are given in this section.

### 2.4.1 Reduction of Equations to Finite-Difference Form

The first step is to derive finite-difference equivalents of the partial differential equations. The transformation is brought about by integrating the equations over small volumes in space which surround the nodes of a finite-difference grid. The grid consists of a lattice of intersecting lines which completely cover the calculation domain in the  $yz$  plane, (a portion of this grid is shown in FIG. 2.2). The upstream and downstream faces of the integration cells are made up of two planes of constant  $x$  separated by the forward step length  $\Delta x$ ; the grid spacing in the  $yz$  plane and the step size  $\Delta x$  may both be non-uniform.

The fluid properties are presumed to be known at the nodes of the grid at the inlet plane; the solution procedure must establish the values at the locations given by the nodes of the grid covering a plane  $\Delta x$  downstream. The solution then proceeds by making further steps downstream in the usual marching-integration manner mentioned earlier.

FIG. 2.2 shows that not all fluid properties are stored at the same grid locations; the axial velocity, pressure and other scalar fluid properties are stored at the nodes of a 'main' grid system, but the lateral velocities  $v$  and  $w$  are stored at grid locations 'staggered' from the main grid nodes; in fact they lie precisely midway between the main nodes,  $v$  velocities displaced in the negative  $y$  direction and  $w$  velocities in the negative  $z$  direction. This arrangement is similar to that used by other finite-difference schemes (e.g. Harlow et al [43]) and has two main advantages:-

- a) The lateral velocities are stored at the locations at which they are needed for the calculation of lateral convection fluxes in the balance equations for  $u$  and  $\phi$ 's (this will become clearer shortly when the integration control volumes are sketched).
- b) The calculation of the pressure gradients which drive the lateral velocities is made easier.

In FIG. 2.2 the "boomerang-shaped" envelopes enclose the triads of points referred to by a single letter in a

"points-of-the-compass" notation i.e. N,S,E,W,P.

A typical integration control volume surrounding each grid node (the staggering of the grid means different cells surround u,v and w nodes) is shown in FIG. 2.3 for a typical node P. The upstream and downstream faces have been dealt with above, the other faces are located midway between grid nodes so that, for u or  $\phi$  cells, the lateral velocities lie on the faces themselves; this now explains the first of the advantages of the staggered grid system mentioned above. For v and w cells, when the lateral convection flux is calculated, an average of neighbouring values is used; this also applies in general wherever a variable is required at a point in space other than where it is located.

Closer examination of FIG. 2.2 reveals that a slight modification has been made in the region of the boundaries for the lateral velocities. The boundaries are most usefully located along lines passing through points where the velocity components normal to the boundaries are stored. The near-wall lateral velocities are considered shifted in space so that they do lie on the boundary; this results in the control volumes for the next lateral velocity being enlarged compared to the normal size; FIG. 2.4 illustrates this practice.

The manner in which the integrations\* are performed is given in detail in Reference [36]; before the integration can be completed, assumptions must be made about the way in which each variable is distributed between grid nodes, further information can be obtained

---

\*Integration over control-volumes is preferred to the normal Taylor-series expansion of the differential coefficients since it ensures that the conservation laws are obeyed over each control-volume cell.

in [36] and it is merely stated here that all variables are assumed to vary linearly in the y and z directions and in a step-wise fashion in the x direction (i.e. the downstream value prevails over the interval  $\Delta x$  except at the upstream station itself where it changes discontinuously; this makes the numerical scheme an implicit one).

The result of these manipulations is an algebraic equation set representing the discretized form of the transport equation; one equation exists for each variable and for each grid location. The common form of the equations allows attention to be focussed on just one equation for the general variable  $\phi$ , namely equation (2.2.6); the discretized form is:-

$$\begin{aligned}
 & (C_{P\phi_P} - C_{P,U} \phi_{P,U}) + [C_n^y (\phi_N + \phi_P) - C_s^y (\phi_P + \phi_S)] \\
 & + [C_e^z (\phi_E + \phi_P) - C_w^z (\phi_P + \phi_W)] = S_{\phi,P} + \\
 & [D_n^y (\phi_N - \phi_P) - D_s^y (\phi_P - \phi_S)] + [D_e^z (\phi_E - \phi_P) - D_w^z (\phi_P - \phi_W)] \quad (2.4.1)
 \end{aligned}$$

The C's refer to coefficients derived from convective contributions in the transport equation and the D's are appropriate to the integrated diffusion terms;  $S_{\phi}$  is of course a result of the presence of a source or sink term. The individual terms are defined below with subscripts referring to locations in space (see FIG. 2.5) and superscripts referring to the co-ordinate direction for which the coefficient is appropriate;

reference may be made to FIG. 2.5 for definitions of the geometrical quantities.

$$C_{P,U} = (\rho u)_{P,u} \cdot \Delta y \cdot \Delta z \quad (a)$$

$$C_i^y = \left(\frac{\rho v}{2} u\right)_i \Delta z \Delta x \quad (b)$$

$$C_j^z = \left(\frac{\rho w}{2} u\right)_j \Delta y \Delta x \quad (c)$$

$$C_P = C_{P,U} - 2C_n^y + 2C_s^y - 2C_e^z + 2C_w^z \quad (d) \quad (2.4.2)$$

$$D_i^y = \prod_{\emptyset i} \frac{\Delta z \Delta x}{\delta y_i} \quad (e)$$

$$D_j^z = \prod_{\emptyset j} \frac{\Delta y \Delta x}{\delta z_j} \quad (f)$$

$$S_{\emptyset,P} = S_{\emptyset} \Delta x \Delta y \Delta z \quad (g)$$

here: i and j stand for locations (n,s) and (e,w) respectively in FIG. 2.5.

$\Delta x$  is the forward step size (FIG. 2.3).

Re-arranging the terms gives:-

$$\sum_{i=E,W,N,S,PU} A_i' \phi_P = \sum_{i=E,W,N,S} A_i' \phi_i + S_P^{\emptyset} \quad (2.4.3)$$

where:-

$$A'_N = D_n^y - C_n^y \quad (a)$$

$$A'_S = D_s^y + C_s^y \quad (b)$$

$$A'_E = D_e^z - C_e^z \quad (c)$$

$$A'_W = D_w^z + C_w^z \quad (d)$$

$$A'_{PU} = C_{P,U} \quad (e)$$

$$S_P^\emptyset = S_{\emptyset,P} + C_{P,U} \emptyset_{P,U} \quad (f)$$

(2.4.4)

Before proceeding to discuss the computational algorithm itself, one further modification must be mentioned. It is relevant to the calculation of the lateral convective fluxes in the equations (2.4.4). It is possible that, if the lateral convective contribution is large, the relevant coefficient  $A'$  can become negative and this causes physically implausible results\*. A discussion of this phenomenon has been given by Patankar and Spalding [11] for their finite-difference method for two-dimensional boundary layers. The cure they introduced, called the high-lateral-flux modification, has also been included in the present computational procedure. It consists of modifying the diffusion coefficients  $D$  to  $\bar{D}$ 's defined by:-

$$\bar{D} \equiv \frac{1}{2} \left\{ D + |C| + |D - |C|| \right\} \quad (2.4.5)$$

where the  $D$  and  $C$  coefficients correspond (i.e.  $D_n^y$  with  $C_n^y$ ).

---

\*The same problem causes divergence in numerical solution methods for two-dimensional recirculating flow problems; Gosman et al proposed the "upwind-difference" method as a remedial measure, similar to the cure used here, see reference [44] for details.

### 2.4.2 The Computational Algorithm

Patankar and Spalding [36] derived the SIMPLE scheme for three-dimensional parabolic flows in an effort to produce a non-iterative solution procedure. The realisation of this idea required firstly that the equations be linear; this was achieved by calculating the coefficients  $A'$  in equation (2.4.3) from values of the variables at the upstream station (any errors associated with this practice may be rendered negligible by the use of small forward step sizes). The source term  $S_P^\phi$  is also linearised by using partly upstream and partly downstream values of  $\phi$  in its calculation; further details are provided in Appendix 1. Secondly an efficient means of solving the linearised equations accurately was required; this was achieved by employing double sweeps of the well known tri-diagonal matrix algorithm (TDMA, see reference [11] for details). Thus, if equation (2.4.3) is normalised, there results:-

$$\phi_P = a_N \phi_N + a_S \phi_S + a_E \phi_E + a_W \phi_W + b_\phi \quad (2.4.6)$$

This equation is solved by applying the TDMA algorithm first say in the North-South direction, and then repeating the process by sweeping East-West. Thus, for the first (y-direction) sweep the equation is considered as:-

$$\phi_P' = a_N \phi_N' + a_S \phi_S' + (a_E \phi_E + a_W \phi_W + b_\phi) \quad (2.4.7)$$

The expression in parentheses is treated as known so that for  $\phi_E$  and  $\phi_W$ , values existing at the upstream station would be used; the dashed variables are thus the result of the first TDMA sweep; this is performed for all vertical grid lines in the calculation domain. The second, z-direction sweep is the solution of:-

$$\phi_P' = a_E \phi_E'' + a_W \phi_W'' + (a_N \phi_N' + a_S \phi_S' + b_\phi) \quad (2.4.8)$$

The results of the first sweep are thus used in the bracketed expression, and the double dashed variables constitute the result of the double TDMA sweep. This practice has been found to give accurate solution of the equations for very small numbers of sweep (usually one double sweep is sufficient for most equations).

If the pressure distribution were known, this treatment would enable the equations to be solved immediately; since this is however not usually the case, Patankar and Spalding developed a process by which the pressures could first be guessed, an approximate velocity field calculated using these pressures, and then corrections made to the pressure field in such a way as to bring the velocity field into agreement with the continuity equation. This is the central idea of the method and the exact manner in which it is accomplished is now illustrated.

Firstly consider the finite-difference forms of the continuity and momentum equations:-



Continuity

$$\begin{aligned}
 & ((\rho v)_n - (\rho v)_s) \Delta z \Delta x + ((\rho w)_e - (\rho w)_w) \Delta y \Delta x \\
 & = ((\rho u)_{P,U} - (\rho u)_{P,D}) \Delta y \Delta z
 \end{aligned} \tag{2.4.9}$$

Momentum

Axial

$$u_P = \sum_{i=N,S,E,W}^u A_i \cdot u_i + S_P^u + D_P^u \left( \frac{\partial \bar{p}}{\partial x} \right) \tag{2.4.10}$$

Lateral, Vertical

$$v_P = \sum_{i=N,S,E,W}^v A_i \cdot v_i + S_P^v + D_P^v (p_P - p_S) \tag{2.4.11}$$

Lateral, Horizontal

$$w_P = \sum_{i=N,S,E,W}^w A_i \cdot w_i + S_P^w + D_P^w (p_P - p_W) \tag{2.4.12}$$

Here FIG. 2.5 may again be referred to for geometrical quantities and the same rules apply to sub- and superscripts. The buoyancy source term has been included in  $S_P^v$  and the de-coupling of pressures is also evident; other coefficients may be defined:-

$$A_i^\phi = \left( \frac{A_i'}{\sum_{i=E,W,N,S,PU} A_i'} \right) \tag{2.4.13}$$

for each variable  $\phi$   
in equation (2.4.3)

$$D_P^u = - \Delta_x \Delta_y \Delta_z \quad (2.4.14)$$

$$D_P^v = - \Delta_x \Delta_z \quad (2.4.15)$$

$$D_P^w = - \Delta_x \Delta_y \quad (2.4.16)$$

The following steps are performed to obtain a solution to the downstream velocity and pressure field from these equations:-

- (1) Assume for the time being that  $\frac{\partial \bar{p}}{\partial x}$  is known and equation (2.4.10) has been solved to obtain the downstream u distribution. The first approximations to the lateral velocity field are determined from:-

$$v_P^* = \sum_{i=N,S,E,W} A_i^v \cdot v_i^* + S_P^v + D_P^v (p_P^* - p_S^*) \quad (2.4.17)$$

and

$$w_P^* = \sum_{i=N,S,E,W} A_i^w \cdot w_i^* + S_P^w + D_P^w (p_P^* - p_W^*) \quad (2.4.18)$$

The starred superscript on v and w indicates these are values based on a guessed pressure field  $p^*$  (usually the upstream values of pressure are the best estimate). These values of lateral velocity will not, in general, satisfy the continuity equation, but, for the point P in FIG. 2.2, will produce a net mass source for the control volume around P given by:-

$$m_P = ((\rho v^*)_N - (\rho v^*)_P) \Delta z \Delta x + ((\rho w^*)_E - (\rho w^*)_P) \Delta y \Delta x + ((\rho u)_{P,D} - (\rho u)_{P,U}) \Delta y \Delta z \quad (2.4.19)$$

(2) This mass source is reduced to zero by correcting the starred velocity and pressure field. If the correct pressure field is  $p$  then:-

$$p = p^* + p' \quad (2.4.20)$$

where  $p'$  represents the pressure-correction. The corresponding velocity corrections are expressed as:-

$$v_P = v_P^* + D_P^V (p'_P - p'_S) \quad (2.4.21)$$

$$w_P = w_P^* + D_P^W (p'_P - p'_W) \quad (2.4.22)$$

It should be emphasised that equations (2.4.21) and (2.4.22) are approximate forms of the velocity correction equations. Terms of the form:-

$$\sum_{i=N,S,E,W} A_i^V (v_i - v_i^*) \quad \text{and} \quad \sum_{i=N,S,E,W} A_i^W (w_i - w_i^*)$$

have been neglected, thus introducing further linearisation errors; however, these errors are expected to be small since, if we use a good estimate for the pressure field, the starred velocities will be close to the correct values; the saving in computer time introduced by this

approximation is appreciable.

The substitution of equations (2.4.21) and (2.4.22) into the continuity equation for the sub-domain given by the control volume surrounding P results in an equation for the pressure-correction:-

$$p'_P = \sum_{i=N,S,E,W} A_i^{P'} p'_i + S_P^{P'} \quad (2.4.23)$$

The A's involve D's,  $\rho$ 's and other geometric quantities and the mass source  $m_p$  is included in  $S_P^{P'}$ . This equation can be solved by the TDMA double sweep procedure given earlier and the correct downstream p's, v's and w's are computed from equations (2.4.20) to (2.4.22). (It may be mentioned here that equation (2.4.23) indicates why the de-coupling of pressures is necessary. This equation is of a type known as a Poisson equation and (2.4.23) is elliptic in the two space co-ordinates y and z; if  $\frac{\partial p}{\partial x}$  were not treated as known, (2.4.23) would be elliptic in all three co-ordinates and the equation set would have lost its parabolic nature; to ensure the equation is solved accurately, usually three double TDMA sweeps are employed).

- (3) The foregoing manipulations assumed that  $\frac{\partial p}{\partial x}$  was known, the way in which the value is obtained also follows a "guess and correct" procedure. Suppose an estimate of

the pressure gradient is made,  $\frac{\partial \bar{p}^*}{\partial x}$  (again normally the value determined at the previous step); a first estimate of the axial velocity field is calculated from:-

$$u_p^* = \sum_{i=N,S,E,W} A_i^u \cdot u_i^* + S_P^u + D_P^u \left( \frac{\partial \bar{p}^*}{\partial x} \right) \quad (2.4.24)$$

This preliminary velocity field may be summed over the river cross-section to deduce the total mass-flow rate over the flow domain:-

$$\dot{m}^* = \sum_{\text{all } P} \rho u_p^* \Delta y \Delta z \quad (2.4.25)$$

In general this implied mass-flow rate is different from the true mass-flow rate in the river  $\dot{m}$ . The difference leads to the correct value of axial pressure gradient; the following definitions are made:-

$$\frac{\partial \bar{p}}{\partial x} = \frac{\partial \bar{p}^*}{\partial x} + \frac{\partial \bar{p}'}{\partial x} \quad (2.4.26)$$

and

$$u_p = u_p^* + D_P^u \left( \frac{\partial \bar{p}'}{\partial x} \right) \quad (2.4.27)$$

Hence:-

$$\dot{m} = \sum_{\text{all } P} \rho u_p^* \Delta y \Delta z + \sum_{\text{all } P} \rho D_P^u \left( \frac{\partial \bar{p}'}{\partial x} \right) \Delta y \Delta z$$

and hence by manipulation and substitution of (2.4.25):-

$$\frac{\partial \bar{p}'}{\partial x} = \frac{\dot{m} - \dot{m}'}{\sum_{\text{all } P} \rho D_p^u \Delta y \cdot \Delta z} \quad (2.4.28)$$

this enables the correct axial pressure gradient to be calculated and hence the correct U velocity field.

- (4) Once the correct velocity field has been obtained, solutions for all other  $\phi$  eqns can be obtained as explained earlier in this section.

Steps (1) to (4) complete one forward step and result in values of all variables at the downstream solution plane, further forward steps are then accomplished as desired.

## 2.5 Initial and Boundary Conditions

Initial conditions are simply supplied, the known velocities at inlet are merely stored in each of the grid node locations, interpolating if necessary. The pressure too can be fed into the calculation procedure but, for the subsonic flows considered here, an arbitrary value may be supplied. Values of all other  $\phi$ 's are input in a similar manner.

An important feature of the SIMPLE method is the ease with which hydrodynamic boundary conditions are supplied. When solving for the starred velocities, the actual velocity boundary conditions can be used since the starred velocities are expected to be close to the actual values. The boundary conditions for the pressure correction are also simple; at solid boundaries and at planes of symmetry (for example the centre-plane of the river) the normal velocities are known to be zero, hence starred and actual velocities

are identical and equations (2.4.21) and (2.4.22) show that the gradient of  $p'$  normal to the boundary should be zero. At symmetry planes, boundary conditions for other variables are also of the zero gradient variety since it is known for example that the heat flux across the boundary is zero; in cases of specified flux (not always zero e.g. at a wall where the heat flux is specified), the finite-difference equations for the cell adjacent to the boundary are adjusted so that the coefficient linking the wall node to the internal node is zero, the correct flux may then be fed in via the source term.

Close to walls, the variations of velocities, temperatures etc. are often very steep and the linear profile assumptions mentioned above provide inaccurate estimates of the diffusion flux at the wall. This is particularly true in turbulent flow and the solution is to use wall-functions to calculate the true wall flux; the transport properties may then be modified so that, even when a linear profile is assumed, the correct diffusional flux is fed into the finite-difference equations; more details of this method are given for turbulent flows in the next chapter and for laminar flows in Chapter 4.

## 2.6 Stability, Accuracy and Convergence

With regard to stability, the major determinant is the forward step size  $\Delta x$ , this is particularly true for buoyant flow problems since the source term in the  $v$  momentum equation

contains the upstream temperature and to take large steps would obviously introduce instabilities. The calculations reported in this thesis have all been checked for step-length errors by repeated runs with smaller and smaller step sizes; further details are given in Chapter 6 where the predictions are presented and details of the step sizes used are presented in Appendix 1.

In order to check the accuracy of the predictions, wherever possible they are compared with exact analytical solutions. Unfortunately this is only possible for the laminar flow predictions which form only a small part of those presented; comparison with experimental data also aids confidence in accurate predictions but usually two sets of tests were performed to ensure the numerical method was truly convergent. Firstly the step size tests mentioned above were employed to check that the linearization assumptions introduced at various stages in the SIMPLE method had no effect on predictions. Secondly the grid size was successively refined in the yz plane to ensure that the discretization errors unavoidable in finite-difference methods were rendered negligible; a maximum grid size of 25 x 25 was used but usually 20 x 20 was found sufficient. At no time was it found necessary to increase the number of TDMA sweeps on the equations, except in the p' equation when three sweeps have been used throughout.



This concludes the description of the mathematical model used in this thesis; further information which was deemed not to fit well into the description given here has been relegated to Appendix 1; in particular, provided there are details of the computer program which embodies the mathematical model. The present discussion was restricted mainly to laminar flows, the flow problem of interest is however always a turbulent flow and the next chapter presents the manner in which this problem is handled.

CHAPTER 3

MATHEMATICAL MODELLING OF TURBULENCE

3.1 The Turbulence Model Approach and its Historical Background

In principle there is no need to adopt a special approach to turbulent flow, since the Navier-Stokes equations apply equally to turbulent motions as to laminar ones. The reason that this is not a practicable approach lies in the fact that important processes of turbulence take place in eddies of the order of a millimetre in size, whereas the overall flow domain (e.g. the near-field problem studied here) can extend over hundreds of metres; to apply a finite-difference method to this problem would require such a large number of grid nodes as to exceed the storage of modern computers by orders of magnitude.

The way round this problem is to concentrate attention on the time-averaged quantities of velocity, pressure etc. Hence the instantaneous value of any fluid property is expressed in terms of its time-average and fluctuating components e.g.:-

$$u = \bar{U} + u \quad , \quad p = \bar{P} + p \quad , \quad \vartheta = \bar{\vartheta} + \vartheta \quad (3.1.1)$$

(for brevity, the overbars indicating average values are now omitted from  $U, P$  etc). When the above relationships are substituted into the general equations applicable to the instantaneous flow, and these are time-averaged, there results (see e.g. Hinze [45] for details): (constant density flow is assumed).

Continuity:-

$$\frac{\partial U_i}{\partial x_i} = 0 \quad (3.1.2)$$

Momentum:-

$$\rho U_j \frac{\partial U_i}{\partial x_j} = - \frac{\partial P}{\partial x_i} + \frac{\partial}{\partial x_j} \left( \mu \frac{\partial U_i}{\partial x_j} - \overline{\rho u_i u_j} \right) \quad (3.1.3)$$

Energy:-

$$\rho U_j \frac{\partial T}{\partial x_j} = \frac{\partial}{\partial x_j} \left( \Gamma_T \frac{\partial T}{\partial x_j} - \rho t u_j \right) \quad (3.1.4)$$

Scalar Property:-

$$\rho U_j \frac{\partial \phi}{\partial x_j} = \frac{\partial}{\partial x_j} \left( \Gamma_\phi \frac{\partial \phi}{\partial x_j} - \rho \phi u_j \right) \quad (3.1.5)$$

In the above equations tensor notation has been used and all symbols are defined in the nomenclature. It can be seen however that the process of time-averaging has introduced correlations between fluctuating velocities, temperatures etc. This is the so-called "closure" problem; the Reynolds stresses ( $-\overline{\rho u_i u_j}$ ) and turbulent fluxes of heat and  $\phi$  ( $-\overline{\rho t u_j}$ ,  $-\overline{\rho \phi u_j}$ ) must be approximated or modelled (hence the name turbulence model) in terms of quantities which are known or can be determined; the modelling process is usually aided by the available experimental knowledge on turbulent flow behaviour.

Reviews of the various attempts to model the Reynolds stresses have been given recently by Launder and Spalding [46] and Harlow [47], hence only a brief resumé of the various proposals is given below so that the reasons for the choice of model adopted in this thesis are clear.

The models may be classified with reference to the number of partial differential equations they propose to solve. The earliest attempts proposed a simple algebraic equation for the Reynolds stresses ('zero-equation' level) and typical of this group is the mixing-length model of Prandtl [48]. This has most often applied to two-dimensional boundary layers with only one non-zero shear stress  $-\overline{\rho u_1 u_2}$  viz:-

$$-\overline{\rho u_1 u_2} = \rho \ell_m^2 \cdot \left| \frac{\partial U_1}{\partial x_2} \right| \cdot \frac{\partial U_1}{\partial x_2} \quad (3.1.6)$$

$\ell_m$  is the mixing length usually given in terms of the flow geometry.

In an attempt to introduce more universality into the turbulence model, researchers tried to introduce effects of local turbulence properties as well as mean-flow properties into the Reynolds stress relations. A generalisation of the Reynolds stress modelling may be written as:-

$$-\overline{\rho u_i u_j} = \mu_t \left( \frac{\partial U_i}{\partial x_j} + \frac{\partial U_j}{\partial x_i} \right) - \frac{2}{3} k \delta_{ij} \quad (3.1.7)$$

where  $\mu_t$  is the eddy- or turbulent viscosity

$k$  is the turbulence kinetic energy ( $\equiv \frac{1}{2} \overline{u_i^2}$ )

and  $\delta_{ij}$  is the Kronecker delta function.

Attention has thus been directed towards the specification of  $\mu_t$ , and this too is written in terms of local turbulence quantities; Prandtl [49] proposed:-

$$\mu_t = \rho k^{\frac{1}{2}} \ell \quad (3.1.8)$$

$k$  is obtained from a differential transport equation which can be derived from equation (3.1.3) (see Hinze [45]). The turbulence length scale  $\ell$  was originally specified algebraically making this a one-equation model.

Recently however, the difficulty of specifying  $\ell$  in complicated flows such as those containing regions of recirculation led workers to propose solving a differential transport-equation for this quantity also (two-equation model). Launder and Spalding [46] show that actually an equation is solved for another variable 'z' defined as shown below:-

$$z = k^m \ell^n \quad m, n \text{ constants} \quad (3.1.9)$$

and, knowing the distributions of  $k$  and  $z$  from solution of the differential equations,  $\ell$  can be determined. Several choices have been made for the second variable, resulting in different two-equation models; for example the  $k-k\ell$  model ( $m=n=1$ ), Rotta [50], the  $k-W$  model ( $W = k/\ell^2$ ), Spalding [51] and the  $k-\mathcal{E}$  model ( $\mathcal{E} = k^{3/2}/\ell$ ), Harlow and Nakayama [52], Jones and Launder [53].

Finally, a group of models which may be termed 'multi-equation' have been proposed. In these the concept of a turbulent viscosity

is abandoned and differential equations are solved for the Reynolds stresses themselves. Launder and Spalding [46] give details of several such models but they are still not completely developed even for two-dimensional flows; it would seem unwise therefore to consider them at present for three-dimensional boundary layer flows.

Accordingly the model used in this thesis is the two-equation  $k$ - $\epsilon$  model; a paper by Launder and Spalding [54] has explained why this model is to be preferred to others of the two-equation variety and details may be obtained in this reference; here only one justification is given, without proof, and that is that only the  $k$ - $\epsilon$  model can be applied to free-turbulent flows and turbulent flows near walls without modification; the other two-equation models all require adjustments either to the terms in the equations themselves or to some of the empirical constants which appear due to the modelling process. The reason a model at the two-equation level has been chosen is that only at this stage of complexity can reasonable universality be obtained; this has been shown by calculations with the  $k$ - $\epsilon$  model of two-dimensional boundary layers (Reference [17]), two-dimensional recirculating flows (Date [55]) and recently some three-dimensional boundary layer flows (Sharma [40], Tatchell [56]).

### 3.2 The k- $\mathcal{E}$ Turbulence Model

The derivation of the exact and modelled equations for k and  $\mathcal{E}$  is a lengthy process, the details have been given by Hanjalic [57] and are thus not included here. The model requires the solution of two differential equations, one for k the turbulence energy, and one for its rate of dissipation  $\mathcal{E}$ . The equations applicable to three dimensional flow are set out below.

$$\frac{\partial}{\partial x}(\rho uk) + \frac{\partial}{\partial y}(\rho vk) + \frac{\partial}{\partial z}(\rho wk) = \frac{\partial}{\partial y}(\Gamma_{k,t} \frac{\partial k}{\partial y}) + \frac{\partial}{\partial z}(\Gamma_{k,t} \frac{\partial k}{\partial z}) + G - \rho \mathcal{E} \quad (3.2.1)$$

$$\frac{\partial}{\partial x}(\rho u \mathcal{E}) + \frac{\partial}{\partial y}(\rho v \mathcal{E}) + \frac{\partial}{\partial z}(\rho w \mathcal{E}) = \frac{\partial}{\partial y}(\Gamma_{\mathcal{E},t} \frac{\partial \mathcal{E}}{\partial y}) + \frac{\partial}{\partial z}(\Gamma_{\mathcal{E},t} \frac{\partial \mathcal{E}}{\partial z}) + C_1 G \frac{\mathcal{E}}{k} - C_2 \rho \frac{\mathcal{E}^2}{k} \quad (3.2.2)$$

The expression for Reynolds stresses given by equation (3.1.7) is used in the momentum equations and the turbulent fluxes of temperature and  $\phi$  are modelled in a similar way:-

$$-\rho \overline{tu_j} = \Gamma_{T,t} \frac{\partial T}{\partial x_j}, \quad -\rho \overline{\phi u_j} = \Gamma_{\phi,t} \frac{\partial \phi}{\partial x_j} \quad (3.2.3)$$

The turbulent transport coefficients ( $\mu_t, \Gamma_{T,t}, \Gamma_{k,t}$  etc.) are modelled as follows:-

$$\mu_t = C_\mu \rho k^2 / \mathcal{E} \quad (3.2.4)$$

$$\Gamma_{\phi,t} = \frac{\mu_t}{\sigma_{\phi,t}} \quad \phi = T, k, \mathcal{E} \text{ etc.} \quad (3.2.5)$$

Equation (3.2.4) is an extension of the Prandtl-Kolmogorov formula (3.1.8) derived by incorporating the relationship between the length scale  $\ell$  and  $\mathcal{E}$  (obtained from dimensional analysis):-

$$\ell = \frac{k^{3/2}}{\mathcal{E}} \quad (3.2.6)$$

The laminar and turbulent diffusion terms may then be grouped together by defining 'effective' exchange coefficients:-

$$\mu_{\text{eff}} = \mu + \mu_t \quad (3.2.7)$$

$$\Gamma_{\sigma, \text{eff}} = \Gamma_{\sigma} + \Gamma_{\sigma, t} = \frac{\mu}{\sigma_{\sigma}} + \frac{\mu_t}{\sigma_{\sigma, t}} \quad (3.2.8)$$

where  $\sigma_{\sigma}$  and  $\sigma_{\sigma, t}$  are the laminar and turbulent Prandtl/Schmidt numbers, usually however the laminar contribution to the exchange coefficient is negligible.

When all these relationships are substituted into the momentum and energy equations (the continuity equation is unchanged), a final set of six differential equations results which may all be cast in a common form:-

$$\frac{\partial}{\partial x}(\rho u \vartheta) + \frac{\partial}{\partial y}(\rho v \vartheta) + \frac{\partial}{\partial z}(\rho w \vartheta) = \frac{\partial}{\partial y} \left( \Gamma_{\sigma, \text{eff}} \frac{\partial \vartheta}{\partial y} \right) + \frac{\partial}{\partial z} \left( \Gamma_{\sigma, \text{eff}} \frac{\partial \vartheta}{\partial z} \right) + S_{\sigma} \quad (3.2.9)$$

The table below shows the various coefficients in this equation for each of the variables  $u, v, w, T, k, \mathcal{E}$ .



Variable ( $\phi$ )	$\Gamma_{\phi, \text{eff}}$	$S_{\phi}$
u	$\mu_{\text{eff}}$	$-\frac{\partial p}{\partial x}$
v	$\mu_{\text{eff}}$	$-\frac{\partial p}{\partial y} + \rho \beta g (T - T_{\text{ref}})$ $+ \frac{\partial}{\partial y} (\mu_t \frac{\partial v}{\partial y}) + \frac{\partial}{\partial z} (\mu_t \frac{\partial w}{\partial y})$
w	$\mu_{\text{eff}}$	$-\frac{\partial p}{\partial z} + \frac{\partial}{\partial y} (\mu_t \frac{\partial v}{\partial z}) + \frac{\partial}{\partial z} (\mu_t \frac{\partial w}{\partial z})$
k	$\frac{\mu_{\text{eff}}}{\sigma_{k,t}}$	$G - \rho \epsilon$
$\epsilon$	$\frac{\mu_{\text{eff}}}{\sigma_{\epsilon,t}}$	$C_1 G \frac{\epsilon}{k} - C_2 \rho \frac{\epsilon^2}{k}$
T	$\frac{\mu_{\text{eff}}}{\sigma_{T,t}}$	-

TABLE 3.1 Coefficients in Turbulent Flow Equations

In the above table G represents the generation of turbulence energy due to shear forces and is written in tensor notation as:-

$$G = \mu_t \frac{\partial U_i}{\partial x_j} \left( \frac{\partial U_i}{\partial x_j} + \frac{\partial U_j}{\partial x_i} \right) \quad (3.2.10)$$

For three-dimensional boundary layer flows this reduces to:-

$$G = \mu_t \left[ 2 \left( \left( \frac{\partial v}{\partial y} \right)^2 + \left( \frac{\partial w}{\partial z} \right)^2 \right) + \left( \frac{\partial u}{\partial y} \right)^2 + \left( \frac{\partial u}{\partial z} \right)^2 + \left( \frac{\partial w}{\partial y} + \frac{\partial v}{\partial z} \right)^2 \right] \quad (3.2.11)$$

The equations in Table 3.1 thus represent the final form used for the turbulent flow calculations presented in this thesis. The introduction of the Reynolds stress relation (3.1.7) into the momentum equations (3.1.3) introduces two slight complications which have not yet been mentioned. Firstly the  $2/3k$  term in (3.1.7) has been added to the pressure term in (3.1.3) as they both are first order differentials; this has been done for convenience and has no other effect than  $p$  must be thought of as a 'modified' static pressure just as when the hydrostatic pressure field was neglected. Secondly, the Reynolds stress relation leads to diffusion terms identical with those appropriate to laminar flows but with additional terms containing gradients of  $\mu_t$  and velocities. In the present work these terms have been expressed as additional sources or sinks of momentum and hence appear in the  $S_\phi$  column in Table 3.1. They are non-zero in the lateral momentum equations only in boundary layer flow; for more details see Sharma [40].

Finally, to complete the model, values of the various constants must be supplied. Launder and Spalding [46] have shown how the values of the constants may be estimated from the available experimental data for turbulent flow. The recommended set is given in the table below; the only comment which must be made concerns the value given to the Prandtl number. In the review given in

Chapter 1 the experimental data showed that temperature diffused faster than momentum, the value of Prandtl number quoted below (0.7) is the value which reproduces this behaviour (see reference [46]).

$c_{\mu}$	$c_1$	$c_2$	$\sigma_{k,t}$	$\sigma_{\epsilon,t}$	$\sigma_{T,t}$
.09	1.44	1.92	1.0	1.3	0.7

TABLE 3.2 Values of Constants in Turbulent Flow Equations

### 3.3 Initial and Boundary Conditions in Turbulent Flow

#### Initial Conditions

The practice proposed in an earlier section for specifying the inlet velocities and temperatures obviously still applies in turbulent flow; additional arrangements must be made for input of the values of  $k$  and  $\epsilon$  at the starting plane and these are now outlined.

If the experimental data has included measurements of turbulent kinetic energy at the inlet, then these can be fed into the program in a similar manner to velocity. Usually however this is not the case; some means must be established for estimating the likely value of  $k$ . The normal practice is to estimate the turbulence

intensity at each grid point; this is defined as:-

$$i = k_p / U_p^2 \quad (3.3.1)$$

In the calculations presented here, a uniform value of  $i$  has been assumed, usually at a level which corresponds to an intensity of approximately 3%. This is a typical figure for low intensity free stream turbulence; the value of  $i$  has been varied to determine its effect and this is discussed in a later chapter.

Once the value of  $k$  is fixed, equation (3.2.6) provides a means for calculating  $\mathcal{E}$ ; this equation may be re-written:

$$\mathcal{E}_p = k_p^{3/2} / \ell$$

The problem now becomes one of estimating  $\ell$ , the 'dissipation' length scale at each point in the inlet plane. It may be shown that the mixing-length  $\ell_m$  is related to  $\ell$  via:

$$\ell = c_\mu^{-3/4} \cdot \ell_m \quad (3.3.2)$$

where  $c_\mu$  is a constant in the turbulence model with a value given in TABLE 3.2. The problem of estimating  $\ell_m$  is easier than guessing  $\ell$  as more information is known about the values of  $\ell_m$  suitable for various flows. In the calculation of developing rectangular duct flows for example, Tatchell [56] has found that the relation below produces good agreement with experiment

$$\ell_m = .07 H \quad (3.3.3)$$

where  $H$  is the height of the duct. In Tatchell's calculations the precise value for  $\ell_m$  did not affect the predictions. In the present study, this was found not to be the case but a fuller explanation and discussion is left to Chapter 6 where predictions are presented.

### Boundary Conditions

For the problems studied here, three kinds of boundary occur; FIG. 1.4 shows that they are solid boundaries, planes of symmetry (the presence of symmetry is always taken advantage of in the calculations so that the available grid nodes are spread over as small an area as possible) and finally the water surface. In this thesis this last mentioned boundary has been treated also as a plane of symmetry; certainly for most variables this assumption is reasonable; for example in the near field it is known that the heat flux through the water surface is very small (see reference [1]). Exactly how the turbulence quantities vary in the region of a water/air interface is not well understood, in the first instance therefore the present treatment seems justified.

At planes of symmetry, the zero flux condition is easily enforced merely by nullifying the link between boundary node and internal node; this is done for all variables except of course for the velocity normal to the boundary which has been set to zero.

The solid boundaries pose a more difficult problem in turbulent flow due to the steep variations which were mentioned

in the previous chapter. The 'wall-function' method is used here and this is explained below although it must be noted that for many of the experiments to be predicted, the wall boundaries are so far removed from the region in which the buoyant jet spreads that they exert negligible influence on the flow.

FIG. 3.1 indicates three typical near-wall cells; only velocities parallel to walls are considered because, for normal velocities, the diffusion towards the wall is merely assumed to be zero and hence no special practice is necessary. For parallel velocities however, the diffusion flux at the wall would normally be calculated inaccurately via the usual linear profile method. The wall-function method still applies the same formula for the wall flux, so that when considering the diffusional flux of  $\phi$  through the wall in FIG. 3.1(a), the linear profile assumption implies:-

$$\dot{\phi}''_s = \int_0^s \left( \frac{\phi_P - \phi_S}{\delta} \right) \quad (3.3.4)$$

but now a modified transport coefficient is used so that the wall flux has the correct value. For velocities it is well known that the universal logarithmic profile describes the variation normal to the wall (this applies to the cells sketched in FIG. 3.1 only if the point P lies far enough away from the wall to lie in the 'fully-turbulent' region, for the grids considered here this is always the case); this profile may be written

$$\frac{u}{u_\tau} = \frac{1}{\kappa} \ln \left( E \frac{\delta u_\tau}{\nu} \right) \quad (3.3.5)$$

here  $u$  is the velocity parallel to the wall,  $\delta$  is the distance normal to the wall,  $E$  and  $\chi$  are constants in the log-law (given values here of 9.0 and 0.42 respectively), and  $u_\tau$  is the friction or shear velocity defined as:-

$$u_\tau = \sqrt{\frac{\tau_w}{\rho}} \quad (3.3.6)$$

where  $\tau_w$  denotes the wall shear stress. Thus equations (3.3.4) (written for  $\phi = u$ ) and (3.3.5) may be combined to give a value for the transport coefficient which, when used in (3.3.4) will give the correct shear stress. This modified value is then stored at the near wall point and used in diffusion flux calculations.

An analysis of the variation of other variables  $\phi$  near walls shows that a relationship similar to (3.3.5) can be devised. The relationship used in this thesis is:-

$$\frac{\phi_P - \phi_{wall}}{\left(\frac{\phi''_{wall}}{\rho u_\tau}\right)} = \frac{1}{\chi} \ell_n \left( E \frac{\delta u_\tau}{\nu} \right) + P_\phi \quad (3.3.7)$$

$P_\phi$  denotes a function representing the relative resistance of the wall region to fluxes of  $\phi$  and velocity;  $P_\phi$  is a function of the laminar and turbulent Prandtl/Schmidt numbers and, for heat transfer, Spalding and Jayatilaka [58] deduced the function shown below from experimental data; this formula is used here:-

$$P_\phi = 9.24 \left( \left( \frac{\sigma_T}{\sigma_{T,t}} \right)^{0.75} - 1 \right) \cdot \left( 1 + 0.28 e^{(-0.007 \frac{\sigma_T}{\sigma_{T,t}})} \right) \quad (3.3.8)$$

So equations (3.3.4) and (3.3.7) are again combined to deduce a value for a modified near-wall  $\int_{\phi}^{\Gamma}$ .

The boundary conditions for the turbulence properties are also derived from experimental evidence. The existence of a region near walls where the shear-stress is almost uniform is well established. It is also observed that there is near-balance between the generation and dissipation of turbulence energy and that the diffusion of  $k$  is negligible (see, for example Rodi [5]). The simplified form of the  $k$  equation then leads to a formula for  $k$  at the near-wall point:-

$$k_p = u_{\tau}^2 / C_{\mu}^{\frac{1}{2}} \quad (3.3.9)$$

The value of  $k_p$  is fixed at this level for all points near walls, how the 'fixing' is accomplished is explained in the next chapter. Similarly, it is known that, in the constant-stress layer the mixing length is proportional to distance from the wall (the proportionality constant is Von-Karman's constant  $\mathcal{K}$ ). This fact, together with equations (3.3.9) and (3.2.6) enables the near-wall  $\mathcal{E}$  value to be calculated from:-

$$\mathcal{E}_p = \frac{u_{\tau}^3}{\mathcal{K} \delta} \quad (3.3.10)$$

Again, the value at the near wall point is 'fixed' at this level; this then completes the boundary conditions for turbulent flow.



CHAPTER 4

A PROCEDURE FOR HANDLING IRREGULAR BOUNDARIES

4.1 Outline of the Problem

The application of the finite-difference method outlined in chapter 2 to the calculation of fluid flow problems requires the use of a network of grid nodes linked by a suitable co-ordinate system. The system used here is the rectangular cartesian system  $(x,y,z)$  but often a cylindrical polar system  $(r,\theta,z)$  or, rarely, a general orthogonal set  $(\xi_1, \xi_2, \xi_3)$  has been proposed. However the solid boundaries in many problems will rarely conform to the first two and the derivation of a convenient orthogonal set is often a laborious task. In the interests of economy and generality it would be useful to be able to treat any shape of solid boundary whilst retaining the same (and simple) co-ordinate system for use in the finite-difference equations. This is especially true in river flow problems and FIG. 4.1 sketches the situation if a cartesian finite-difference grid was set up over a typical river cross-section or a typical non-uniform duct flow.

The present chapter outlines a procedure which has been developed for handling irregular boundaries; this is contained in the next section; since the grid system used is a cartesian one, the method is suitable for flows contained within non-rectangular boundaries. In Section 4.3 the procedure is validated for laminar flows and in the following section predictions of turbulent flow are presented. A procedure which accomplishes

the same aims as the present method has been reported by LeFeuvre [59] who studied (two-dimensional recirculating) flow over cylinders; the calculation procedure used there was, however, based on a different approach with stream function and vorticity as the dependent variables, it hence bears only superficial similarity with the present method.

#### 4.2 A Method for Irregular Boundaries

An illustration of the kind of situation which arises in irregular boundary problems is given in FIG. 4.2; this may be considered as a magnified picture of a small part of the river bed or the duct wall in FIG. 4.1, the solid boundary (shown cross-hatched) does not now lie along the grid lines and indeed some of the grid nodes do not even lie in the region of fluid flow (W and N in FIG. 4.2). The overall problem may be sub-divided as follows:-

- |   |                               |
|---|-------------------------------|
|   | a) External to solid boundary |
| 1) Identification of position of grid nodes | b) Internal and near boundary |
|   | c) "Fully" Internal           |
| 2) Special treatment for nodes of type a)   |                               |
| 3) Special treatment for nodes of type b)   |                               |

Obviously the fully internal nodes may be treated as before; each of the above will now be dealt with in turn.

#### 4.2.1 Grid Node Identification

The difficulty here is overcome by attaching a 'tag' to each node. Because of the staggering of the grid system, three separate arrays are used to indicate exactly where each node lies; the arrays are two-dimensional with the three different node types identified as follows:-

external points	-	tagged as 3
internal, near wall points	-	tagged as 2
completely internal points	-	tagged as 1

The arrays are examined by the program to decide whether any special treatment is necessary at any grid point. Those tagged as 1 can be treated exactly as before; for the 2 and 3 locations the particular treatment is outlined below.

#### 4.2.2 Handling of External Nodes

This problem arises because the equations are still solved at the external nodes, even though this is strictly unnecessary (it is done so as to keep intact as much of the standard computer program as possible). The solution at these points should be one which will not upset the rest of the calculations at the more important nodes inside the flow domain; this is achieved by 'fixing' the solution at external nodes to some chosen value - this practice was also referred to in the last chapter, where the wall boundary conditions for the turbulence quantities were enforced by fixing the near-wall values; how this is achieved

is now outlined.

Consider the point N in FIG. 4.2 as a typical external node, the finite-difference equation for a general fluid property solved at this point has been given by equation (2.4.3); this may be re-written:-

$$\phi_N = \sum_{\substack{i=\text{points} \\ \text{surrounding N.}}} a_i \phi_i + S_{U,N} + S_{P,N} \cdot \phi_N \quad (4.2.1)$$

The equation has been normalised to make the coefficient of  $\phi_N$  unity and the source term has been linearised (details have been given of the reasons for using linearised sources in Appendix 1).

A value of  $\phi_N$  may be fixed by putting:-

$$\begin{aligned} S_{U,N} &= M \cdot \phi_{N, \text{Desired}} \\ S_{P,N} &= -M \end{aligned} \quad (4.2.2)$$

where M is a very large number (say  $10^{30}$ ). All the other terms in the equation are thus rendered negligible and the desired value is always returned at N when the equation is solved. For velocities it is necessary to store zero (or very small) values outside the walls so that calculations of the total duct mass flow rate are undisturbed.

### 4.2.3 Handling of Near-Wall Nodes

The solution here falls into two parts. Firstly, the links between external and internal nodes are broken; the usual formulae used to express convection and diffusion along these links are obviously no longer applicable, so the treatment adopted here is to put both these influences to zero (convection towards the wall will certainly be negligible in many cases for the near-wall region). Secondly the effects of the presence of the solid boundary are taken into account; this includes allowing for walls of the control volume being cut short by the presence of the boundary, modifying the area of the control volume face perpendicular to the predominant flow direction, and introducing the effects of wall shear stress (or flux of  $\phi$ ) into the equations via the wall-function method described earlier.

For the three velocities, pressure, and all  $\phi$ 's, the links are broken in the same manner; consider the finite-difference equation for point P in FIG. 4.2:-

$$\phi_P = \sum_{\substack{i=\text{nodes} \\ \text{surrounding P}}} a_i \phi_i + S_{U,P} + S_{P,P} \cdot \phi_P \quad (4.2.3)$$

this may be re-arranged to give:-

$$0 = \sum_{i=S,E,W} C_i' (\phi_i - \phi_P) + C_N' (\phi_N - \phi_P) + S_{U,P} + S_{P,P} \cdot \phi_P \quad (4.2.4)$$

The second term represents the convection and diffusion processes

along the N-P link (an external/internal one) which must be nullified; the following substitutions are made:-

$$S_{U,P} = -C'_N \varphi_N \tag{4.2.5}$$

$$S_{P,P} = C'_N$$

and the link is thus completely severed. Other devices having the same effect could have been employed, however the use of the linearised source terms has again been adopted as the one requiring a minimum of disruption to the computer program.

Having broken the external/internal link, the presence of the solid boundary must now be fed into the finite-difference equation for points such as P; it has been found necessary to vary the modifications depending on the variable in question, each one will thus be considered in turn.

#### u velocity and $\varphi$ 's

$\varphi$  here is restricted to mean the temperature equation; the  $k$  and  $\mathcal{E}$  values at near-wall cells are fixed at the values given by equations (3.3.9) and (3.3.10). As long as the near-wall point is in the fully turbulent region, equation (3.3.9) is correct; the effect of the wall shape is felt in (3.3.10) by using for the distance  $\delta$  in that equation the distance normal to the wall as shown in FIG. 4.2; these treatments have been found sufficient for the turbulence quantities.

For axial velocity and temperature, other arrangements are made; at each boundary cell, the following parameters are stored (see FIG. 4.2).

- . The length of wall present in the cell -  $\ell$
- . The distance of the node from the wall -  $\delta$
- . The area of cell (enlarged or decreased) -  $A$
- . The new lengths of cell walls - e.g.  $\ell_1$
- . The value of  $\phi$  on the wall -  $\phi_{\text{wall}}$

The area  $A$  is used instead of  $\Delta y \Delta z$  as the area of the control volume face in the  $yz$  plane in all calculations at node  $P$  (for example in the  $x$ -direction convection terms). The new cell wall lengths are used to modify the combined convection and diffusion flux across the respective cell walls. It should be borne in mind that in FIG. 4.2 the new length  $\ell_1$  is less than the length used in the standard calculations (in this case  $\Delta y$ ) but it may equally be greater for other boundary shapes. If the combined flux calculated in the normal way is  $J_\phi$  then the corrected flux is fed in by simple modifications e.g. for the east cell wall in FIG. 4.2:-

$$J_{\phi, \text{new}} = J_\phi \cdot \frac{\ell_1}{\Delta y} \quad (4.2.6)$$

The other parameters are used to calculate the shear-stress or heat flux due to the wall on the control volume cell. The wall function method is again used here; for example the wall shear stress is written:

$$\tau_{\text{wall}} = \mu_P \frac{U_P}{\delta} \quad (u_{\text{wall}} = 0) \quad (4.2.7)$$

with the normal linear profile assumption made for the velocity gradient terms; to ensure this is accurate enough, a modified value of  $\mu_P$  is used to transfer the correct wall shear into the finite-difference equation at P. An example of a turbulent wall function was given in the last chapter. Here a laminar example is included. The equivalent of the log-law which tells us the shape of the velocity profile in the near-wall region is (see Patankar and Spalding [11]) for laminar flow:-

$$S = \frac{\tau_{\text{wall}}}{\rho U_P^2} = \frac{1}{\text{Re}} - \frac{F}{2} \quad \text{where} \quad \text{Re} = \frac{\rho U_P \delta}{\mu_{\text{lam}}} \quad (4.2.8)$$

$$F = \frac{\frac{dp}{dx} \cdot \delta}{\rho U_P^2}$$

hence:-

$$\tau_{\text{wall}} = S \rho U_P^2 = \mu_{P,\text{mod}} \cdot \frac{U_P}{\delta}$$

$$\text{i.e.} \quad \mu_{P,\text{mod}} = S \cdot \rho U_P \cdot \delta = S \cdot \mu_{\text{lam}} \cdot \text{Re} \quad (4.2.9)$$



where  $\mu_{\text{lam}}$  is the laminar viscosity. The shear stress is fed into the finite-difference equations via the linearised source arrays:-

$$S_{U,P} = 0 \quad S_{P,P} = S_{P,P} - \mu_{P,\text{mod}} \cdot \frac{\ell \cdot \Delta x}{\delta} \quad (4.2.10)$$

Obviously  $S_{U,P}$  would be finite for the temperature equation where the wall value is not zero; in (4.2.10)  $\ell \cdot \Delta x$  is the area of wall over which the wall shear acts,  $\Delta x$  being the forward step length.

#### lateral velocities v and w

Several modifications have been tried for the near wall lateral velocities, all of which have produced acceptable results. The final method bears similarities to the treatment of these velocities near rectangular walls as outlined in section 2.4.1; the near-wall v and w velocities are considered displaced so that they lie on the duct wall; they are displaced along the link with the external node which is the shortest, thus in FIG. 4.3 the v velocity has been moved horizontally. This lateral velocity may then be fixed to zero (for a non-rotating wall) by the method outlined earlier. The question now arises how the surrounding v velocity nodes may realise this node has been shifted (for example  $v_w$  in FIG. 4.3). Analagous with the treatment given for boundaries which coincide with grid lines, the cell wall AB should also be considered shifted so that it

lies along CD in FIG. 4.3. However this would require new areas to be stored at the lateral velocity locations just as they were at near-wall u nodes; in the calculation performed here, this amount of refinement has been found unnecessary and the only modification which has been made is to the diffusion flux along the link which has been tampered with (the W-P link in the example sketched in FIG. 4.3). For cell wall AB, the diffusion coefficient calculated in the standard manner is (see equation (2.4.2)):-

$$D^z = \int_{\emptyset}^1 \frac{\Delta_y \Delta_x}{\delta z_1} \quad (4.2.11)$$

this is modified for all situations such as the one sketched to read:-

$$D_{\text{mod}}^z = \int_{\emptyset}^1 \frac{\Delta_y \Delta_x}{\delta z_2} \quad (4.2.12)$$

This is done for all near-wall v and w nodes.

One final consequence of the displacement has not been mentioned; if the near-wall velocities are moved alternative means must be used for calculating some lateral convection fluxes for near-wall u cells. In FIG. 4.4 a typical situation is illustrated. Although the v and w velocities of cells P and E are considered moved to the wall, lateral convection fluxes are still required at points w, s, e and se. These are interpolated from the nearest v and w velocities for which solutions are

obtained; again the interpolation has usually been chosen to be in the direction in which the near-wall velocity has been displaced so that the vertical flux at point  $s$  in FIG. 4.4 is estimated from:-

$$(\rho v)_s = (\rho v)_{ss} \frac{(y_2 - y_1)}{y_2} \quad (4.2.13)$$

This is equivalent to a linear interpolation, but in turbulent flow other formulae have been used e.g. log-law or power-law variation away from the wall, negligible differences in predictions resulted.

#### pressure correction $p'$

For this equation, no wall functions are necessary; as long as the mass-source in each cell is evaluated correctly using the distorted area  $A$  for longitudinal velocity and also perhaps the interpolated lateral fluxes above (combined with new cell wall lengths), the external/internal links are merely broken and the equation is solved as before; the velocity correction is then only affected at those lateral velocity nodes not fixed at zero values.

The above description has referred to several parameters to be specified at each near-wall cell, how this is done depends on the shape of the boundary. In general, having chosen the grid, this may be drawn out, the irregular boundary superimposed and the near-wall cells noted for all variables. The parameters

necessary in the irregular boundary treatment can then be measured (distances areas etc.) and fed into the program as data to merely fill out the relevant arrays. For the calculations presented here this has sometimes been done; for convenience however, since the boundaries used for testing could be described as functions of  $y$  and  $z$ , a subroutine was written which, for any specified grid automatically determined which nodes lay inside and outside, assigned the relevant tags and calculated the various parameters; however, the remarks about arbitrary irregular boundaries still apply so that the method is quite general.

#### 4.3 Testing in Laminar Flows

##### 4.3.1 Introduction

The procedure developed in the last section has been applied to two cases of laminar duct flow. Firstly it was applied to laminar flow inside circular tubes; this geometry was chosen since, although the flow is actually two-dimensional, the non-conformity of the circular boundary to the rectangular grid presents a simple example of an irregular boundary problem. In addition, solutions exist for both fully-developed and developing velocity fields and the success of the method can be checked against these solutions. The fully-developed velocity profile is of course the well known parabolic Poiseuille profile; analytical approaches to the developing flow have been made in References [61-66] (a useful summary of these methods is contained in the first reference); the most commonly

quoted experimental data are those of Nikuradse [67] but these have sometimes been questioned (Reference [64] and discussion of Reference [65]); accordingly they are not used here but the more recent data of References [68] and [69] are used instead.

The above calculations are unsatisfactory in some ways since they do not take full advantage of the three-dimensional nature of the computer program. A search was thus made for a suitable duct geometry which could be used to test the program in a more complex situation. After reviewing the literature a choice was made to predict flow in ducts of elliptic cross-section (a review of the literature on elliptic duct flow is given in Appendix 2). The reasons for the choice of this section are as follows:-

- In laminar fully-developed flow an exact solution exists for comparison purposes.
- In turbulent fully-developed flow a source of experimental data was found (References [70] to [74]), these will be used in the following section.
- An attempt has been made (Reference [72]) to calculate the turbulent fully-developed flow with the two-dimensional elliptic flow method of Reference [44] and a "regular" boundary finite-difference grid (using con-focal elliptical cylindrical co-ordinates). This resulted in numerical problems due to the geometrical properties of the co-ordinates; an opportunity therefore presented itself to underline the advantages of the irregular boundary treatment.

- Both laminar and turbulent flows have practical relevance; elliptic tubes are used in compact heat exchangers where the flow may often be laminar; the turbulent flow problem is relevant to the cooling channels in gas turbine blades which are sometimes of elliptic cross-section.
- The cross-section of a straight river away from the influence of bends can be approximated by an ellipse of large aspect ratio; to test the irregular boundary procedure in an elliptic duct flow is a preparatory step to making illustrative calculations of full scale river thermal discharge calculations. These predictions form the basis of Chapter 7 of this thesis.

The results for laminar flow in circular and elliptic ducts are presented in the next two sub-sections and the turbulent flow predictions follow; in all cases, because of the symmetry of the problem, only one quadrant of the duct has been considered; the usual zero gradient boundary conditions have been imposed on the vertical and horizontal planes of symmetry; the equations solved are those outlined in section 2.2.2.

#### 4.3.2 Application to Laminar Circular Duct Flow

##### Uniform inlet conditions

The first predictions were obtained with plug-flow conditions specified at the inlet. FIG. 4.5 shows axial velocity profiles

at various axial stations predicted with a 10 x 10 uniform grid. The calculations are compared with predictions that have been made with the Patankar and Spalding two-dimensional boundary layer computer program [11] and agree very well. Points are plotted from both symmetry axes and from the 45° diagonal (AC in FIG. 4.5). Since all points fall on the same profile then it can be seen that symmetry results at all stations even though a cartesian grid system has been used. The final profile matches the parabolic fully-developed Poisseuille solution to a very good accuracy.

The velocity profile is plotted in a different way in FIG. 4.6 which concentrates attention on just two radial locations. Comparison is made here with other analytical data from the references quoted above, and again good agreement is obtained. It should be noted that the largest discrepancies occur when comparing with the methods of References [63] and [65]. Both these involved approximations (either linearisations of the momentum terms or profile assumptions) and so will be less accurate than References [61], [64] and [11] which involve finite-difference solutions of the unmodified flow equations. The agreement with these latter methods is very good, being everywhere within two per cent. In FIG. 4.7 the same predictions of the three-dimensional boundary layer program (3DBL) are plotted against the available experimental data; satisfactory agreement is again achieved.

The pressure development predictions are shown in FIG. 4.8,

corroborated by the results of Manohar as reported by Shah and London [61]. This graph shows also how little change is observed as the cross-stream grid is refined from 10 x 10 to 20 x 20 (both uniform) and hence the velocity results given earlier were grid independent; step length tests showed that results were independent of this parameter also. The two-dimensional program produces a slightly different curve, but this is thought to be due to inaccuracy in the treatment of the near-wall region in the program used; certainly the fully-developed value of the axial pressure gradient is predicted better by the 3DBL program.

As a final comparison, the pressure drop coefficient may be plotted; this is defined as:-

$$K_p = \frac{(p_o - \bar{p})}{\frac{1}{2}\rho\bar{u}^2} - \frac{f \cdot x}{r_o} \quad (4.3.1)$$

where  $f$  is the laminar flow friction factor. Hence  $K_p$  may be thought of as the additional pressure loss due to entrance effects. FIG. 4.9 shows that the predictions are again in accord with other analyses (Sparrow's [63] calculations involved a linearisation of the momentum terms and so will be less accurate).

#### Non-uniform inlet conditions

As an example of the handling of different inlet conditions, a confined jet-mixing problem was considered. In this case a radial discontinuity is present in the inlet velocity profile (see FIG. 4.10); the following method was devised for ensuring



the correct jet and annulus mass flow rates at the start of calculations, and the correct distribution of mass flow amongst the rectangular control volume cells.

Consider an area of the duct cross-section in the region of the velocity discontinuity (FIG. 4.12). The velocity in the shaded region  $A_1$  will normally be treated as that of the jet since  $A_1$  is part of a cell whose node lies inside the discontinuity. However, the velocity should really be that of the annular flow since  $A_1$  actually lies outside the discontinuity. In the program it is easier to change densities than areas, hence a 'modified density' approach has been adopted; accordingly the densities at points such as X are changed so that the correct flow rate is used. For the case illustrated the density at X would be changed to:-

$$\rho_X = \rho \cdot \frac{((A - A_1) \cdot u_{JET} + A_1 \cdot u_{annulus})}{A \cdot u_X} \quad (4.3.2)$$

where  $\rho$  is the normal fluid density and A is the area of the rectangular cell surrounding X.

FIGS. 4.10 and 4.11 show the velocity development in this situation. The profiles are again compared with predictions obtained with the Reference [11] program and are once more satisfactory. In FIG. 11 we can see that the modifications described above have only a small effect; when the program is run without the alterations to the densities, the discrepancy in mass flow rates is (for the grids shown) not enough to cause

large differences in the predictions. Grid refinement to 20 x 20 uniform also does not increase the accuracy of the plots. The pressure development is very similar to that for uniform inlet conditions and so has not been included.

#### 4.3.3 Application to Laminar Elliptic Duct Flow

As mentioned above, a review of flow and heat transfer in elliptic ducts is given in Appendix 2; in this section the results for laminar flow will be used to check the predictions made. For the purpose of the test the geometry of the duct was chosen to be that shown in FIG. 4.13 with an aspect ratio of 0.5, all relevant parameters are defined there.

For the developing flow field, the review shows that no analytical solutions are available; therefore recourse had to be made to the grid refinement and step length tests referred to in Chapter 2, examples are now given of these tests to illustrate how they are used. FIG. 4.14 gives the axial pressure development in the duct for a Reynolds number of 130\* and a mean velocity of 100 m/s (both density and viscosity have been specified as unity for convenience). Four separate grids have been used (all uniform) and it can be seen that only for the two coarsest grids does the prediction alter. These calculations have been made with just one set of forward step parameters, so these must now be scrutinised. The forward stepping mechanism is governed by three

---

\*The Reynolds number has been defined using the hydraulic diameter, as given in Appendix 2.

parameters, the initial step length, the maximum step length and the rate at which the actual step length moves between these extremes. The simplest way of defining the forward step is by taking it as some specified fraction of a fixed geometrical quantity; the duct height (b in FIG. 4.13) has been used in these calculations so that the initial and maximum step sizes are defined as:-

$$\begin{aligned}\Delta x_{\text{initial}} &= \text{FRAS}_{\text{initial}} \cdot b \\ \Delta x_{\text{max}} &= \text{FRAS}_{\text{max}} \cdot b\end{aligned}\tag{4.3.3}$$

at steps intermediate between these locations, the value of FRAS to be used is increased from the value at the last step by the expansion rate parameter EX:-

$$\text{FRAS}_{\text{step I}} = \text{EX} \cdot \text{FRAS}_{\text{step I-1}}\tag{4.3.4}$$

this is of course over-ridden if the value exceeds the specified maximum. The reason for using this type of variation is that the step size may easily be changed from the small size necessary near the inlet of the duct where rapid changes occur, to relatively large steps when a fully developed state is approached.

FIG. 4.15 indicates the behaviour for a mean velocity of 300 m/s (Reynolds number = 390) in the same elliptic duct. This time just one grid has been used and the graph is drawn for a 20 x 20 uniform grid. Very little variation in the pressure development can be observed and the conclusion is that the step size parameters are exerting no influence. In all further calculations to be presented, a 20 x 20 grid and the first set of step size parameters in FIG. 4.15 have been used.

In fully-developed flow an exact solution exists in which the axial velocity is a parabola along both axes. FIG. 4.16 shows that the predictions agree well with this. FIG. 4.18 shows the predicted fully-developed friction factor/Reynolds Number relationship and again the agreement with the exact solution given by Shah and London [61] is excellent. The final comparison in fully-developed flow emphasises the three-dimensional nature of the problem. Previously, for the circular duct, the wall shear stress was constant around the periphery due to the axial symmetry FIG. 4.17 shows that for an elliptic cross-section this is not the case, the graph also illustrates that the irregular boundary can adequately cope with this situation as it reproduces the exact solution of Barrow and Roberts [71] very well.

As an example of how the developing flow solutions could be used, FIG. 4.19 has been included. This deduces from the program output the law which governs the hydrodynamic development length (an important quantity in compact heat exchanger design). This latter quantity has here been defined as the length of duct

required for the centre-line axial velocity to reach 95% of its fully developed value. FIG. 4.19 has been drawn for an aspect ratio of 0.5 but obviously other ellipses or other duct shapes could be used to discover the development length law. The points collapse onto the line:-

$$\frac{x_{dev}}{d_h} = .036 \cdot Re_{d_h} \quad (4.3.5)$$

where  $d_h$  is the hydraulic diameter defined as:-

$$d_h = \frac{4 \times \text{Cross-Sectional Area}}{\text{Wetted Perimeter}} \quad (4.3.6)$$

#### 4.4 Testing in Turbulent Flows

##### 4.4.1 Introduction

The preceding section has applied the irregular boundary procedure to two cases of laminar duct flow; this section now extends the treatment to include turbulent flows. In the first instance only the hydrodynamic problem is considered and the calculation of turbulent flows with buoyancy is left until Chapter 7. For turbulent flow no exact solution exists and the numerical tests are again used to check predictions; where possible, experimental results are used to assess the accuracy of the calculations. Again circular and elliptic ducts have been

considered; the results of applying the  $k-\epsilon$  model as described in Chapter 3 with the irregular boundary treatment will now be presented.

#### 4.4.2 Application to Turbulent Flow in Circular Duct

For fully-developed flow, the experimental results of Laufer [75] are available for comparison; FIG. 4.20 gives the predictions of the mean velocity profile for a Reynolds number based on centre-line velocity of  $5 \times 10^5$ . The predictions show that when the grid is refined from  $16 \times 16$  to  $20 \times 20$  only a very small change results; the symmetry of the predictions is also confirmed by the points plotted for the diagonal profile. The agreement is everywhere to within 4% of the experimental results and is very close to predictions made with the two-dimensional boundary layer program of reference [11]. The next graph shows comparisons of the predicted turbulent kinetic energy profiles with Laufer's measurements; the discrepancies are slightly larger in this case but, once more, the results are in good agreement with the two-dimensional predictions.

The developing flow in a circular tube has been studied experimentally by Barbin and Jones [76]; in addition some predictions using the program of Reference [11] have been made available by Ammar [77]. FIG. 4.22 presents the longitudinal velocity profiles at three axial stations (non-dimensionalised by the pipe diameter), agreement is very good with both two-dimensional analysis and experiments. In a similar manner to

the laminar flow results, FIG. 4.23 is plotted to show the axial development at just three radial positions; the experimental behaviour is reproduced very faithfully with the largest discrepancy being for the point closest to the wall. For the centre-line velocity it should be noted that at the downstream end both sets of predictions decrease whereas the experiments tend if anything to remain constant. Much further downstream the experimental value must drop as the level shown in FIG. 4.23 is above the fully developed centre-line value. Finally, the axial development of mean pressure is given in FIG. 4.24; the agreement with the developing flow solution of Reference [77] is good and the graph also indicates excellent agreement for the fully-developed pressure gradient as calculated from Prandtl's friction law for circular tube flow (see Reference [37]):-

$$\frac{1}{\lambda} = 2.0 \log \left( \rho \frac{\bar{u}d}{\mu} \cdot \lambda \right) - 0.8 \quad (4.4.1)$$

where  $\lambda = \frac{-\frac{dp}{dx} \cdot d}{\frac{1}{2}\rho\bar{u}^2}$  (4.4.2)

#### 4.4.3 Application to Turbulent Flow in Elliptic Ducts

The theses of Cain [70], [72] contain the only source of experimental data for turbulent flow in elliptic ducts which has been discovered. Air flow through stainless steel ducts was used and one of the ducts was of aspect ratio 0.5 as in the laminar flow calculations, hence this has been used for the present study

for convenience. Heat transfer results were also obtained but only the hydrodynamic problem is considered here.

For fully-developed flow, the experiments produced a friction factor versus Reynolds number relationship as shown in FIG. 4.25. The predictions using the irregular boundary treatment underpredict the data by 12%; the results shown are for a 20 x 20 grid but both grid and step length tests failed to alter the predictions. The probable explanation for this discrepancy lies in the phenomena known as turbulence driven secondary flows. This phenomena was first observed by Nikaradse [37] who made velocity measurements in rectangular and triangular ducts and noticed that the velocity contours bulged outwards towards the corners of the duct (this distortion of the velocity contours is also present in elliptic ducts as will be seen later). Further research (Brundrett and Baines [78]) enabled the cause to be attributed to variations in the normal Reynolds-stresses in the duct cross section, these variations give rise to a source of stream-wise vorticity causing lateral flows in the fully-developed state which are absent in circular geometries; it is the lateral flows which distort the velocity contours. It is also well known that no turbulence model which assumes an isotropic viscosity can predict the presence of secondary flows and this then explains the underprediction of the friction factor. Recently several approaches have been made to include the effects of anisotropic viscosity without solving the full Reynolds-stress equations; the technique is known as an algebraic Reynolds-stress model



(see Rodi [5]) and has been successfully applied to the prediction of secondary flows in ducts of square cross-section (see Tatchell [56], Launder and Ying [79]).

FIG. 4.26 presents predictions of the local wall shear stress measured around the periphery of the duct. The agreement is very good except near the major axis where the predictions tail off but the data remains approximately level; again the flows in the plane of the duct will affect the wall shear. Absence of secondary flows also causes errors in the velocity profile predictions as shown in FIG. 4.27. The agreement is good, to within 10%, but the experiments show the profile along the major axis to lie above the minor axis data whereas for the prediction the reverse is true; it may be expected that this is due to secondary flows since these cause fluid to be directed towards the corners of the duct i.e. along the major axis increasing the velocities in the corner regions.

The inadequacy of the turbulence model is shown best in FIGS. 4.28a and 4.28b; the predicted fully developed velocity contours (top graph), although showing reasonable agreement with the contour values, show no distortions and individual contours do not enclose the same areas as do the corresponding contours in the bottom graph. It may be noticed that the outermost contour ( $u/\bar{u} = 0.8$ ) is well predicted as this lies in the region near the wall where the experiments show secondary flows have negligible influence.

The experiments did not include measurements of turbulence quantities so no comparisons can be made; however, since the results have been found grid independent, FIG. 4.29 shows how the turbulence kinetic energy varies in fully-developed elliptic duct flow. The behaviour is similar to that in a circular pipe, but the results from the two axes do not now collapse onto the same line as they are normalised with respect to the mean wall shear stress and this is obviously different to the wall shear at the end of each axis.

For the developing flow, only the static pressure variation was measured and FIG. 4.30 indicates that agreement is only reasonable. The axial development of the centre-line velocity and turbulence energy are drawn (predictions only) in FIG. 4.31; the velocity curve shows similar behaviour to the circular tube results with the velocity increasing above its fully-developed level and then gradually decreasing downstream. The energy develops in a similar manner although the start of the curve is delayed until the plug-flow core region of the velocity profile has decreased to zero; only then do velocity gradients arise near the centre-line and hence only then can there be generation of turbulence energy; the rise of the energy line is very steep but once more this eventually levels off and asymptotes to its fully developed value.

#### 4.5 Summary

The chapter began with a statement of the range of problems which require some kind of irregular boundary treatment; a method has been developed which is quite general and the technique outlined in some detail. As a demonstration of the validity of the method, it was tested in both laminar and turbulent flows for two irregular boundaries namely circular and elliptic duct flows; the results show that the method is capable of handling the hydrodynamic problem, but only isothermal flows were considered. As one of the motivations concerned river-flow discharge, it remains to extend the application of the method to this kind of problem, this is dealt with in Chapter 7.

## CHAPTER 5

### EXPERIMENTAL INVESTIGATION

#### 5.1 Objectives of Present Experiments

The review given in Chapter 1 emphasised the great shortage of data for three-dimensional submerged buoyant jets; in particular most investigations only considered jets into (effectively) infinite surroundings, only one (Winiarski and Chasse [28]) including measurements for jets injected along the channel bottom. Buoyant jets which interfere with the water surface are however of prime importance; the buoyancy forces carry the jet towards the free surface and, if the receiving body is shallow (as in the case of most rivers), the plume interferes with the surface soon after discharge. The experimental studies of jets discharged near a water surface have, as far as is known, been restricted to zero buoyancy jets. Accordingly, in an attempt to provide data for this important situation, an experimental investigation was made into buoyant jets discharged in a co-flowing stream close to the free surface.

Usually only jet trajectories, dilutions and widths have been reported in the literature; the theoretical method used in this thesis does however provide details of velocities, temperatures and indeed turbulence quantities as well. It was decided in the limited time available to concentrate attention on the measurement of temperature, but the data to be presented includes not just plume centre-line temperatures, but vertical profiles and,

in some cases, temperature contours over the plume cross-section which, to the author's knowledge, have not previously been reported. The main objectives are therefore as follows:-

- To construct an apparatus for the investigation of buoyant jets discharged close to the surface of a co-flowing stream.
- To make measurements on this situation for a range of jet Froude numbers, jet to stream velocity ratios, and jet submergence depths.
- The measurements are to be of the temperature profiles and contours at various stations downstream of the discharge location so that these may be used to test the validity of the prediction procedure described in Chapters 2 and 3 of this thesis.
- To aid comprehension of the flow behaviour, photographs are to be taken of the jet flow using dye to colour the jet.

## 5.2 Experimental Apparatus

FIG. 5.2.1 shows an overall view of the experimental apparatus; the individual components in this will shortly be

examined in detail, but first some background information is given. The open channel in which the measurements were made is the same as the one used by Ayoub [4] who studied downward-buoyant jets of sugar solution with salt added as a tracer. In those experiments, because the plume was deflected downwards, the effects of the water surface were negligible; the opportunity was taken to use the same flume, as this was readily available in the Hydraulics Laboratory of the Civil Engineering Department, Imperial College. The flume had been specially constructed for the experiments of Ayoub and to use this offered a great saving in time. A similar injection system was also used although, since the experiments were intended to study the interference with the free surface, an upward-buoyant jet was necessary and hence some means of heating the jet fluid had to be introduced; the following sections give more details.

#### Co-flowing Stream

The provision of a co-flowing stream necessitated the discharge taking place in the flume which is shown diagrammatically in FIG. 5.2.2. The overall length of the channel was 8.84 metres with a test section length of 6 metres; the flow channel was 1.525 metres wide and had a maximum depth of 0.51 metres. The flume was constructed of wood but had perspex windows for observation purposes.

The flow in the channel was recirculated and controlled through a system of four 2HP axial flow pumps manufactured by

Armfield Engineering Co. Ltd. The pump suction lines were located in the outlet tank at the downstream end of the channel and a pair of pumps fed each of two 15 cm mains pipes which returned the water to a 30 cm overhead manifold at the inlet end. To distribute the flow evenly, the returned water was fed into the bottom of the inlet settling tank via five evenly spaced 12.5 cm pipes.

It was essential that as uniform a flow as possible be established in the channel. To achieve this the channel had been provided with two screens of wire mesh containing small stones and pebbles to even out the flow at the start of the test section. To this was added an 8 cm length of honeycomb covering the whole width of the channel up to a depth of 30 cms (the top of the honeycomb can be seen above the water surface in FIG. 5.2.1). To check the efficacy of this arrangement, velocity measurements were made over the channel cross-section; these measurements also enabled the plane of injection of the jet to be located at a position determined by the following three factors:-

- The injection plane should be at a position where uniformly distributed channel flow exists.
- Allow for a working length downstream of the injection point of at least 100 jet diameters in which to take measurements.

- Avoid end effects in the downstream end of the channel caused by the suction of the pump.

The velocity measurements were initially made with a pitot-static probe and a micromanometer; however the low pressure difference being measured meant that each reading took an appreciable time and the distribution in the cross-section was therefore finally measured with a miniature propellor flowmeter as manufactured by Kent Instruments (Stroud) Ltd.; the makers quote an accuracy of  $\pm 2\%$  for velocities between 7 cm/sec and 15 cm/sec.

It was decided to keep the channel velocity constant during the experiments and to alter the velocity ratio by changing the jet velocity, on which much finer control could be established; the channel velocity chosen was 10 cm/sec. Just two pumps were required for this velocity and the controlling valves were adjusted to keep the flow as symmetrical in the channel as possible. FIG. 5.2.3 indicates the velocity distribution at a plane situated at the middle of the test section; the deviations from the nominal average of 10 cm/sec are shown and reasonable symmetry is achieved with all deviations less than 10%. The distribution 1 metre downstream was substantially the same, as were the measurements taken when the jet nozzle and feed pipe were immersed in the flow. The depth of water in most runs was 27 cms but this was altered to change the jet submergence so that for one series of runs it was only 24 cms.



From the measurements made it was decided that the channel velocity was acceptably uniform and steady at 10 cm/sec and that the injection point should be half way along the test section with the jet nozzle located on the centre-line of the flume.

#### Jet Fluid Feed System

The next essential for the experimental study was to provide a means of creating the buoyant jet. Hot water was used for this purpose and the feed system control board is shown in FIG. 5.2.1 and in detail in FIG. 5.2.4. A perspex constant head tank was used to ensure a steady supply pressure, the tank having a built-in overflow chamber; the water supply for the jet was the laboratory domestic supply. Flexible pvc tubing was used to connect the tank to a commercial rotameter to measure the flow rate; the water was then led through a water heater of 9 KW maximum capacity supplied by Eltron (London) Ltd. The supply then looped over the control board to where two valves controlled its direction; one merely sent the water to the laboratory drain, the other directed it to the jet nozzle feed line. It was the latter valve which controlled the rate of flow as indicated by the rotameter and an indication of the water temperature was given by a thermometer glued into the feed line.

The rotameter was calibrated by simply weighing the output of water over a known time with the rotameter at a constant setting; FIG. 5.2.5 shows the results of this calibration

indicating an acceptable accuracy for the rotameter. The temperature which the jet fluid assumed was fixed not only via the jet flow rate, but also by controlling the heat output of the water heater. This was done by connecting the heater to the 440 volt three-phase laboratory AC supply via a three-phase variable transformer (to be seen at the bottom left of FIG. 5.2.1). The heating coils were arranged in star formation in the heater so that one transformer was connected across each phase of the supply and used to step down the voltage across each of the heating coils; in this manner the power supplied could be varied from a maximum of 9 KW down to as low as required.

After the flow control valve, the hot water was fed through a durapipe feed line horizontally across the top of the channel; a vertical down pipe on the channel centre-line was followed by a 90° elbow and 60 cms of 2.54 cm perspex tube. The transition from durapipe to perspex tube under the water was moulded into a smooth cone-shape using plasticene and at the end of the perspex tube the jet nozzle was screwed on to give a 1 cm diameter jet outlet; the nozzle was made from machined perspex with its outside surface smoothly profiled to assure as even a flow as possible for the channel fluid\*. (The nozzle can be seen in FIG. 5.2.6). To ensure the rigidity of the nozzle, the horizontal feed pipe was held to two bracing struts by four brackets; the cross member itself was rigidly fixed at either end to the walls of the channel. The 60 cm perspex tube was used in the immersed part of the feed line to remove the jet outlet from the region of the wake behind the

---

\*The nozzle used was identical to one used by Ayoub [4].

down pipe; the velocity measurements mentioned earlier confirmed this had the required effect. Finally the nozzle pipe was fixed in the horizontal plane by using the perspex pipe itself as a level; a bubble was trapped in the pipe and the retaining brackets adjusted until the bubble was symmetrical about a mark scratched at the centre of the perspex pipe, the feed line was then fixed rigidly in position.

The jet submergence was altered by controlling the level of water in the channel. With the water flowing steadily, the drain valves for the channel (one at either end, see FIG. 5.2.1) were opened until the water-level was at the required distance above the centre-line of the nozzle. This measurement was made by focussing a travelling microscope onto the nozzle centre-line, traversing upwards the required submergence depth and then arranging for the water-level to coincide with the cross-wires in the microscope, a mark was then made on the perspex window of the channel so that this procedure did not have to be repeated. In the experiments to be reported two submergence depths were investigated, 6 cms and 3 cms. It should be noted that during the experimental runs it was necessary to keep a constant check on the depth of the channel water as extra water was being added all the time via the jet; usually one of the channel drain valves was left partially open at a position which stabilised the water level, the position of the valve being determined by trial and error.

### Instrumentation

To measure the water temperature a thermocouple probe was constructed which can be seen in FIG. 5.2.6. The body of the probe was made from 3 mm diameter steel tubing and the copper/constantan thermocouple bead was cemented into the centre of the tube with the wires being led up the hollow tubing. The normal cold junction as recommended by the British Standard (Reference [80],[81]) was constructed and the thermos flask containing this can be seen in FIG. 5.2.7. The probe itself was fixed to traversing gear which had a travelling screw mechanism for vertical movement and could slide on two rails across the channel; the rails themselves were mounted into end pieces which could move along the length of the channel, again using rails as supports. The cross-channel and upstream-downstream movements were measured relative to scales fixed to the probe support carriage and channel side-wall respectively; the scales could be read to the nearest half millimetre. The vertical movement could be read to within 0.1 mm and the normal procedure was to zero the probe with the bead in the jet exit plane and at the centre of the nozzle (using the travelling microscope to view the nozzle exit as above); all measurements were then taken using this position as datum.

The signal from the thermocouple was checked to agree with the British Standards Calibration (reference [80]) and FIG. 5.2.8 shows this is indeed the case (the thermocouple output was recorded against the reading of a standard mercury-in-glass thermometer placed near the thermocouple in the same container

of hot water). When the probe was placed just inside the nozzle to check the exit temperature then this chart could be used to evaluate the temperature as the digital voltmeter connected into the thermocouple circuit (2 in FIG. 5.2.7) gave a steady signal; when the probe was in the jet spreading region however, the turbulent fluctuations caused the signal to vary rapidly. Accordingly, to obtain the time-mean thermocouple e.m.f. and hence the time-mean temperature, the system shown in FIG. 5.2.7 was used.

The instantaneous signal was first amplified using a stabilized amplifier manufactured especially for thermocouple circuits by Analog Devices Inc. The gain of the amplifier was approximately 50 so the signal level was lifted from about 1 mv to about 50 mv; this level was now in the range which could be input to a DISA true integrator (Type 52830) which was used to find the time mean of the signal and display this on a second digital voltmeter (5 in FIG. 5.2.7). The amplifier/integrator system was calibrated by feeding into the amplifier a known voltage from a variable millivolt source manufactured by Comark Electronics Ltd. and recording the output on the final digital voltmeter. This graph is shown in FIG. 5.2.9 and together with FIG. 5.2.8 it corresponds to a transfer function between the display on the final DVM due to the thermocouple e.m.f., and the time-mean temperature at the thermocouple bead. Since both graphs are linear to a good degree of accuracy, the transfer function too is linear and was found to have the form:-

$$T = 50.2e + 0.98 \quad (5.2.1)$$

where  $e$  is the integrated e.m.f. in volts and  $T$  is the time-mean temperature in  $^{\circ}\text{C}$ . The integrator sweep time could be varied between one and one hundred seconds; for most readings a ten second interval was sufficient to remove any effects of the sweep time but for some measurements close to the jet discharge, twenty seconds was used. In reducing the data recorded, equation (5.2.1) was used in all cases.

### Photography

Ayoub [4] has used photography as a method of tracing the trajectories and spreading of the jet; in the present investigation, the increased detail of the measurements removes the necessity of taking photographs but some were taken as visual aids. The jet fluid was coloured by the addition of potassium permanganate dye fed into the stream through a hypodermic needle, the needle itself fed from an overhead bottled supply (see FIG. 5.2.1). The camera used was a 35 mm single-lens reflex Yashica TC-Electro XITS, the aperture was F5.6 with a shutter speed of  $1/125$ th of a second, and the film was black and white Ilford FP4 ASA125. The camera was positioned about 5 feet from the channel side-wall at the level of the nozzle centre-line. To facilitate the judgement of distance in the photographs, the back side-wall of the channel was covered with graph paper with 2 inch squares ruled out in black; the jet was illuminated through the graph paper by two banks of lights each of 1000 KW capacity.

5.3 Discussion of Measurements Made

At the start of the investigation, several trial runs were made to discover the range of velocity ratios and Froude numbers which could easily be covered with the apparatus described above. The table below shows the nine Froude number/Velocity ratio combinations for which experiments were finally performed and in each case gives the jet temperature excess above ambient (in degrees Centigrade) at the nozzle exit.

↓K	→ FR	5	10	15	20	30
2		43	15	8		
4			43	24	15	
6				43	28	15

$T_{\text{excess}} (^{\circ}\text{C})$

TABLE 5.1 Range of Experimental Parameters

For a jet submergence depth of 6 cms, the apparatus was run for each of the combinations shown above; it was found that the rig took approximately half an hour to stabilise at a steady state and measurements were only begun after this time had elapsed. For each experimental run vertical centre-line temperature profiles were taken at five downstream stations, usually 10, 20, 40, 60 and 80 jet diameters downstream. For three FR/K combinations (15/2,

15/4, 15/6) further measurements were taken over half the channel cross-section (only half was necessary because of symmetry, see below). Those measurements were then repeated for the three FR/K combinations mentioned above and for a submergence depth of 3 cms. To obtain accurate profiles, at least 10 readings were taken at each position and it was found the experiments could be repeated to a good accuracy as will be shown in the following chapter. The readings were taken as far downstream as possible upto the limit of accuracy of the thermocouple probe - this meant that measurements were discontinued when the indicated maximum jet temperature was less than one degree Centigrade above ambient.

Most of the measurements will be presented in the next chapter (and tabulated values are contained in Appendix 3), but to conclude this description of the experimental investigation some typical results are now discussed. Firstly FIG. 5.3.1 shows one of the checks that were made to ensure that horizontal symmetry had been achieved and measurements in one half of the channel only were necessary; the graph is typical of several checks made and indicates that the flow was indeed symmetrical.

FIGS. 5.3.2 and 5.3.3 indicate the behaviour of the plume trajectory when the jet Froude number or velocity ratio are changed. The first shows the expected behaviour when the Froude number is increased at a constant velocity ratio; higher Froude numbers at a constant jet velocity indicate lower jet temperatures and hence reduced buoyancy forces; the jet therefore should rise less quickly and the experiments bear this out. Also included on this



graph is Ayoub's measured plume trajectory for a Froude number and velocity ratio close to one of the present experiments. The two trajectories are in good agreement until the downstream distance exceeds forty jet diameters, the present experiments then rise more quickly than Ayoub's results. This can again be expected; past this point the present jet is affected by the water surface, this reduces the cooler water entrained into the jet and the resulting higher jet temperatures produce larger sources of vertical velocity than in Ayoub's case (Ayoub's trajectory has of course been inverted since the actual measurements show downwards deflection as the jet was denser than its surroundings).

FIG. 5.3.3 gives plume trajectories at a Froude number of 15 (approximately constant) for the three velocity ratios of this investigation. Higher velocity ratios cause the plume to rise more quickly and this can be explained in the following way: one way of achieving larger velocity ratios at constant Froude number is to simply decrease the ambient stream velocity with all else kept constant; the vertical deflecting buoyancy forces remain the same but the ability of the surrounding stream to deflect the jet in the downstream direction has been decreased, the trajectory is therefore steeper. A comparison is made with the correlation of Shirazi [30] and again reasonable agreement is achieved.

A typical plume dilution curve is shown in the next graph, FIG. 5.3.4; the hyperbolic rate of decrease of jet excess temperature can be clearly seen in both the present measurements and the correlations given of two other sets of data, Winiarski and Chasse [29] and Shirazi [30]. The Shirazi curve has been taken from

the dilution information contained in Reference [30] and not from equation (1.3.8), the correlation produced from the original data. The curve drawn was deduced in Reference [30] using the method of Hirst [27] after this had been fitted to Shirazi's data. This illustrates very well the inadequacy of such empirical correlations and the dangers of using them outside the range of parameters from which they were deduced. For the parameters in FIG. 5.3.4 (FR = 15 K = 4, not in the original experimental range of Shirazi's data), equation (1.3.8) reduces to:-

$$\frac{\Delta_T}{\Delta_T^0} = 49 \cdot \left(\frac{x}{d_J}\right)^{-1.024}$$

which does not even produce a dilution less than unity until about 45 jet diameters downstream. Two further points can be made about the comparisons shown; firstly, in the close-to-discharge region (i.e. the first 20-30 jet diameters) the spread of dilution rates is large; this is probably due to the fact that in this region the dilution is strongly affected by the particular discharge configuration used - this point is dealt with more fully in the following chapter. Secondly the far downstream dilution (greater than sixty diameters) is slower in the present experiments than in the other data shown. Again this can be explained by reference to the free surface; as mentioned above this reduces the area over which entrainment of cooler fluid can take place, and the jet temperatures may thus reasonably be expected to be higher

than if discharge had been into an infinite ambient.

A pictorial representation of the buoyant jet is shown in FIGS. 5.3.5 and 5.3.6. The first set of photographs are taken for an injection depth of 3 cms and for a constant Froude number of 15; the behaviour with increasing velocity ratio can clearly be seen by estimating the location where the upper jet boundary hits the water surface using the background of lines as a guide (the water surface is reached when the dye finally coalesces with its image reflected from the water surface). By counting squares it can be observed that the higher velocity ratios rise more quickly. The highly turbulent nature of the jet mixing region can also be judged by the distortion of the jet boundaries by the turbulent eddies.

The second group of photographs are relevant to the larger submerged depth of 6 cms and this time the velocity ratio has been kept constant ( $K=2$ ) while three different jet Froude numbers are used (5, 10 and 15). Once more an illustration is provided of the trajectory behaviour outlined above; higher Froude numbers promote faster rising jets. In the top photograph particularly, the tendency of the hot water to form a layer when it has risen to the surface is also noticeable, the thickness of this layer does not grow as the jet travels downstream as the buoyancy forces are all the time lifting the warm water to the surface.

Finally, it may also be noticed that the curvature of the jet is by no means steep; in Chapter 2 it was pointed out that shallow curvature was a pre-requisite for the suitability of a parabolic prediction procedure. The photographs indicate that such a procedure may justifiably be applied to the buoyant jet problem and this is the subject of the following chapters.

CHAPTER 6

PREDICTION OF TURBULENT BUOYANT JETS IN CO-FLOWING STREAMS

6.1 Introduction

In this chapter the numerical solution procedure described in Chapter 2 in conjunction with the turbulence model described in Chapter 3 is applied to the prediction of turbulent buoyant jets in a co-flowing stream. In Chapter 1 the review of previous work disclosed several sources of experimental data on this problem and it is the purpose of this chapter to present predictions of this data. The calculation procedure has also been applied to the experiments described in Chapter 5 and these predictions too are given here. In all the cases examined the laboratory set-up has been of the form shown earlier in FIG. 1.4.

Although some validation of the computer program has been provided in both laminar and turbulent flows, it still remains to prove the program for flows involving heat transfer; this is the subject of the next section and deals with non-buoyant flow. For the prediction of the laboratory data, special practices have been found necessary for supplying the inlet conditions and section 6.3.1 outlines the details. The predictions presented for the buoyant jet problem have all been subjected to the grid and step length tests which are necessary when numerical procedures are involved; examples of the grid sizes and step length parameters used are given in Appendix 1; the predictions presented in this chapter may thus be considered free from effects of cross-stream grids or forward step size.

## 6.2 Validation of Mathematical Model in Non-Buoyant Flows

### Turbulent flow and heat transfer in square ducts

The test case considered was developing and fully-developed flow and heat transfer in a duct of square cross-section. A detailed survey of previous work on this problem has been given by Tatchell [56], here only those experimental and analytical results which are used to assess predictions will be referred to. For fully-developed isothermal flow experiments have been performed by Leutheusser [82] and Hartnett et al [83]. The first reference measured the contours of the mean axial velocity in fully-developed flow. A comparison is given in FIG. 6.2.1 of Leutheusser's results with predictions using the present method, and also the predictions of Tatchell [56]. The top graph shows the velocity profile along the bisector of the duct walls and indicates good agreement; the present predictions lie 5% above the experimental data while Tatchell's predictions are 3% below. The second graph examines profiles along the corner bisector and illustrates the difference between the two sets of predictions; Tatchell's now lie within a few per cent of the data along the whole diagonal, but the present predictions are well below the experimental measurements in the near-wall region. The explanation lies in the superiority of Tatchell's turbulence model to the one used in this thesis; it has already been mentioned in Chapter 4 when predicting turbulent elliptic duct flow that the  $k-\epsilon$  model cannot predict the presence of secondary flows. It is these motions in the plane of the duct

which cause the velocity contours in square duct flow to bulge towards the corners and result in the data lying above predictions. Tatchell in his work has also used a  $k-\epsilon$  model, but has allowed for anisotropy of the effective viscosity by calculating the Reynolds stresses in the lateral momentum equations not from an equation such as (3.1.7) but from simplified versions of the full Reynolds stress equations. The simplifying assumptions remove the convection and diffusion terms in this equation and hence transform the partial differential equation into an algebraic one - hence the term referred to earlier, "algebraic Reynold's Stress model". The secondary flows now exist even in fully-developed flow and FIG. 6.2.1 shows that the correct behaviour is obtained when a model of this type is used.

Although the present model cannot predict the fine details of the flow correctly, FIG. 6.2.2 shows that the variation of the overall friction factor with bulk Reynolds Number is well predicted; also included on the top graph in addition to the experimental data are the predictions of Ying [84] who used a one-equation turbulence model in which the length scale was prescribed as an algebraic function of the duct geometry. Whereas the first set of comparisons showed the superiority of Reynolds Stress models over two-equation effective viscosity models, the improvement in the predictions of the friction factor in FIG. 6.2.2 emphasises the benefits of solving a differential equation for a length-scale-related variable.

For heat transfer in fully-developed flow, the available experimental data is much scarcer and the measurements used here

have been taken by Brundrett and Burroughs [85]. The measurements were taken for air flow in an electrically heated duct and a development length of 96 hydraulic diameters ensured fully-developed flow at the measurement station. The heating system used produced a thermal boundary condition in which the wall and bulk fluid temperatures both increased linearly (at the same gradient) in the established flow region, i.e. the heat flux per unit length of duct was a constant in the axial direction. The wall temperature at any station could be considered a constant around the periphery of the duct due to conduction in the duct wall and it was also found that the local wall heat flux,  $\dot{q}''$ , varied around the perimeter. This particular thermal boundary condition requires a slightly different treatment in the finite-difference scheme since the wall temperature at any axial station is not known explicitly, especially in the developing flow region. The known parameter in any forward step is the total heat transfer into the duct:-

$$\dot{q}_{tot} = \dot{q}' \cdot \Delta x \quad (6.2.1)$$

where  $\dot{q}'$  is the (known) axial heat input to the duct walls (constant along the duct) and  $\Delta x$  is the forward step length. If typical near-wall cells are considered, as shown in FIG. 1.4, then the finite-difference expression for the total heat flux over the next forward step is:-

$$\Delta x \cdot \sum_{\substack{\text{duct} \\ \text{wall}}} -k_{eff} \frac{\partial T}{\partial y} \cdot ds = \Delta x \cdot \sum_{\substack{\text{duct} \\ \text{wall}}} -k_{eff} \frac{(T_p - T_{wall})}{\delta n} \cdot \delta s = \dot{q}_{tot} \quad (6.2.2)$$

In this expression  $k_{eff}$  is the effective thermal conductivity given by:-

$$k_{eff} = \frac{\mu_{eff}}{\sigma_{T,eff}} \quad (6.2.3)$$

and  $\mu_{eff}$  is evaluated via the wall-function method using values from the previous location; similarly in equation (6.2.2)  $T_p$  is the local near-wall temperature, and values from the upstream step are used. The summation in equation (6.2.2) is performed over all near wall cells as shown in FIG. 1.4;  $\delta_s$  indicates the length of duct wall present in each near-wall cell and  $\delta_n$  is the normal distance between near-wall grid node and duct wall, whether vertical or horizontal (see FIG. 1.4). Combining the above equations, the wall temperature (constant peripherally) applicable to the present forward step may be calculated from:-

$$T_{wall} = \frac{\dot{q}'_{duct\ wall} + \sum_{duct\ wall} k_{eff} \cdot T_p \frac{\delta_s}{\delta_n}}{\sum_{duct\ wall} k_{eff} \cdot \frac{\delta_s}{\delta_n}} \quad (6.2.4)$$

This is evaluated from known and upstream values and is stored in all the boundary nodes prior to the calculation of the coefficients in the temperature equation; the local wall heat fluxes into the various control volumes are left to the normal finite-difference calculations. To check that this method is correct, the wall temperature as calculated above may be examined, and a separate check is given by the calculated bulk mean fluid temperature, deduced from the following equation (in finite-



difference form):-

$$T_b = \frac{\sum_{\text{all cells}} A_p \cdot u_p \cdot T_p}{\bar{u} \cdot A} \quad (6.2.5)$$

where  $A_p$ ,  $u_p$  and  $T_p$  are the local area, velocity and temperature for any grid node P;  $\bar{u}$  and A are the mean velocity and total area of fluid flow respectively.

The above treatment of the thermal boundary condition has been applied to the experiments of Brundrett and Burroughs and the results have been compared for the fully-developed heat transfer problem. FIG. 6.2.2 shows the variation of Stanton number with Reynolds number (defined using the duct hydraulic diameter); the Stanton number has been defined as:-

$$St = \frac{-\dot{q}'_{\text{wall}} / (B+H)}{\rho C_p \bar{u} (T_b - T_{\text{wall}})} \quad (6.2.6)$$

where  $\dot{q}'_{\text{wall}}$  is the heat flux into unit length of one quadrant of the duct and  $(B+H)$  is the quadrant perimeter (see FIG. 1.4); since the thermal boundary condition results in a constant difference between wall and bulk temperatures, then the above definition leads to an asymptotic value in the established flow region, it is this value which is plotted in FIG. 6.2.2. The present predictions underestimate the data by 8 - 16% over the Reynolds Number range shown but are consistently better than Ying's one-equation predictions. It must be mentioned however that Ying

[84] also provided predictions which included the presence of secondary flows and, for the same reasons as given above, these improve on results at the two-equation level.

Predictions in the developing flow region were now examined. One of the few sets of data has been presented by Ahmed and Brundrett [86]; measurements were given of both velocity and turbulence energy contours; Tatchell [56] has however pointed out that in these experiments the inlet conditions were probably not the uniform conditions which the authors claimed. Good agreement with the velocity development was only obtained by Tatchell when he considered the flow to develop from a "virtual origin" of -6 hydraulic diameters. The present predictions were therefore assessed using a more recent set of measurements as provided by Melling [87]; unfortunately only turbulence energy contours at one station were provided and hence the predicted development of the turbulence energy could not be assessed. FIG. 6.2.3 shows that good agreement is obtained with the axial development of the centre-line velocity without any assumptions concerning the origin of the flow (the bulk Reynold's numbers are slightly different but this should not affect comparison). Both measurements and data exhibit a peaking of the centre-line velocity prior to the value falling towards the fully-developed level. The predictions show a higher and more pointed maximum than the measurements and this is caused by two factors. Firstly the duct in which the experiments were performed was less than 40 diameters long and the far downstream measurements may have been modified due to

end effects; a more likely explanation however lies again in the absence of the turbulence driven secondary flows. The consequence of this absence is that, in the predictions, the high momentum fluid near the axis is not distributed sufficiently across the duct, and this results in the excess velocities as shown.

No experimental data were available for the developing heat transfer problem, but FIG. 6.2.4 presents some typical results obtained when predicting the fully-developed heat transfer data presented above. The graph shows that the bulk temperature calculated from equation (6.2.5) does indeed vary linearly with axial distance as the thermal boundary condition of constant  $\dot{q}'$  would indicate. The wall temperature distribution deduced as outlined above also produces the correct asymptotic behaviour as this too varies linearly and parallel to the bulk temperature after a short development length. Finally a curve is also presented for the variation of friction factor with axial distance, the friction factor (or local pressure gradient) decreases from the high value at the duct inlet necessary to accelerate the core of the fluid flow;  $f$  eventually asymptotes to a fully-developed value whose variation with Reynolds number was plotted in FIG. 6.2.2.

### 6.3 Prediction of Laboratory Data

#### 6.3.1 Inlet Conditions for Jet Discharge into a Co-Flowing Stream

A previous section (3.3) has outlined the methods normally used for specifying the inlet values at the start of calculations; the

predictions presented so far for the various duct flows have all used these methods for velocities, temperature and turbulence quantities and have justified their accuracy. In the predictions of laboratory data which follow, the co-flowing stream has been treated in exactly the same way at inlet since this is essentially a duct flow region; the jet discharge area (shown in detail in FIG. 6.3.1) has however been treated differently and this section outlines the reasons for the difference and the particular method adopted.

FIG. 6.3.1 shows that the problem is similar to the confined jet problem which was presented in the laminar flow predictions of Chapter 4. The same method as was used there to distribute the incoming mass flow correctly (the 'modified density' method) has also been used for the buoyant jet problem, but tests have shown that this is unnecessarily complicated and the final method used is as follows. The semi-circular nozzle area is replaced by a rectangular region of the same area; thus, in FIG. 6.3.1:

$$w \cdot d_J = \frac{\pi d_J^2}{8} \quad (6.3.1)$$

The rectangle has been given the same vertical dimension as the nozzle firstly since, in buoyancy flows, the vertical location of the jet is of prime interest and so this has not been tampered with; secondly of course this is also convenient to arrange in the computer program. The main grid lines are then specified in such a way that the boundaries of specified control volumes lie along the rectangle of dimensions  $(d_J \times w)$  (shown dotted in FIG. 6.3.1)

The grid nodes inside the rectangle are then treated as pertaining to the jet, while those outside are considered as part of the ambient flow. Although this method does distort the jet region, particularly in the horizontal direction, and certainly affects predictions in the very close to discharge area, experience has shown that, in the region of experimental measurements for buoyant jets (greater than 10 jet diameters), this method produces reasonable results. In particular, one of the tests made was to examine the vertical and horizontal profiles predicted for a very high Froude number discharge (i.e. virtually non-buoyant); in this case the development of vertical and horizontal profiles should be the same as buoyancy is ineffectual, with the method outlined above this was found to be true to within 5%.

The actual specification of jet conditions will now be dealt with and for all variables uniform distributions have been used. For velocities and temperature the conditions are easily specified since the jet velocity ratio and the ambient velocity gives the jet axial velocity; also the Froude number and the ambient temperature may be manipulated to give the jet temperature if this is not known explicitly. For turbulence energy too, most experiments have specified low intensity jet streams so a typical value may be used in equation (3.3.1) as explained in Chapter 3. To assign a value to the dissipation in the jet region is more difficult; combining equations (3.2.6) and (3.3.2) given earlier a formula for  $\mathcal{E}$  may be derived in terms of the mixing length  $l_m$ :-

$$\mathcal{E}_{\text{Jet}} = k_{\text{Jet}}^{3/2} / (c_{\mu}^{-3/4} \cdot \ell_m) \quad (6.3.2)$$

and the problem now is to specify the value of  $\ell_m$  for the jet flow at inlet. It was discovered that the predictions (in particular the dilution rate in the first 10-20 jet diameters) were sensitive to the value of  $\ell_m$ . This is not altogether unexpected behaviour since by changing the value of  $\mathcal{E}$  via  $\ell_m$  the value of the effective viscosity in the inlet region (calculated from  $k$  and  $\mathcal{E}$ ) is also changed and hence the rate of mixing and dilution in the near-discharge region must vary; the problem becomes what value to give to  $\ell_m$ .

A similar problem was faced by Launder et al [17] who required detailed initial profiles for all dependent variables, but usually only had sufficient information for velocity and sometimes  $k$ . The method adopted there was to use a number of trial calculations based on a constant effective viscosity, adjusting the value of the constant until the predicted development in the vicinity of the discharge agreed with the measurements. This value of the effective viscosity was then used, for example, to specify the inlet  $\mathcal{E}$  value by inverting equation (3.2.4):-

$$\mathcal{E} = c_{\mu} \rho k^2 / \mu_t \quad (6.3.3)$$

A similar method is used here and equation (6.3.2) has been modified to give:-

$$\mathcal{E}_{\text{Jet}} = k_{\text{Jet}}^{3/2} / (c_{\mu}^{-3/4} \cdot \ell_m \cdot A_{\mathcal{E}}) \quad (6.3.4)$$

The mixing length in all cases has been specified as:-

$$l_m = .07 d_J \quad (6.3.5)$$

Various values for  $A_\epsilon$  have been tried until the dilution rate in the first 10 jet diameters is correct and it can be seen that this is equivalent to the method of Launder et al, but concentrating attention on  $A_\epsilon$  instead of an overall  $\mu_t$ . It should be emphasised that this has been done for just one experimental run (i.e. one FR/K combination) and this value of  $A_\epsilon$  has then been used for all other experimental runs.

It must also be mentioned however that the value of  $A_\epsilon$  has been found to be different for each set of experiments and some explanation for this must also be given. In each experimental configuration there are physical factors which affect the rate of dilution; the review in Chapter 1 has already pointed out that different turbulence intensities at inlet affect the length of the potential core, although this would probably be of only minor importance here. Two factors which are of major significance are the boundary layers on the jet nozzle and the recirculation zones which may exist just downstream of the nozzle lips.

The former will appear both inside and outside the nozzle and will contribute to a faster rate of mixing since they cause velocity gradients to occur in regions where they would not normally and these gradients act to generate turbulence energy and promote mixing; if the nozzle is streamlined then smaller

boundary layers are more likely. The present assumption of uniform distributions of all variables cannot allow for the presence of such boundary layers and since the size of these is likely to vary from one experimental configuration to the next (but not vary widely from experiment to experiment) then it is reasonable to assume that the value of  $A_{\epsilon}$  must be changed to allow for their effects.

A similar argument can be given for the effects of separation at the nozzle lips; the small recirculating region generates larger eddies than would occur by shear alone, these large length scales diminish the level of dissipation at the point where jet and ambient streams meet and hence again increase the turbulence energy and viscosity in this region. This explanation has been given by Matthews [88] who studied the film cooling of solid surfaces by wall-jets injected along the solid surface and separated from the hot main stream gas by a thick dividing lip. Matthews used an equation akin to (6.3.3) to specify the dissipation just downstream of the dividing lip; a value 1/20th of the expected value was necessary before turbulence energies in the recirculating region were predicted at the same level as in the experiments. Again, for the buoyant jet discharge experiments, different nozzles will produce different zones of recirculation and indeed, for thin lips and streamlined nozzles, such separation zones might be absent altogether; in the present method, only the value of  $A_{\epsilon}$  can take into account these variations and, as explained above, it may be expected that the presence of boundary layers and recirculation



regions enhance mixing and thus require a value of  $A_{\epsilon}$  greater than unity to reproduce their effects.

Finally, it should be remembered that numerical factors can also play a role in modifying the value of  $A_{\epsilon}$ . Since the whole of the duct area shown in FIG. 1.4 is covered with the finite-difference grid, then the jet area itself has relatively few nodes even though the grid spacing is made large in regions far away from the expected area of jet spread. This is especially true in the near-discharge area until the jet has spread to cover more nodes; the distortion of the jet area described above will also affect the dilution in the vicinity of the nozzle. Unfortunately it has been found impossible to separate the combined effects of physical and numerical factors; the methodology has therefore been as described above: to fix the value of  $A_{\epsilon}$  for one experiment so that the correct dilution has been achieved at a position where the numerical factors may be expected to be of negligible importance (i.e. after about 10 jet diameters when the jet region is resolved by a relatively large number of nodes). The mathematical and turbulence models may then be assessed by the manner in which they reproduce the profiles further downstream and for different experiments.

This concludes the description of the specification of the inlet conditions; in the predictions which follow the values ascribed at inlet are usually obvious but when this is not the case they are given in the relevant place. In particular the value of  $A_{\epsilon}$  used in each set of data is outlined and where applicable its value is discussed.

### 6.3.2 Prediction of Winiarski and Chasse Data [28]

The first problem to which the above treatment was applied was the experimental configuration of Winiarski and Chasse in which a hot water jet was injected along the bottom of an open channel whose dimensions have been given in Table 1; additional measurements were also made in which the jet was injected at increasing angles in the vertical plane, but only the co-flow data are of interest here. Using the formulae given by equations (6.3.4) and (6.3.5) and a jet turbulence level  $i$  of .001 (see equation 3.3.1) the value of  $A_{\epsilon}$  which gave best predictions was a value of 3. It may be mentioned that this flow has similarities to the wall-jet flow of Matthews [88] although the nozzle lips were by no means substantial, nevertheless a value of  $A_{\epsilon}$  greater than unity seems appropriate.

Although vertical temperature profiles were taken in the experiments the method of measurement (hot-film anemometer linked to x-y plotter) was such that the temperature oscillations, even when fully damped produced sizeable fluctuations in the plots (of the order of  $\pm 1^{\circ}\text{C}$ ) and the profiles were thus not given in the report. Two Froude numbers and velocity ratios have been predicted. The jet and ambient temperatures and velocities were known at each Froude number and could easily be fed into the computer program; it only remained therefore to ascribe a value to  $\beta$  the volumetric expansion coefficient, for use in the  $v$  momentum source term. This was fixed by merely combining and inverting the definitions for Froude number and  $\beta$ , equations (1.3.2) and (2.2.9), hence:-

$$\beta = \frac{u_{\text{Jet}}^2}{FR^2 \cdot (T_{\text{Jet}} - T_{\text{amb}}) \cdot g \cdot d_{\text{Jet}}} \quad (6.3.6)$$

This is the value of  $\beta$  which gives the correct density difference at inlet between jet and ambient, according to equation (2.2.9). Typical predicted temperature profiles are shown in FIG. 6.3.2. The rapid dilution at the inlet can be seen by the maximum excess temperature having halved by 11 diameters downstream. The similarities with the wall jet flow can also be drawn again as the predicted maximum temperature has moved towards the wall; further downstream the buoyancy forces lift the maximum upwards and by 75 diameters downstream the highest temperature is between 3 and 4 jet diameters above the channel bottom.

The locus of the maximum temperature, as usual, was referred to by Winiarski and Chasse as the plume trajectory and experimental measurements were reported for this quantity. Comparisons of prediction and measurement are given in FIG. 6.3.3; the experimental measurements are not plotted as single points as examination of the data revealed the scatter indicated in the graphs. For the first Froude number and velocity ratio the agreement is good apart from the region near the discharge; in the predictions the plume trajectory actually sinks below the original level and this is due to the formation of a wall-jet like profile as discussed above. The measurements however were only begun at the original discharge level and it is thus not surprising that no fall in trajectory was recorded, further downstream the rate of rise of the plume is well predicted.

The second graph shows results for the same FR value but a higher velocity ratio, and agreement is now not so good. The predictions show the behaviour expected with an increased K value that is, a faster rate of plume rise; the data on the other hand indicate about the same rate of rise as for the first graph, although the velocity ratio has increased almost threefold. One reason for this is perhaps the flatness of the temperature profiles in the downstream region, coupled with the difficulty of locating the maximum value from the rapidly oscillating plots as indicated above, this could perhaps explain the discrepancy (the far downstream jet excess temperature is only of the order of 2 deg C). The same rate of plume rise for both K values is in any case a very dubious result.

The final comparison is with a high Froude number discharge; both predictions and experiments show the same qualitative behaviour of a much slower rising plume. The present results indicate that the buoyancy forces are so reduced that only after about 50 diameters does the effect of the wall-jet start to be overcome; the data indicate the same pattern, but again the measurements are all above the original injection level.

FIG. 6.3.4 presents results for the same three FR/K combinations but the graphs now show the dilution of the hot water as it travels downstream, the vertical co-ordinates being the local jet excess temperature normalised by its original value. All three curves show acceptable agreement with data, exhibiting the hyperbolic rate of dilution which is typical of jet mixing. If any point is to be

made it is that the data usually lie below the predictions; this is in accord with the predicted trajectories lying below the experimental ones, as temperatures measured higher up the profiles would give lower values and hence lower dilution readings; this is especially true in the first 40-50 diameters.

The final parameter quantified in the experiments was the vertical spreading of the plume; this was identified in the experiments by the vertical location on the profile where the temperature reached its ambient value and the temperature fluctuations died out, since the ambient stream was of low intensity turbulence. The predictions are in terms of finite temperatures at discrete locations, so some interpolation was necessary, and for the purposes of these comparisons the usual assumption was made that the edge of the jet was the location where the temperature fell to within one per cent of the ambient value. FIG. 6.3.5 shows that the agreement with experiments is excellent; all three jets spread very rapidly in the near-discharge region and it is this which has been reproduced via the inlet value ascribed to  $A_g$ . Further downstream the growth of the plume follows the measurements closely and reproduces the correct variations with both FR and K. Thus for the high FR case the plume spreads more slowly, whereas the high K value produces a jet edge which has reached the water surface in both experiments and predictions by 60 diameters downstream. This agreement with both dilution and jet spread measurements indicates that the model is predicting the rate of mixing of jet and ambient very well; the lack of agreement with the plume trajectory for K=7 is thus even

more difficult to understand, since the determining factor in the plume rise is the magnitude of the buoyancy force, this is a function of the local fluid temperatures which the model predicts quite well for the  $K=7$  case.

### 6.3.3 Predictions of Shirazi et al Data [23]

The second set of data considered was that presented by Shirazi et al [23]; again this deals with a hot water jet, but this time issuing into the centre of a fully-developed channel flow. The fact that the ambient stream is not now uniform was thought possibly to affect the jet development; hence this was allowed for by arranging for the program to run for 100-200 large steps, just calculating the channel flow until fully-developed velocity fields were obtained; the values of all variables in the jet region were then overwritten as normal and the calculation of the buoyant jet began. The vertical variation of the axial velocity on the channel centre-line and on a line half way to the channel side wall is given in FIG. 6.3.6; agreement is reasonable with the experimental measurements. The inlet conditions were specified in the normal manner, with the value of  $\beta$  again taken from equation (6.3.6). The experiments used a constant temperature difference between jet and ambient and changed the Froude number and velocity ratio by changing the jet velocity and also the nozzle diameter; three different nozzles were used, each made simply from copper tubing curved so that injection was parallel to the flow. Predictions were obtained for one  $FR/K$  combination for each nozzle so that the

range of Froude numbers and velocity ratios could be covered. It was expected that the value of  $A_{\epsilon}$  would vary since changing the nozzle diameter corresponds to a different experimental set-up and hence also different discharge characteristics; it was discovered however that the values of  $A_{\epsilon}$  varied widely from one nozzle to the next, and indeed the best predictions were obtained with very large values i.e. 100 for the large nozzle, 25 for the medium nozzle and 10 for the small nozzle (nozzle diameters are given on the FIGS. which follow). This range and value of  $A_{\epsilon}$  was unexpected and a discussion of the probable causes follows the presentation of the results.

FIGS. 6.3.7 and 6.3.8 present vertical + horizontal temperature profiles for the large nozzle; the velocity ratio was in this case less than one and the Froude number was 6.3. The vertical profiles are of the temperature excess above ambient along the channel centre-line and the horizontal profiles are for the same quantity plotted along a horizontal line through the location of the maximum temperature; the predictions for the horizontal profile are of course symmetrical about the centre-line. The agreement is reasonable although discrepancies occur in several areas; the worst agreement is at the third downstream station, although by this location the maximum excess temperature is less than 0.5 deg. C above ambient; the accuracy of measuring such small temperature differences can certainly be questioned. In examining the horizontal profiles it can be seen that at two locations the maximum temperature has actually been measured off-centre, this too is probably due to measurement error. The initial dilution is certainly very rapid;

the original excess temperature was 19 degrees Centigrade and this has already fallen to just one degree at the first station downstream; to reproduce this effect has required the exceptionally large value of  $A_{\epsilon}$  quoted above.

The same comparisons are made in FIGS. 6.3.9 and 6.3.10 for the medium nozzle and K and FR values of 3.82 and 72 respectively. The agreement is fairly good at the first two axial locations, although for the data the maximum temperature location at the first station is below and off-centre in the horizontal plot. This cannot be explained other than that the nozzle was originally below the intended discharge location or possibly at an angle to the channel centre-line. The far downstream profile is again at a very low excess temperature above ambient. (It should be mentioned that all the experimental data for the medium nozzle exhibit the same distortion of the temperature maximum below  $y/H = 0.5$  and to the right of the centre-line).

When the predictions for the small nozzle are examined (FIGS. 6.3.11, 6.3.12), the agreement with experiment is seen to be very poor. It seems odd that in all the predictions the vertical and horizontal limits of the hot water are well predicted and yet the maximum value at the jet centre in some cases is very different from the experiments; this is particularly true in the small nozzle case. Although the whole temperature field is not given, there seems to be a discrepancy in the heat content of the jet between data and predictions; a check was made to ensure that no heat was being lost as the jet area grew in the calculations and certainly



this was not the case. Accurate comparisons of heat content cannot be made however without information on the velocity distribution in the jet, the measurements however contained no information other than the jet discharge velocity. Altering the value of  $A_{\epsilon}$  cannot produce infinite dilution rates and the value of  $A_{\epsilon}$  shown is that value beyond which increasing  $A_{\epsilon}$  had no effect; the explanation for this is that lowering the inlet  $\epsilon$  values decreases the level of the upstream convection term in the equation and also lowers the dissipation term in the k equation, enabling higher energies to exist and thus promoting mixing. Obviously there comes a level of  $\epsilon$  below which it has no effect since the other terms in the equations are then dominant.

#### Discussion of $A_{\epsilon}$ values

Even though agreement with experiment is not good, some explanation must be given as to why the  $A_{\epsilon}$  values should be so large and why they vary from one nozzle to the next. It has been pointed out that the rate of dilution was very large at inlet and this can only be reproduced by increasing  $A_{\epsilon}$  but why is dilution so fast? The arguments given above on nozzle boundary layers and recirculation zones could certainly apply in this case as the copper tubing was not streamlined. In addition however there are two further features of the discharge which are unsatisfactory: firstly the bending of the copper tubing will certainly affect the flow distribution in the nozzle, the velocity and temperature profiles will distort so that the maximum values are carried to the outside

of the bend; this would cause faster mixing since velocity gradients have been introduced and these generate turbulence energy. This would also explain why the value of  $A_\epsilon$  increases from small to large nozzles since, for the same radius of bend, the radius ratio would increase and this causes more distortion (see Patankar et al [38]). Secondly, upon examining photographs in the original data report [23], it can be seen that not only is the tubing bent, but the nozzle outlet is very close to the vertical part of the feed pipe; the likelihood is that the wake of this pipe is still affecting the channel velocity and this too would affect the dilution. Finally, further evidence that different  $A_\epsilon$  values are required for different nozzles is given in FIG. 6.3.13; this shows experimental data for two nozzles, but for approximately the same Froude number and velocity ratio; the curves should almost coincide, but this is by no means the case. It should be noticed that the small nozzle dilution, which could not be reproduced in the predictions, is approximately two to three times smaller than the medium nozzle values.

In the light of the above discussion, and the comments made above on measurement difficulties and inaccuracies of nozzle alignment, it is believed that this set of data is not a reliable test of the mathematical model. A second assessment of the model's performance for jets discharged remote from flow boundaries is contained in the next section.

#### 6.3.4 Prediction of Ayoub Data [4]

This set of experiments also investigated buoyant jets discharged into flowing surroundings, but the jet was now downward buoyant as the jet fluid was denser than the ambient (sugar solution for the jet, plain water in the channel). Three different nozzles were used and the same jet Froude number was realised with different combinations of jet velocity, nozzle diameter, and jet excess density. Salt was added to the jet as a tracer and a conductivity probe was used to determine dilution rates and the location of maximum concentration (plume trajectory). A few jet profiles were measured but the width of the jet was in general determined by the addition of dye to the jet, this was then photographed against a background grid; tracings of the jet boundary were then taken directly from the photographs.

To reproduce a sinking jet, the computer program was run for a jet of cold water injected into a warmer ambient stream; for convenience the jet temperature was fixed at  $10^{\circ}\text{C}$  and the ambient at  $20^{\circ}\text{C}$ ; the actual jet dimensions and jet and channel velocities were used and the Froude number of the run was varied to suit a particular experimental run by altering the value of  $\beta$  as given by equation (6.3.6). Comparison was made with data on the basis of plume trajectories, dilution curves and jet spreading, as for the Winiarski and Chasse data; each of these is dealt with in turn. The value of  $A_{\epsilon}$  used in all the calculations on the basis of equation (6.3.4) and a turbulence level of .001 was a value of  $1/5$ . As a streamlined nozzle was used, then it is not

surprising that the value was close to unity; the fact that it was less than unity indicates that, for a plug-flow velocity profile, the expression used for the mixing length (equation (6.3.5)) is only an approximation.

### Plume Trajectories

These have been compared on the basis of the location of maximum concentration in the experiments and minimum temperature in the predictions. FIG. 6.3.14 shows the effect of varying the jet Froude number whilst the velocity ratio remains the same. Agreement is very good showing that increasing FR implies that buoyancy forces have decreasing influence on the flow and the jet sinks more slowly; this result is to be expected. The next comparison (FIG. 6.3.15) demonstrates that the effect of different velocity ratios is also well predicted. Again the qualitative results match expectations, higher velocity ratios promote a steeper rate of sinking of the trajectory; quantitatively the predictions follow experiments very closely.

### Dilution Curves

Three examples are given in FIG. 6.3.16 of dilution predictions compared with experimental measurements; the curves cover three different Froude numbers and three different velocity ratios and the results are typical of the agreement obtained for all runs made. The vertical axis measures the non-dimensional maximum concentration or minimum temperature at any axial location;

these quantities are defined below:

$$C^* = \frac{C_{\max} - C_{\text{amb}}}{(C_{\max} - C_{\text{amb}})_{\text{inlet}}}, \quad T^* = \frac{T_{\min} - T_{\text{amb}}}{(T_{\min} - T_{\text{amb}})_{\text{inlet}}} \quad (6.3.7)$$

### Jet Spreading

The horizontal spread of the jet was measured using the conductivity probe for only a few runs; FIG. 6.3.17 compares predictions and experiments for just one Froude number/velocity ratio combination. The agreement is certainly acceptable considering the difficulties inherent in locating the boundaries of a jet, the horizontal locations of the jet edge are well predicted. All the profiles shown are for a horizontal traverse through the maximum (non-dimensional) concentration or temperature location.

For vertical spread, no experimental measurements were presented; instead the jet boundaries were deduced by the photographic method as explained above. For the predictions, the development of the temperature profile along the centre-line followed a pattern similar to that shown in FIG. 6.3.18; the locations of the minimum temperature on this figure may be compared with the plume trajectory data in FIG. 6.3.15. For the purposes of comparison with the vertical jet spreading, the same assumption was made as with the Winiarski and Chasse data; the jet edge was taken as the location where the temperature approached to within 1% of the ambient value. On this basis FIGS. 6.3.19 and 6.3.20 compare the development of the plume width with downstream distance for

both predictions and experiments. The first figure shows that discharges with small and with large buoyancy effects are both well predicted. In the top graph the jet travels over 50 diameters downstream before **appreciable** downward deflection takes effect; for the lower figure, however, the bottom jet boundary shows no sign of axi-symmetric behaviour and by 70 diameters downstream the top jet edge has crossed the original discharge level. In FIG. 6.3.20 the comparisons indicate that the mathematical model accurately predicts the effect of varying K on the jet spread. The low velocity ratio discharge exhibits appreciable buoyancy effects as the whole jet has fallen below the injection level after only 50 diameters. Increasing the velocity ratio magnifies this effect and the increased curvature of both upper and lower jet boundaries is reproduced very well in the predictions.

It is believed that the measurements in this case exhibit none of the doubtful features of the previous set of data; for example runs with different nozzle sizes and jet velocities, but with the same FR and K values show the same behaviour in these experiments whereas this was not so for the Shirazi data. In addition, Ayoub's results, unlike the previous data, do exhibit noticeable buoyancy effects, and these have been well predicted. For these reasons, the comparisons presented in this section were taken to validate the mathematical model for buoyant jets discharged into co-flowing streams with no effects of boundary surfaces; the next section deals with predictions which remove the last mentioned restriction for jets close to the water surface.

### 6.3.5 Predictions of Present Experimental Data

This section contains the predictions obtained when the model was applied to the experimental investigation described in Chapter 5 with a hot water jet discharged close to the water surface. Since measurements provided the actual temperature profiles and contours, then comparisons are made directly with these without extracting from them such information as plume trajectory or jet width; the performance of the model can thus be more accurately assessed.

The value of  $A_{\epsilon}$  used in all predictions was  $1/7$ ; this is close to the value used in the Ayoub predictions and this is certainly to be expected since an almost identical nozzle was used; details of grid and step sizes may be found in Appendix 1. (The submergence was measured from the jet nozzle centre-line to the water surface).

#### 6 cm Submergence

The centre-line temperature profile development was measured for three Froude numbers and three velocity ratios; FIGS. 6.3.21 - 6.3.29 contain comparisons of prediction and experiment for all **nine** cases. Before discussing the agreement in detail it is mentioned here that the remarks made in Chapter 5 on the repeatability of the experiments are verified in these Figures; several graphs (e.g. 6.3.21, 6.3.23, 6.3.29) contain experimental points plotted from two separate runs for the same values of the parameters FR and K; in general the same profiles are obtained to within  $0.5^{\circ}\text{C}$ .

The first three Figures show temperature profiles for a velocity ratio of 2 and decreasing Froude numbers (15, 10 and 5). The agreement is good for the lowest Froude number except at the first station where the predicted maximum temperature is 1 deg. C too low. The measured rate of plume rise for FR = 15 is a little faster than the predicted rate; examination of the FR = 10 and FR = 5 plots shows that this discrepancy appears in the other comparisons for the K = 2 value, indeed for the lowest Froude number the error is large, although when the jet hits the surface the layer-like nature of the hot water region is reproduced well by the predictions.

As will be shown later, it is only this low velocity ratio case which exhibits this discrepancy between measured and predicted plume rise. It was thought that a possible explanation was that the nozzle was angled slightly upwards and in an attempt to reproduce this, the program was re-run for the low Froude number case with the jet velocities at inlet having a vertical component corresponding to a small inclination. FIG. 6.3.23 shows that even when this inclination was increased to  $5^{\circ}$  (dotted profiles), the rate of plume rise was still insufficient, although the rate had increased. Certainly no angling of the nozzle to this degree was present in the experiments since over the 60 cm horizontal feed pipe length, an angle of  $5^{\circ}$  would move the nozzle outlet appreciably nearer the surface and this was not observed in any experimental run. It is possible that the angle was smaller than this and the program is not capable of producing the correct effects of angled discharge, but otherwise no explanation was found. In general the dilution



rates and spreading of the jet are still quite well predicted for this velocity ratio.

FIGS. 6.3.24 - 6.3.26 contain comparisons for a velocity ratio of 4 and it can be seen that plume trajectory is well predicted in this case except when the jet axis is very near the surface, however some difficulty was experienced in locating the thermocouple bead exactly at the water surface due to surface tension effects, so this discrepancy is perhaps not surprising. On the whole the profiles follow the measurements very well except for the three downstream positions in FIG. 6.3.24 when the data show a hotter jet.

It can be noticed however that the constant temperature part of the profile indicating the ambient stream has increased in temperature over the downstream distance shown in FIG. 6.3.24. The explanation for this lies in the recirculating nature of the ambient stream; obviously since hot water is being discharged into the channel, this will slowly heat up; in most runs the change in ambient temperature was only slight, but in this one case the apparatus had been running for over two hours with the result as shown. That the discrepancy between data and predictions is due to this effect has been shown by repeating predictions with a higher ambient temperature; this worsens agreement for the upstream stations, but, as shown in FIG. 6.3.24, the increased downstream jet temperatures are reproduced very well.

For the highest velocity ratio the experimental results and the predictions are in excellent agreement as indicated by

FIGS. 6.3.27 - 6.3.29. Plume rise, jet widths and dilution rates are all accurately calculated and the change in all these quantities as the Froude number varies from 30 to 16.5 is predicted accurately by the computer program.

For a Froude number of 15 temperature contours were measured for all three velocity ratios and for three downstream stations.

FIG. 6.3.30 presents predictions and data for the low velocity ratio and agreement is certainly reasonable. Two main areas are in error, firstly the innermost contour at the first axial station, but as this station is only 5 diameters downstream, it is probable that the jet has not yet spread to cover enough grid points for accuracy to be achieved. Secondly the outermost contour is not well predicted, but for this case this is due to the too slow rate of rise of the jet.

FIGS. 6.3.31 and 6.3.32 give the cross-sectional contours for the  $K = 4$  and  $K = 6$  runs. The predictions are now in much better agreement, but the same two areas of error still apply; for these runs however the errors in the outermost contour are due to the difficulty of locating the edge of the jet exactly. For the furthest downstream station the edge of the plume has just reached the surface for the medium velocity ratio run while for the high  $K$  value the plume has started to spread along the surface; to study this area in more detail the same experiments were performed but with the injection level moved to within 3 cms of the surface; these results are now described.

### 3 cms Submergence

Experiments were performed for all three velocity ratios and for a Froude number of 15 at this submergence depth; for the lowest velocity ratio, the results (and the predictions) were exactly as for the larger submergence and hence only the two larger velocity ratio cases are discussed below.

FIGS. 6.3.33 and 6.3.34 show that the program can handle a change in the proximity of the free surface very well. Both velocity ratios show the trajectory hits the surface before 40 diameters downstream and the model also predicts this behaviour. Subsequently the warm water forms a layer which the experiments show remains of almost constant depth as it travels downstream (this comment was also made in Chapter 5 when examining the photographs of the plume); these figures show that the predictions exhibit exactly the same behaviour. Finally FIGS. 6.3.35 and 6.3.36 compare the cross-sectional temperature contours for this low submergence depth; the upstream contours are very similar to the ones presented earlier but the final cross-section comparisons illustrate the layer-like nature of the flow very well. The warm water jet has now become a 'puddle' lying on the surface of the ambient stream and the predictions too exhibit this feature. The one area of disagreement is the amount of lateral spread of the puddle along the water surface, the predictions underestimate this spread. Partly, this may be due to the difficulty mentioned above of measuring precisely at the water surface, however the treatment of the free surface as a plane of symmetry is certainly an over-simplification and would probably contribute to this discrepancy.

#### 6.4 Summary

In this chapter, the mathematical and turbulence models outlined earlier have been used to provide predictions for the turbulent buoyant jet in a co-flowing stream. Detailed comparison with experimental data has been used to check the validity of the model over as wide a range of flow parameters as was available; where these comparisons have shown discrepancies between predictions and data, explanations have been given where possible to resolve the reasons for the discrepancies. The computer program has been applied to previously unpredicted phenomena such as buoyant jets discharged near solid surfaces (Winiarski and Chasse data), and also near a water/air interface (present data). Both of these problems could not be tackled with the other available methods for buoyant jet discharge as these methods usually involve assumptions of rotational symmetry about the jet axis, which is invalidated when the axis approaches boundary surfaces. For the near-water-surface discharge the model has been shown to be capable of predicting the transition from a jet-like flow to a layer-like flow accurately, a demonstration which to the author's knowledge, has not been provided elsewhere.

CHAPTER 7

FURTHER PREDICTIONS - A RIVER DISCHARGE PROBLEM

7.1 Introduction

It was mentioned in Chapter 1 that the complexity of most real river thermal-pollution problems had until recently prevented any attempts to use analytical techniques for their solution. Zelazny and Baker [34] made a start in this direction by applying a finite-element method to the solution of a river flow problem; the turbulence model used was a zero equation model which the authors stressed was too simplistic to characterise the important turbulence parameters of a buoyant jet problem accurately. This chapter demonstrates how the mathematical and turbulence models used in this thesis, which were shown in the last chapter to be adequate for buoyant jet problems, may be combined with the irregular boundary treatment described in Chapter 4 to form a powerful computational tool which it is believed is capable of predicting the quantitative behaviour of river thermal-pollution problems. It is emphasised that the irregular boundary treatment must be combined with the mathematical model since some means must be found for handling typical river beds which are often very irregular, in the results presented below a simple shape has been chosen for the cross-section as the purpose of this chapter is mainly illustrative.

## 7.2 Some Sample Calculations

### 7.2.1 The Problem Considered

To illustrate the capability of the combined mathematical model, predictions have been obtained for the following imaginary thermal discharge into a river: the river is 100 metres wide and 10 metres deep at the centre (symmetry of the river about a vertical centre-plane has been assumed); the river bed is assumed to be elliptical in cross-section so that FIG. 7.2.1 represents the overall river geometry. In this Figure the area of discharge of thermal pollution is shown shaded and this area (in the half of the river being considered) is 2 m deep and 1 m wide. In all the calculations the warm water temperature is 40°C and the ambient (river) temperature is 20°C. In what follows the effect of varying several parameters is studied but the standard values at the inlet cross section are given below

$$\left. \begin{array}{l} \text{River velocity (uniform)} = 0.33 \text{ m/s} \\ \text{Jet velocity (uniform)} = 1.32 \text{ m/s} \end{array} \right\} \text{Hence } K = 4$$

$$k_{\text{riv}} = .001 u_{\text{riv}}^2$$

$$k_{\text{jet}} = .001 u_{\text{jet}}^2$$

$$\epsilon_{\text{riv}} = k_{\text{riv}}^{3/2} / (C_{\mu}^{-3/4} .0.07.D)$$

$$\epsilon_{\text{jet}} = k_{\text{jet}}^{3/2} / (C_{\mu}^{-3/4} .0.07.d_j)$$

The value of  $\beta$  was taken from tables at the jet temperature of  $40^{\circ}\text{C}$  and combined with the above conditions this corresponded to a Froude number of 3.87. In the definition of the dissipation in the jet and in the river it can be seen that the value of  $A_{\xi}$  has for the time being been left at unity. An example of the grid used to calculate this problem is contained in Appendix 1 as are the forward step parameters which produced step-independent results.

### 7.2.2 Results

In a real thermal pollution problem, the extent of the buoyant jet at various stations down the river would be the information primarily sought after; accordingly the temperature contours at various downstream sections form the most useful part of the results. The major advantage of computational methods such as the one used here is the ease with which the effect of different discharge characteristics on the plume rise and spread may be calculated; accordingly this is the method of presentation adopted for the present illustrative study.

#### Effect of Jet Velocity Ratio

The first discharge parameter studied was the K value of the jet, this was changed by simply altering the river velocity with all else the same. Thus FIG. 7.2.2\* presents comparisons for a Froude number of 4 (3.87) for three K values (2, 4, 10); temperature

---

\*For clarity, the vertical scale is twice the horizontal in FIGS. 7.2.2 - 7.2.4.

contours at three stations downstream are drawn in each case. Considering first the standard case, the behaviour is very much as expected; with increasing downstream distance the plume rises and spreads while the temperatures fall, the rate of rise may be estimated from the location of the maximum temperature location also marked in FIG. 7.2.2. By 20 diameters downstream the jet has already undergone transition to a puddle-like form spreading on the surface of the river. It may be noticed that the maximum temperature location eventually hits the surface and is then carried out along it by the same lateral velocities which cause the spreading of the puddle; by 26 jet heights downstream the warm water has reached half way to the river bank and covers approximately one third of the river cross-section.

As may be expected, for a lower velocity ratio, the buoyancy forces have less prominence and the plume rises more slowly. The contours show that the rate of spread is also less, so that although the warm water has polluted less of the river, the plume temperatures are higher than in the standard case. For a higher velocity ratio the reverse is true, the plume rises and spreads very quickly reaching the river bank only 26 jet heights downstream; the dilution is of course greater in this case as evidenced by the lower maximum temperature.

#### Effect of Froude Number

To examine the effect of Froude number at constant velocity ratio was also very simple to arrange, the jet and river velocities



were merely increased or decreased by the same ratio, thus leaving  $K$  the same but altering  $FR$  via  $u_j$ . FIG. 7.2.3 presents temperature contours for three Froude numbers; the standard case is given again for comparison purposes and to the right are the contours for a tenfold increase in Froude number and also a tenfold decrease. The high  $FR$  case shows a much slower rate of rise and the warm water is contained within 20% of the river, the buoyancy forces are so small that the jet also spreads downwards almost as quickly and by 26 diameters downstream has reached the river bottom. The slower rate of rise has also produced slower mixing and the plume temperatures are higher. Quite the opposite effect is seen for the low  $FR$  case, the rate of plume rise is exceptionally rapid and the maximum temperature location has hit the surface and moved along it by the first location; the dilution rate is correspondingly large. Only one set of contours is presented as it is probable that the curvature of the plume in this final case is so steep that it might well invalidate the parabolic assumptions; this level of Froude number would probably not occur in practice.

#### Effects of Discharge Location

The final discharge parameter investigated was the actual discharge position. The warm water source was moved so that it lay off the centre-line half way to the river bank. FIG. 7.2.4 presents the temperature contours at four downstream stations for the standard values of  $FR$  and  $K$ . The plume rises in a similar manner but when the maximum temperature hits the water

surface, it now splits into two and travels both towards the centre-line and towards the river bank. This implies that the rising water has set up two counter rotating vortices and this fact is also borne out by the distorted shape of the temperature contours at the further downstream stations.

### Surface Temperature Contours

An often-used indication for the severity of a thermal pollution source is the surface temperature distribution of the river. Licensing authorities use the concept of a 'mixing zone' to limit the area of river which is polluted; the mixing zone is defined as the area of the river surface which is greater than  $1^{\circ}\text{C}$  above ambient; and permission is only granted for any thermal discharge if the area is within a specified size. FIGS. 7.2.5 and 7.2.6 show that the predictions obtained with the present method can easily be used to assess the size of the mixing zone.

The first graph illustrates the effect of the velocity ratio on the amount of surface water which is polluted. In the low velocity ratio case the surface zone is fairly thin and elongated; for  $K = 4$  the outermost contour moves further towards the bank, and for the high velocity ratio the whole surface is above ambient by 200 metres downstream.

Figure 7.2.6 shows how the location of the discharge changes the shape of the surface contours. The off-centre-line case exhibits quicker spreading and dilution, but this may be expected since by moving the discharge location, entrainment of cold ambient

fluid has taken place over a larger jet perimeter than when the warm water is injected on the centre-line.

### 7.3 Summary

This chapter has brought together the two techniques developed in this thesis for buoyant jet predictions and for irregular boundaries. The model has been applied to a typical river thermal-pollution problem and reasonable predictions have been presented and discussed. The effects of several parameters have been examined and the ease with which these effects may be assessed was emphasised. The sample calculations only illustrated the kind of investigations that are possible and the examples given of the parameters which were varied were by no means exhaustive.

## CHAPTER 8

### CONCLUSIONS AND SUMMARY

#### 8.1 Review of Work Presented

In Chapters 2, 3 and 4 of this thesis a description was provided of a mathematical model for turbulent buoyant jets discharged into co-flowing rivers. The first chapter outlined the governing differential equations for the transport of mass, momentum and energy, and categorised them as three-dimensional parabolic or boundary-layer partial differential equations. A numerical scheme was then outlined for the solution of these equations, the central idea being the SIMPLE algorithm. Chapter 3 reviewed the available methods for modelling the turbulent nature of the flow and described a model which affected closure at the two equation level. Finally, Chapter 4 extended the numerical scheme to allow the treatment of solid boundaries which did not coincide with the lines of the finite-difference grid; this latter treatment is necessary if the river bed is to be handled in the same computational scheme as the buoyant jet.

A review of previous work revealed several sources of experimental data for turbulent buoyant jets, and these were complemented by the present experimental investigation which studied hot water jets discharged close to a water surface. A thermocouple probe was used to measure temperature profiles for a range of Froude numbers, velocity ratios, and jet submergence depths and, for selected runs, complete cross-sectional temperature

contours were obtained. The results were compared with the results of other experiments and other analyses; photographs of the buoyant plume were also presented.

The theoretical model was then validated by comparison with analytical and experimental data. The irregular boundary treatment was tested by predicting both laminar and turbulent duct flows; circular and elliptical boundaries were considered. Detailed comparison was made with all the buoyant jet data and agreement was generally good over the whole range of conditions.

Finally, in Chapter 7, the model was used to present sample calculations for a river thermal discharge problem. The demonstration illustrated how the effects of various parameters could be varied to assess the severity or otherwise of any particular thermal discharge configuration.

In the preceding chapters, an assessment has been given in the relevant place of the performance of the model; it is thus only necessary here to summarise the main achievements of the present work; these are as follows:-

- 1) The development of the irregular boundary treatment.

This method is now available for the solution of many problems in the field of non-circular duct flow; the mathematical nature of the solution algorithm means that the developing flow field can now also be studied.

- 2) The provision of a complete mathematical model for three-dimensional buoyant jets in co-flowing rivers. The advanced nature of the turbulence model has overcome many of the problems which complicate analyses of the entrainment method type. Together with (1) this now brings within reach the prediction of real river discharge problems, and a demonstration of how actual river discharges may be predicted was provided.
- 3) The experimental investigation has added to the available data on buoyant jets; previously all data had considered infinite ambients and the present experiments are the first to investigate the effect of the proximity of the free surface, and to demonstrate the jet to layer transition by measurement of the complete temperature contours.

## 8.2 Suggestions for Future Work

The following areas are suggested as profitable areas for future work:

- 1) On the experimental side the present investigation was exclusively restricted to temperature measurements; information on the velocity development and if possible also of turbulence quantities would be useful in assessment

of predictions. An extension of the Froude number/  
velocity ratio range is also required.

- 2) If full advantage is to be taken of the capability for predicting irregular duct flows, it will be necessary to use higher order turbulence models to account for the secondary flows which are so important in non-circular ducts. The first step in this direction should be made via the algebraic Reynolds stress models mentioned earlier.
- 3) Many river discharge problems take place in stretches of rivers with bends; the mathematical model is certainly capable of handling this situation but the modifications necessary to take account of the curvature of the main flow direction must be incorporated.
- 4) On the numerical side the treatment of the inlet conditions in buoyant jet flows, although satisfactory for the purposes of this thesis, could certainly be improved. One possible solution would be to concentrate the grid in the jet region alone and not in the river, where most variables change very slowly; the grid should then expand outwards to cover the region of interest as this grows with distance downstream as is arranged in the two-dimensional method of Patankar and Spalding [11].

- 5) Interest has been concentrated in this thesis on the near-field region of discharge. The far-field is however just as important and could be studied using the present method, with two modifications. Firstly, in the far-field, surface heat transfer is an important process and the treatment of the water surface used in this thesis would have to be improved. Secondly, in this region the effects of buoyancy on the turbulence structure is also important and would have to be taken into consideration.
  
- 6) Finally, it was mentioned in Chapter 1 that, although the study of single-port discharge was of prime importance, most practical situations were of the multi-port type and also not co-flow but usually angled discharge with respect to the main flow. The mathematical model would increase tremendously in usefulness if the capability of handling both these situations was introduced.



REFERENCES

1. D.R.F. Harleman, K.D. Stolzenbach. "Fluid Mechanics of Heat Disposal from Power Generation". Annual Review of Fluid Mechanics 4 1972.
2. G.N. Abramovich. "The Theory of Turbulent Jets". M.I.T. Press 1963.
3. W. Forstall, A.H. Shapiro. "Momentum and Mass Transfer in Co-Axial Gas Jets". J. of Applied Mechanics 17 1950.
4. G.M. Ayoub. "Dispersion of Buoyant jets in a flowing ambient fluid". Ph.D. Thesis University of London 1971.
5. W. Rodi. "The Prediction of Free Turbulent Boundary Layers by use of a Two-Equation Model of Turbulence". Ph.D. Thesis University of London 1972.
6. S. Sami, T. Carmody, H. Rouse. "Jet diffusion in the region of flow development". Journal of Fluid Mechanics 27 1967.
7. I. Wygnanski, H.E. Fiedler. "Some measurements in the self-preserving jet." Journal of Fluid Mechanics 38 1969.
8. J.O. Hinze, B.G. Van der Hegge Zijnen. "Transfer of Heat and Matter in the turbulent mixing zone of an axially-symmetrical jet". Applied Scientific Research A1 1949.
9. S. Corrsin, M.S. Uberoi. "Further Experiments on the Flow and Heat Transfer in a Heated Turbulent Air Jet." NASA Tech. Note 1865 1949.
10. H.A. Becker, H.C. Hottel, G.C. Williams. "The nozzle-fluid concentration field of the round, turbulent, free jet." Journal of Fluid Mechanics 30 1967.
11. S.V. Patankar, D.B. Spalding. "Heat and Mass Transfer in Boundary Layers". 2nd edition Intertext Books London 1970.
12. D.B. Spalding. "Concentration fluctuations in a round turbulent free jet." Chemical Engineering Science 26 1971.
13. F. Landis, A.H. Shapiro. "The turbulent mixing of co-axial jets". Heat Transfer and Fluid Mechanics Institute Reprints of Papers 1951.
14. J.G. Knudsen, D.L. Katz. "Fluid Dynamics and Heat Transfer." McGraw-Hill London 1958.

15. T.S. Lundgren, E.M. Sparrow, J.B. Starr. "Pressure drop due to the entrance region in ducts of arbitrary X-Section." Trans. ASME Jnl. Basic Eng. 86 1964.
16. "Free Turbulent Shear Flows". A Conference held at Langley Research Centre Hampton, Virginia, U.S.A., NASA SP321 Vol. 1 - Conference Proceedings July 1972.
17. B.E. Launder, A. Morse, W. Rodi, D.B. Spalding. "The Prediction of Free Shear Flows - A Comparison of Six Turbulence Models". Paper submitted to NASA conference on free shear flows Langley 1972.
18. R.L. Frankel, J.D. Cumming. "Turbulent mixing phenomena of ocean outfalls". Proceedings ASCE Sanitary Engineering Div. 91 1965.
19. G. Abraham. "Horizontal Jets in stagnant fluid of other density". Proceedings ASCE Hydraulics Div. HY4 1965.
20. H.O. Anwar. "Behaviour of buoyant jet in calm fluid." Proceedings ASCE Hydraulics Div. HY4 1969.
21. L.N. Fan, N.H. Brooks. "Numerical Solutions of Turbulent Buoyant Jet Problems". California Institute of Technology E.M. Keck Laboratory Report KH-R-18 1969.
22. B.R. Morton, G.I. Taylor, J.S. Turner. "Turbulent Gravitational Convection from Maintained and Instantaneous Sources." Proceedings Royal Society of London A234 1956.
23. R.S. McQuivey, T.N. Keefer, M.A. Shirazi. "Basic data report on the turbulent spread of heat and matter." U.S. Department of Interior Geological Survey and the U.S. Environmental Protection Agency, Open file report, Fort Collins, Colorado, U.S.A. 1971.
24. M.A. Shirazi, R.S. McQuivey, T.N. Keefer. "Heated water Jet in Co-flowing turbulent stream." Proceedings ASCE Hydraulics Div. HY7 1974.
25. M.A. Shirazi, L.R. Davis, K.V. Byram. "An evaluation of ambient turbulence effects on a buoyant plume." Proceedings, Summer Computer Simulation Conference Montreal 1973.
26. E. Hirst. "Zone of Flow Establishment for Round Buoyant Jets." Water Resources Research 8 1972.
27. E. Hirst. "Buoyant jets with three-dimensional trajectories". Proceedings ASCE Hydraulics Division HY11 1972.

28. L. Winiarski, J.P. Chasse. "Plume temperature measurements of shallow, submerged model discharges with current." U.S. Environmental Protection Agency, Pacific Northwest Environmental Research Laboratory Report EPA-660/2-73-001 1973.
29. J.P. Chasse, L. Winiarski. "Laboratory Experiments of submerged discharges with current." U.S. Environmental Protection Agency, Pacific Northwest Environmental Research Laboratory Working Paper 12 1974.
30. M.A. Shirazi, L.R. Davis. "Workbook of thermal plume predictions Volume 1 Submerged Discharge". U.S. Environmental Protection Agency Report EPA-R2-72-005a 1972.
31. W.H.C. Maxwell, H. Pazwash. "Axisymmetric shallow submerged turbulent jets." Proceedings ASCE Hydraulics Division HY4 1973.
32. J.P. Narain. "Swirling shallow submerged turbulent plumes." Proceedings ASCE Hydraulics Division. HY9 1974.
33. W.H.C. Maxwell, H. Pazwash. "Boundary Effects on Jet Flow patterns related to water quality and pollution problems." Research Report No. 28. University of Illinois 1967.
34. S.W. Zelazny, A.J. Baker. "Predictions in Environmental Hydrodynamics using Finite-Element method - II - Applications." AIAA Journal 13 1975.
35. D.B. Spalding. "The Mathematical Modelling of Rivers." Imperial College Mech. Eng. Dept. Report HTS/74/4 1974.
36. S.V. Patankar, D.B. Spalding. "A calculation procedure for heat, mass and momentum transfer in three-dimensional parabolic flows." Int. Jnl. Heat and Mass Transfer 15 1972.
37. H. Schlichting. "Boundary Layer Theory". McGraw-Hill New York 1960.
38. S.V. Patankar, V.S. Pratap, D.B. Spalding. "Prediction of turbulent flow in curved pipes." Journal of Fluid Mechanics 67 3 1975.
39. R.B. Bird, W.E. Stewart, E.N. Lightfoot. "Transport Phenomena." Wiley International Edition New York 1960.
40. D. Sharma. "Turbulent convective phenomena in straight, rectangular-sectioned diffusers." Ph.D. Thesis, University of London 1974.
41. J.S. Turner. "Buoyancy effects in fluids." Cambridge University Press 1973.

42. S.V. Patankar. "On available calculation procedures for steady, three-dimensional boundary layers." Imperial College Heat Transfer Section Report BL/TN/A/44 1971.
43. F.H. Harlow, J.E. Welch. "Numerical calculation of time-dependent viscous incompressible flow of fluid with free surface." *The Physics of Fluids* 8 1965.
44. A.D. Gosman, W.M. Pun, A.K. Runchal, D.B. Spalding, H. Wolfshtein. "Heat and Mass Transfer in Recirculating Flows." Academic Press London 1969.
45. J.O. Hinze. "Turbulence". McGraw-Hill New York 1959.
46. B.E. Launder, D.B. Spalding. "Mathematical Modelling of Turbulence". Academic Press London 1972.
47. F.H. Harlow (Editor). "Turbulence transport modelling." AIAA Selected Reprint Series vol. XIV 1973.
48. L. Prandtl. "Bericht über Untersuchungen zur ausgebildeten Turbulenz." *Z.A.M.M.* 5 1925.
49. L. Prandtl. "Über ein neues Formalsystem für die ausgebildeten Turbulenz". *Nachrichten van der Akad. der Wissenschaft in Göttingen* 1945.
50. J. Rotta. "Über eine Methode zur Berechnung turbulenter Scherströmungen." *Aerodynamische Versuchsanstalt Göttingen Report 69AH* 1968.
51. D.B. Spalding. "The prediction of two-dimensional steady turbulent flows." Imperial College Heat Transfer Section Report EF/TN/A/16 1969.
52. F.H. Harlow, P.I. Nakayama. "Transport of turbulence energy decay rate." Los Alamos Sci. Lab. Univ. California Rep. LA-3854 1968.
53. W.P. Jones, B.E. Launder. "The prediction of laminarisation with a two-equation model of turbulence." *Int. Jnl. Heat and Mass Transfer* 15 1972.
54. B.E. Launder, D.B. Spalding. "The numerical computation of turbulent flows." *Computer methods in applied mechanics and engineering* 3 1974.
55. A.W. Date. "Prediction of friction and heat transfer characteristics of flow in a tube containing a twisted tape." Ph.D. Thesis University of London 1972.

56. D.G. Tatchell. "Convection Processes in confined three-dimensional boundary layers." Ph.D. Thesis University of London 1975.
57. K. Hanjalić. "Two-dimensional asymmetric turbulent flow in ducts." Ph.D. Thesis University of London 1970.
58. D.B. Spalding, C.L.V. Jayatillaka. "A survey of the theoretical and experimental information on the resistance of the laminar sub-layer to heat and mass transfer." Proceedings 2nd All Soviet Union Conference on Heat and Mass Transfer Minsk, USSR. 1964.
59. R.F. LeFeuvre. "Laminar and Turbulent Forced Convection Processes through in-line Tube banks." Ph.D. Thesis University of London 1973.
60. J. Boussinesq. "Theorie analytique de la chaleur." Vol. 2 Paris: Gathier-Villars. 1903.
61. R.K. Shah, A.L. London. "Laminar flow forced convection heat transfer and flow friction in straight and curved ducts - A summary of analytical solutions." Technical Report No. 75, Dept. of Mechanical Engineering, Stanford University, California 1971.
62. H.L. Langhaar. "Steady flow in the transition length of a straight tube." ASME Journal of Applied Mechanics, 1942.
63. E.H. Sparrow, S.H. Lin, T.S. Lundgren. "Flow development in the hydrodynamic entrance region of tubes and ducts." Physics of Fluids 7 1964.
64. M.W. Collins. "Developing laminar flow in a circular tube." A Symposium on Internal Flows. University of Salford. 1971.
65. J.C. Slattery, W.D. Campbell. "Flow in the entrance region of a tube." ASME Journal of Basic Engineering 1963.
66. F.W. Schmidt, B. Zeldin. "Laminar Flows in inlet sections of tubes and ducts." American Institute of Chemical Engineers Journal 11 1965.
67. L. Prandtl, O.G. Tietjens. "Applied Hydro-and Aero-Mechanics." Dover Publications. New York, 1957.
68. B. Atkinson, Z. Kemblowski, J.M. Smith. "Measurements of velocity profiles in developing liquid flows." American Institute of Chemical Engineers Journal 13 1967.
69. E. Reshotko. Progress Report No. 20-364. Jet Propulsion Laboratory California Institute of Technology.

70. D. Cain. "Flow in Elliptic Ducts." M.Phil. thesis Liverpool College of Advanced Technology 1969.
71. H. Barrow, A. Roberts. "Flow and Heat Transfer in elliptic ducts." Paper FC4-1 Fourth International Heat Transfer Conference 1970.
72. D. Cairn. "Turbulent flow and heat transfer in elliptical ducts." Ph.D. Thesis Liverpool Polytechnic. 1971.
73. J. Duffy, D. Cain. "On the use of the Preston tube in elliptical ducts." The Aeronautical Journal 76 1972.
74. D. Cain, J. Duffy. "An experimental investigation of turbulent flow in elliptical ducts." International Journal of Mechanical Sciences 13 1971.
75. J. Laufer. "The Structure of Turbulence in Fully-Developed Pipe Flow." NACA Report 1174 1952.
76. A.R. Barbin, J.B. Jones. "Turbulent Flow in the Inlet Region of a Smooth Pipe." ASME Journal of Basic Engineering March 1963.
77. M. Ammar. Private Communication. Imperial College 1974.
78. E. Brundrett, W.D. Baines. "Production and Diffusion of Vorticity in Duct Flow." Jnl. Fluid Mechanics 19 1964.
79. B.E. Launder, W.M. Ying. "Prediction of Flow and Heat Transfer in Ducts of Square Cross-Section." Heat and Fluid Flow 3 1973.
80. B.S. 1828. Reference tables for Copper/Constantan Thermocouples. 1961.
81. Robert C. Dean Jr. (Editor). "Aerodynamic Measurements." Gas Turbine Laboratory, M.I.T., M.I.T. Press 1953.
82. H.J. Leutheusser. "Turbulent flow in rectangular ducts." Proceedings ASCE Jnl. Hydraulics Division 89 1963.
83. J.P. Hartnett, J. Koh, S.T. McComas. "A comparison of predicted and measured friction factors for turbulent flow through rectangular ducts." Trans. ASME Jnl. Heat Transfer 84 1962.
84. W.M. Ying. "Fully-Developed Flow with Swirl in Non-Circular Ducts." Ph.D. Thesis University of London 1971.

85. E. Brundrett, P.R. Burroughs. "The temperature inner-law and heat transfer for turbulent air flow in a vertical square duct." Int. Jnl. Heat and Mass Transfer. 10 1967.
86. S. Ahmed, E. Brundrett. "Turbulent flow in non-circular ducts Part 1 - Mean flow properties in the developing region of a square duct." Int. Jnl. of Heat and Mass Transfer. 14 1971.
87. A. Melling. "Investigation of Flow in Non-Circular Ducts and Other Configurations by Laser-Doppler Anemometry." Ph.D. Thesis University of London 1975.
88. L. Matthews. "Performance of Some Two-Dimensional Film-Cooling Geometries." Ph.D. Thesis University of London 1972.
89. R.S. Varga. "Matrix Iterative Analysis". Prentice-Hall International. London 1962.
90. S.T. McComas. "Hydrodynamic entrance lengths for ducts of arbitrary X-Section." Trans. ASME Jnl. Basic Eng. 89 1967.
91. N.T. Dunwoody. "Thermal results for forced convection heat transfer through elliptical ducts." Trans. ASME Jnl. Applied Mech. 29 1962.
92. J. Schenk, B.S. Han. "Heat transfer from laminar flows in ducts with elliptic cross-section." Appl. Scientific Research 17, 1967.
93. P.A. James. "Forced convective heat transfer in narrow passages." Canadian Jnl. Chemical Eng. 48 1970.
94. L.N. Tao. "On some laminar forced convection problems." Trans. ASME Jnl. Heat Transfer 83 1961.
95. V.P. Tyagi. "Laminar forced convection of a dissipative fluid in a channel." Trans. ASME Jnl. Heat Transfer 88 1966.
96. V.P. Tyagi. "A forced convective heat transfer including dissipation and compression work for a class of non-circular ducts." Int. Jnl. Heat and Mass Transfer 14 1971.
97. M. Iqbal, A.K. Khattry, B.D. Aggarwala. "On the second fundamental problem of combined free and forced convection through vertical non-circular ducts." Applied Scientific Research 26 1972.
98. L.N. Tao. "Variational Analyses of forced heat convection in a duct of arbitrary X-Section." Proceedings 3rd Int. Heat Transfer Conference Chicago 1966.

99. S.S. Rao, N.A.P. Ramachangulu, V.G. Krishnamurty.  
"Laminar Forced Convection in Elliptic Ducts."  
Appl. Scientific Res. 21 1969.
100. D.E. Gilbert, R.W. Leay, H. Barrow. "Theoretical Analysis  
of Forced Laminar Convection Heat Transfer in the Entrance  
Region of an Elliptic Duct." Int. Jnl. Heat and Mass  
Transfer 16 1973.
101. D. Cain, A. Roberts, H. Barrow. "A Theoretical Study of  
Fully-Developed Flow and Heat Transfer in Elliptical Ducts."  
Paper C-120 Inst. Mech. Eng. Conference on "Recent Developments  
in Compact High Duty Heat Exchangers." London 1972.
102. D.G. Ainley. "The high-temperature Turbo-Jet Engine."  
Jnl. Royal Aero. Soc. 60 1956.
103. D.E. Gilbert. Private Communication. 1973.



NOMENCLATURE

<u>Symbol</u>	<u>Meaning</u>	<u>Eqn. of First Occurrence</u>
A	area	
$A_i^i$	Coefficient in finite-difference equation	2.4.3
$A_i^0$	Normalised finite-difference coefficient	2.4.13
$a_j$	Normalised finite-difference coefficient	2.4.6
a	Semi-major axis of ellipse	FIG. 4.13
$A_\epsilon$	Parameter in definition of inlet jet $\epsilon$ value	6.3.4
b	Semi-minor axis of ellipse	FIG. 4.13
b	width of jet	FIG. 1.2
B	Width of open channel	FIG. 1.4
$C_\mu, C_1, C_2$	Constants in turbulence model	Table 3.2
$C_j^i$	Convective terms in finite-difference eqns.	2.4.1
$C^*$	Non-dimensional concentration	6.3.7
$D_j^i$	Diffusion terms in finite-difference eqns.	2.4.1
$D^u, D^v, D^w$	Coefficient of pressure gradient term	2.4.10
$d_j$	Jet nozzle diameter	1.3.2
$d_h$	hydraulic diameter	4.3.6
E	Constant in universal log-law	3.3.5
EX	Expansion rate parameter for step size	
FR	Densimetric Froude number	1.3.2
f	friction factor	4.3.1
FRAS	forward step size parameter	
G	Generation of turbulence energy	3.2.10
g	gravitational acceleration	1.3.2

<u>Symbol</u>	<u>Meaning</u>	<u>Eqn. of first occurrence</u>
H	Height of open channel	FIG. 1.4
h	Height of nozzle above channel flow	FIG. 1.4
i	turbulence intensity	3.3.1
K	Jet to ambient velocity ratio	1.3.1
k	turbulence kinetic energy	3.1.7
K <sub>p</sub>	pressure drop coefficient	4.3.1
L	length of potential core	1.3.1
ℓ	turbulence length scale	3.1.8
ℓ <sub>m</sub>	Prandtl mixing length	3.1.6
$\dot{m}'_{ent}$	mass flow rate of jet entrained fluid	1.3.6
m <sub>p</sub>	mass source at node P	2.4.19
p	pressure	2.2.3
P <sub>ø</sub>	function in wall law for ø transfer	3.3.7
q'	wall heat flux per unit duct length	6.2.1
r	radius	1.3.3
s	distance along jet axis	1.3.5
s	distance along duct wall	FIG. 4.26
S <sub>p</sub> <sup>ø</sup>	Source ↓ sink term in finite-difference eqn.	2.4.3
St	Stanton number	6.2.6
T	Temperature	2.2.3
$\overline{tu}_j$	turbulent heat flux	3.1.4
T*	non-dimensional temperature	6.3.7
u, v, w	Velocity components in x, y, z direction	
$\overline{u_i u_j}$	Reynolds stresses	3.1.3
u <sub>τ</sub>	Friction velocity	3.3.6

<u>Symbol</u>	<u>Meaning</u>	<u>Eqn. of First Occurrence</u>
w	distorted nozzle width	6.3.1
W	Vertical width of plume	1.3.11
x,y,z	Cartesian coordinates	

Greek Symbols

$\alpha$	Turbulent entrainment coefficient	1.3.7
$\beta$	Volumetric expansion coefficient	2.2.9
$\Gamma_{\phi}$	Transport coefficient for scalar property $\phi$	2.2.6
$\delta_{ij}$	Kronecker delta function	3.1.7
$\Delta, \delta$	Difference of	2.4.2
$\delta$	distance of node from wall	3.3.5
$\epsilon$	dissipation rate of turbulence energy	
$\kappa$	constant in universal log law	3.3.5
$\mu$	viscosity	2.2.3
$\rho$	density	1.3.2
$\sigma$	Prandtl/Schmidt number	
$\tau_w$	wall shear stress	3.3.6
$\dot{\phi}_s''$	wall flux of $\phi$	3.3.4
$\overline{\phi u_j}$	turbulent flux of $\phi$	3.1.5
$\phi$	General scalar fluid property	2.2.6
$\phi$	Angle between jet axis and horizontal plane	1.3.5
$\lambda$	Spreading parameter	1.3.4
$\eta$	non-dimensional downstream distance	1.3.8
$\theta$	angle in jet natural co-ordinate system	1.3.5
$\xi_1, \xi_2, \xi_3$	General orthogonal co-ordinates	

Symbol

Meaning

Subscripts

$\zeta$	centre-line
P,N,S,E,W	grid node locations
m, max	maximum
in,o	inlet
J,Jet	Jet
a, amb	ambient
w, wall	wall
b, bulk	Bulk
t	turbulent
eff	effective
mod	modified
riv	river

Superscripts

—	relating to pressure in axial momentum equation
'	relating to pressure correction
*	starred values

APPENDIX 1

SOME COMPUTATIONAL DETAILS

Al.1 Introduction

This Appendix contains information relevant to the numerical solution procedure described in Chapter 2 and used for the predictions presented in the Thesis. The information comprises details which were considered too cumbersome to include in the main body of the Thesis, such as step sizes, grid dispositions for various problems, and typical computing times.

Al.2 Finite-Difference Forms of Source Terms

In Chapter 2 the idea of linearisation of the source term which appears in the general transport equation for  $\phi$  was introduced. In more detail, when integrated over the control volume for a typical grid node P, the source term is written:-

$$\int_V S^\phi dV = S_U^\phi + S_P^\phi \cdot \phi_P \quad (\text{Al.1})$$

where V represents the volume of the central volume surrounding P and  $\phi_P$  is the local value of  $\phi$ . This assumption of a linear dependence on the local (downstream)  $\phi$  results in an increased implicitness of the finite-difference equation and also aids stability. This latter claim may be demonstrated as follows: The balance equation in finite-difference form has been given in Chapter 2 and, using (Al.1) above may be written:-

$$\left( \sum_{i=E,W,N,S,P,U} A_i^{\theta'} - S_P^{\theta} \right) \varphi_P = \sum_{i=E,W,N,S} A_i^{\theta'} \varphi_i + S_u^{\theta} \quad (A1.2)$$

The coefficient of  $\varphi_P$  is thus enlarged by an amount  $S_P^{\theta}$  (the quantity itself being always arranged to be negative). Hence the normalised finite-difference equation:-

$$\varphi_P = \sum_{i=E,W,N,S} A_i^{\theta} \varphi_i + S_u^{\theta} \quad (A1.3)$$

has coefficients  $A_i^{\theta}$  which are now more likely to satisfy the condition:-

$$\sum_{i=E,W,N,S} A_i^{\theta} \leq 1 \quad (A1.4)$$

This criterion is known (see Varga [89]) to increase the stability of finite-difference equations, at least when these have constant coefficients. Even if the  $A_i^{\theta}$  are not constant in the present situation, the stability is still increased by this practice of linearisation.

As a final illustration of this practice, consider one of the source terms in the equation for the turbulence kinetic energy  $k$ :-

$$S^k = -\rho \varepsilon \quad (A1.4)$$

this is re-written using the definition of the turbulent viscosity

$$\mu_T = C_{\mu} \rho k^2 / \epsilon$$

hence

(A1.5)

$$S^k = - C_{\mu} \rho^2 k^2 / \mu_T$$

and finally this is linearised with respect to the upstream and downstream values of k i.e.:-

$$S_P^k = - C_{\mu} \rho^2 k_{p,u} / \mu_T$$

(A1.6)

and this value is used to increase the coefficient of  $k_p$  in the finite-difference equations.

### A1.3 Grid Disposition

Most predictions have required non-uniform grid distributions with grid nodes clustered in the expected region of rapid variations. The maximum number of grid lines varied from problem to problem; the range of grids covering 10 x 10 uniform for the laminar circular duct flow up to 25 x 25 non-uniform for the prediction of the present buoyant jet data. In the table which follows are given the grids used for four typical problems, one laminar flow, one turbulent flow without heat transfer and two buoyant jet flows. In all cases these grids have been subject to increasing refinement until grid independent solutions were obtained; it is the final grids which are presented in Table A1.1.

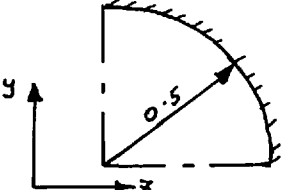
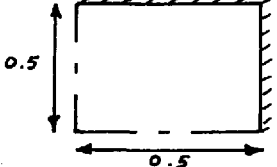

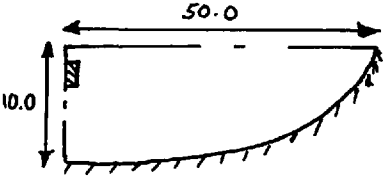
PROBLEM CONSIDERED	CALCULATION DOMAIN	GRID SIZE	GRID CO-ORDINATES
Leminar Circular Duct Flow (1)		10 x 10	$z=0, .0313, .0933, .1565, .219, .2815, .344, .4015, .469, .5$ $y=0, .0313, .0933, .1565, .219, .2815, .344, .4015, .469, .5$
Turbulent flow in a square duct (2)		12 x 12	$z=0, .025, .075, .125, .175, .225, .275, .325, .375, .425, .475, .50$ $y=0, .025, .075, .125, .175, .225, .275, .325, .375, .425, .475, .50$
Present buoyant Jet Exptl. data (3)		25 x 25	$z=0, .0005, .001, .0015, .002, .003, .00486, .006, .008, .012, .02, .028, .04, .06, .08, .1, .13, .18, .24, .32, .4, .5, .6, .7, .7625$ $y=0, .01, .04, .1, .15, .17, .182, .192, .2, .206, .21, .214, .217, .22, .224, .228, .234, .24, .246, .254, .26, .265, .27, .275, .277$
River Flow Thermal Discharge Problem (4)		20 x 20	$z=0, .2, .6, .8, 1.2, 2.0, 3.0, 4.6, 7.0, 10.0, 13.0, 18.0, 22.0, 29.0, 34.0, 39.0, 44.0, 46.5, 49.0, 50.0$ $y=0, .4, 1.0, 1.8, 2.6, 3.4, 4.0, 4.6, 5.2, 5.8, 6.2, 6.6, 7.0, 7.4, 7.8, 8.2, 8.8, 9.4, 9.8, 10.0$

TABLE A1.1



Al.4 Forward Step Sizes

The most efficient means of prescribing the forward step is to use a variable step size which is small near the inlet of the duct and increases in the predominant flow direction. In all cases reported in this thesis, the first forward step was chosen to be small enough so that it did not influence the predictions; the step size was then increased at a constant rate at each subsequent forward step until a specified maximum was reached, whereupon this value was kept constant for subsequent steps in the marching procedure. The expansion rate and the maximum step size were also tested for their influence on predictions. The forward step itself was calculated as a specified fraction of the duct height. The Table below gives examples of the forward step parameters used in each of the same four typical cases as used above (in terms of fractions of duct height).

Problem	FRAS <sub>initial</sub>	FRAS <sub>max</sub>	EX
laminar circular (1) duct flow	.001	.1	1.1
turbulent square (2) duct flow	.01	.5	1.1
Present buoyant (3) Jet data	.00001	.02	1.01
River Thermal (4) Discharge	.0001	.02	1.02

TABLE Al.2

A1.5 Computer Times

Computations were performed with a program written in FORTRAN IV on a CDC 6600 computer.\* Compilation times, using an FTN (Version 4.0) compiler, were of the order of 20 secs. Execution times varied depending upon grid size, turbulence model, whether heat transfer was present etc. The Table below shows the times required for 200 forward steps for the four problems considered in the above tables.

Problem	Time for 200 steps
1	26
2	49
3	264
4	170

all central  
processor  
seconds

TABLE A1.3

---

\*The program was named STABLE (Steady Three-dimensional Analyser of Boundary Layer Equations) and was obtained from CHAM Ltd., 2 Vineyard Hill Road, London S.W.19.

APPENDIX 2      A LITERATURE REVIEW OF FLOW AND HEAT TRANSFER  
IN ELLIPTIC DUCTS

A2.1 Introduction

Chapter 4 of this thesis presented a method for handling irregular boundaries with a three-dimensional boundary layer computer program. The field of developing irregular duct flows forms an area for the application of this procedure and Chapter 4 included calculations for an elliptic cross-section duct. The reasons for this choice of duct shape have been given in Chapter 4 and this Appendix provides a review of earlier work, both theoretical and experimental, on elliptic duct flows; the survey covers both hydrodynamics and heat transfer and laminar and turbulent flows are considered separately; only data for straight ducts are included.

A2.2 Laminar Flow and Heat Transfer

i) Fully-Developed Hydrodynamics

References [61] and [14] contain the analytical solution for the fully-developed velocity field:-

$$u = u_{\max} (1 - (z^2/a^2 + y^2/b^2)) \quad (A2.1)$$

$$\bar{u} = \frac{u_{\max}}{2} = \frac{\frac{dp}{dx} \cdot b^2}{4 (1+\lambda^2)} \quad (A2.2)$$

(the elliptic geometry is given for reference in FIG. 4.13 and all symbols are defined in the Nomenclature).

The friction-factor/Reynolds number relationship has also been given in the Shah and London report [61]:-

$$F = \frac{\bar{\tau}_w}{\frac{1}{2}\rho u^2} = \frac{2}{Re} (1 + \lambda^2) \left(\frac{\pi}{E(m)}\right)^2 \quad (A2.3)$$

in this formula (which was used to assess predictions in FIG. 4.18)  $m$  is a function of the aspect ratio:-

$$m = (1 - \lambda^2)^{\frac{1}{2}}$$

and  $E(m)$  is the complete elliptic integral of the second kind, defined as:-

$$E(m) = \int_0^{\pi/2} \sqrt{(1 - m^2 \sin^2 \theta)} d\theta \quad m < 1 \quad (A2.4)$$

The Reynolds number in (A2.3) uses the concept of the hydraulic diameter as a length scale; this parameter is often used in irregular duct flow and is defined as:-

$$d_h = \frac{4 \times \text{Duct Cross-sectional Area}}{\text{Wetted Perimeter}} = \frac{\pi b}{E(m)} \quad (A2.5)$$

As was pointed out earlier, for non-circular duct flows the wall shear stress varies around the perimeter in fully-developed flow and for elliptic ducts the variation has been given by Barrow and Roberts [71] and Cain [70]:-

$$\tau_w = \frac{-dp}{dx} \left( \frac{1}{1 + \lambda^2} \right) (z^2 \lambda^4 + y^2)^{\frac{1}{2}} \quad (A2.6)$$

$$\frac{\tau_{w,max}}{\tau_{w,min}} = \frac{1}{\lambda}$$

Shah and London also provide tabulated values for the dimensionless pressure-drop coefficient  $K_p(\alpha)$  resulting from flow development. This parameter was used in the circular duct flow predictions presented in Chapter 4 and is here defined as:-

$$\frac{p - p_{inlet}}{\frac{1}{2}\rho u^2} = f \cdot \frac{2x}{d_h} + K_p(x) \quad (A2.7)$$

$K_p(\alpha)$  is evaluated as  $x$  tends to infinity (or past the development length) and was determined by Lundgren et al [15] using an analytic method which only required knowledge of the fully-developed velocity field; this work was then extended by McComas [90] who calculated the hydrodynamic entrance length, again the results are tabulated in Reference [61].

## ii) Fully-developed Heat Transfer

This section must be divided according to the type of thermal boundary condition used; two possibilities arise for the peripheral boundary conditions, uniform temperature (sometimes called 'Dirichlet' conditions) or uniform heat flux (Neumann conditions). In the literature so far, usually only the first (and simpler) of

these has been analytically investigated but one author has recently made calculations for the second situation.

#### Peripherally constant temperature

Dunwoody [91] in his paper of 1962 used this type of boundary condition coupled with the assumption of axially constant wall temperature (i.e. simulating conditions in a condenser or evaporator). He was primarily concerned with the thermal entry region but determined fully-developed Nusselt numbers as asymptotes to his solution. Several years later Schenk and Bong Swy Han [92] extended the calculations of Dunwoody and confirmed the accuracy of his results for two values of  $\lambda$  (.25 and .8); the additional work they achieved will be discussed later. Most recently James [93] has given the Nusselt number for isothermal wall conditions for ducts of very small aspect ratio ( $\lambda \rightarrow 0$ ); his results agree with those of references [91] and [92].

A more common instance of this type of thermal boundary condition is one in which, although the wall temperature is constant peripherally the axial condition is one of constant heat flux. This fully-developed heat transfer problem was first analysed by Tao [94] using the method of complex variables and including the presence of internal heat sources in the fluid. The formulae he derived for the velocity and temperature fields were checked by allowing the aspect ratio to tend to unity (and the heat sources to zero) and hence obtaining the well-known solutions for the circular pipe. Tyagi [95] used Tao's method to attack the same

problem but included the effects of viscous dissipation; in a second paper [96] he also included a term to account for compression work in the temperature equation. Reference [61] has noted that the closed form formula for the Nusselt number in the absence of viscous dissipation and thermal energy sources is given by Tyagi as:-

$$Nu = \left[ \frac{3\pi}{E(m)} \right]^2 \cdot \frac{(1+\lambda^2)[(1+\lambda^4)+6\lambda^2]}{17(1+\lambda^4)+98\lambda^2} \quad (A2.8)$$

and values were tabulated in reference [61] for 30 values of  $\lambda$ .

Schenk and Han [92] in addition to repeating Dunwoody's calculations assumed a slightly different form of thermal boundary condition. They investigated the influence of finite thermal resistance at the wall of the duct and assumed completely isothermal external surroundings, reference [61] may be consulted for more details.

#### Peripherally constant heat flux

Iqbal et al [97], although considering mixed free and forced convection, derived as a special case the Nusselt number versus aspect ratio variation for Neumann boundary conditions. Variational principles were used and this is the only paper so far discovered which has attempted this problem. They concluded that the Nusselt number for these conditions was always lower than for Dirichlet conditions and the difference increased as the aspect ratio tended to zero.

iii) Hydrodynamically developing flow

Due to the three-dimensionality of this problem, and the non-linearity of the momentum equations, no papers have been discovered of attempts to solve the entrance length problem for elliptic ducts.

iv) Developing heat transfer

Wall temperature constant axially and peripherally

As mentioned earlier, the first authors to tackle this problem with completely isothermal boundary conditions were Dunwoody [91] and Schenk and Han [92]. For the Nusselt number development, reference [91] calculated the solution for five aspect ratios and these results were verified in reference [92] for two values of  $\lambda$ ; excellent agreement was obtained. Additionally Schenk and Han provided information on the peripheral variation of Nusselt number at various axial stations both for isothermal conditions and for the finite wall thermal resistance situation mentioned earlier. Later Tao [98] presented a solution for the variation of the mean fluid temperature in the entrance region for two values of  $\lambda$ ; a variational approach was again used.

Rao et al [99] investigated the thermal entrance problem for both axially constant temperature and heat flux. Their work is however only applicable to near-entrance flow as they utilised the Lévy-Étard theory of linear velocity profile near the wall (see reference [14] for details). Although their solution does not asymptote to the fully-developed value, the results near the



entrance agree fairly well (within 15%) with those of reference [92]. The Lévy-Éque technique was also used by James [93] for isothermal conditions and excellent agreement was obtained with Rao's results.

All the above papers assumed the velocity field to be that applicable to fully-developed flow; in a recent paper Gilbert et al [100] have produced an analysis which assumes slug flow (uniform velocity everywhere) and have solved the temperature equation for completely isothermal boundary conditions. Again their analysis only applies in the immediate vicinity of the duct entry as they have simplified the energy equation using this assumption. Amongst other discussion they present the axial development of Nusselt number at two wall positions and for two aspect ratios. The wall locations (the end of the major and minor axes) correspond to the maximum and minimum values of Nusselt number peripherally.

### A2.3 Turbulent Flow and Heat Transfer

The investigations into turbulent flow are severely limited; only straight constant area ducts have been considered and only recently has the developing flow region been included. All the work has been carried out in conjunction between Liverpool Polytechnic and Liverpool University with the analysis being done mainly at the latter and most of the experimental work at the former.

i) Fully-developed flow and heat transfer

The experimental work on elliptic tubes was begun in 1968 by Cain [70]. He was examining the validity of the equivalent (hydraulic) diameter concept for the correlation of non-circular duct flows. To this end he measured the fully-developed friction factors in two elliptic tubes of aspect ratios 0.666 and 0.5 for a Reynolds number range of  $2 \times 10^4$  to  $1.3 \times 10^5$ . When the data was compared with the circular pipe correlation of Prandtl:-

$$\frac{1}{\sqrt{f}} = 4.0 \log_{10} (\text{Re} \sqrt{f}) - 0.4 \quad (\text{A2.9})$$

with Re evaluated using the hydraulic diameter, the friction factors for the ducts were parallel to the Prandtl law but 8 and 13 percent above it respectively. Detailed measurements were made of the variation of local wall shear stress around the periphery of the ducts using Preston tubes [73, 74]. The velocity distributions along the major and minor axes were also given in terms of universal co-ordinates and showed the existence of log-law regions. A velocity contour map across the whole x-section of the duct clearly showed the existence of secondary flows, particularly in the larger aspect ratio duct. The secondary flow pattern was also suggested in reference [70].

This work was later extended to include fully-developed heat transfer in the Ph.D. thesis of Cain [72]. Air flow heat transfer experiments were carried out on the same two ducts as in reference

[70] over a Reynolds number range of  $10^3$  to  $2 \times 10^5$ . Water flow experiments were performed on two smaller ducts of aspect ratios .375 and .341 (Reynolds number range  $2.5 \times 10^3$  to  $8 \times 10^4$ ). Wall temperature measurements were made axially and circumferentially using thermocouples attached to the outer (lagged) walls of the duct.

In air flow, the heat-transfer results were found to agree well with the Dittus-Boelter equation for circular pipes (using integrated mean wall temperatures and the equivalent diameter):-

$$Nu = .023 Re^{0.8} Pr^{0.4} \quad (A2.10)$$

In water flow however, it was found that the above equation only applied above a Reynolds number of about  $2.5 \times 10^4$ . Below this the data were smaller than that predicted by the above equation and agreed well with a correlation suggested by Barrow and Roberts [71]:-

$$Nu = .00165 Re^{1.06} Pr^{0.4} \quad 4 \times 10^3 < Re < 2 \times 10^4 \quad (A2.11)$$

Cain suggested that this deviation may be due to the presence of "localised regions of laminar or transitional flow in the corners of the duct." Free convection is also thought to be a possible cause.

As mentioned above, reference [71] also contains results of fully-developed flow and heat transfer experiments. Frictional

pressure drop measurements were made for elliptic tubes of aspect ratio .316 and .415 and were found to agree to within  $\pm 5\%$  with the Blasius law for turbulent flow:-

$$f = .079 \text{ Re}^{-.25} \tag{A2.12}$$

with the results for the smaller value of  $\lambda$  lying above the line and for the larger  $\lambda$  lying below it. The heat transfer work was done with a tube with a  $\lambda$  value of .284 and peripheral wall temperature distributions were measured at various axial stations. The fully-developed Nusselt numbers were calculated and results were obtained similar to those described above i.e. agreement with equation (A2.10) for Re greater than  $2 \times 10^4$  and with equation (A2.11) for Re lower than this value.

Cain's Ph.D. thesis also contains the first theoretical investigation of fully-developed turbulent flow in elliptic ducts (this work has been published in reference [101]). A finite-difference method was used to analyse the flow and heat transfer in the 0.5 aspect ratio duct, the method being derived from the one published by Gosman et al [44]. An elliptical cylindrical co-ordinate system was used and the Van Driest expression for eddy diffusivity was employed to model the turbulent transport processes. It was pointed out that the use of this particular co-ordinate system, although it was convenient as far as the wall boundary was concerned, caused problems because of the behaviour of the grid lines and the metric coefficients in the region of the focus. This meant that when fully-developed laminar flow was

predicted, some distortion of the velocity contours was present, especially along the major axis.

The predictions of the fully-developed flow solution were only partially successful. Because of the simplicity of the turbulence model, no secondary flows were predicted and hence the velocity contours disagreed with those obtained in the experiments. Discrepancies were also present in the prediction of the velocity profiles along the major and minor axes and of the peripheral distribution of wall shear stress. The overall variation of measured wall shear was limited to 12% whereas the iterative solution resulted in a variation of 43%. Similar errors appeared when the peripheral variation of local heat transfer coefficient was compared with the experimental results. The paper ends with the prediction of fully-developed flow and heat transfer including the effects of variable fluid properties, this being an attempt to simulate turbine blade cooling with elliptic shaped channels (suggested in reference [102]).

ii) Developing flow and heat transfer

The extension of the above work to the developing flow region has been undertaken by Gilbert [103]. The experimental investigation consists of mean velocity, wall shear stress and temperature distributions at several axial stations up to and including the fully-developed state. The thermal boundary conditions correspond to constant temperature peripherally and constant heat input in the axial direction. Two ellipses were used of aspect ratios 0.5 and 0.18; the results, however, have not yet been published and were not available to the author.

APPENDIX 3

Tabulated Experimental Data

A.3.1 Introduction

This Appendix contains the data obtained in the experimental investigation reported in Chapter 5. The tabulated values consist of the measured temperatures (in °C) at specified distances above and below the original jet injection level (shown as  $y/d_J = 0$  in the tables). Only vertical profiles are included as the cross-sectional measurements are best presented as the interpolated temperature contours given in Figures 6.3.30 - 6.3.32 and 6.3.35 - 6.3.36.

A.3.2 6 cm Submergence Depth

FR = 15 K = 2

$z/d_J = 5$	$y/d_J$	0	.2	.4	.6	.8	1.0	1.4	1.6	2.0
	T	25.2	24.8	23.3	23.0	21.8	20.4	19.5	19.5	18.6
	$y/d_J$	-.2	-.4	-.6	-.8	-1.0	-1.4	-2.0		
	T	24.2	23.3	22.2	20.5	19.5	19.2	18.5		
$z/d_J = 10$	$y/d_J$	0	.2	.4	.6	1.0	1.6	2.0	2.6	
	T	21.7	21.7	21.7	21.7	20.7	18.6	18.5	18.5	
	$y/d_J$	-.2	-.6	-1.0	-1.6	-2.0				
	T	21.7	20.5	19.5	18.4	18.4				
$z/d_J = 20$	$y/d_J$	0	.4	.8	1.0	1.4	1.8	2.0	2.6	3.0
	T	20.4	20.5	20.5	20.5	20.0	20.0	19.5	18.5	18.5
	$y/d_J$	-.2	-.4	-.6	-1.0	-1.6	-2.0	-2.6		
	T	20.0	19.5	19.5	18.6	18.5	18.4	18.4		



FR = 10 K = 2

$z/d_J = 10$

$y/d_J$	0	.2	.4	.6	.8	1.0	1.4	2.0
T	25.0	25.6	26.1	26.1	25.8	25.0	22.5	19.9
$y/d_J$	2.4	-.1	-.4	-.6	-.8	-1.0	-1.4	
T	19.5	23.5	22.8	21.6	20.5	19.9	19.5	

$z/d_J = 20$

$y/d_J$	-1.4	-1.0	-.6	-.2	0	.2	.6	1.0	1.4
T	19.5	19.6	20.4	21.1	21.2	21.4	22.1	22.6	22.8
$y/d_J$	1.8	2.2	2.6	3.0	3.6	4.0			
T	23.0	22.5	21.4	20.6	19.9	19.5			

$z/d_J = 40$

$y/d_J$	6.0	5.0	4.6	4.0	3.8	3.4	3.0	2.6	2.0
T	20.2	20.5	20.6	21.0	21.0	21.3	21.4	21.4	21.0
$y/d_J$	1.4	1.0	.4	0	-.4	-1.0	-2.0	-3.0	
T	20.8	20.5	20.4	20.1	20.1	20.3	20.2	20.2	

$z/d_J = 60$

$y/d_J$	-3.0	-2.0	-1.0	0	1.0	2.0	3.0	4.0
T	19.9	19.9	19.9	20.6	20.1	20.3	20.5	20.6
$y/d_J$	5.0	6.0						
T	20.7	20.9						

FR = 20 K = 4

$z/d_J = 10$

$y/d_J$	0	.2	.4	.6	1.0	1.4	1.8	2.4	3.0	
T	26.4	26.1	26.0	25.6	24.6	23.3	21.7	20.5	20.5	
$y/d_J$	4.0	-.2	-.4	-.6	-1.0	-1.4	-1.8	-2.4	-3.0	-4.0
T	20.5	26.2	25.6	25.2	23.7	22.1	21.0	20.8	20.5	20.5



$z/d_J = 20$

$y/d_J$	-4.0	-3.0	-2.0	-1.0	-.4	0	.2	.4	.6
T	21.0	21.0	21.6	22.8	23.7	24.1	24.3	24.3	24.3
$y/d_J$	.8	1.0	1.4	2.0	2.8	3.8	5.0	6.0	
T	24.2	24.1	23.8	23.1	21.7	21.0	20.7	20.5	

$z/d_J = 40$

$y/d_J$	6.0	5.4	4.4	3.8	3.0	2.0	1.6	1.2
T	21.0	21.3	21.7	22.1	22.5	22.8	23.1	23.0
$y/d_J$	.8	0	-.8	-1.6	-2.8	-4.0		
T	22.9	22.7	22.3	22.0	21.7	21.4		

$z/d_J = 60$

$y/d_J$	6.0	5.0	4.0	3.0	2.0	1.0	0	-1.0
T	22.0	22.3	22.5	22.6	22.6	22.5	22.0	22.0
$y/d_J$	-2.0	-3.0	-4.0					
T	21.8	21.6	21.5					

$z/d_J = 80$

$y/d_J$	6.0	5.0	4.0	3.0	2.0	1.0	0	-1.0
T	22.5	22.5	22.3	22.3	22.2	22.1	22.0	21.8
$y/d_J$	-2.0	-3.0						
T	21.5	21.5						

FR = 15 K = 4

$z/d_J = 10$

$y/d_J$	0	.2	.4	.6	.8	1.0	1.2	1.4	1.6	1.8	
T	31.2	32.6	32.6	31.7	30.2	29.4	26.6	25.2	23.8	23.0	
$y/d_J$	2.0	2.4	3.0	-.2	-.4	-.6	-.8	-1.0	-1.4	-2.0	-3.0
T	21.3	20.5	20.5	30.6	29.3	26.6	25.4	23.8	21.3	20.9	20.5

$z/d_J = 40$

$y/d_J$	6.0	5.6	5.0	4.4	4.0	3.6	3.2	2.8
T	21.4	21.4	22.4	23.0	23.2	23.6	23.6	23.6
$y/d_J$	2.2	1.6	1.0	0	-1.0	-2.0	-3.0	-4.0
T	24.0	23.7	23.0	22.4	21.4	21.4	21.4	21.4

$z/d_J = 60$

$y/d_J$	-4.0	-3.0	-2.0	0	2.0	3.0	4.0	5.0	
T	21.4	21.4	21.4	21.5	22.4	22.8	23.0	23.1	
$y/d_J$	5.4	6.0							
T	23.2	23.6							

$z/d_J = 80$

$y/d_J$	6.0	5.0	4.0	3.0	2.0	1.0	0	-1.0	-2.0
T	23.3	23.0	22.6	22.4	22.0	21.9	21.8	21.7	21.7
$y/d_J$									
T									

FR = 10 K = 4

$z/d_J = 10$

$y/d_J$	0	.4	.8	1.2	1.6	2.0	2.8		
T	34.3	36.6	34.7	31.2	27.5	23.6	20.6		
$y/d_J$	-.4	-.8	-1.4	-2.0	-3.0				
T	30.8	26.0	21.0	20.6	20.6				

$z/d_J = 20$

$y/d_J$	5.0	4.2	3.6	3.0	2.6	2.2	1.8	1.4	1.2
T	20.6	21.1	23.0	25.8	27.8	28.6	29.5	29.1	29.1
$y/d_J$	1.0	.8	.4	-.2	-.8	-1.4	-2.0		
T	28.6	28.0	26.0	24.2	22.0	20.8	20.6		

$z/d_J = 40$

$y/d_J$	6.0	5.4	5.0	4.8	4.4	4.0	3.6	3.0	2.2
T	23.9	24.0	24.2	24.4	24.6	24.6	24.3	24.0	23.0
$y/d_J$	1.2	0	-1.0	-2.0					
T	22.0	21.1	20.8	20.8					

$z/d_J = 60$

$y/d_J$	-2.0	-1.0	0	1.0	2.0	3.0	4.0	4.4	
T	20.7	20.8	20.8	20.9	21.1	21.8	22.3	23.2	
$y/d_J$	4.8	5.2	5.6	6.0					
T	23.3	23.7	24.0	24.6					

$z/d_J = 80$

$y/d_J$	6.0	5.6	5.2	4.8	4.4	4.0	3.0	2.0
T	23.8	23.1	22.9	22.6	22.1	21.8	21.4	21.4
$y/d_J$	1.0	0	-1.0	-2.0				
T	21.4	21.2	21.1	20.8				

FR = 30 K = 6

$z/d_J = 5$

$y/d_J$	0	.2	.4	.8	1.2	1.8	2.4
T	32.8	32.4	31.1	28.1	24.2	21.9	21.5
$y/d_J$	-.2	-.4	-.8	-1.2	-1.8	-2.4	
T	31.4	39.8	21.2	22.4	21.8	21.6	

$z/d_J = 10$

$y/d_J$	0	.2	.4	.6	1.0	1.4	1.8	2.4	3.0
T	28.4	27.8	27.6	27.4	26.0	24.4	22.7	21.4	21.2
$y/d_J$	-.2	-.4	-.6	-1.0	-1.4	-2.0	-3.0	-4.0	
T	27.6	27.1	26.4	24.7	22.8	21.5	21.5	21.4	

$z/d_J = 20$

$y/d_J$	-4.0	-3.0	-2.0	-1.0	0	.4	.8	1.2
T	21.5	21.5	22.4	23.7	24.7	25.0	24.8	24.6
$y/d_J$	1.8	2.4	3.0	3.6	4.2	5.0		
T	23.8	23.0	22.1	21.6	21.4	21.4		

$z/d_J = 40$

$y/d_J$	6.0	5.0	4.0	3.2	2.6	2.2	1.8	1.4
T	21.5	21.8	22.5	22.9	23.0	23.1	23.1	23.1
$y/d_J$	.8	.2	-.4	-1.2	-2.0	-3.0	-4.0	
T	23.0	22.9	22.7	22.5	22.2	21.7	21.6	

$z/d_J = 60$

$y/d_J$	-5.0	-4.0	-3.0	-2.0	-1.0	0	1.0	2.0	3.0
T	21.6	21.6	21.8	22.0	22.2	22.4	22.6	22.7	22.7
$y/d_J$	4.0	5.0	6.0						
T	22.3	22.4	22.2						

FR = 20 K = 6

$z/a_J = 10$

$y/a_J$	0	.4	.8	1.2	1.6	2.0	3.0	-.4	-.8
T	33.4	33.2	30.8	27.7	24.1	21.8	20.2	30.7	27.1
$y/a_J$	-1.2	-1.6	-2.0	-3.0					
T	24.2	21.1	20.5	20.2					

$z/a_J = 20$

$y/a_J$	-3.0	-2.0	-1.0	-.6	-.2	.2	.6	1.0	
T	20.5	21.3	23.8	25.0	26.1	26.6	27.2	27.2	
$y/a_J$	1.4	2.0	2.6	3.2	4.0	5.0			
T	26.8	25.3	23.8	22.2	20.8	20.6			

$z/a_J = 40$

$y/a_J$	6.0	5.0	4.0	3.0	2.4	1.6	1.0	.4	
T	21.3	22.0	23.0	23.5	23.8	23.7	23.5	22.5	
$y/a_J$	-.4	-1.0	-2.0	-3.0	-4.0				
T	22.5	22.0	21.2	20.8	20.8				

$z/a_J = 60$

$y/a_J$	-4.0	-3.0	-2.0	-1.0	0	1.0	2.0	3.0	
T	20.8	20.8	20.9	21.2	21.9	22.3	22.5	22.8	
$y/a_J$	3.6	4.0	4.6	5.6	6.0				
T	23.0	23.0	22.8	22.6	22.5				

$z/a_J = 80$

$y/a_J$	6.0	5.0	4.0	3.0	2.0	1.0	0		
T	22.6	22.5	22.3	22.2	22.0	21.6	21.3		
$y/a_J$	-1.0	-2.0	-3.0						
T	21.2	21.0	20.9						

FR = 16.5 K = 6

$z/a_J = 10$

$y/a_J$	0	.2	.4	.8	1.2	1.6	2.0	2.4	3.0
T	38.6	39.6	38.4	36.6	32.6	28.1	24.3	22.4	21.8
$y/a_J$	4.0	-.2	-.4	-.8	-1.2	-1.6	-2.0	-3.0	
T	21.8	38.4	35.8	31.0	26.0	22.5	22.1	22.0	

$z/d_J = 20$

$y/d_J$	-4.0	-3.0	-2.0	-1.0	-.4	.2	.6	1.0	1.4
T	22.0	22.0	22.7	25.8	28.8	30.3	31.1	31.6	31.2
$y/d_J$	2.0	2.6	3.4	4.2	5.0	6.0			
T	29.4	27.8	23.6	22.3	22.3	22.3			

$z/d_J = 40$

$y/d_J$	6.0	5.4	5.0	4.2	3.6	2.0	2.4	1.8	
T	24.1	24.8	25.4	26.1	26.6	26.8	26.8	26.7	
$y/d_J$	1.4	1.0	.6	.2	-.8	-1.6	-2.4	-3.4	
T	26.1	25.7	25.4	24.6	23.6	22.8	22.6	22.5	

$z/d_J = 60$

$y/d_J$	6.0	5.4	5.0	4.4	4.0	3.4	3.0	2.0	
T	25.2	25.2	25.2	25.0	25.0	24.6	24.5	24.6	
$y/d_J$	1.0	0	-1.0	-2.0	-3.0				
T	23.2	22.7	22.5	22.4	22.4				

$z/d_J = 80$

$y/d_J$	-2.0	-1.0	0	1.0	2.0	3.0	4.0		
T	22.4	22.4	22.5	22.6	23.0	22.7	24.0		
$y/d_J$	5.0	6.0							
T	24.6	25.1							

### A.3.3 3 cm Submergence Depth

FR = 15 K = 4

$z/d_J = 10$

$y/d_J$	0	-.5	-.7	-1.0	-1.2	-1.5	.5	1.0	
T	28.6	26.6	25.8	22.6	20.9	19.1	28.9	26.1	
$y/d_J$	1.2	1.5	1.7	2.0					
T	24.6	22.7	21.0	19.2					

$z/d_J = 20$

$y/d_J$	-2.0	-1.5	-1.0	-.5	0	.5	1.0	1.5	
T	19.1	19.7	20.7	21.8	23.4	24.0	23.8	23.4	
$y/d_J$	2.0	2.5	3.0						
T	22.2	21.0	19.8						

$z/d_J = 40$

$y/d_J$	3.0	2.5	2.0	1.5	1.0	.5	0	-0.5
T	21.8	21.7	21.6	21.6	21.2	20.9	20.5	20.2
$y/d_J$	-1.0	-1.5	-2.0	-3.0				
T	19.6	19.3	19.1	19.1				

$z/d_J = 60$

$y/d_J$	-2.0	-1.0	0	1.0	1.5	2.0	2.5	3.0
T	19.1	19.3	20.0	20.4	20.9	21.0	21.3	21.8
$y/d_J$								
T								

$z/d_J = 80$

$y/d_J$	3.0	2.5	2.0	1.5	1.0	0	-1.0	-2.0
T	21.5	20.9	20.5	20.3	20.1	19.5	19.3	19.2
$y/d_J$								
T								

FR = 16.5 K = 6

$z/d_J = 10$

$y/d_J$	0	-.2	-.5	-.7	-1.0	-1.2	-1.5	-2.0	.2
T	37.4	36.6	33.1	30.9	26.9	23.6	21.0	19.6	37.9
$y/d_J$	.5	.7	1.0	1.3	1.5	2.0	2.5		
T	36.6	35.5	31.3	28.6	26.4	20.8	19.7		

$z/d_J = 20$

$y/d_J$	3.0	2.5	2.0	1.5	1.0	.5	0	-.5	-1.0
T	22.8	24.3	26.6	28.4	29.6	29.2	28.0	26.1	24.1
$y/d_J$	-1.5	-2.0	-2.5						
T	21.7	20.3	20.0						

$z/d_J = 40$

$y/d_J$	-3.0	-2.5	-2.0	-1.5	-1.0	-.5	0	.5
T	20.3	20.6	20.7	21.1	21.6	22.3	22.7	23.3
$y/d_J$	1.0	1.5	2.0	2.5	3.0			
T	23.8	24.6	24.8	24.9	25.3			

$z/d_J = 60$	$y/d_J$	3.0	2.0	1.0	0	-1.0	-2.0	-3.0
	T	24.8	23.8	22.6	21.7	20.9	20.4	20.3
	$y/d_J$							
	T							

$z/d_J = 80$	$y/d_J$	3.0	2.0	1.0	0	-1.0	-2.0	-3.0	-4.0
	T	24.0	22.8	21.8	21.3	20.8	20.4	20.3	20.3
	$y/d_J$								
	T								

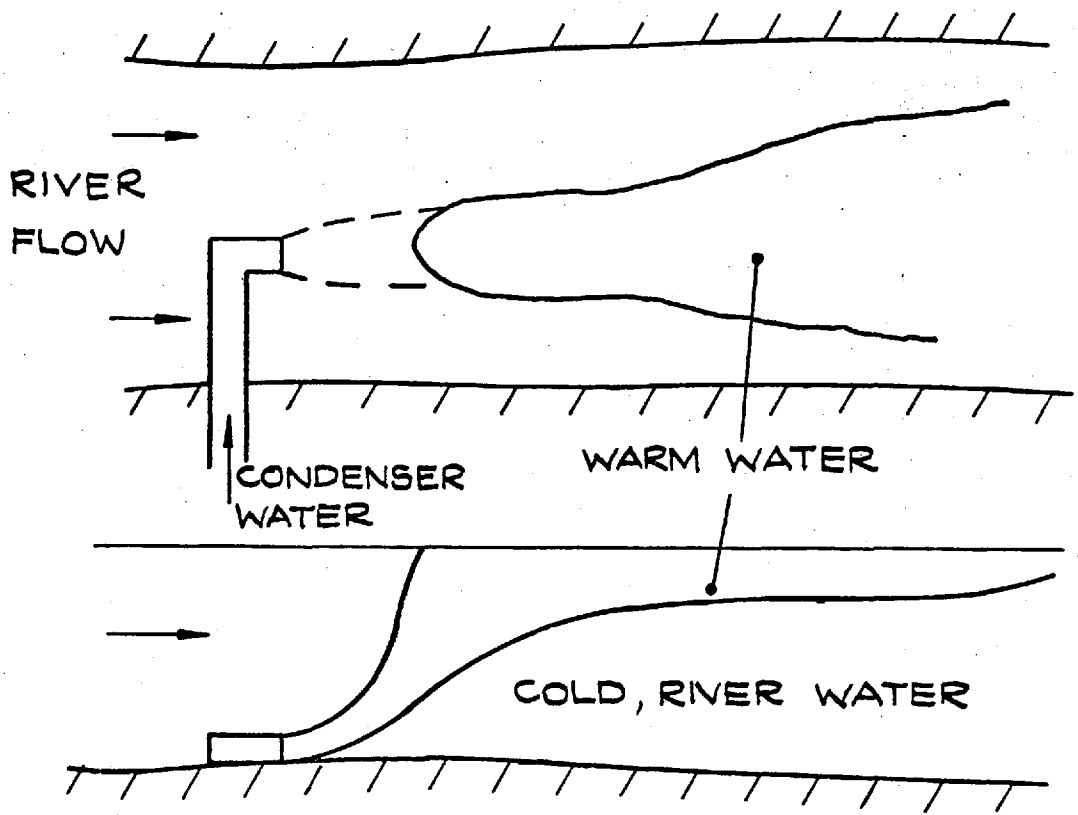


FIG.1.1: SINGLE-PORT, SUBMERGED THERMAL DISCHARGE.

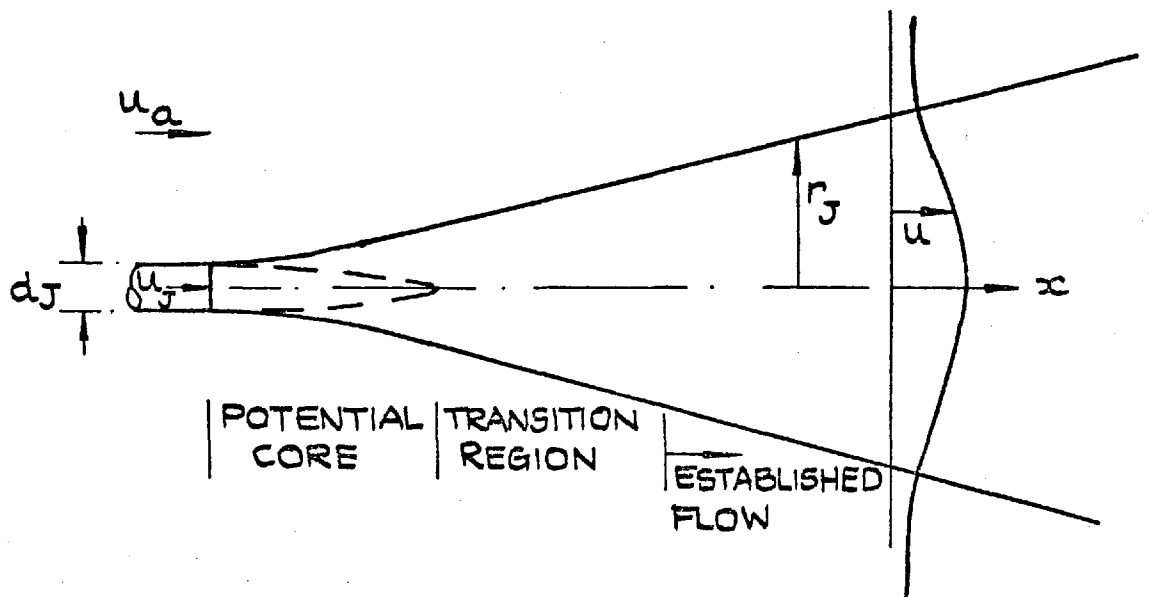


FIG.1.2: NON-BUOYANT JET DEVELOPMENT.



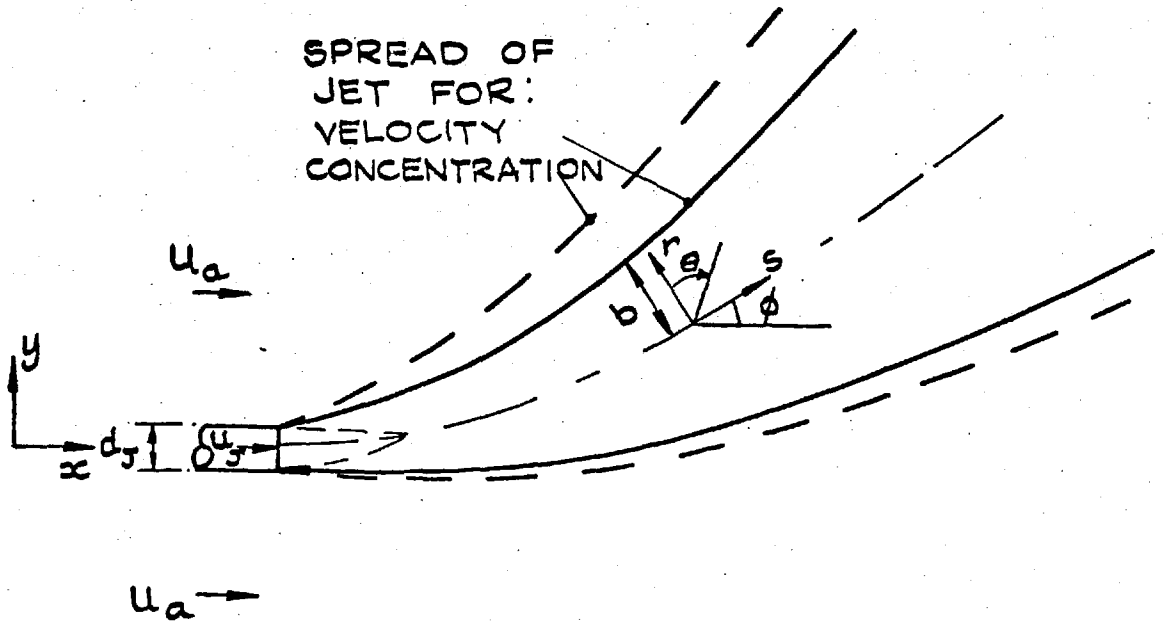


FIG. 1.3: BUOYANT JET DEVELOPMENT.

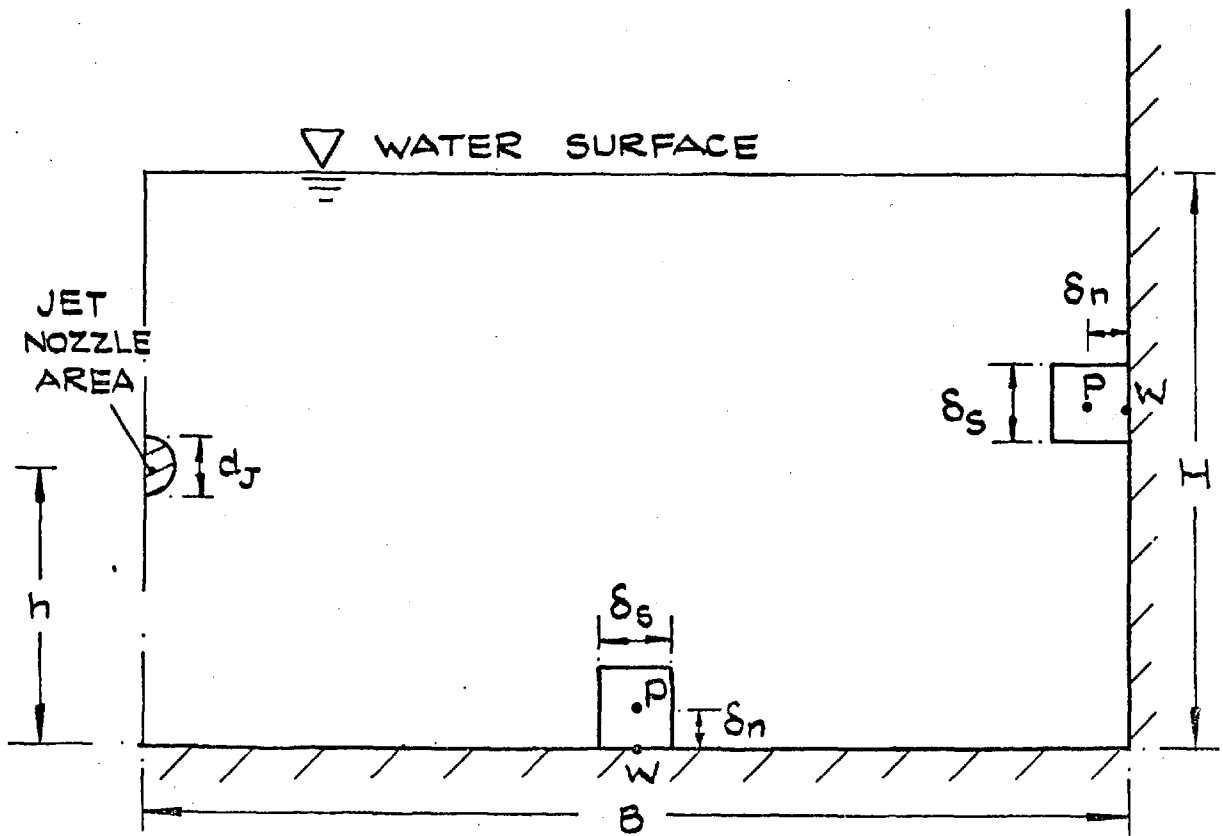


FIG. 1.4: CO-FLOWING JET, EXPERIMENTAL GEOMETRY.

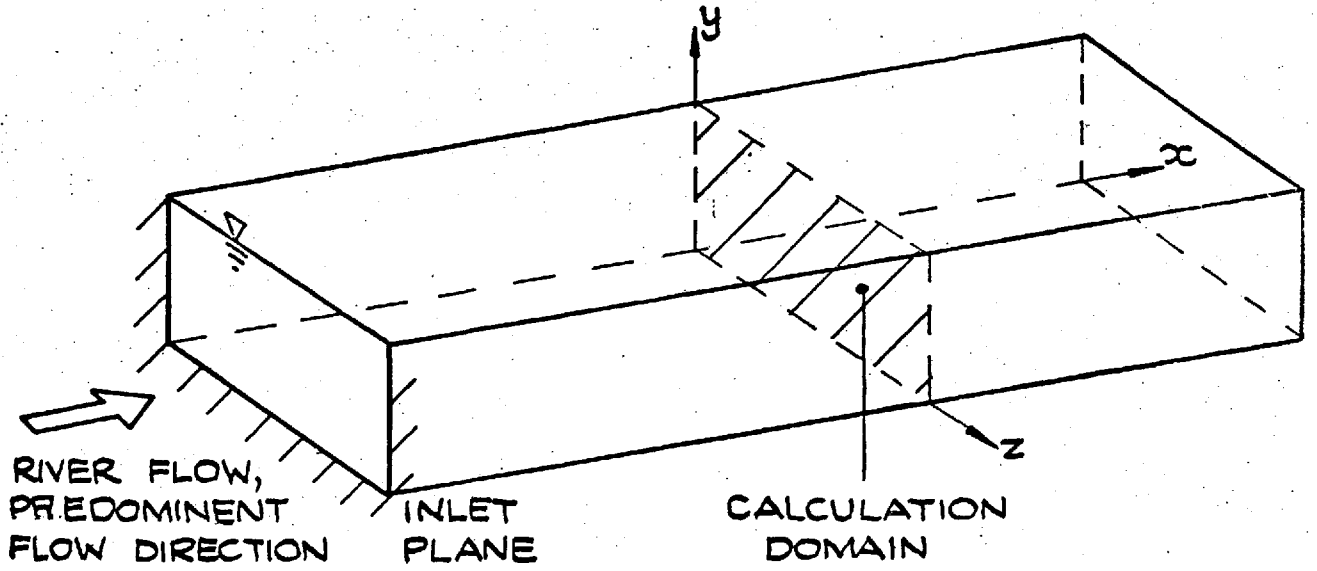


FIG. 2.1: ILLUSTRATION OF CO-ORDINATE SYSTEM.

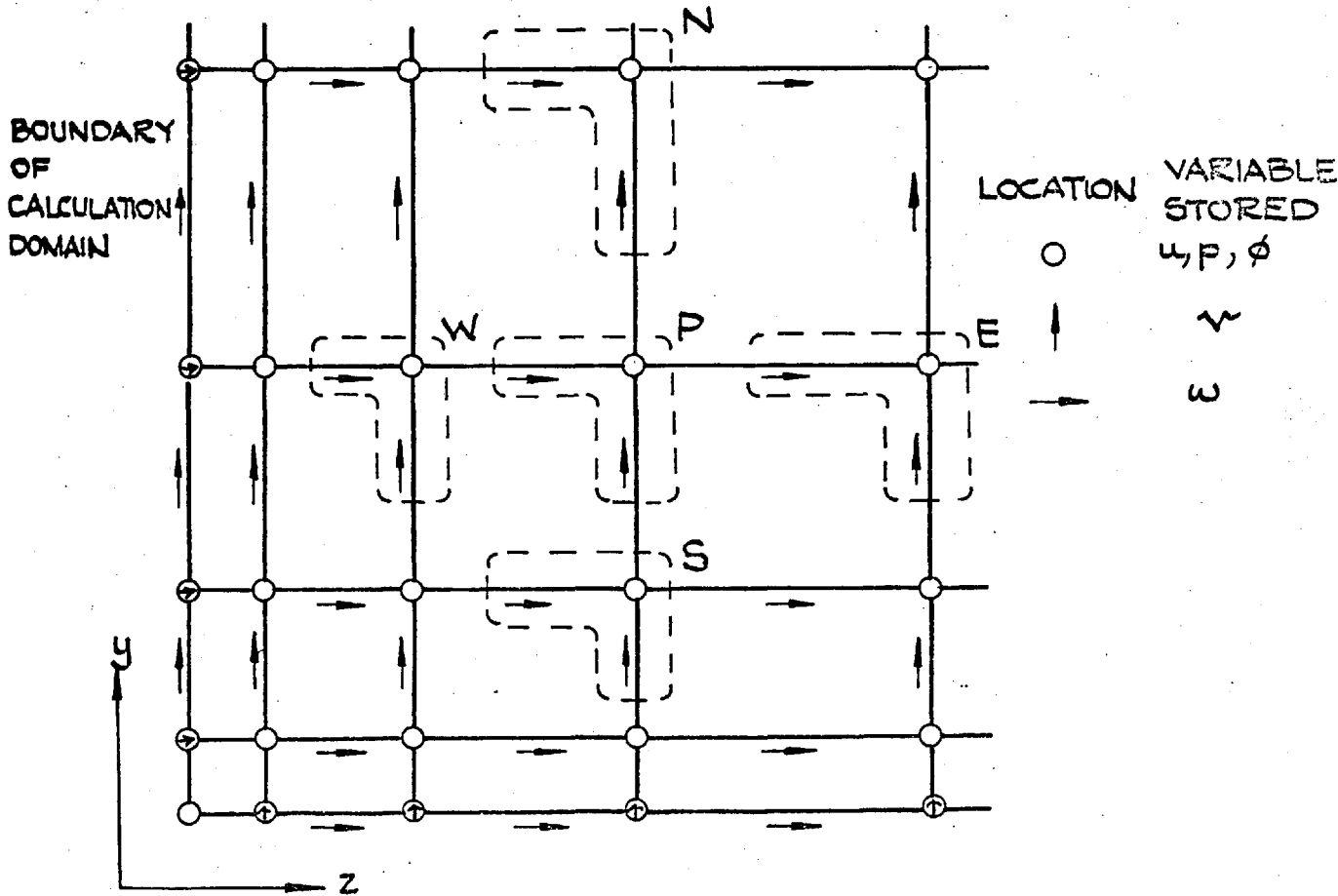


FIG. 2.2: PORTION OF GRID IN  $yz$  PLANE.

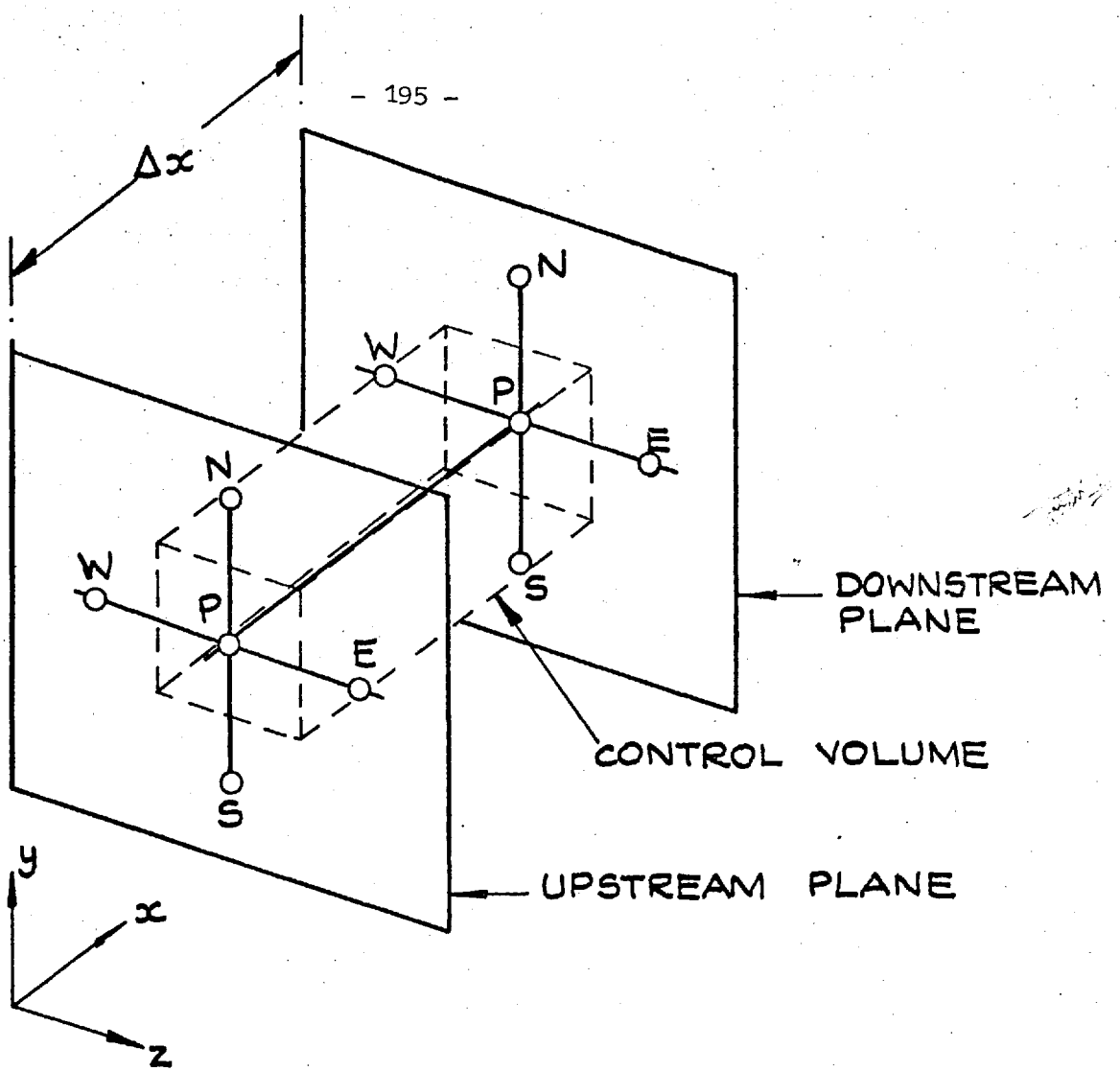


FIG. 2.3: INTEGRATION CONTROL VOLUME

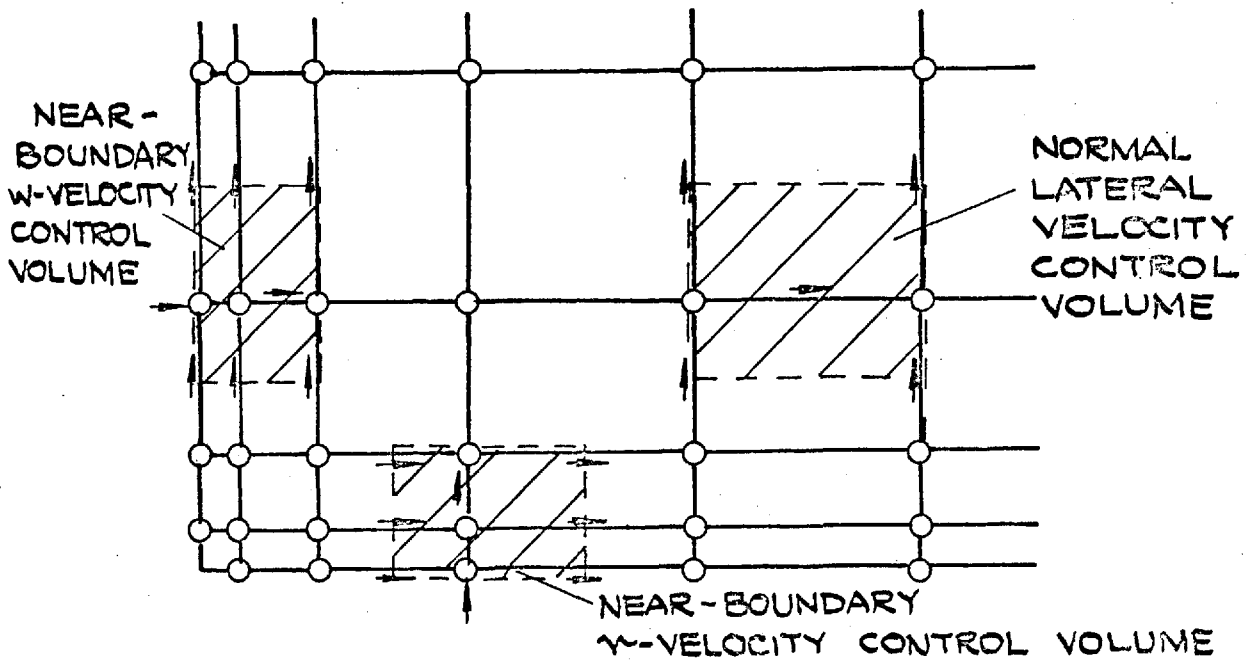


FIG. 2.4: NEAR-BOUNDARY CELLS FOR LATERAL VELOCITY.

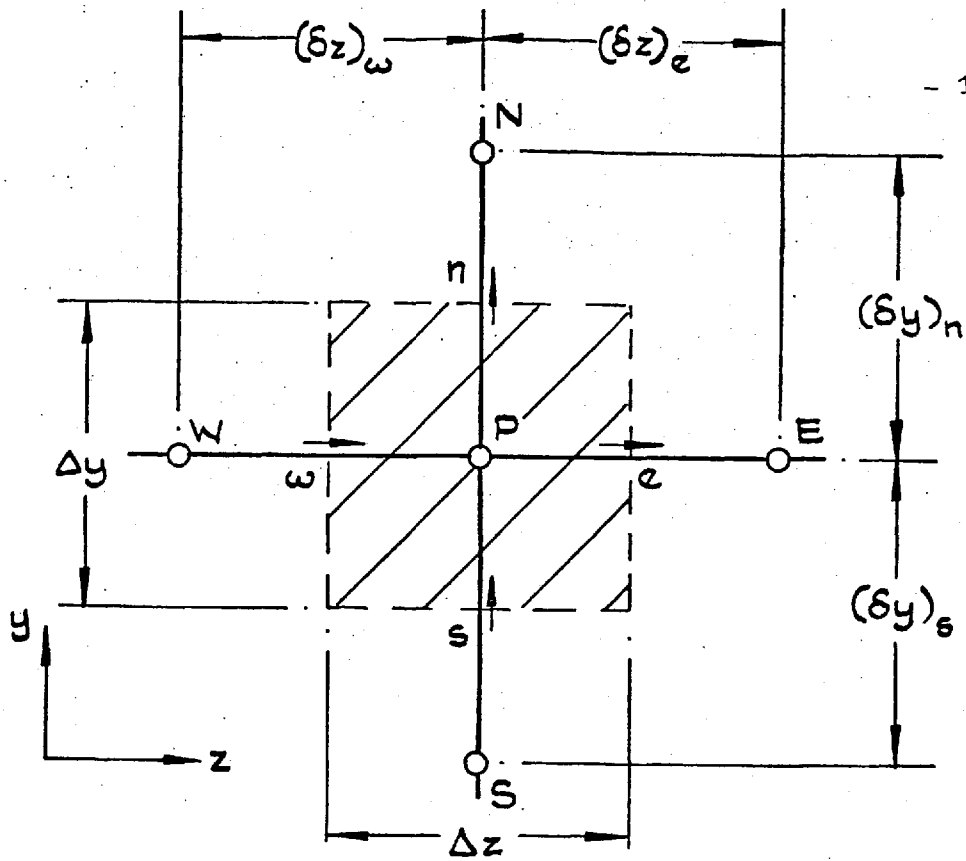


FIG. 2.5: yz FACE OF CONTROL VOLUME, NOMENDATURE.

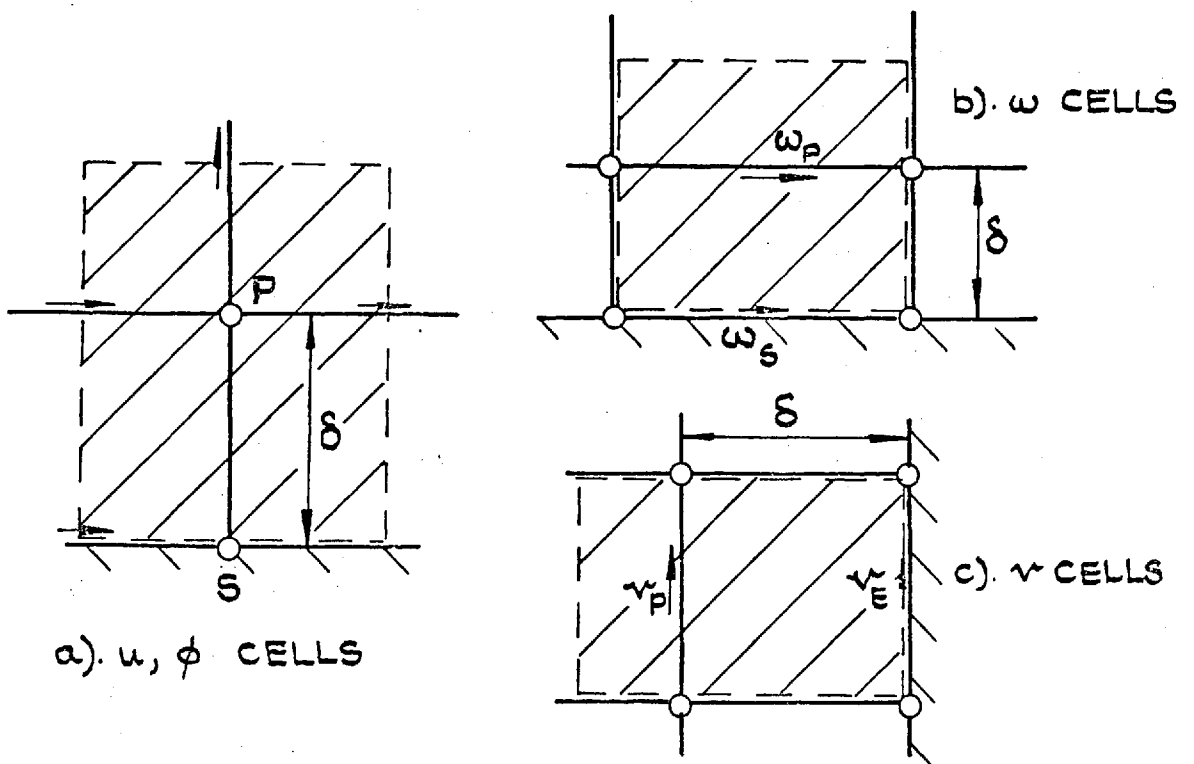


FIG. 3.1: NEAR-WALL CONTROL VOLUMES.

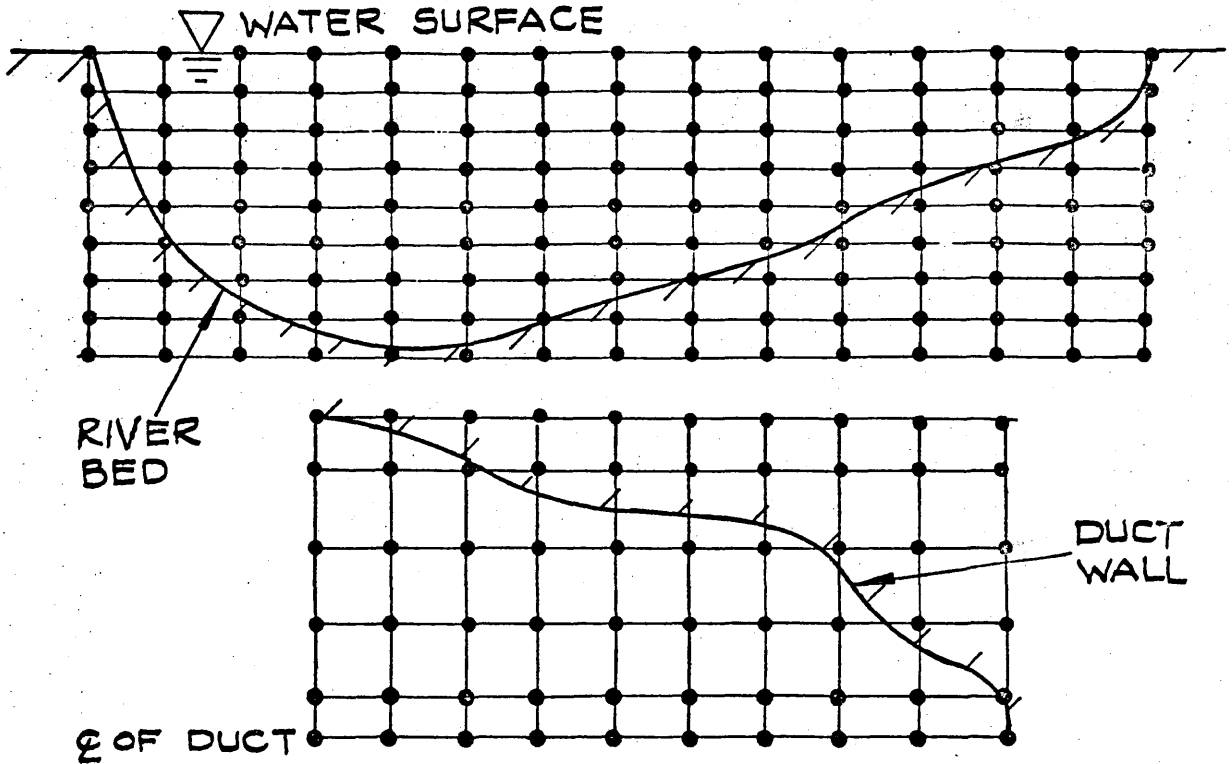


FIG. 4.1: A RIVER FLOW AND A DUCT FLOW AS IRREGULAR BOUNDARY PROBLEMS.

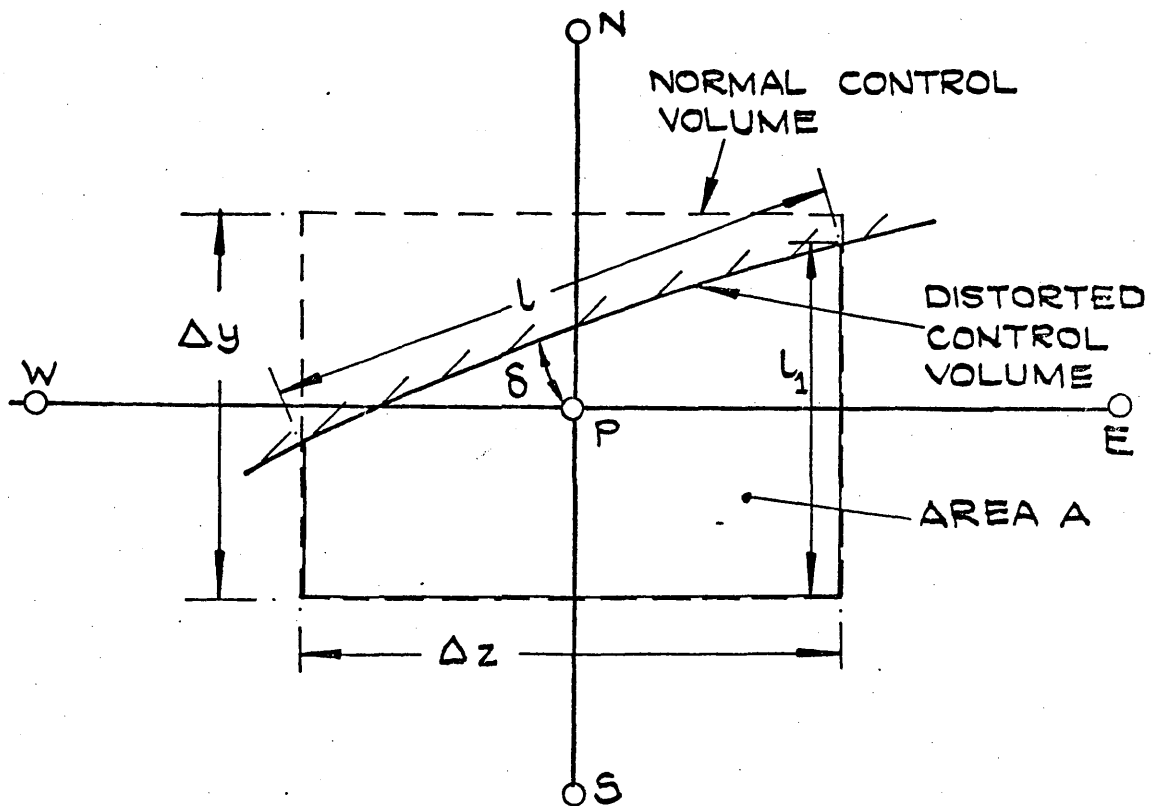


FIG. 4.2: A TYPICAL NEAR-WALL CELL.

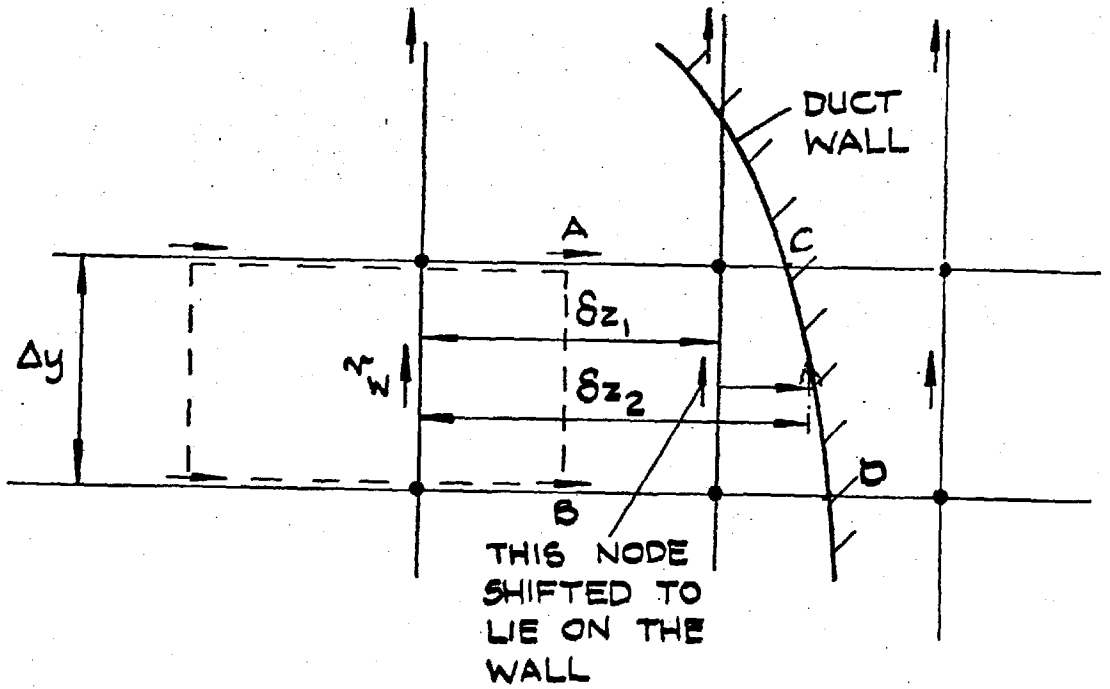


FIG. 4.3: A DISPLACED NEAR-WALL LATERAL VELOCITY.

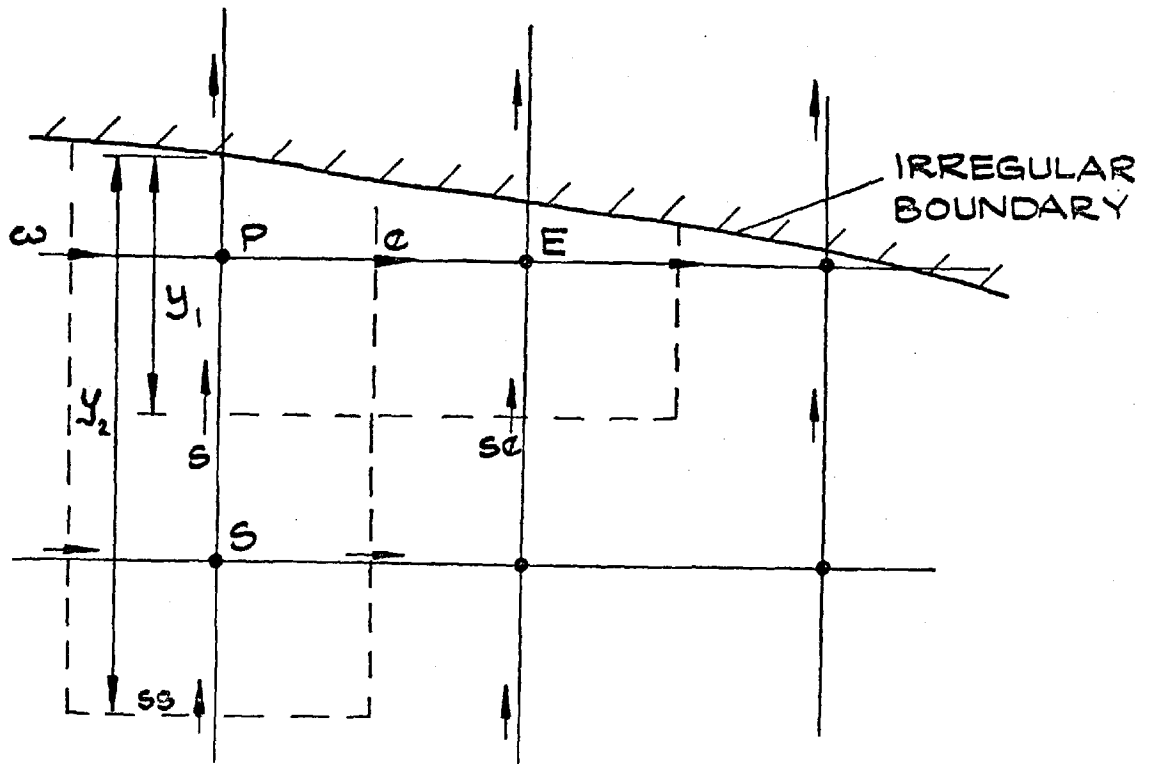


FIG. 4.4: INTERPOLATION OF NEAR WALL LATERAL CONVECTION FLUXES.

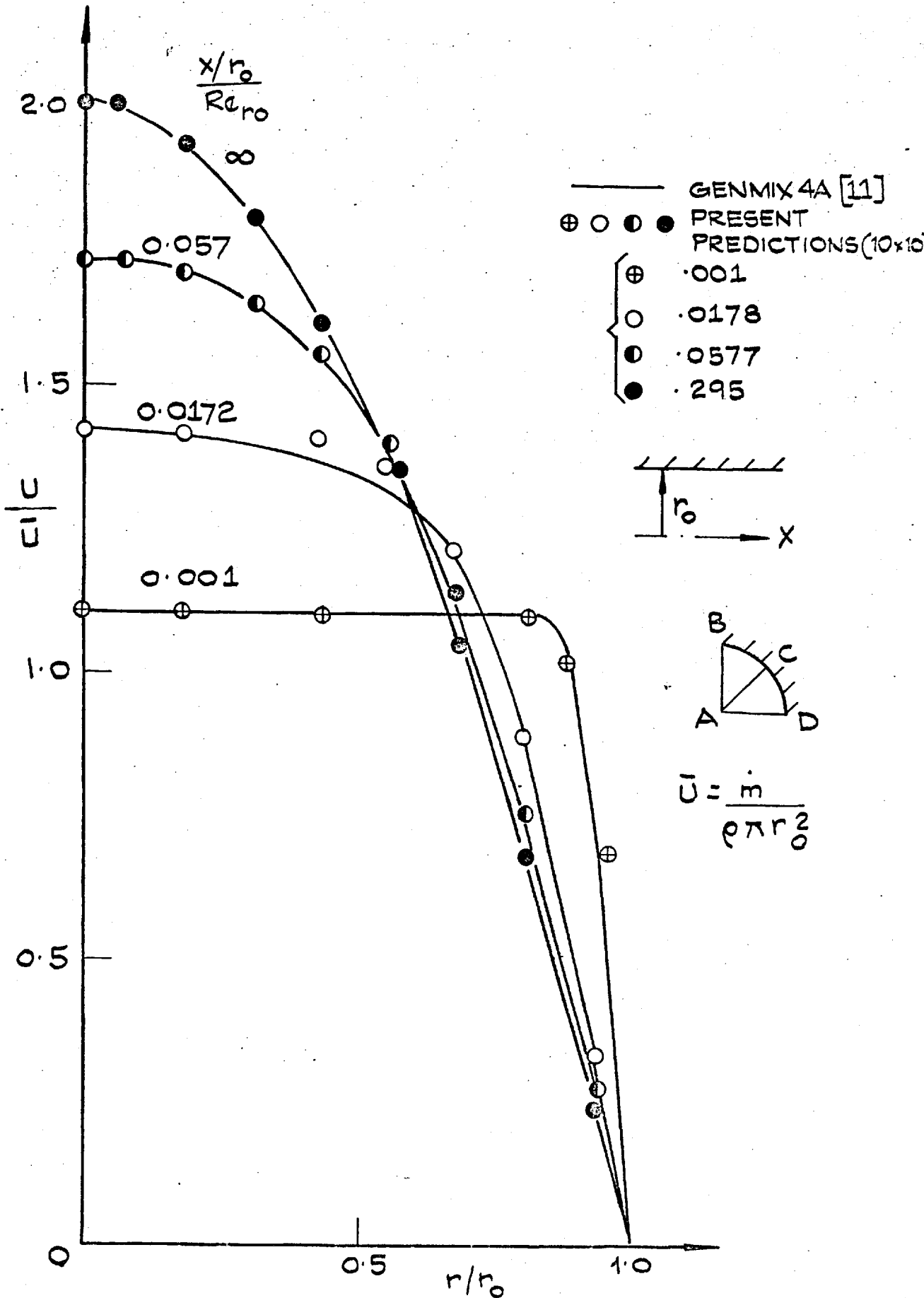


FIG. 4.5: DEVELOPING VELOCITY PROFILES (LAMINAR PIPEFLOW).

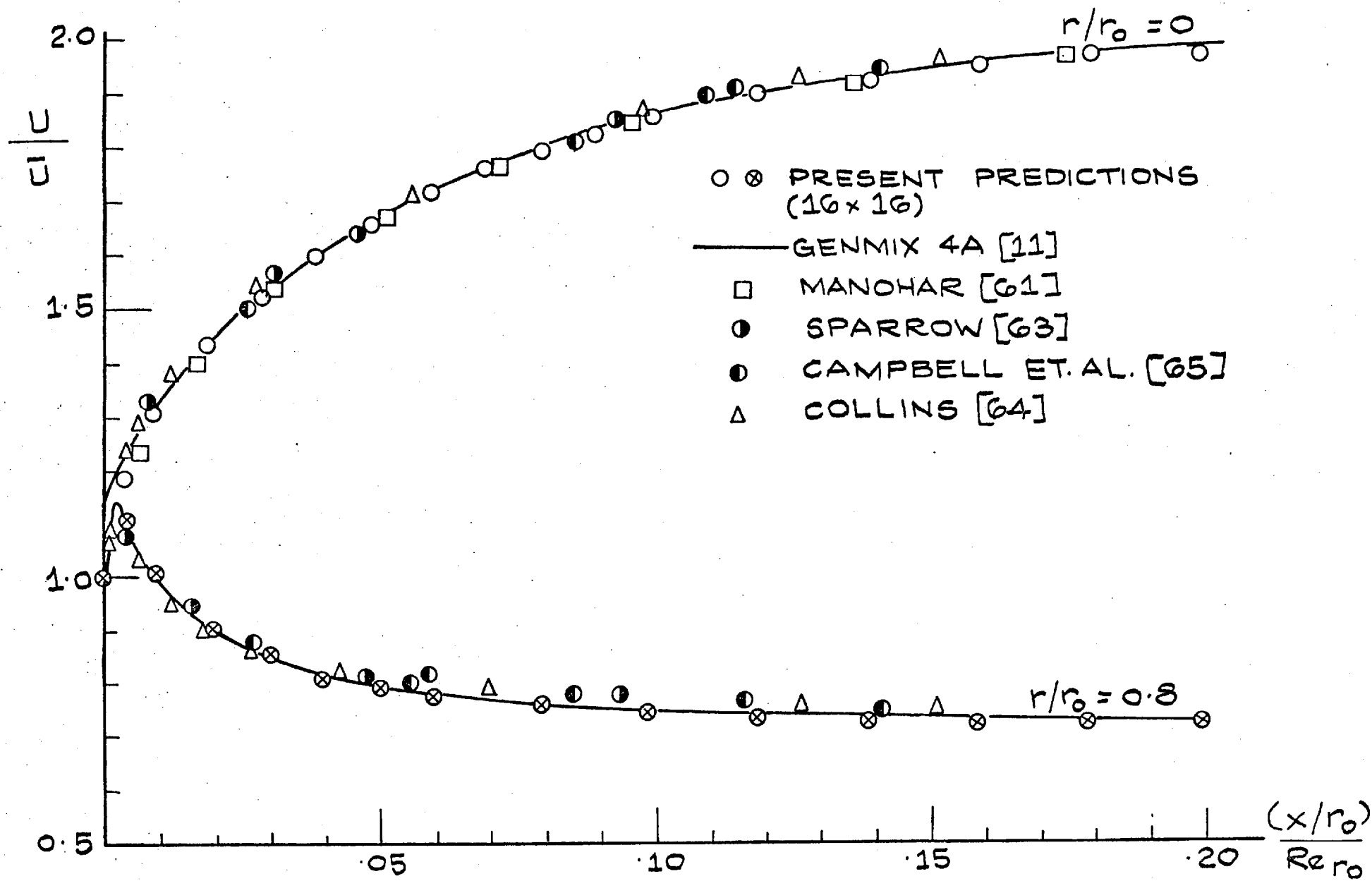


FIG. 4.6: VELOCITY DEVELOPMENT IN LAMINAR PIPEFLOW.  
COMPARISON WITH ANALYTICAL DATA.



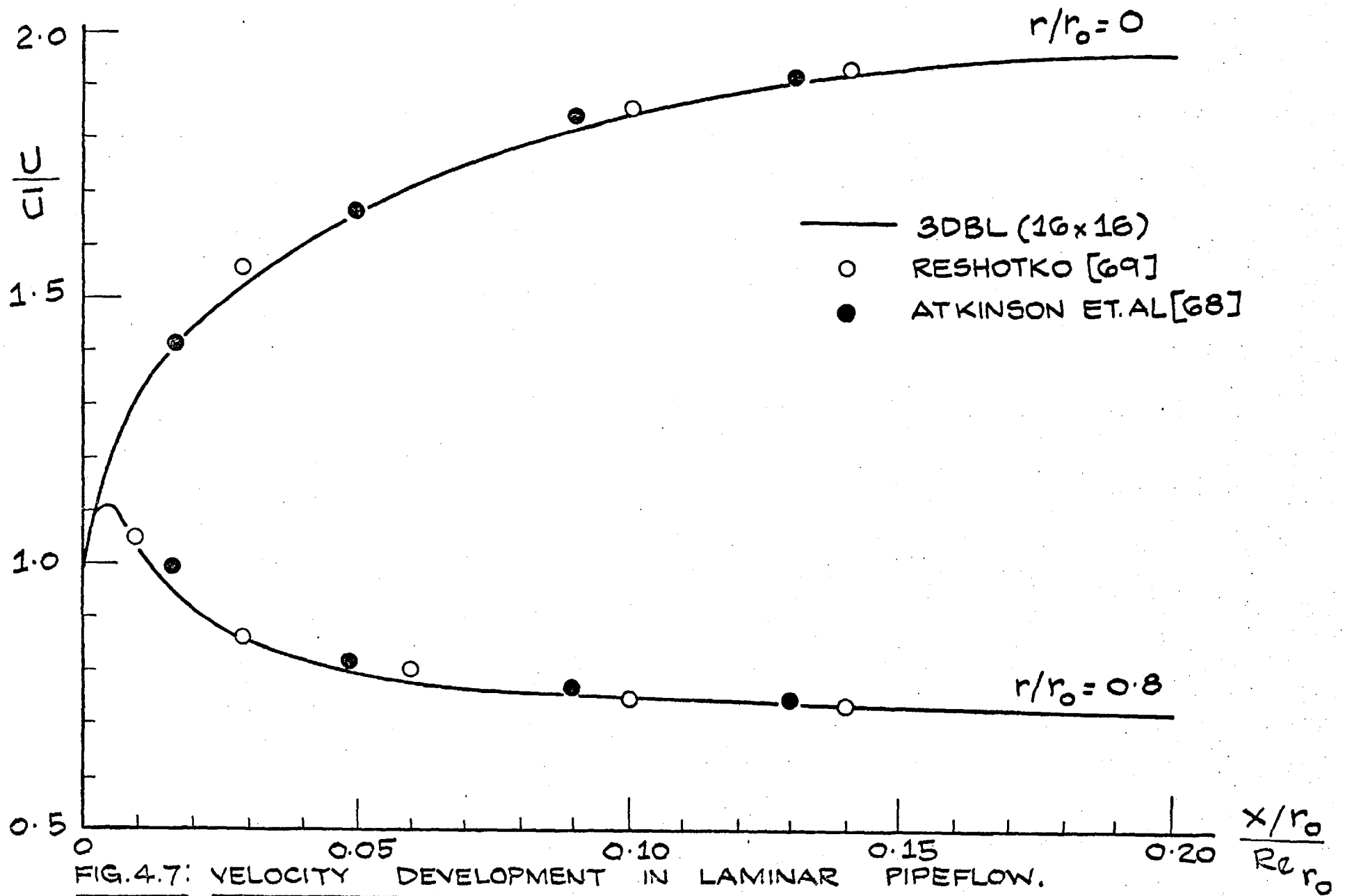


FIG.4.7: VELOCITY DEVELOPMENT IN LAMINAR PIPEFLOW.

COMPARISON WITH EXPERIMENTAL DATA.

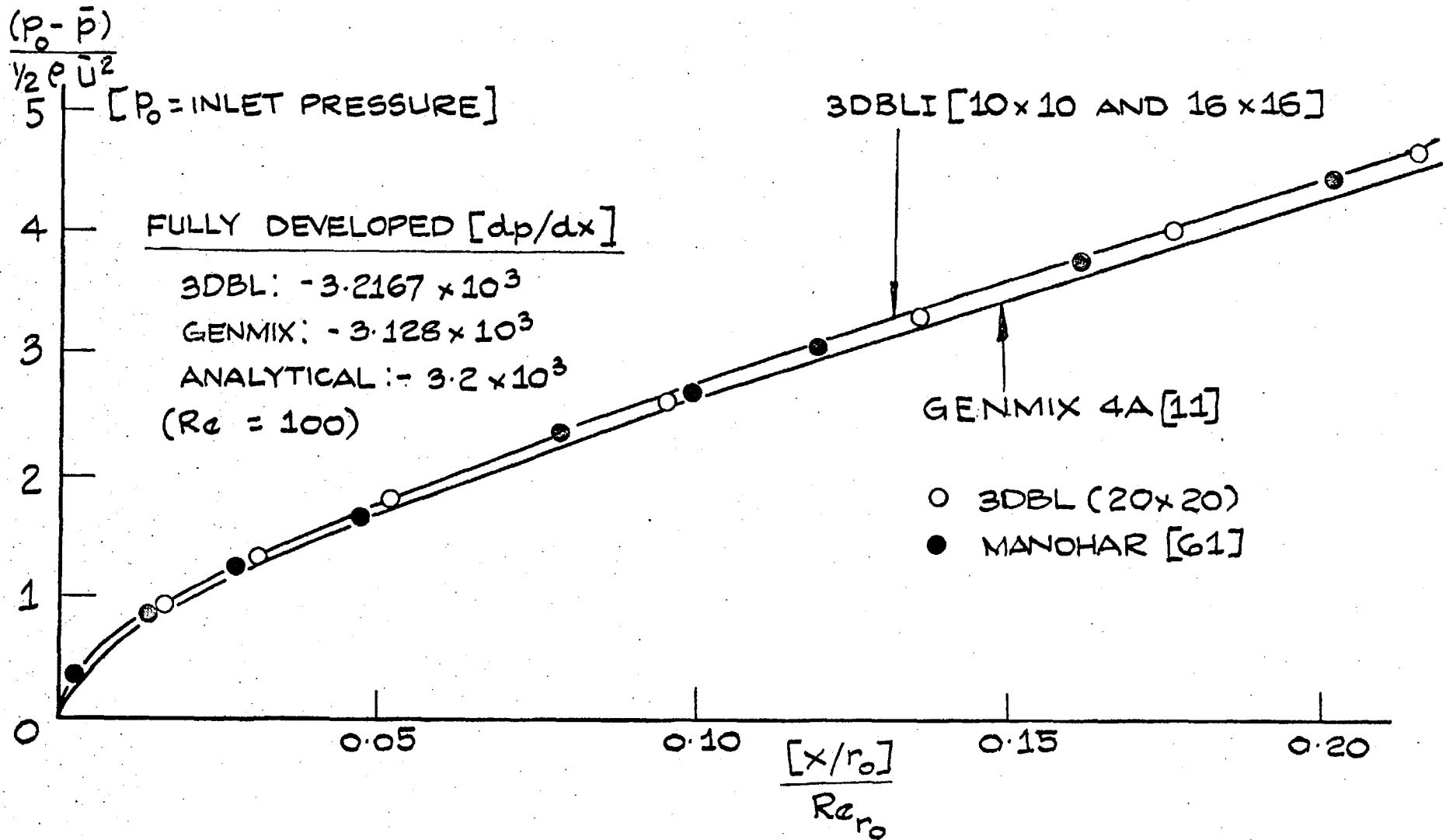


FIG. 4.8: PRESSURE DEVELOPMENT (LAMINAR PIPEFLOW).

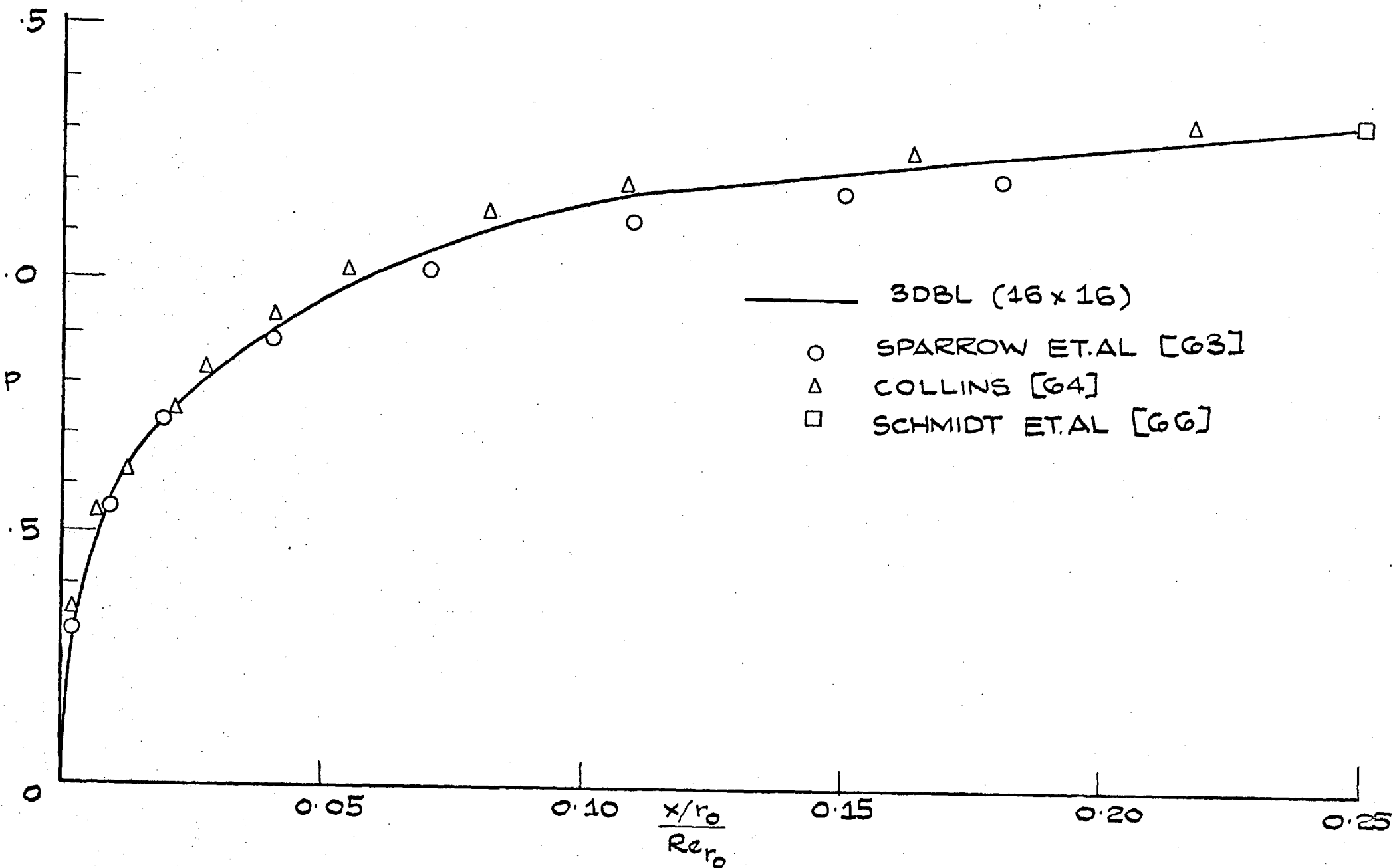


FIG. 4.9: PRESSURE DROP COEFFICIENT.

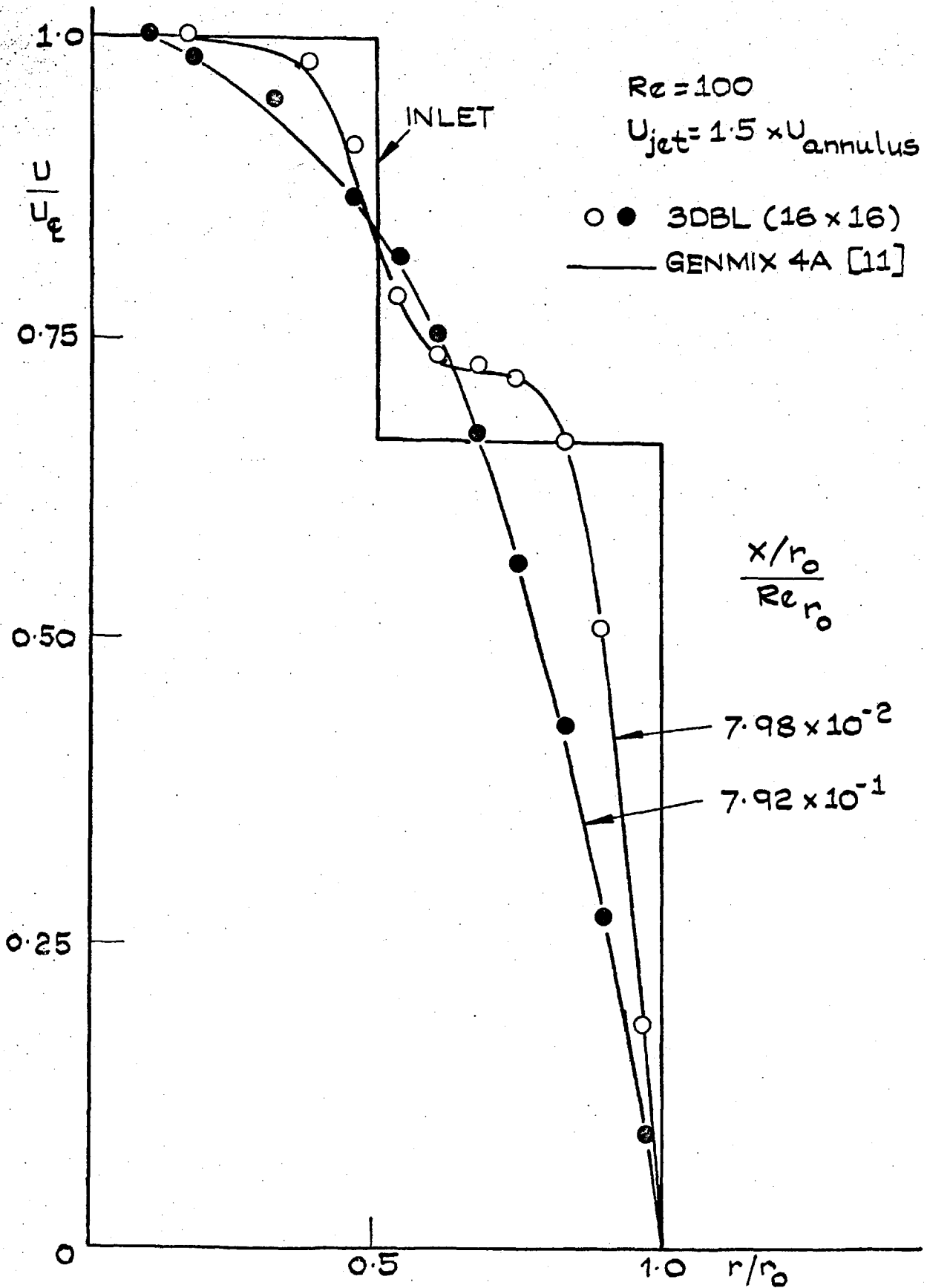


FIG. 4.10: DEVELOPING VELOCITY PROFILES  
(LAMINAR JET MIXING PROBLEM).

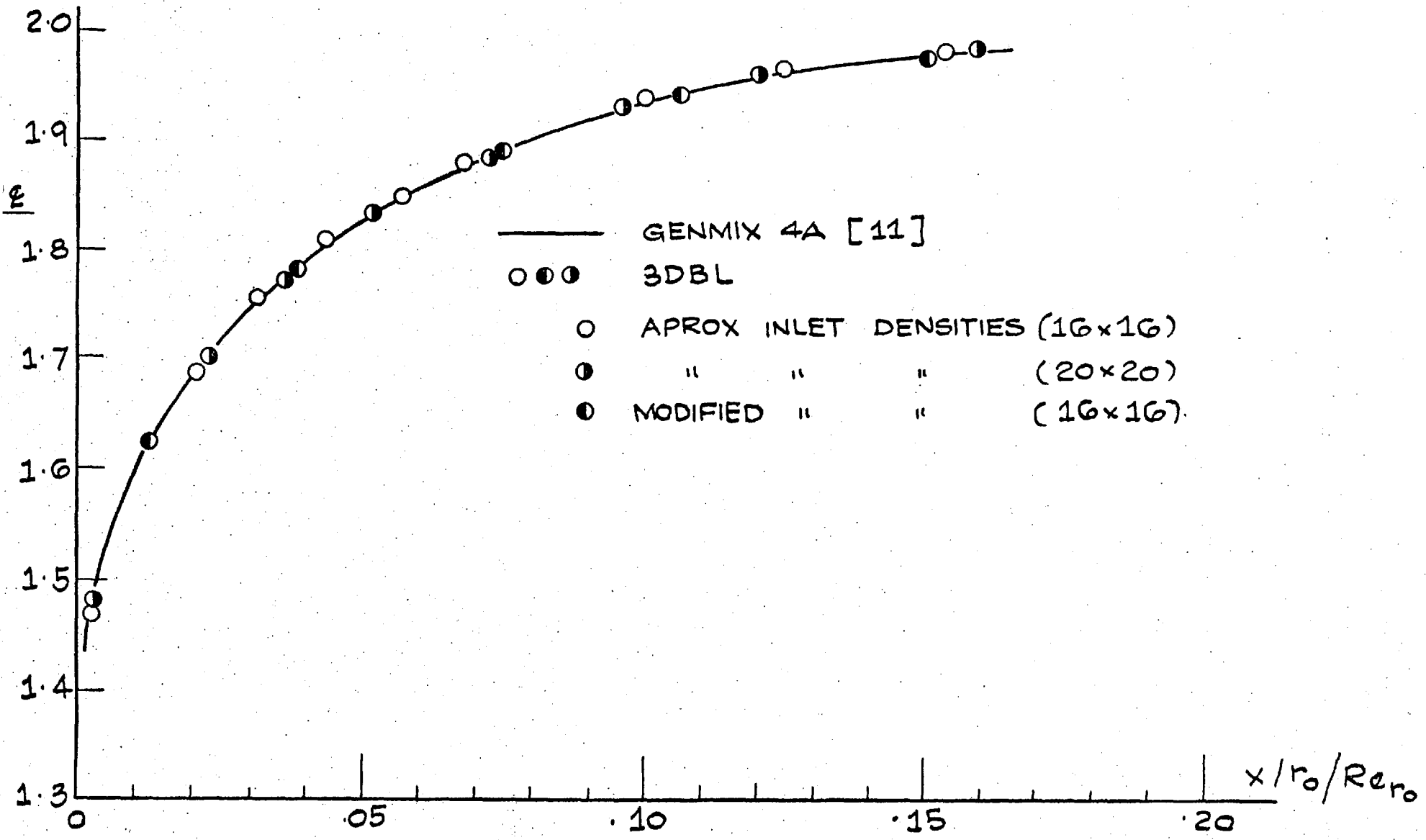


FIG. 4.11: CENTRE-LINE VELOCITY DEVELOPMENT (LAMINAR JET MIXING PROBLEM.)

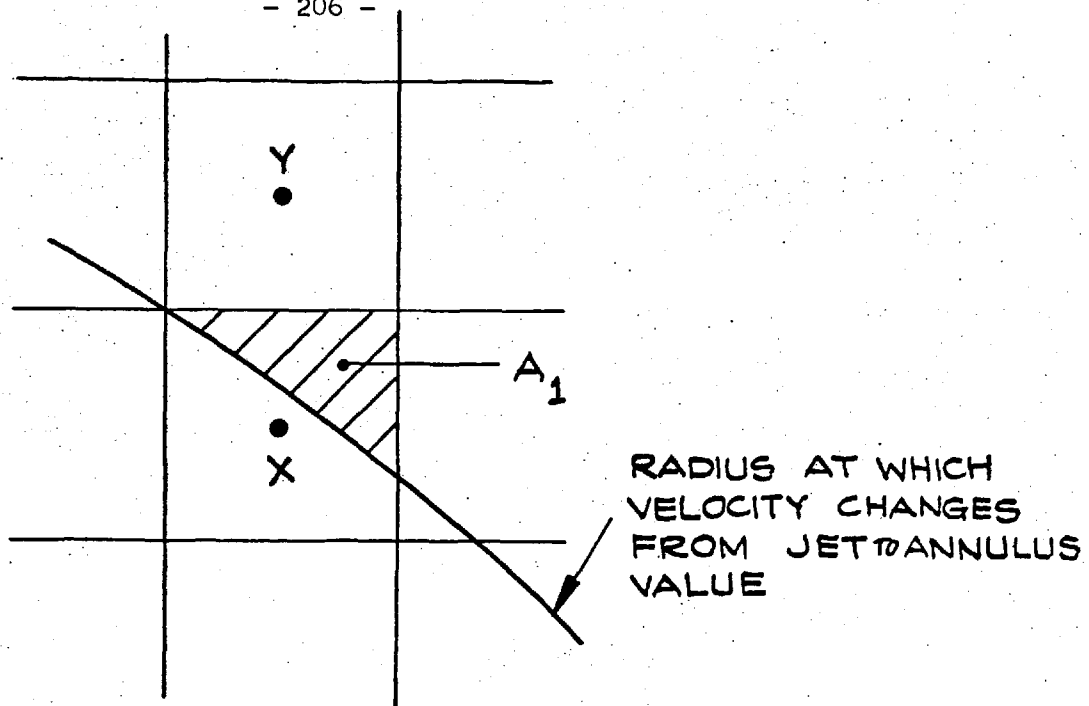


FIG. 4.12: SPECIAL TREATMENT OF INLET REGION IN A JET MIXING PROBLEM.

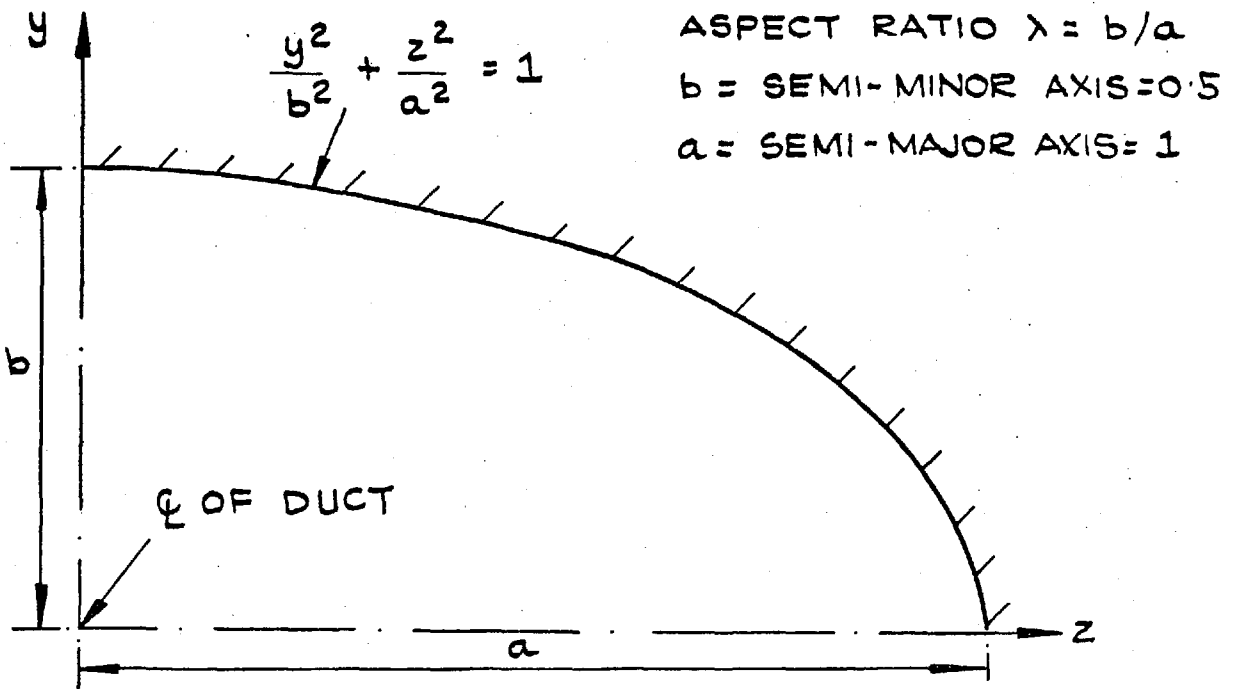


FIG. 4.13: GEOMETRY FOR ELLIPTIC DUCT FLOW TESTS.

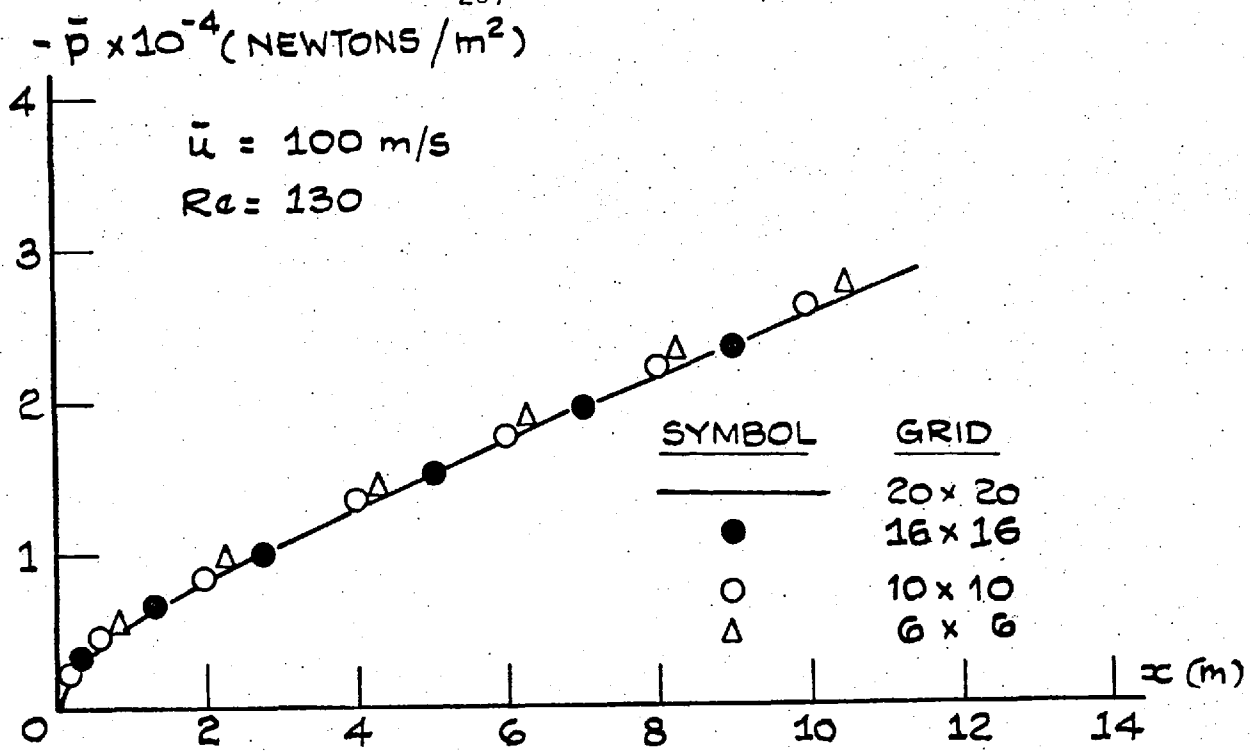


FIG. 4.14: ELLIPTIC DUCT FLOW, GRID REFINEMENT TESTS.

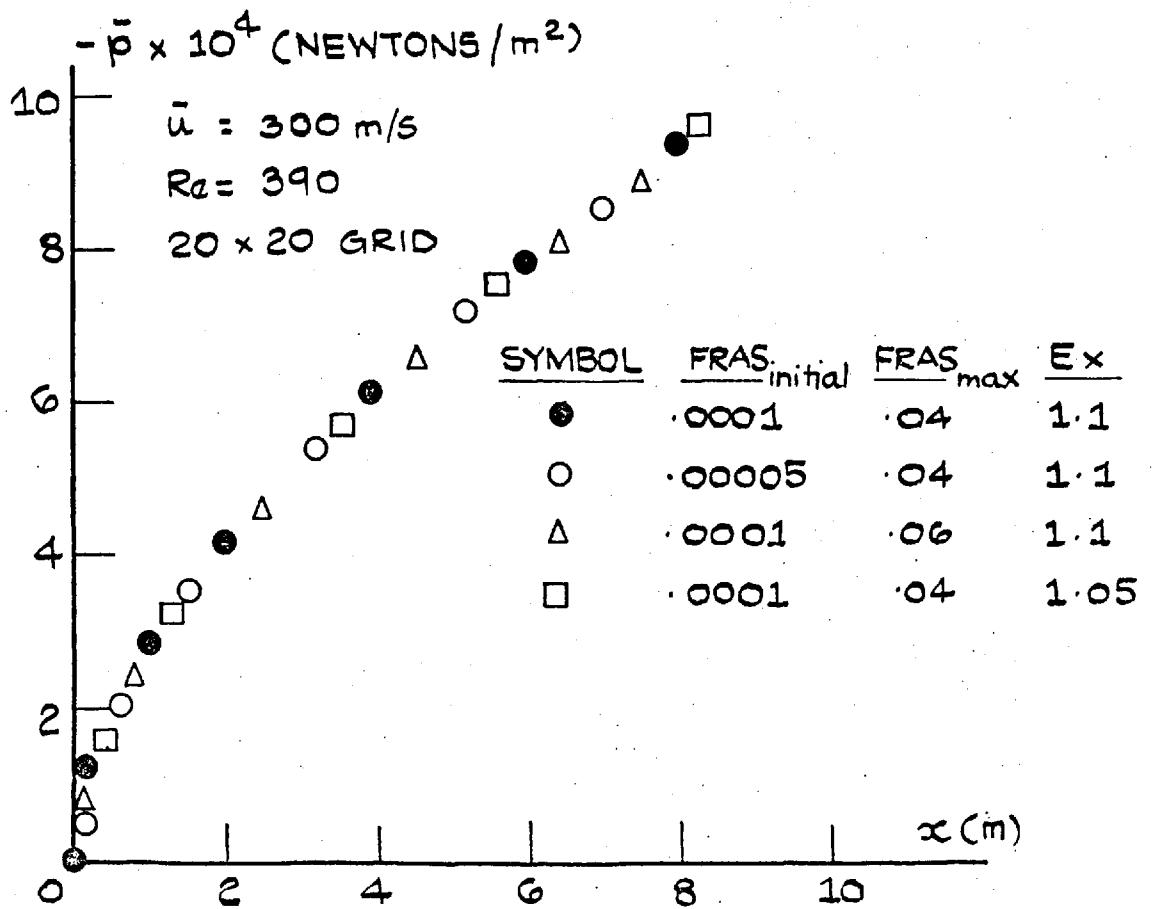


FIG. 4.15: ELLIPTIC DUCT FLOW, STEP SIZE TESTS.

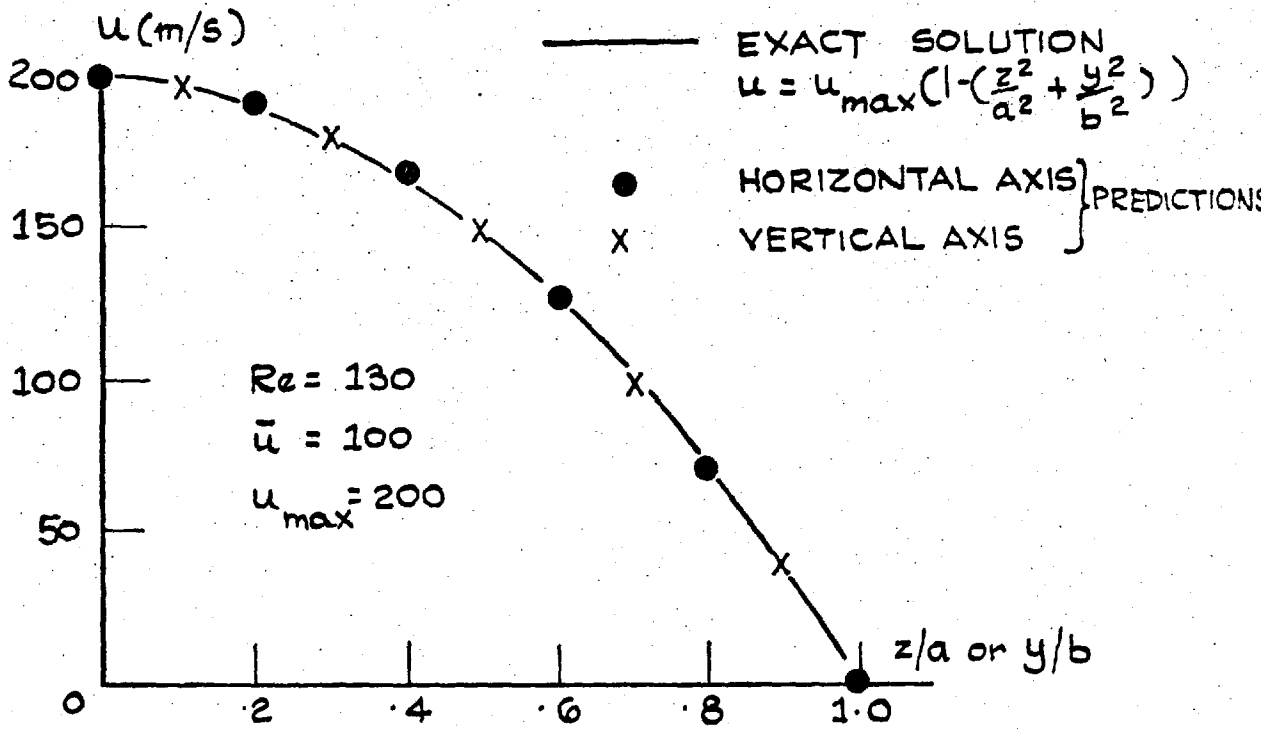


FIG. 4.16: FULLY-DEVELOPED MEAN VELOCITY PROFILE IN AN ELLIPTIC DUCT.

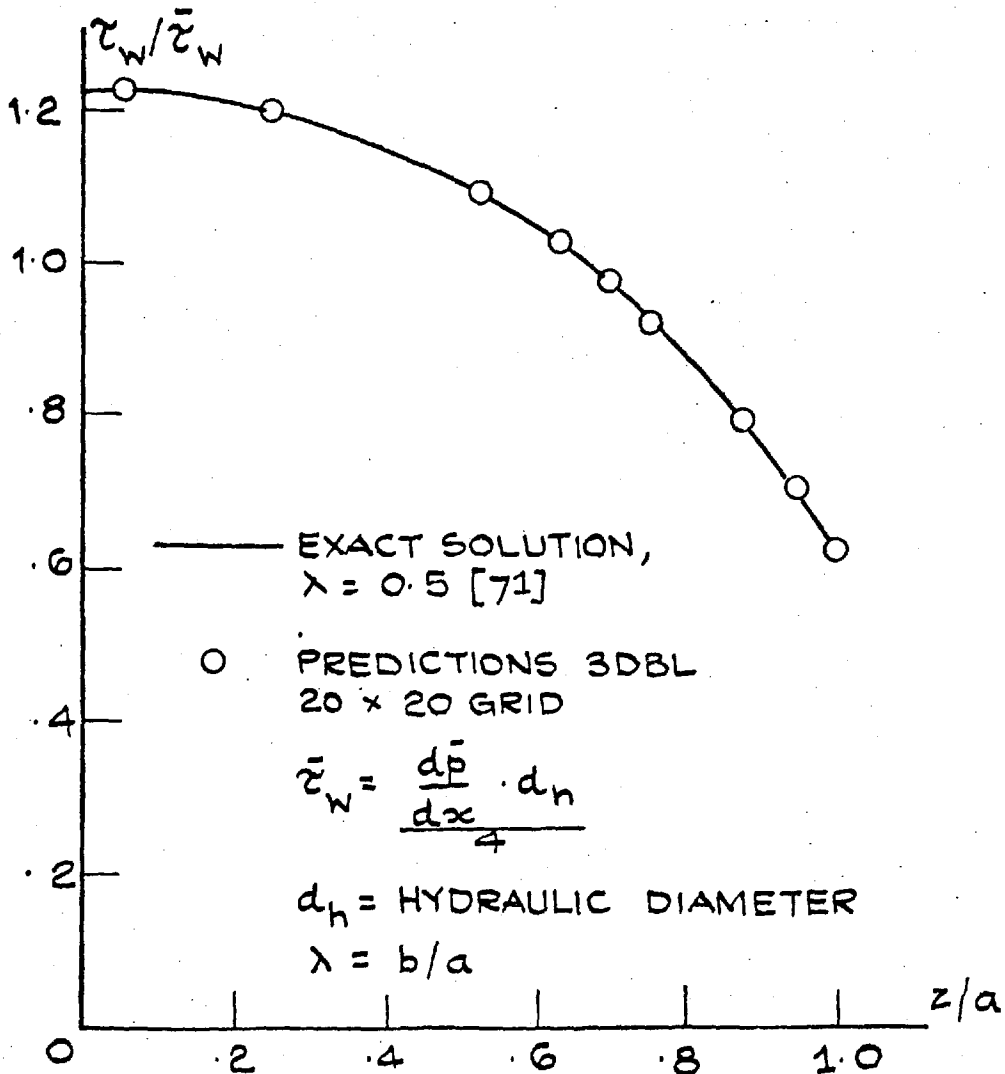


FIG. 4.17: ELLIPTIC DUCT, LAMINAR FLOW, WALL SHEAR STRESS VARIATION.



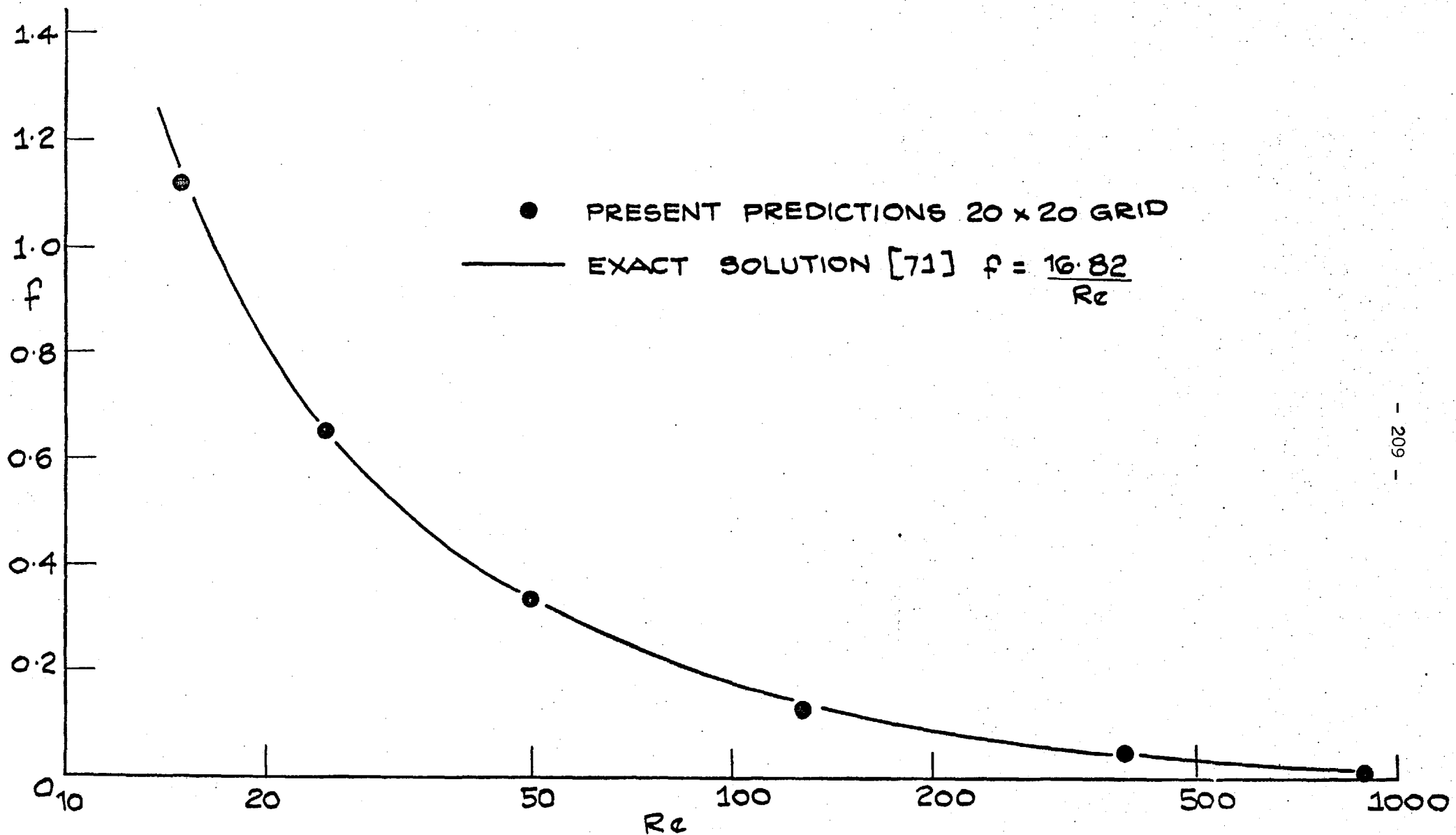


FIG. 4.18: FRICTION FACTOR / REYNOLDS NO. CURVE, LAMINAR ELLIPTIC DUCT FLOW  
 $\lambda = 0.5$   $\lambda =$  ASPECT RATIO  $f = -\left(\frac{dp}{dx} \cdot dh\right) / 2\rho \bar{u}^2$   $Re = \rho \bar{u} dh / \mu$

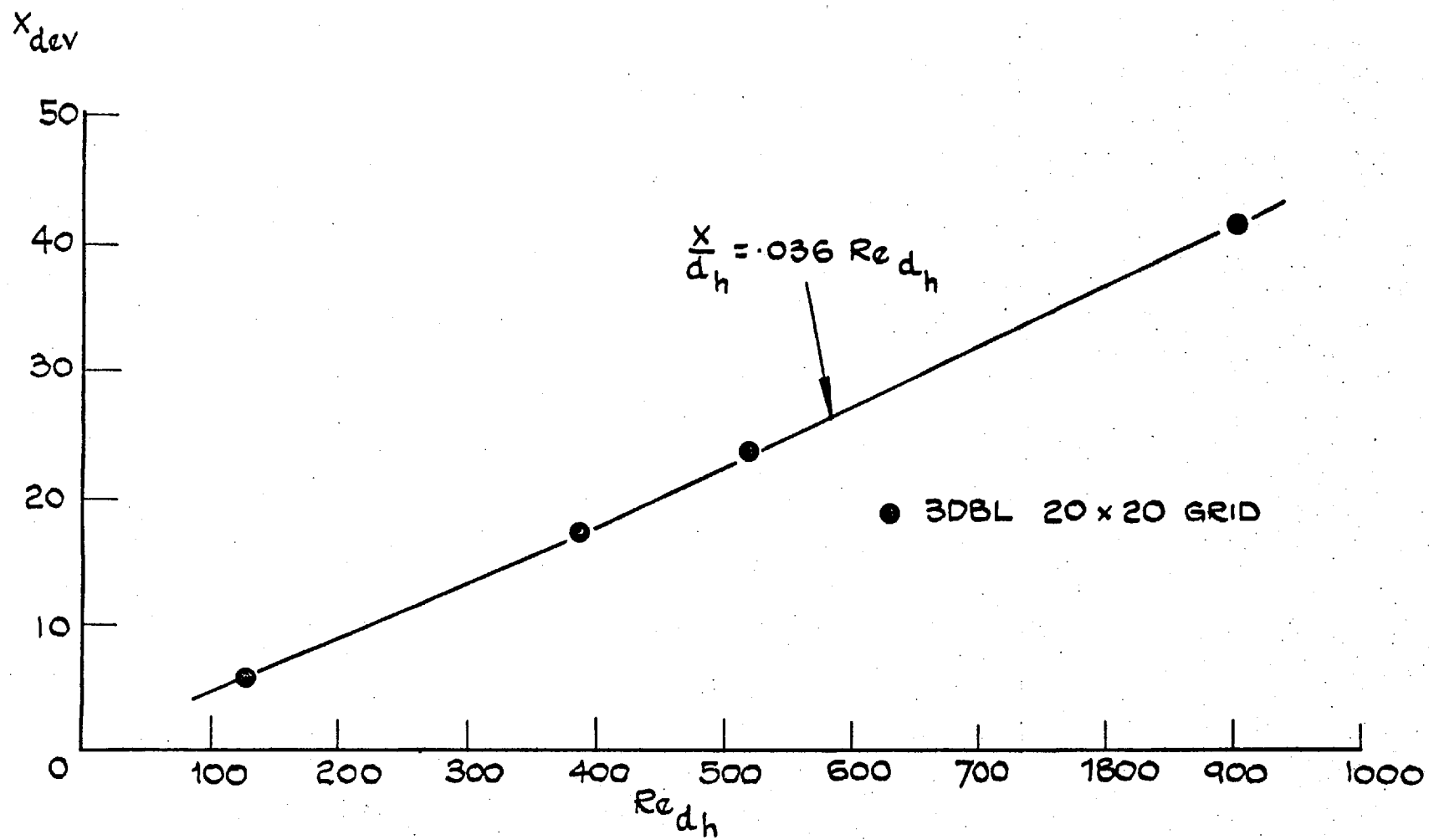


FIG. 4.19: DEVELOPMENT LENGTH FOR ELLIPTIC DUCT OF ASPECT RATIO 0.5.

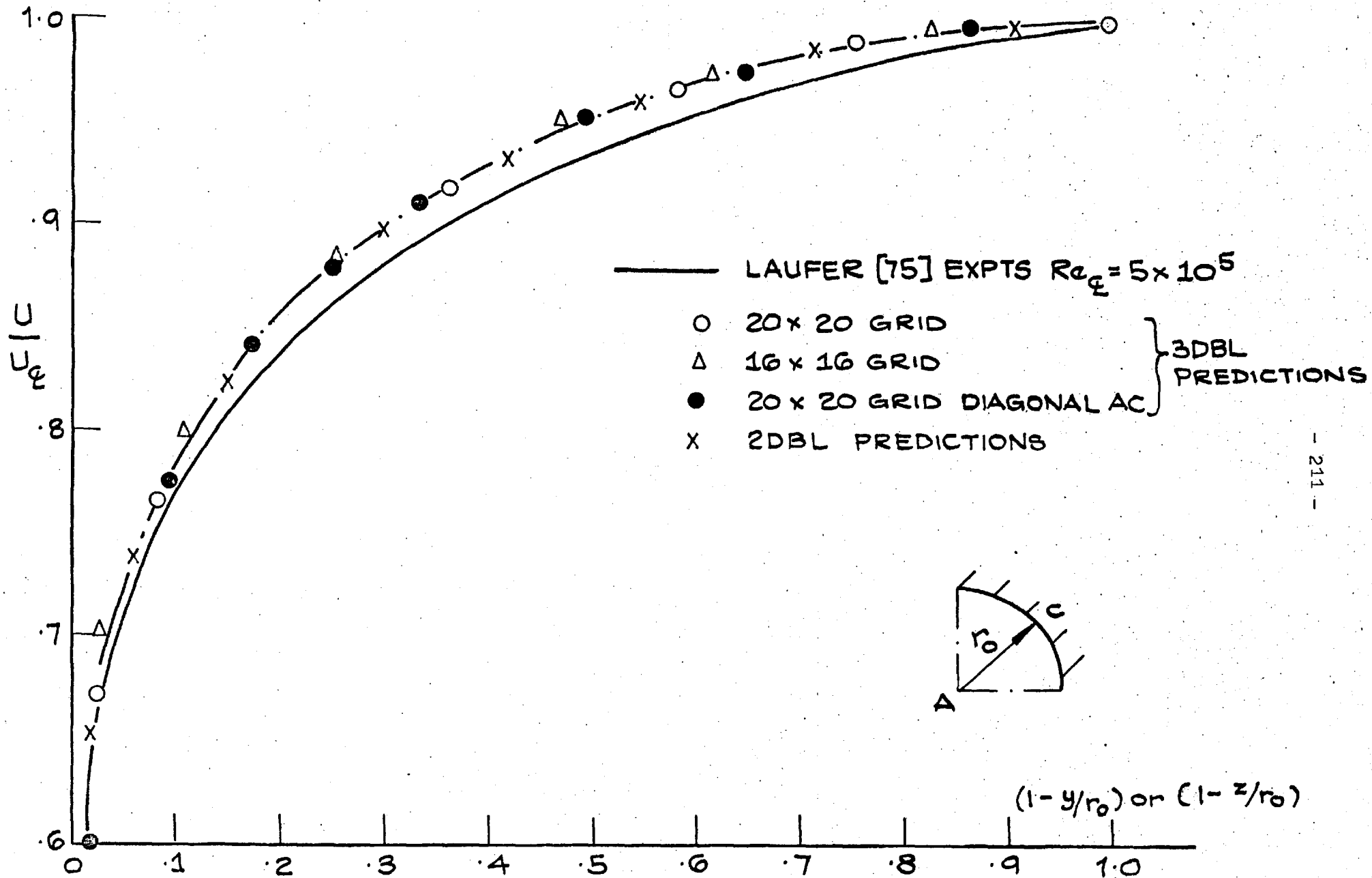


FIG. 4.20: TURBULENT CIRCULAR DUCT FLOW, FULLY-DEVELOPED VELOCITY PROFILE.

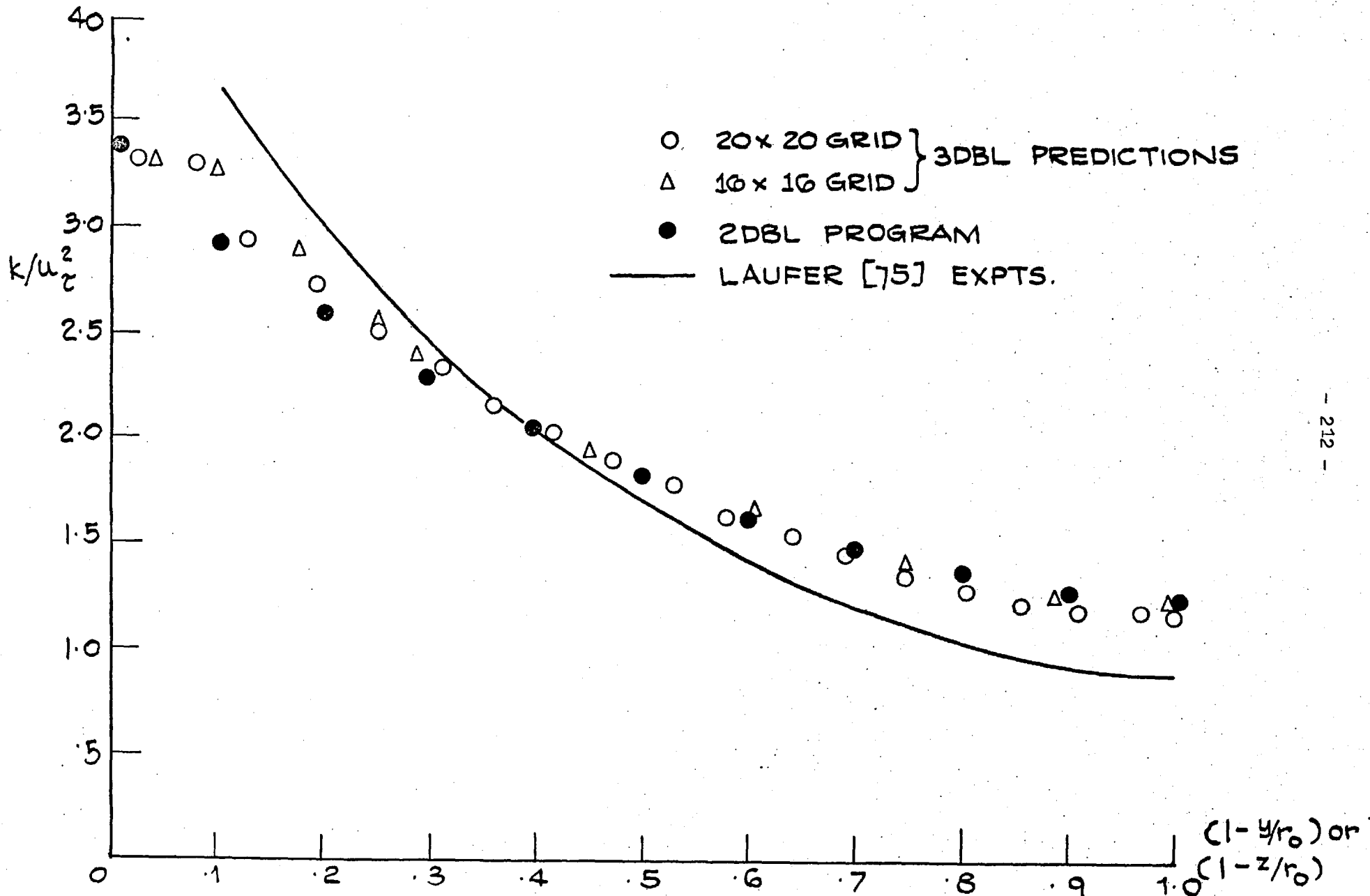


FIG. 4.21: TURBULENT CIRCULAR DUCT FLOW, FULLY DEVELOPED  
TURBULENCE ENERGY.

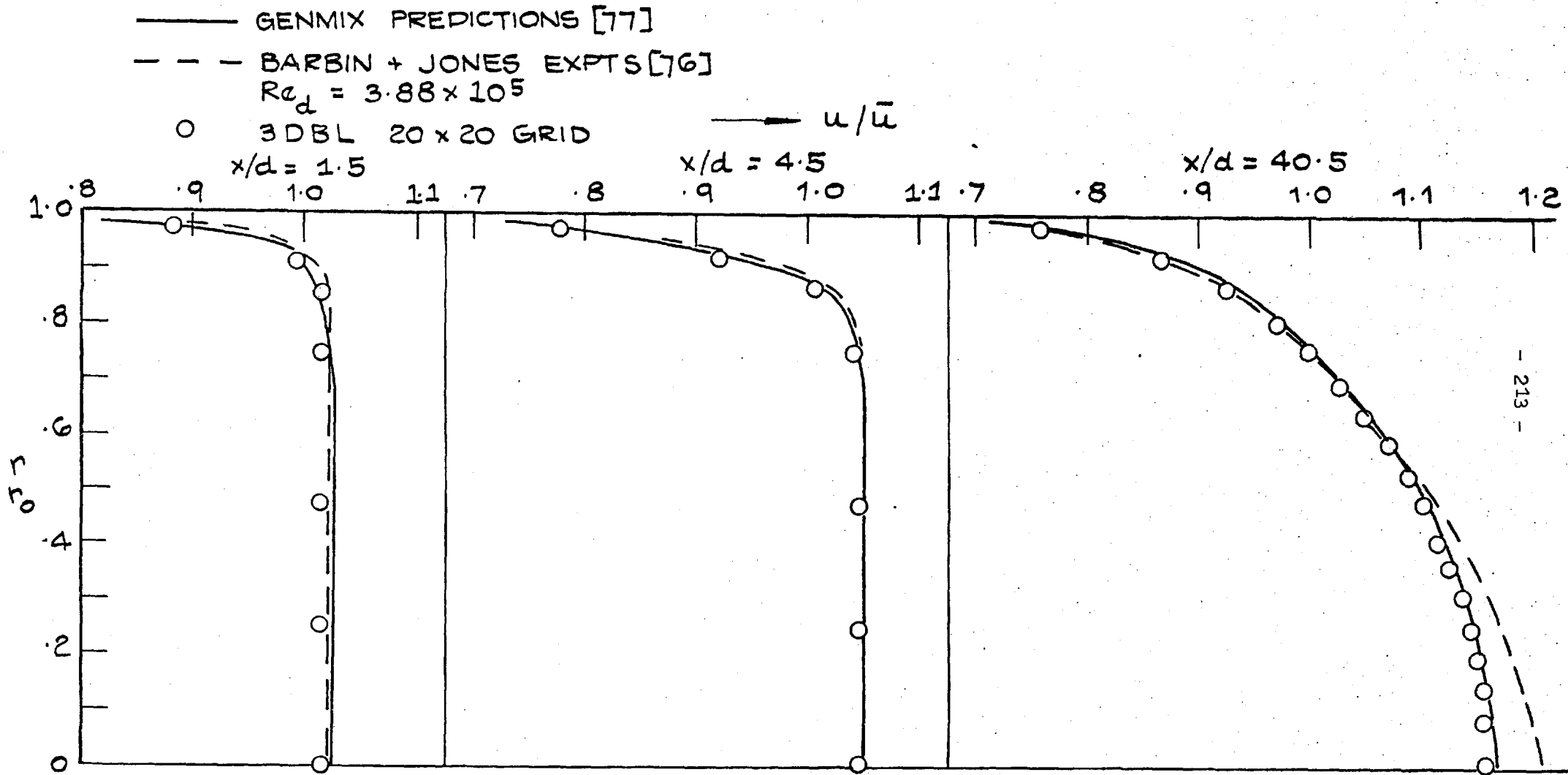


FIG. 4.22: MEAN VELOCITY PROFILES, DEVELOPING TURBULENT PIPE FLOW.

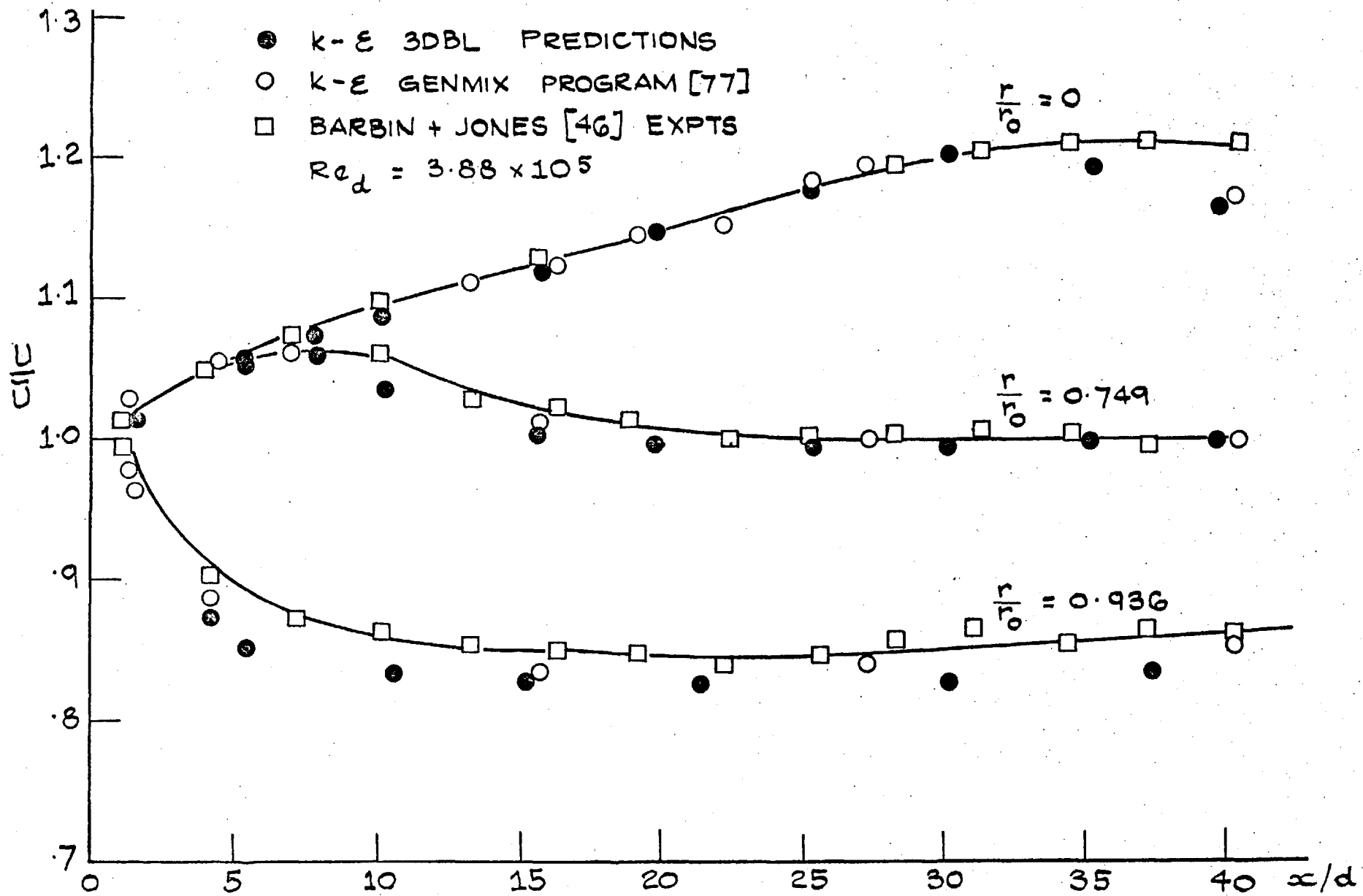


FIG. 4.23: AXIAL DEVELOPMENT OF VELOCITY AT 3 RADIAL POSITIONS - TURBULENT PIPE FLOW.

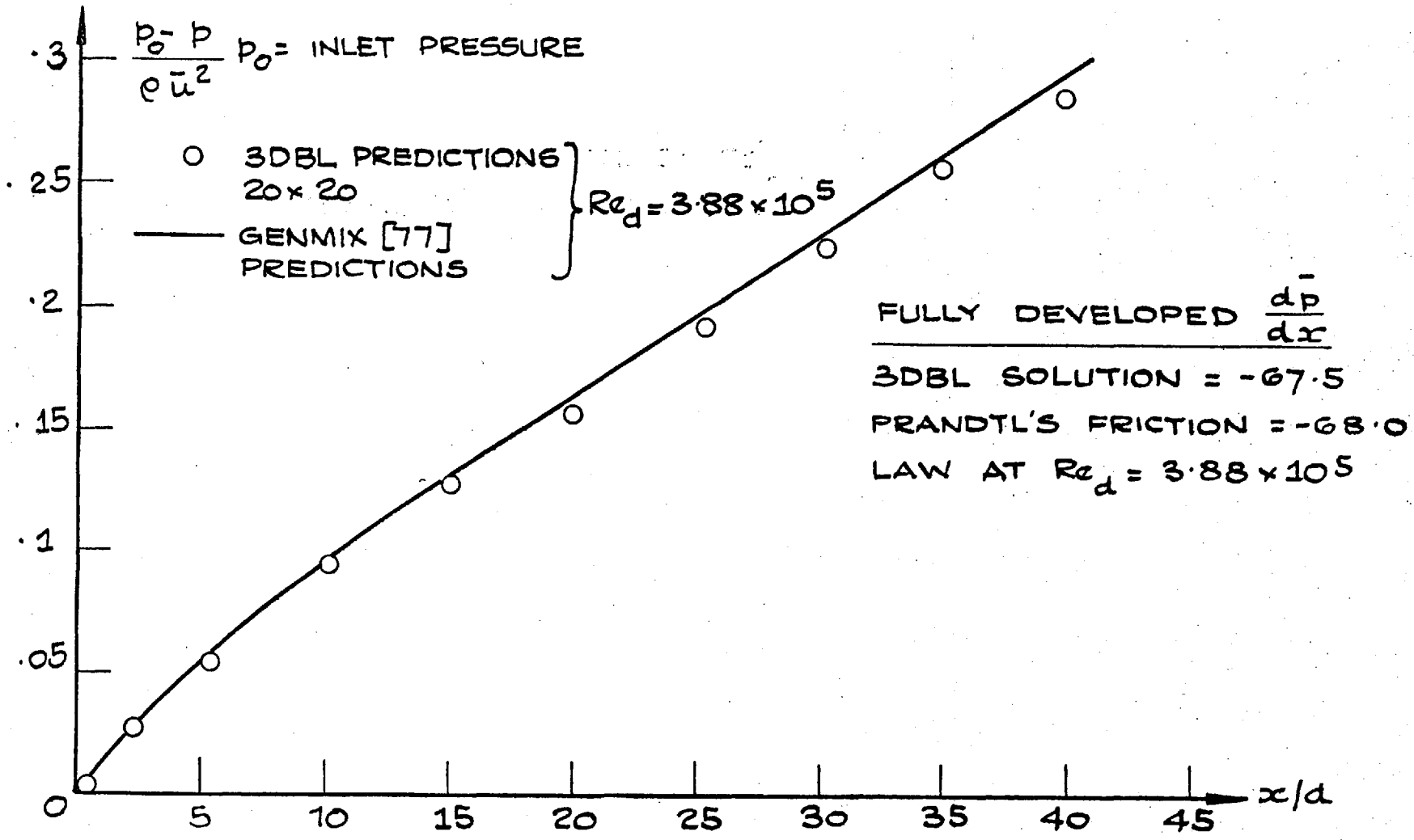


FIG. 4.24: PRESSURE DEVELOPMENT IN TURBULENT CIRCULAR PIPE FLOW.

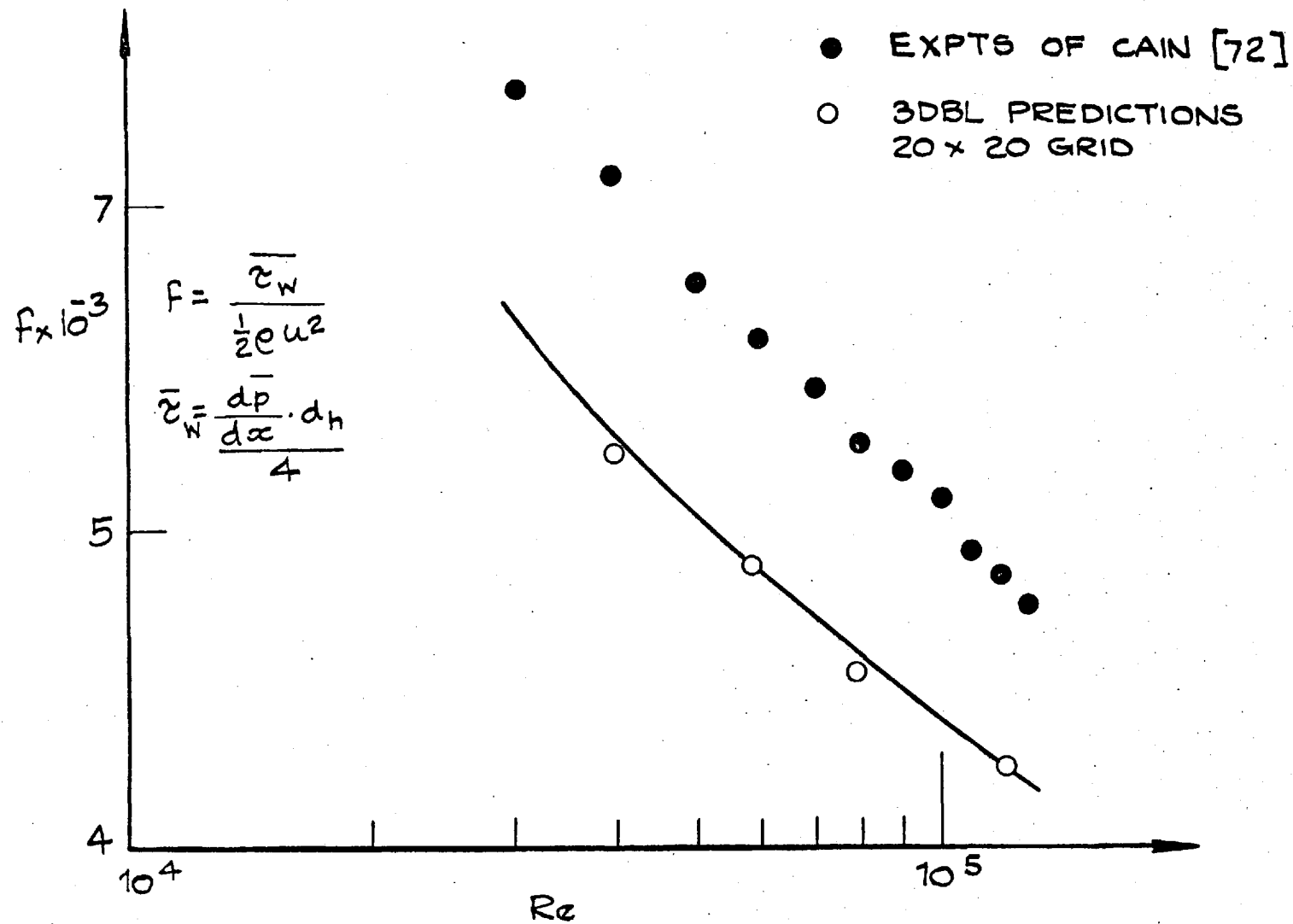


FIG. 4.25: FRICTION FACTOR / REYNOLDS NUMBER RELATIONSHIP,  
FULLY DEVELOPED FLOW IN 4" x 2" ELLIPTIC DUCT.



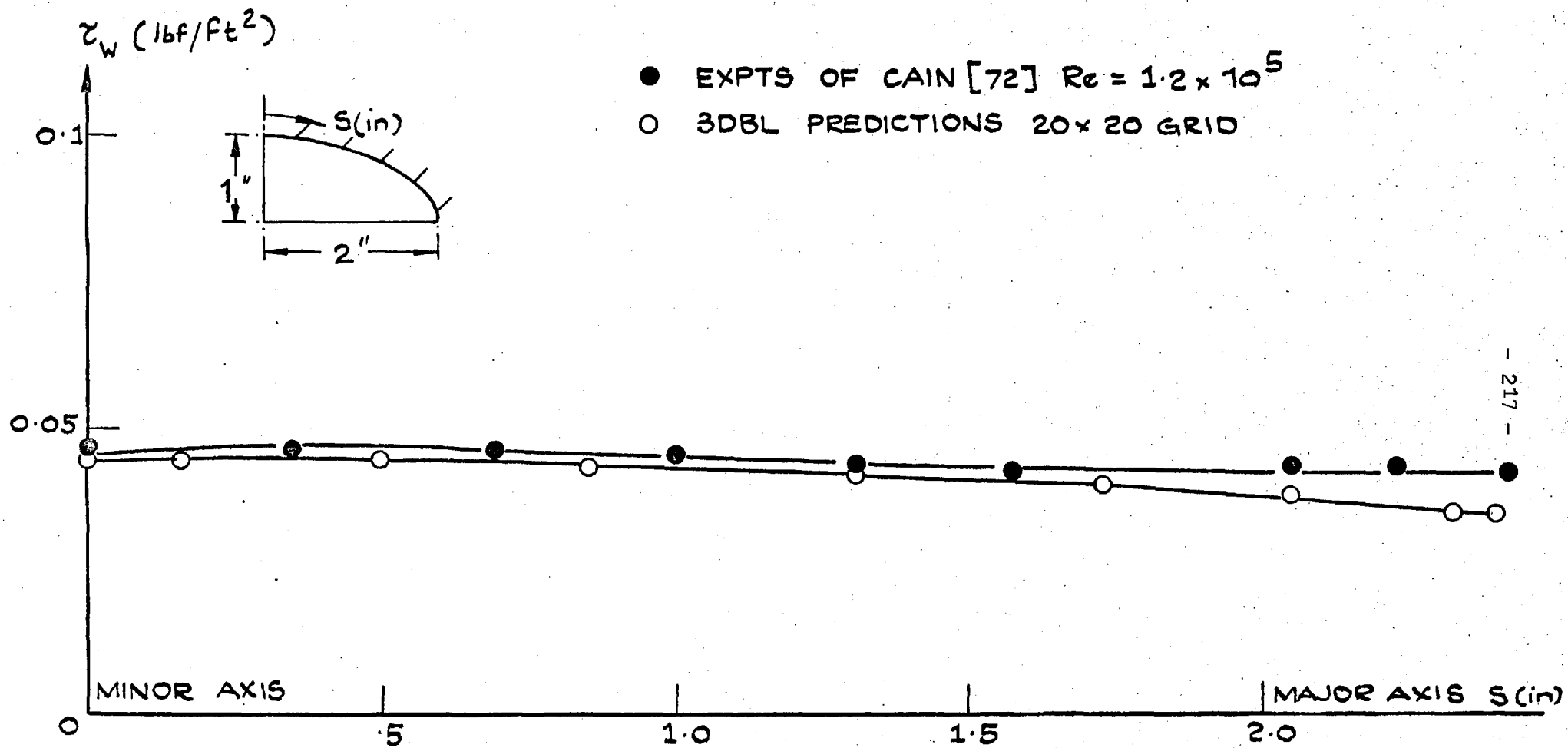


FIG. 4.26: WALL SHEAR STRESS VARIATION IN FULLY-DEVELOPED TURBULENT FLOW IN AN ELLIPTIC DUCT.

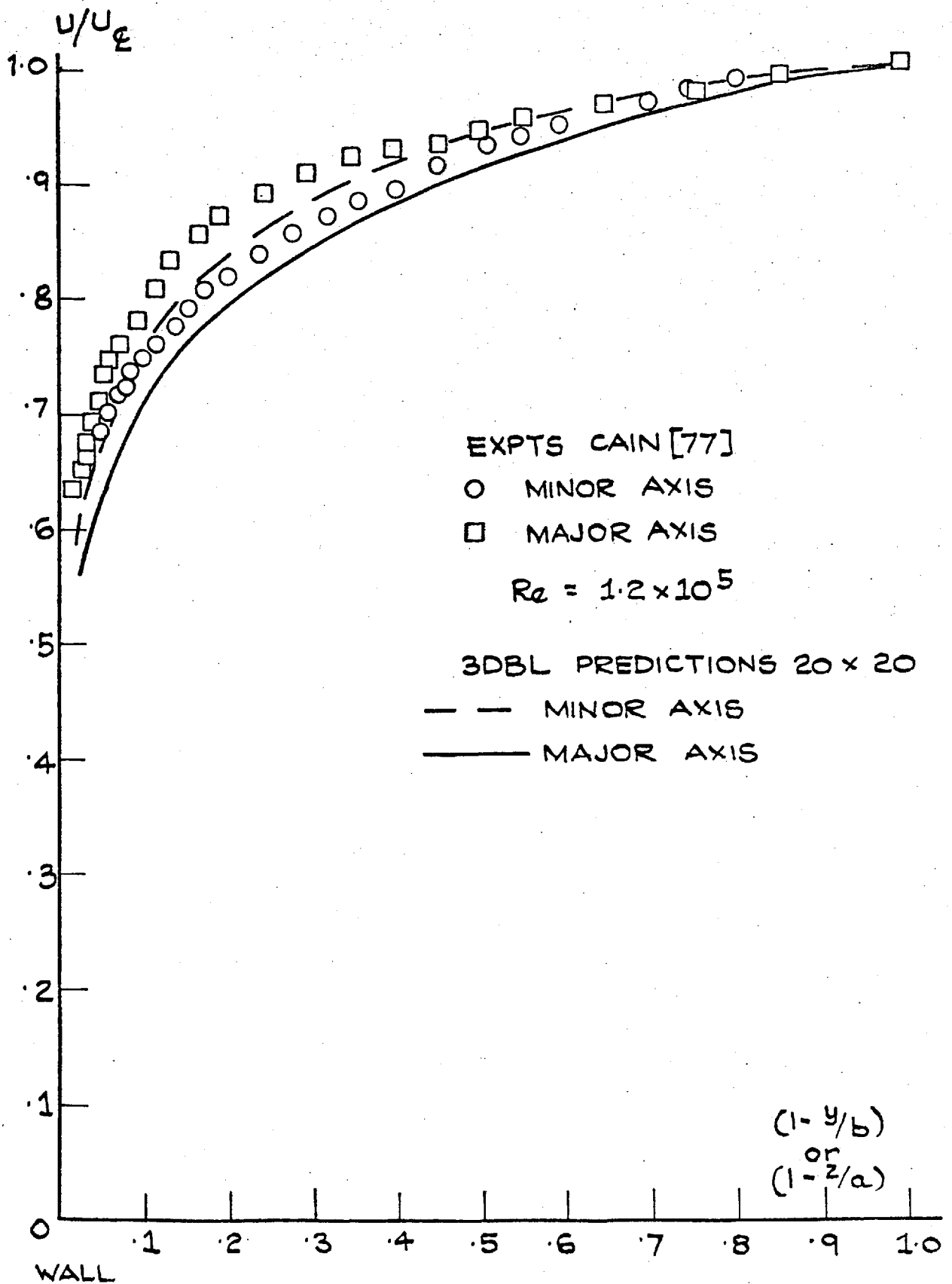


FIG. 4.27: TURBULENT FLOW IN AN ELLIPTIC DUCT, FULLY DEVELOPED VELOCITY PROFILES.

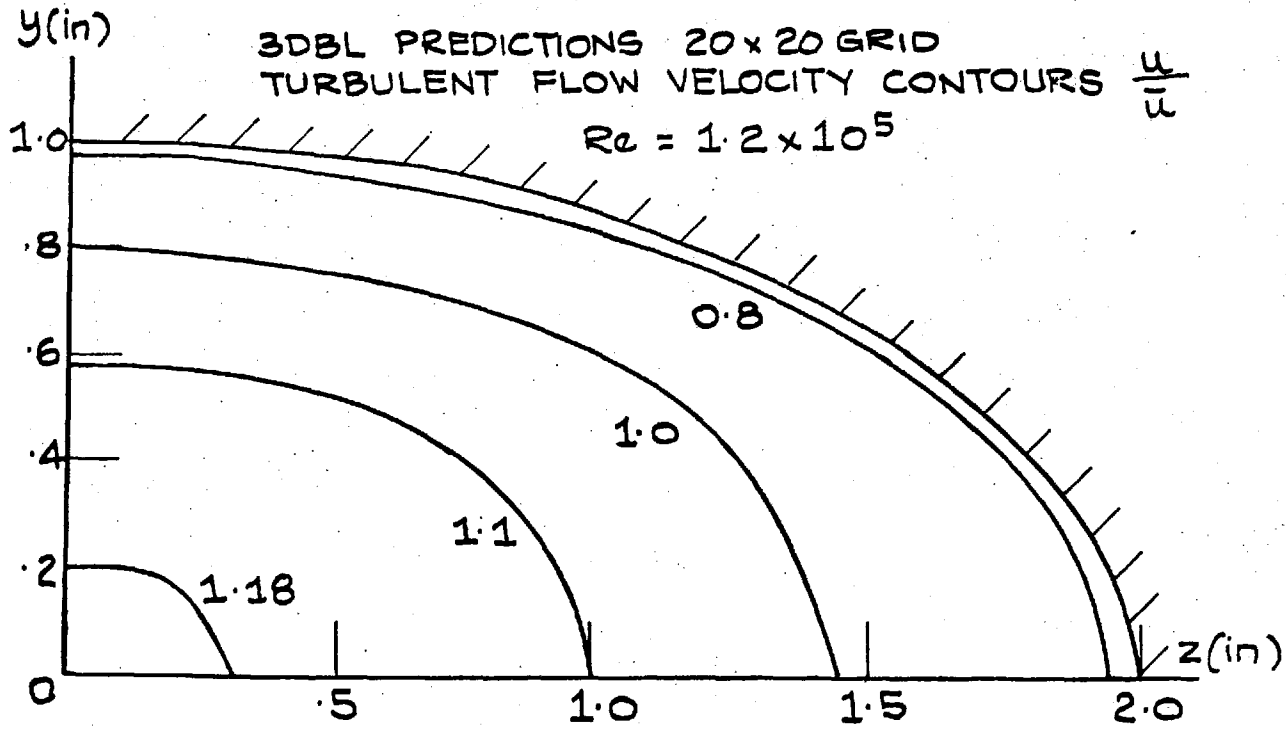


FIG. 4.28 a: FULLY DEVELOPED VELOCITY CONTOURS.

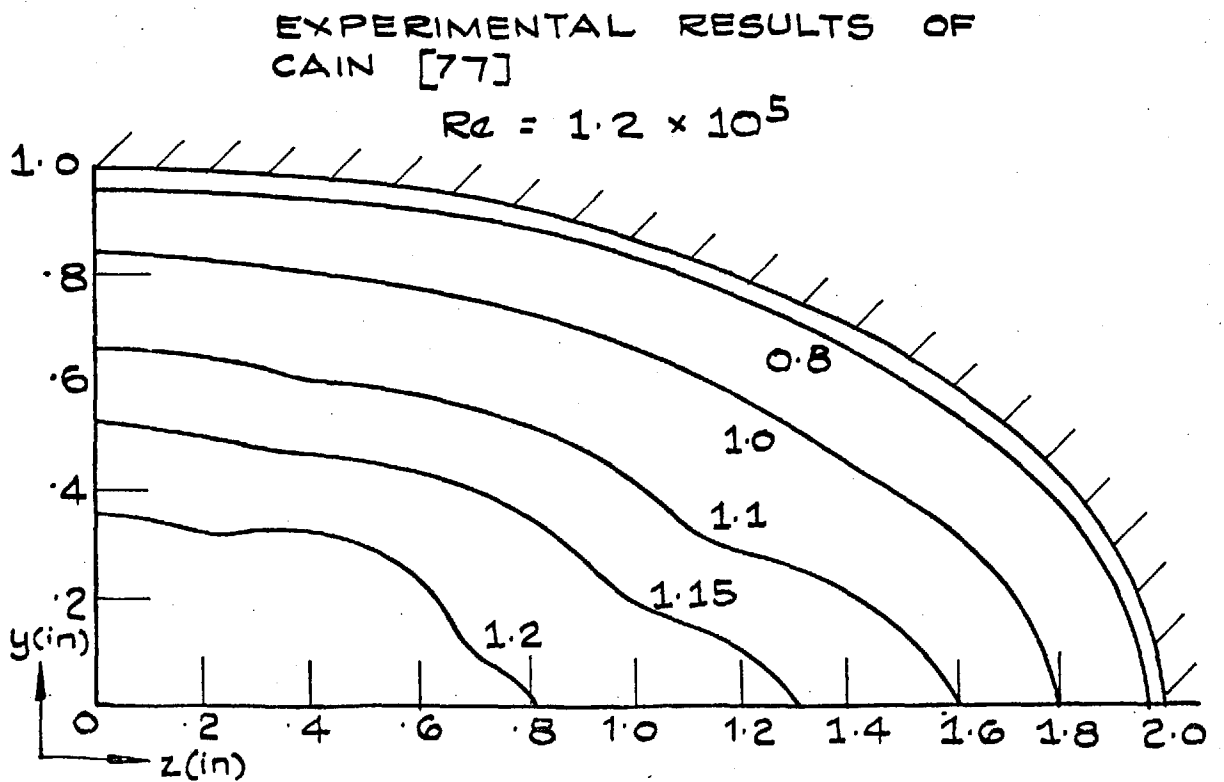


FIG. 4.28 b: FULLY DEVELOPED VELOCITY CONTOURS.

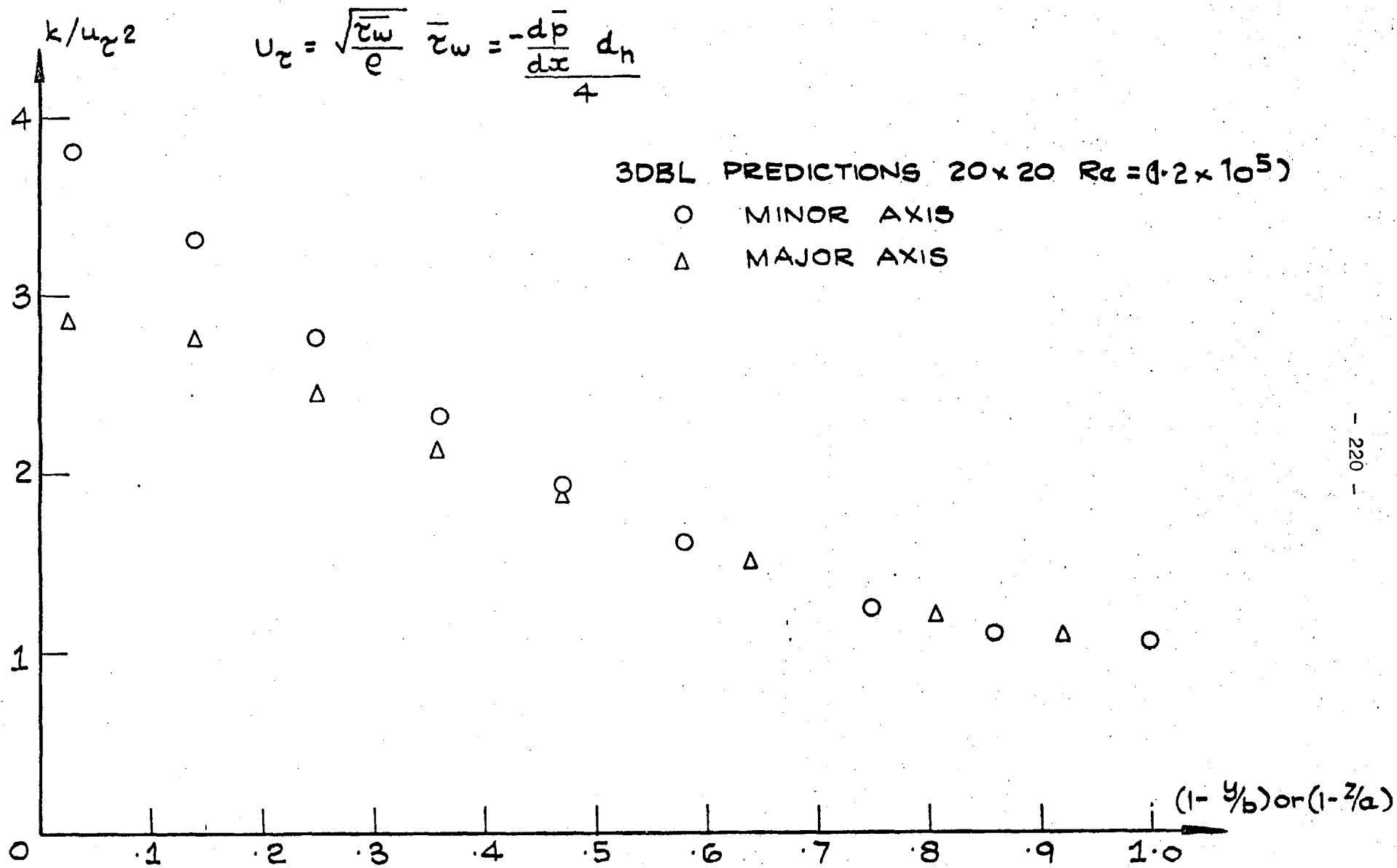


FIG. 4.29: FULLY DEVELOPED TURBULENT KINETIC ENERGY PROFILES IN AN ELLIPTIC DUCT.

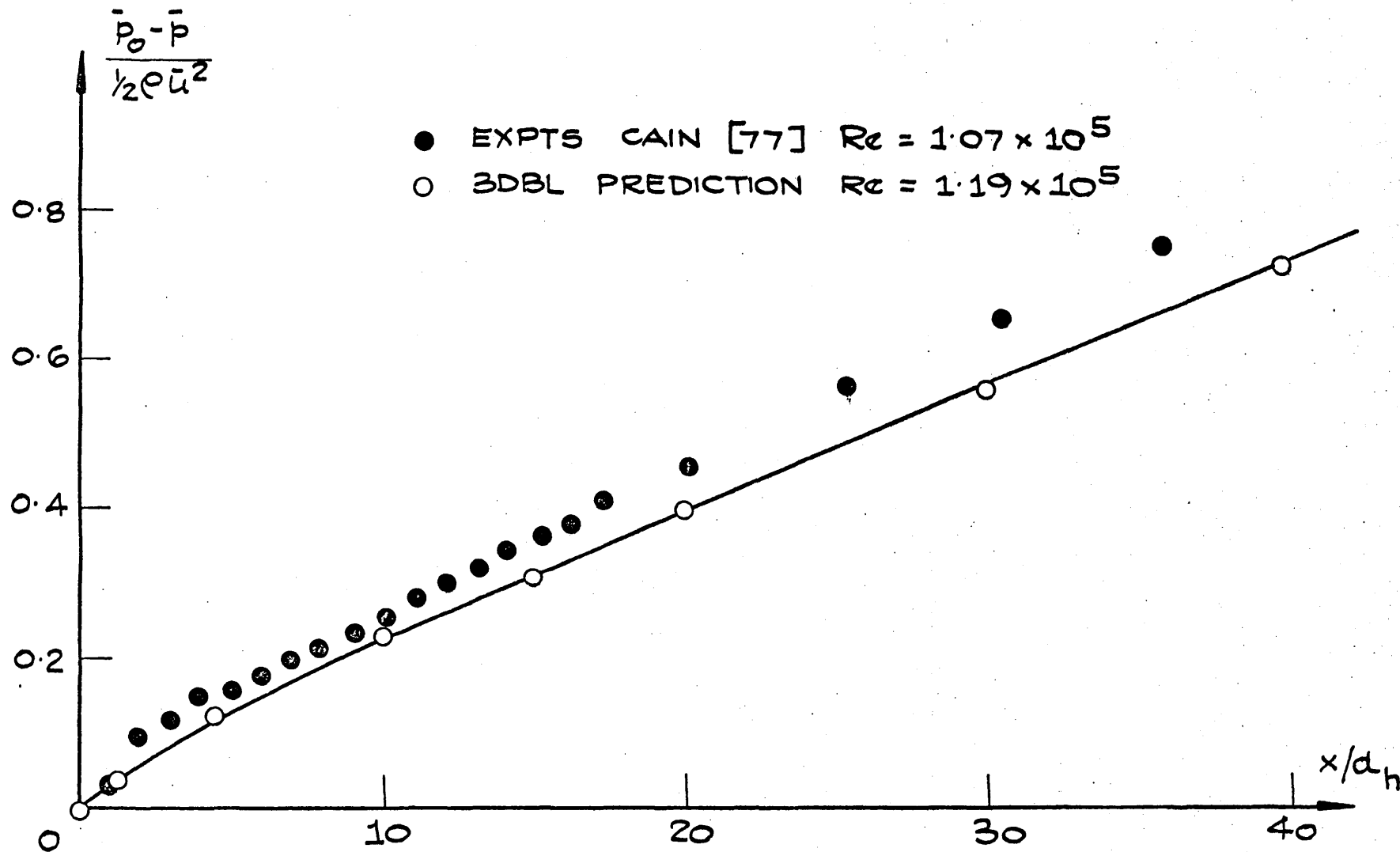


FIG. 4.30: PRESSURE DEVELOPMENT, TURBULENT ELLIPTIC DUCT FLOW.

3DBL 20 x 20 PREDICTIONS

$Re = 1.2 \times 10^5$

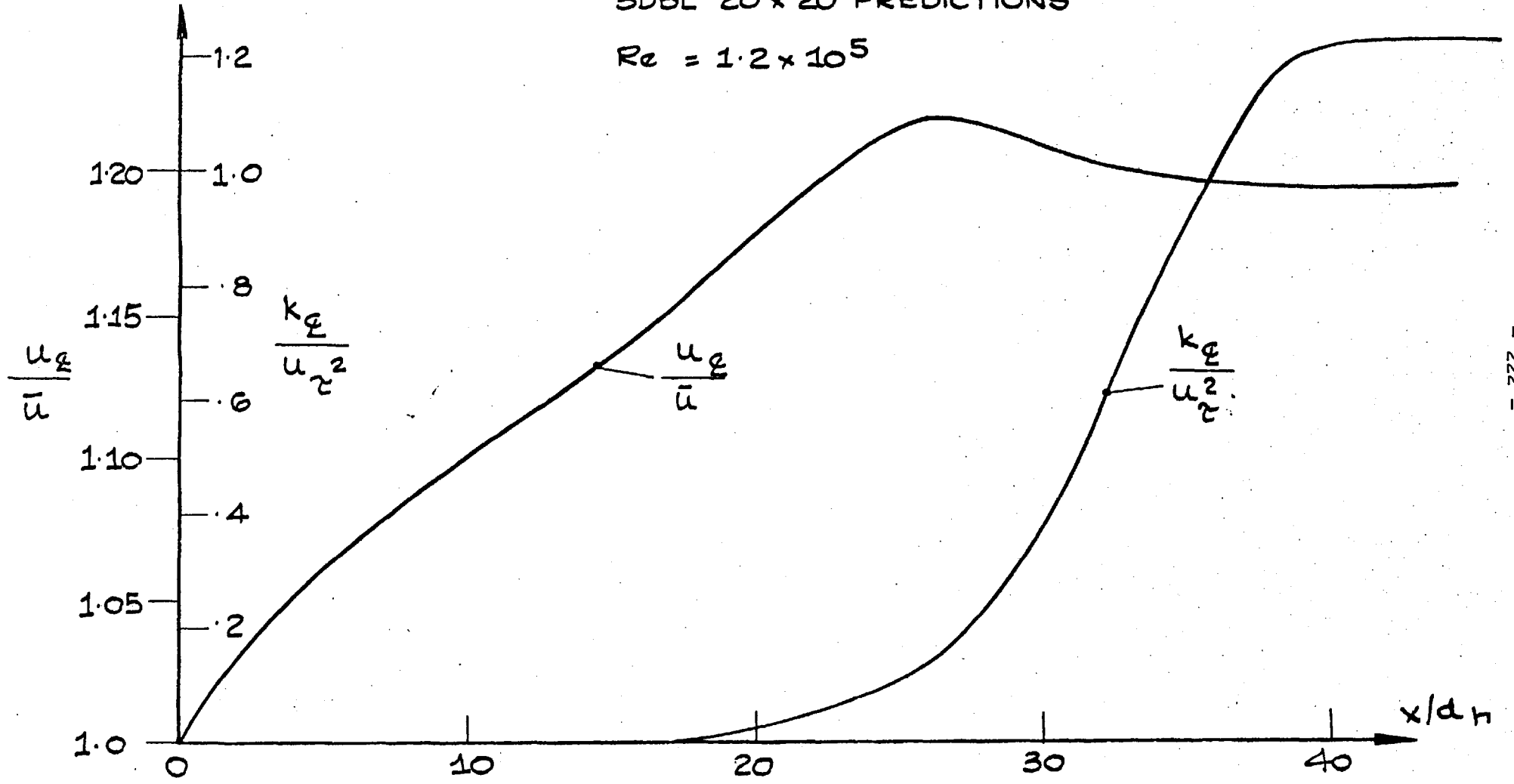


FIG. 4.31: DEVELOPING TURBULENT FLOW IN AN ELLIPTIC DUCT.

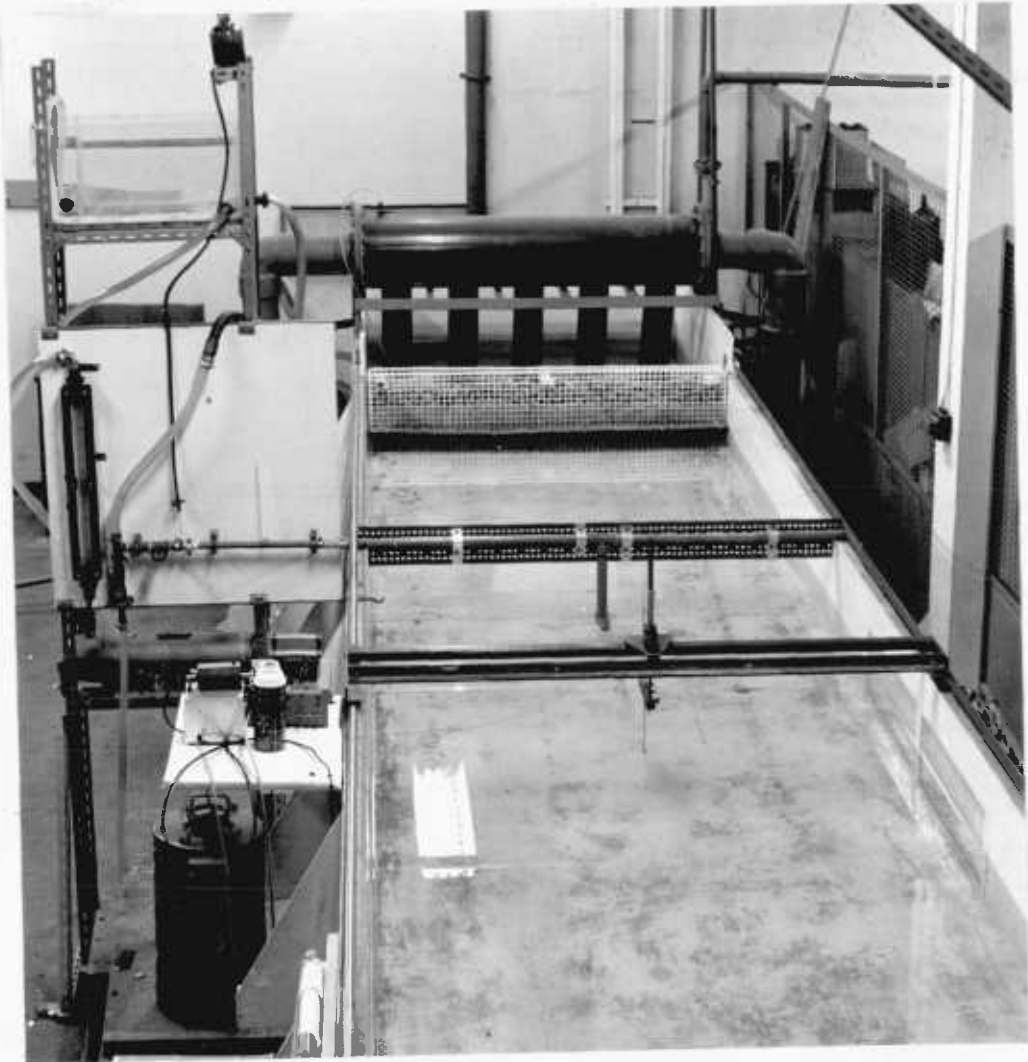
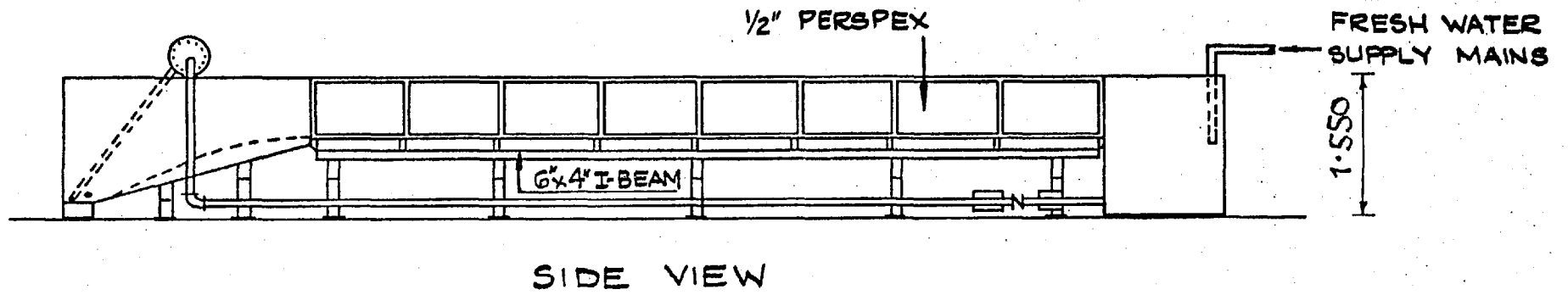
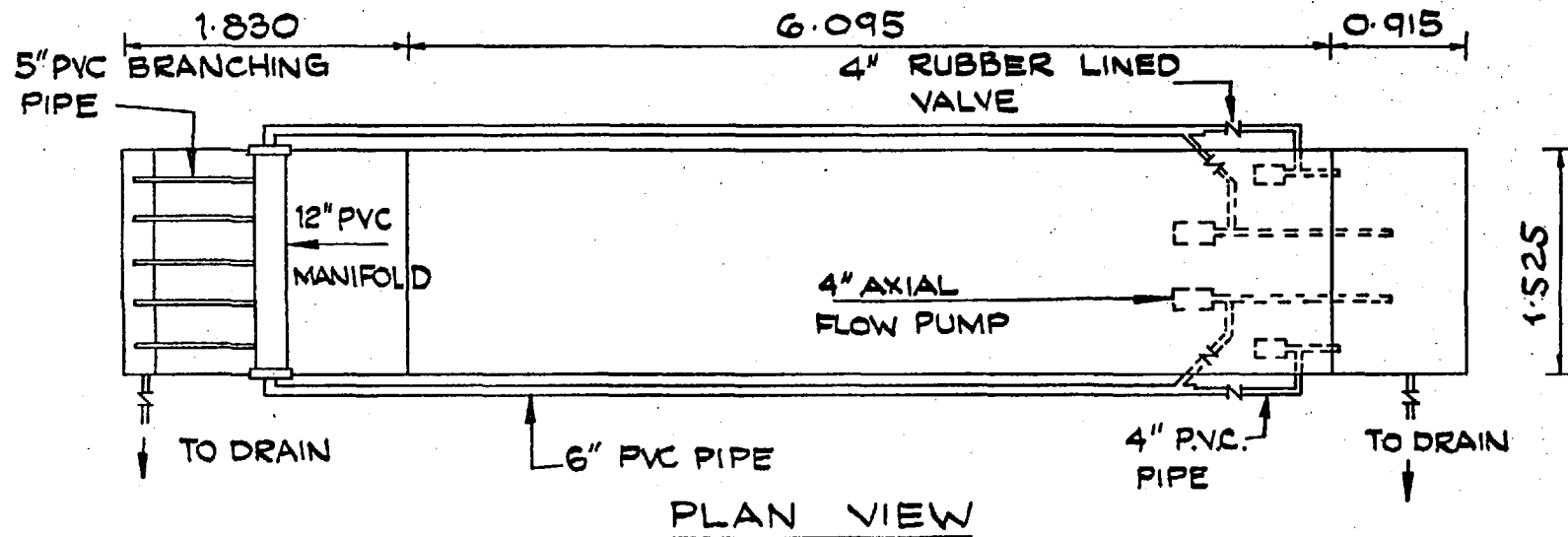


FIG. 5.2.1: OVERALL VIEW OF EXPERIMENTAL  
APPARATUS.



NOTE:  
MAIN TANK DIMENSIONS  
ARE IN METERS

FIG. 5.22: GENERAL LAYOUT OF EXPERIMENTAL RECIRCULATING FLUME.



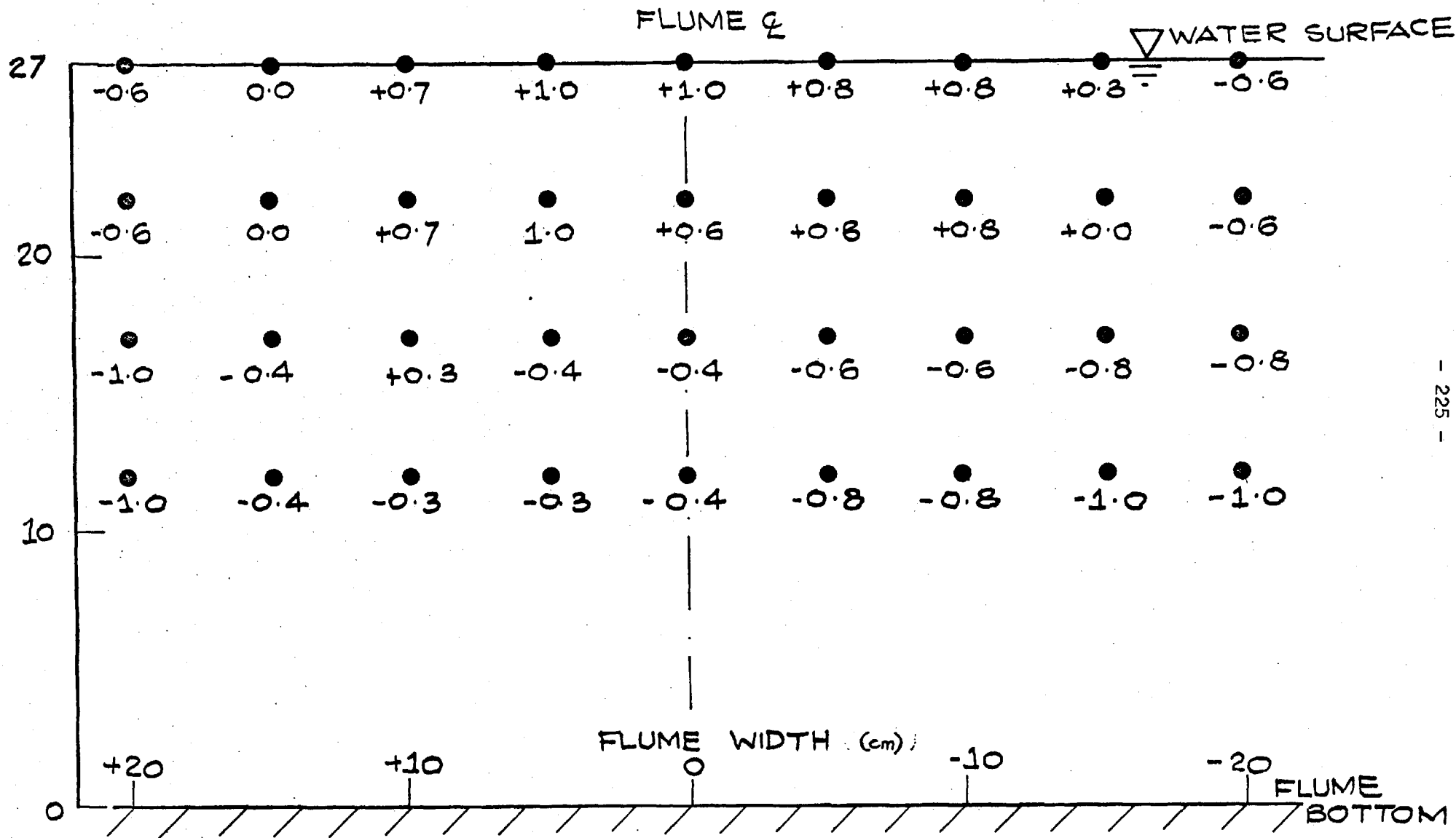
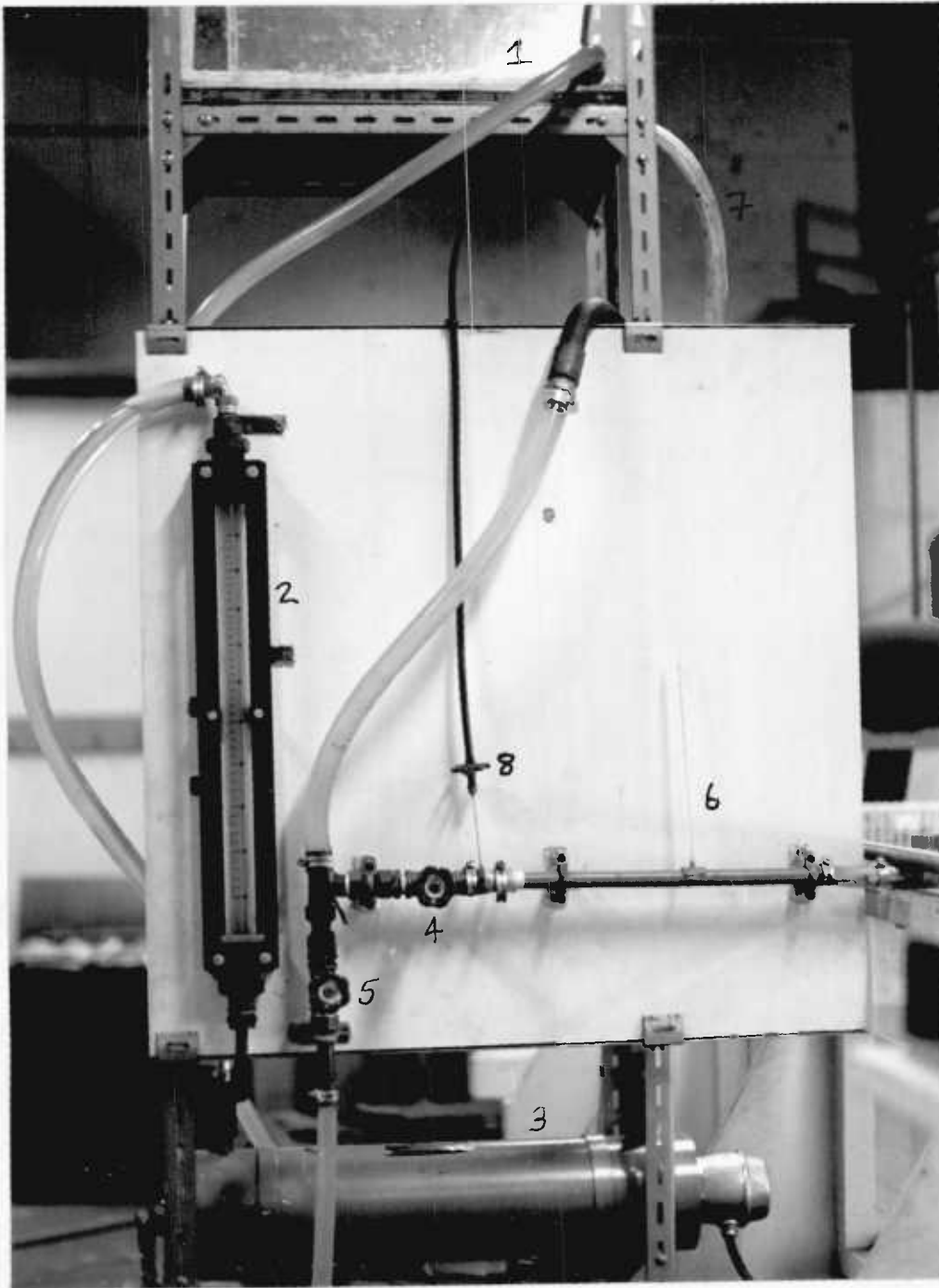


FIG. 5. 2. 3: VELOCITY DEVIATIONS FROM NOMINAL AVERAGE OF 10 cm/sec IN CHANNEL FLOW.



- |   |                       |
|---|-----------------------|
| 1- CONSTANT HEAD TANK                                       | 4- FLOW CONTROL VALVE |
| 2- ROTAMETER  | 5- DRAIN VALVE        |
| 3- WATER HEATER   | 6- THERMOMETER        |
| 7- CONSTANT HEAD TANK OVERFLOW.                             |                       |
| 8- HYPODERMIC USED TO INJECT DYE (Fed from overhead supply) |                       |

FIG. 5.2.4: JET FEED SYSTEM.

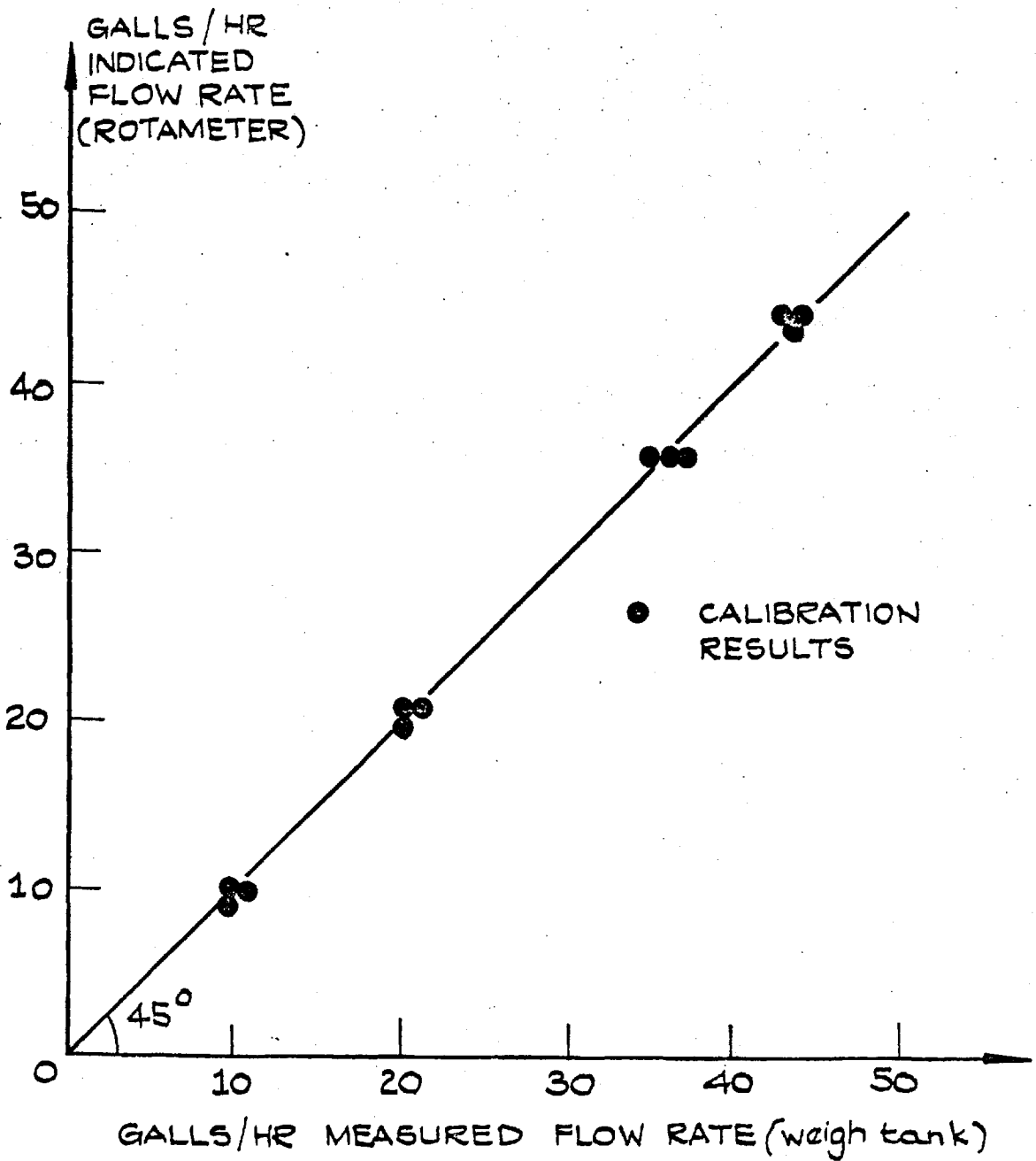


FIG. 5.2.5: CALIBRATION OF ROTAMETER.

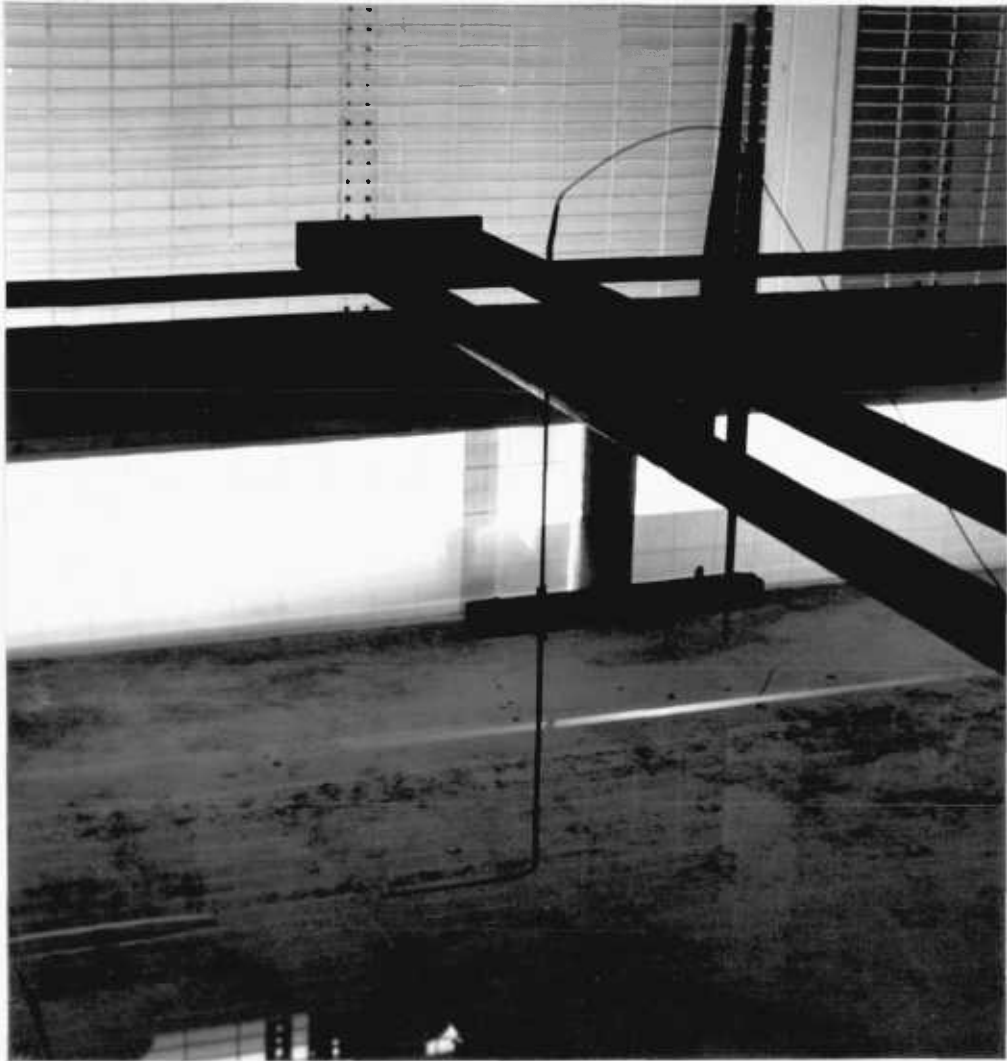


FIG. 5.2.6: JET NOZZLE, THERMOCOUPLE PROBE,  
AND TRAVERSING GEAR.



- 1- THERMOCOUPLE COLD JUNCTION
- 2- DVM FOR INSTANTANEOUS THERMOCOUPLE SIGNAL
- 3- AMPLIFIER AND POWER SUPPLY
- 4- DISA INTEGRATOR
- 5- DVM FOR INTEGRATED THERMOCOUPLE SIGNAL.

FIG. 5.2.7: INSTRUMENTATION.

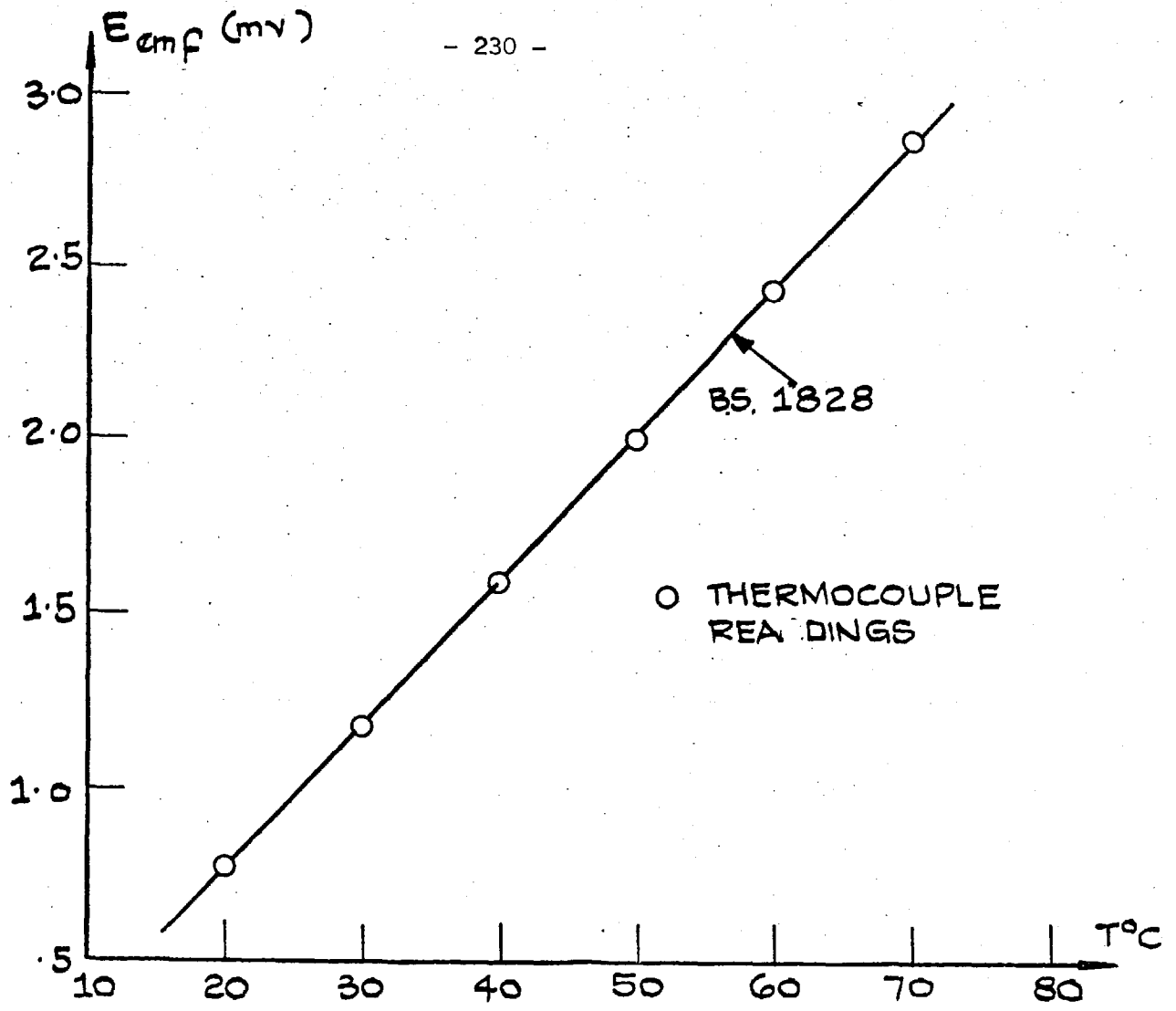


FIG. 5.2.8: THERMOCOUPLE CALIBRATION CHECK.

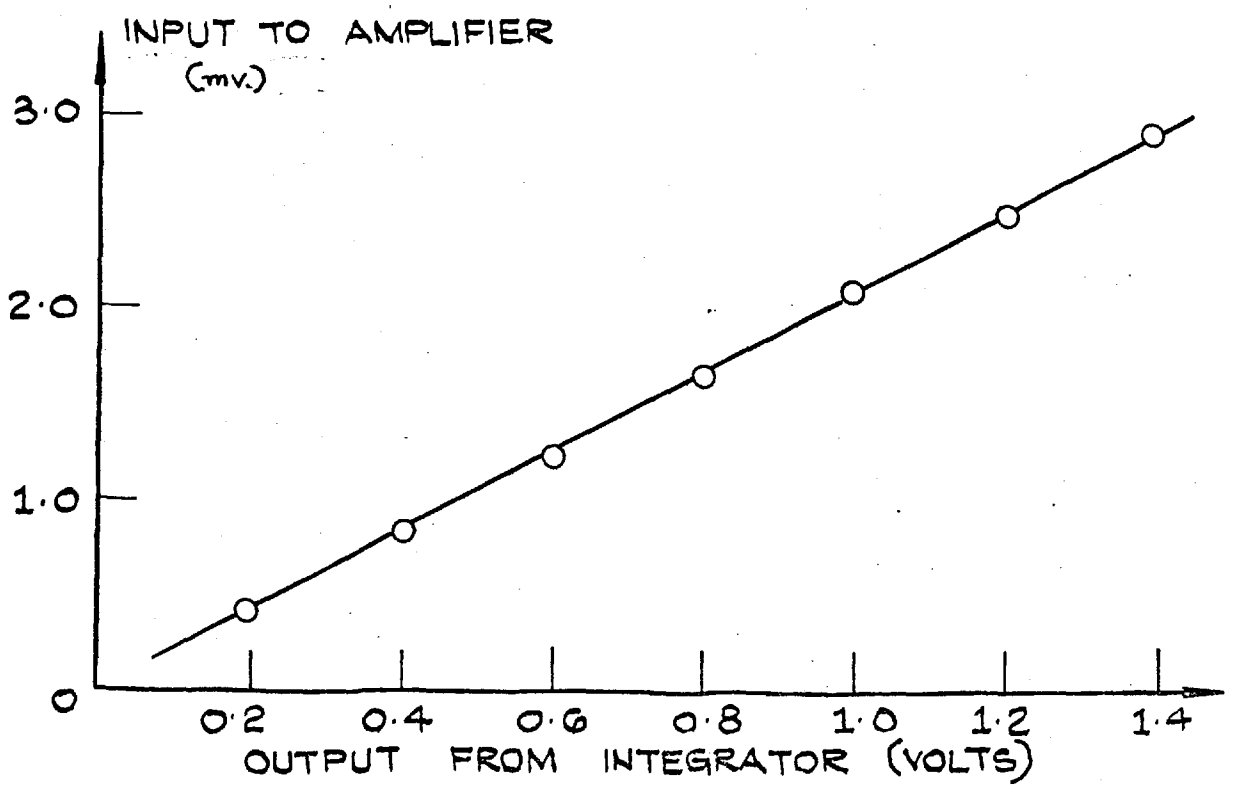


FIG. 5.2.9: AMPLIFIER / INTEGRATOR CIRCUIT CALIBRATION.

HORIZONTAL TRAVERSE AT  $\frac{y}{d_J} = 0.0$   $Fr = 15$   
 $\frac{x}{d_J} = 5.0$   $K = 2$

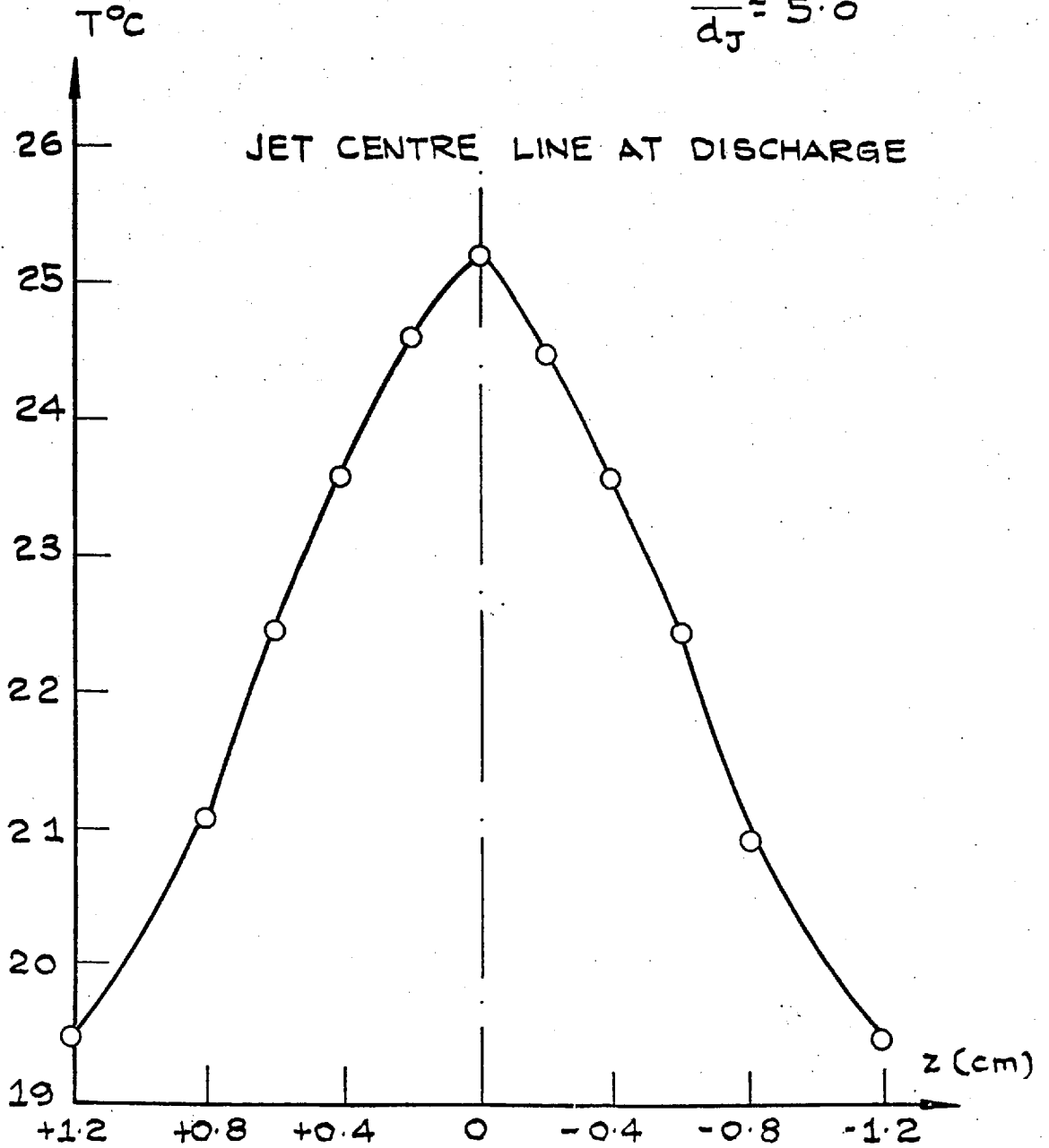


FIG. 5.3.1: HORIZONTAL SYMMETRY OF JET.

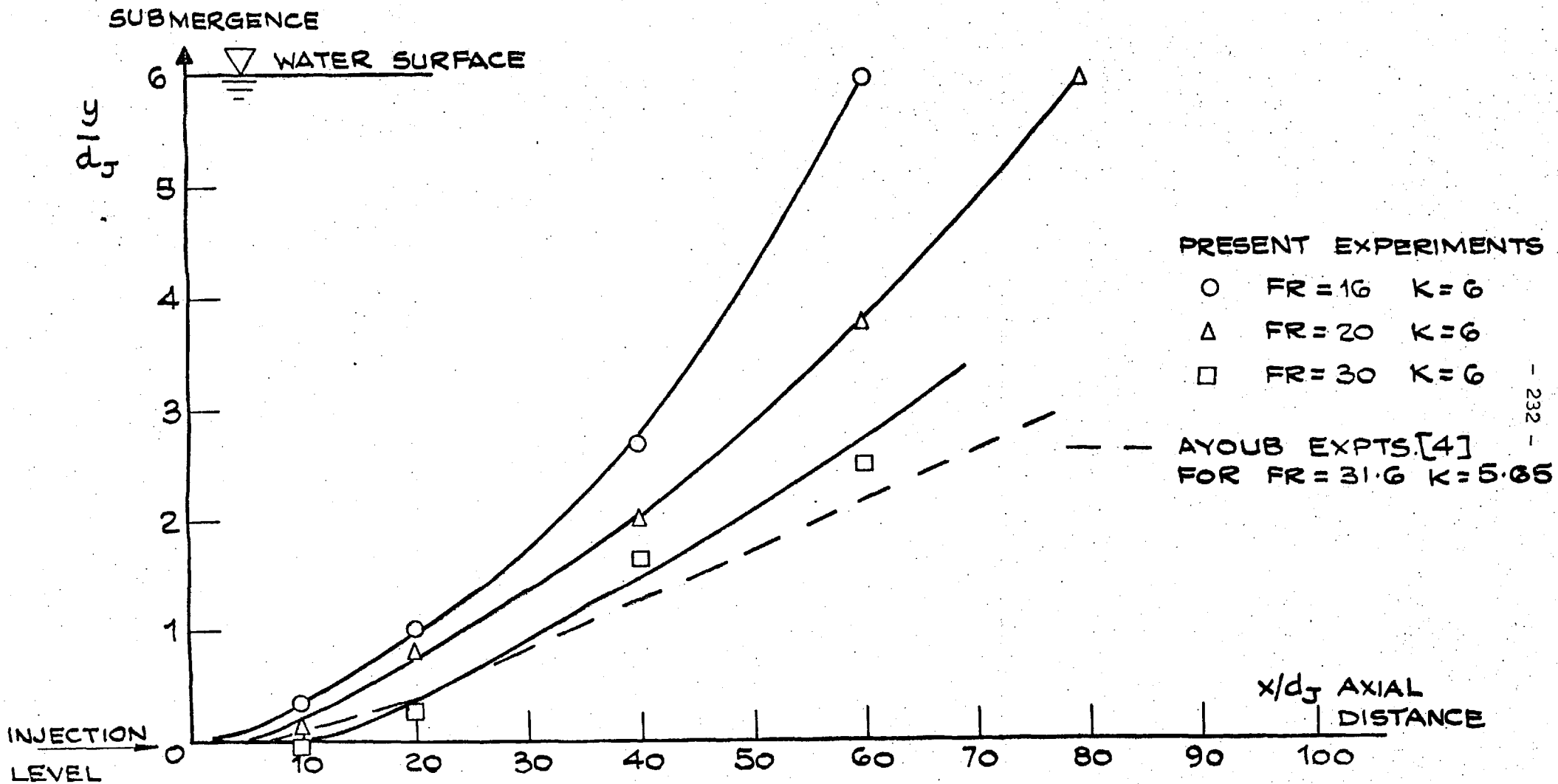


FIG. 5.3.2: EXPERIMENTAL RESULTS, PLUME TRAJECTORIES AT DIFFERENT FROUDE NUMBERS.



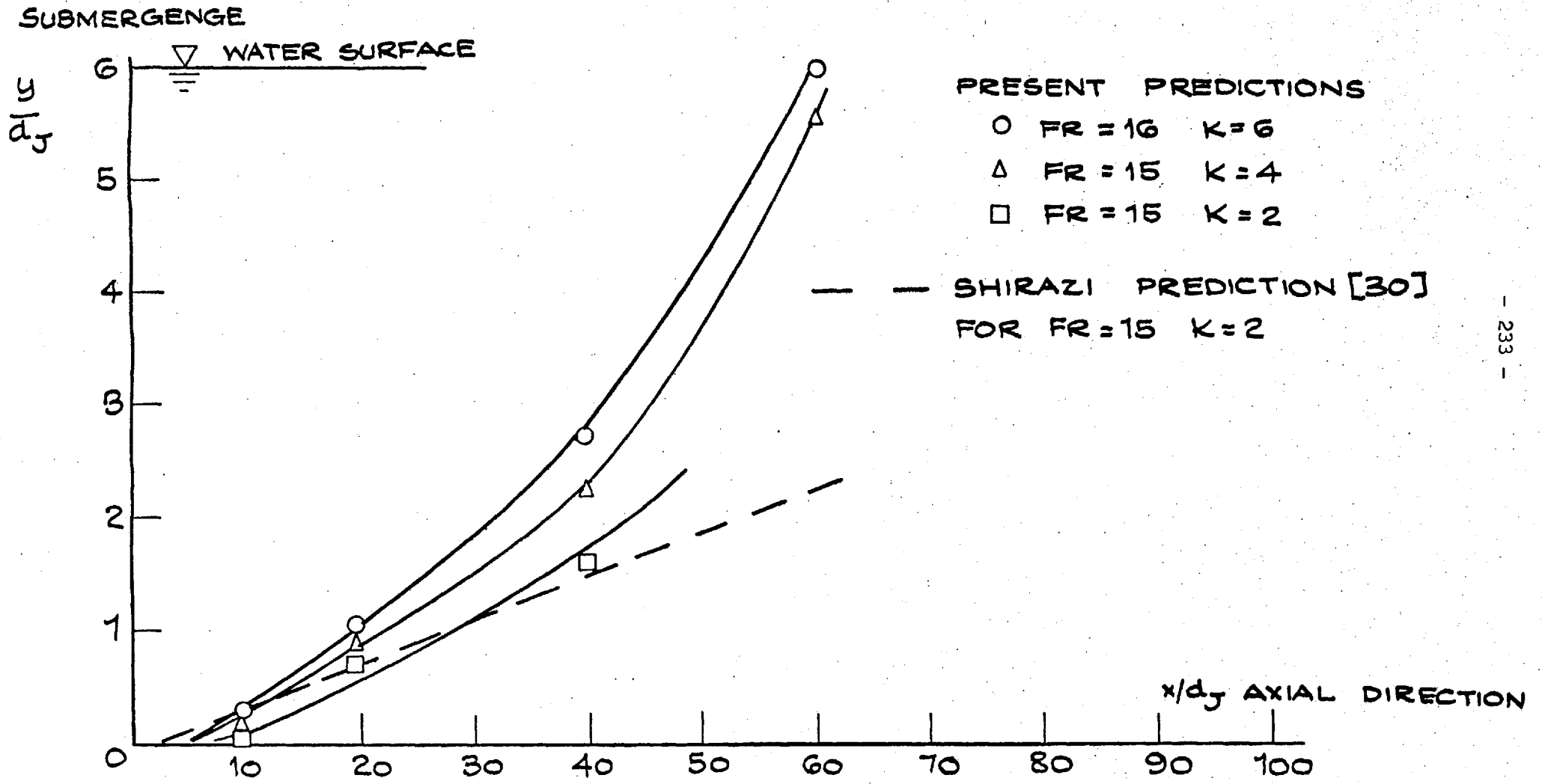


FIG. 5.3.3: EXPERIMENTAL RESULTS, PLUME TRAJECTORIES AT DIFFERENT VELOCITY RATIOS.

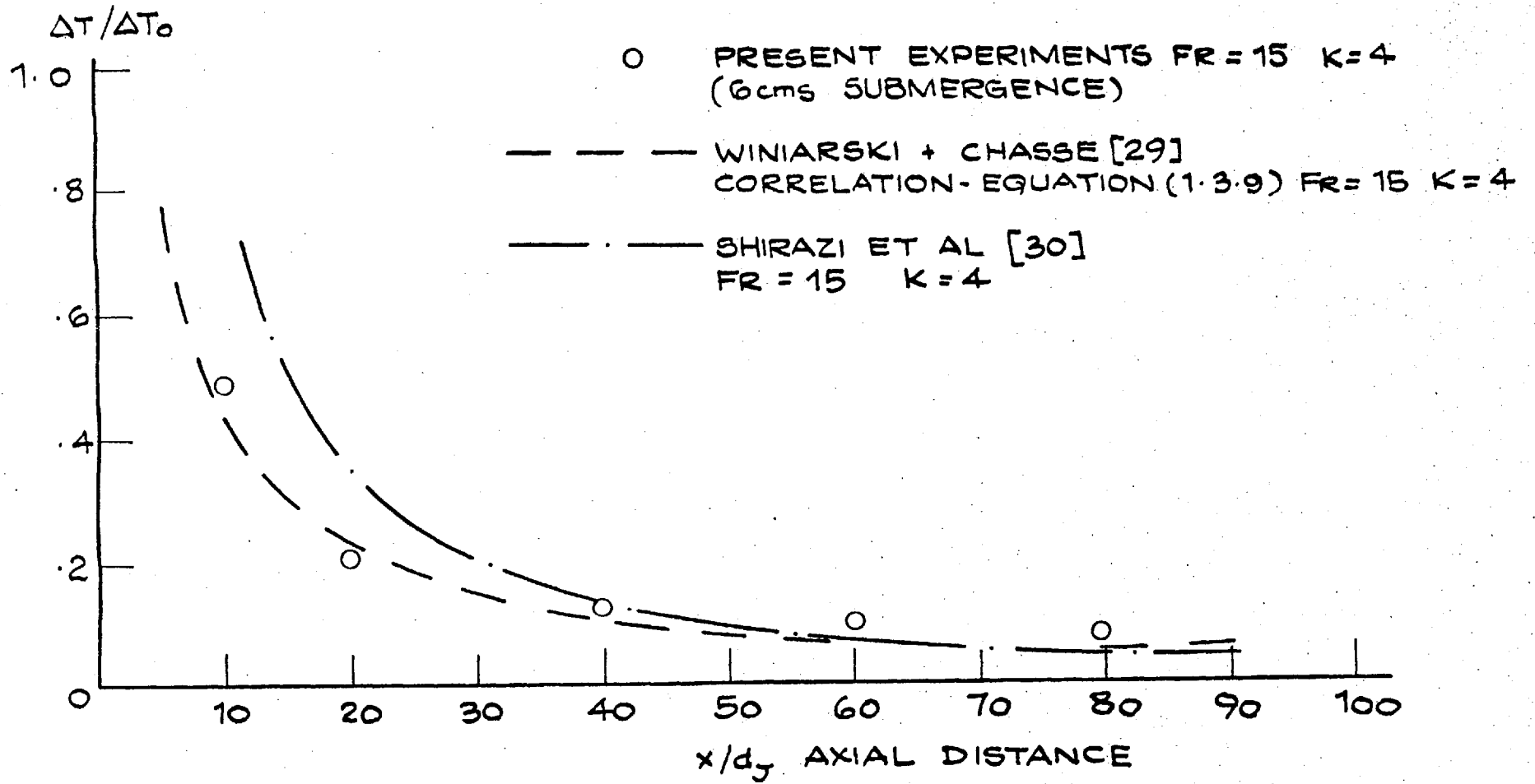
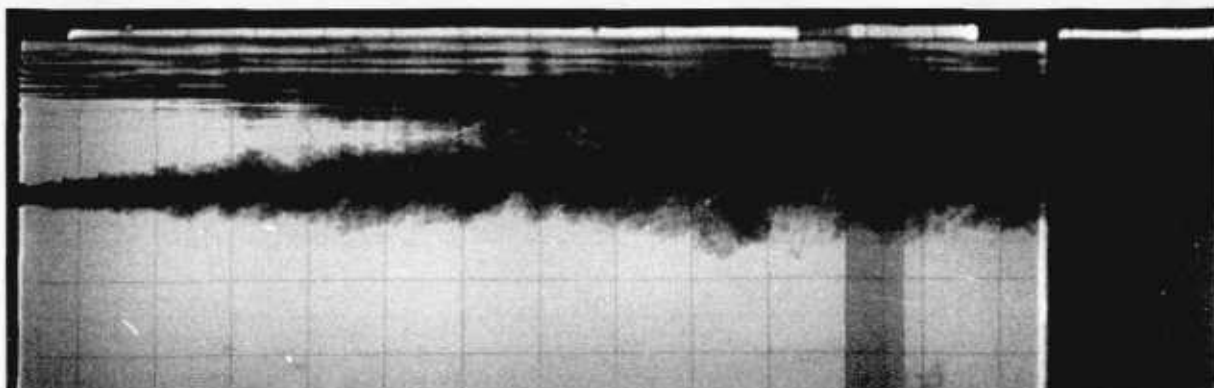
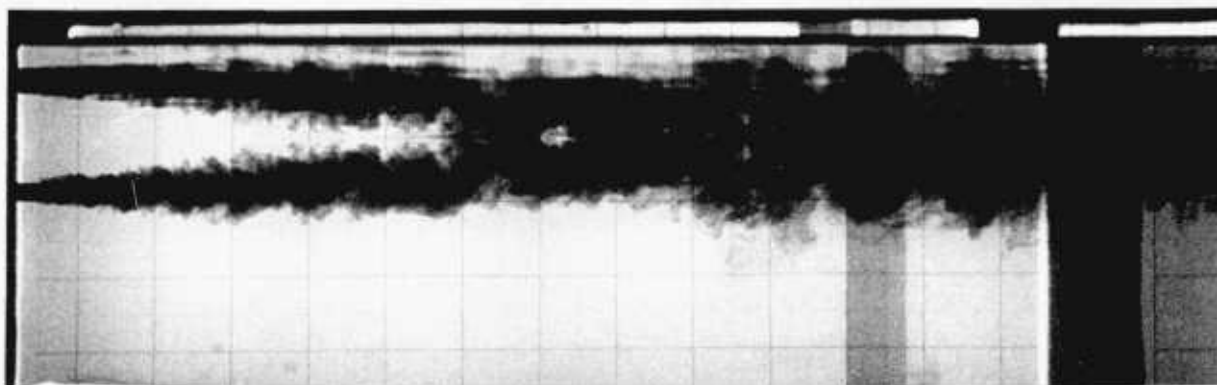


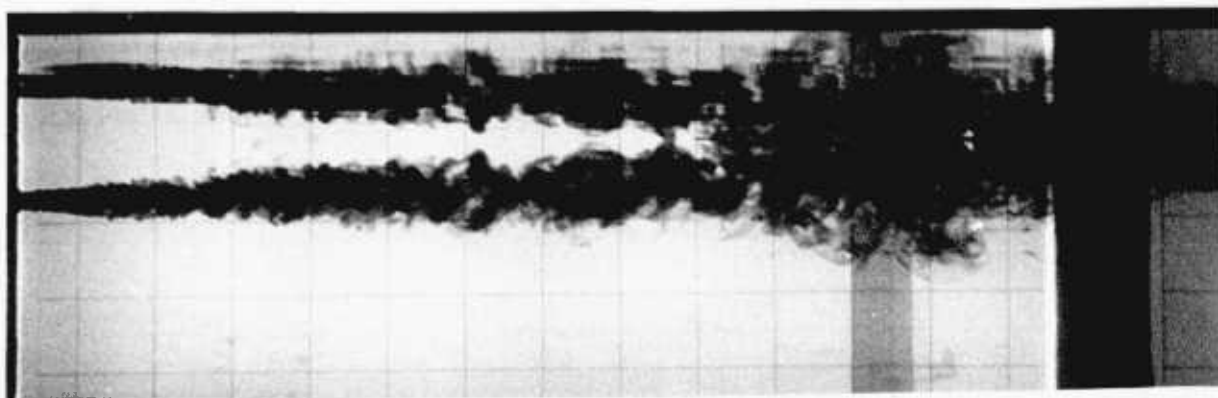
FIG. 5.3.4: PLUME DILUTION CURVES.



FR=16      K=6

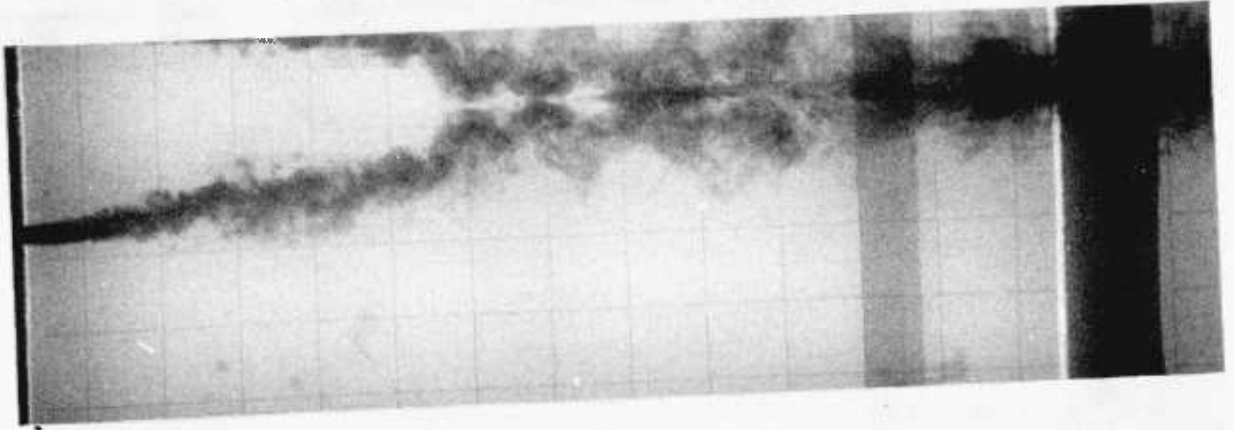


FR=15      K=4

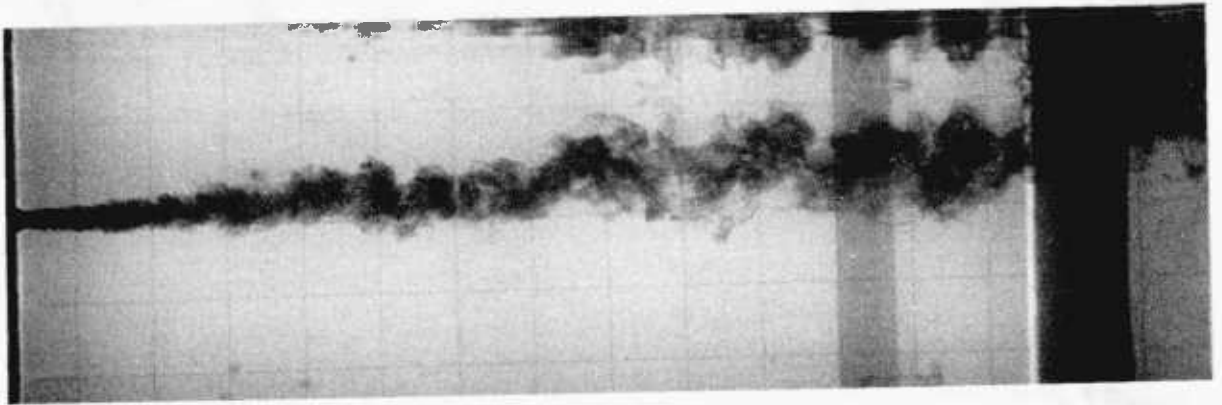


FR=15      K=2

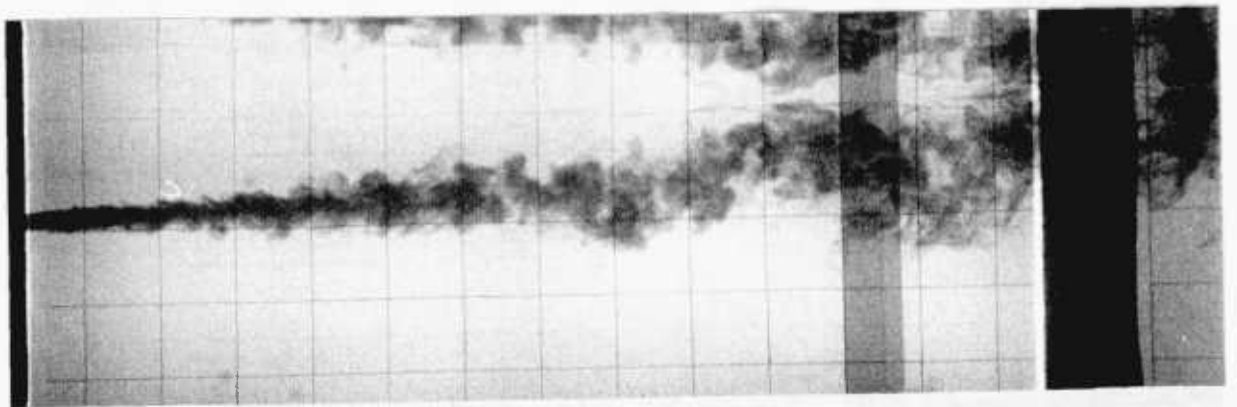
FIG. 5.3.5: PLUME PHOTOGRAPHS.



FR = 5      K = 2



FR = 10      K = 2



FR = 15      K = 2

FIG. 5.3.6: PLUME PHOTOGRAPHS.

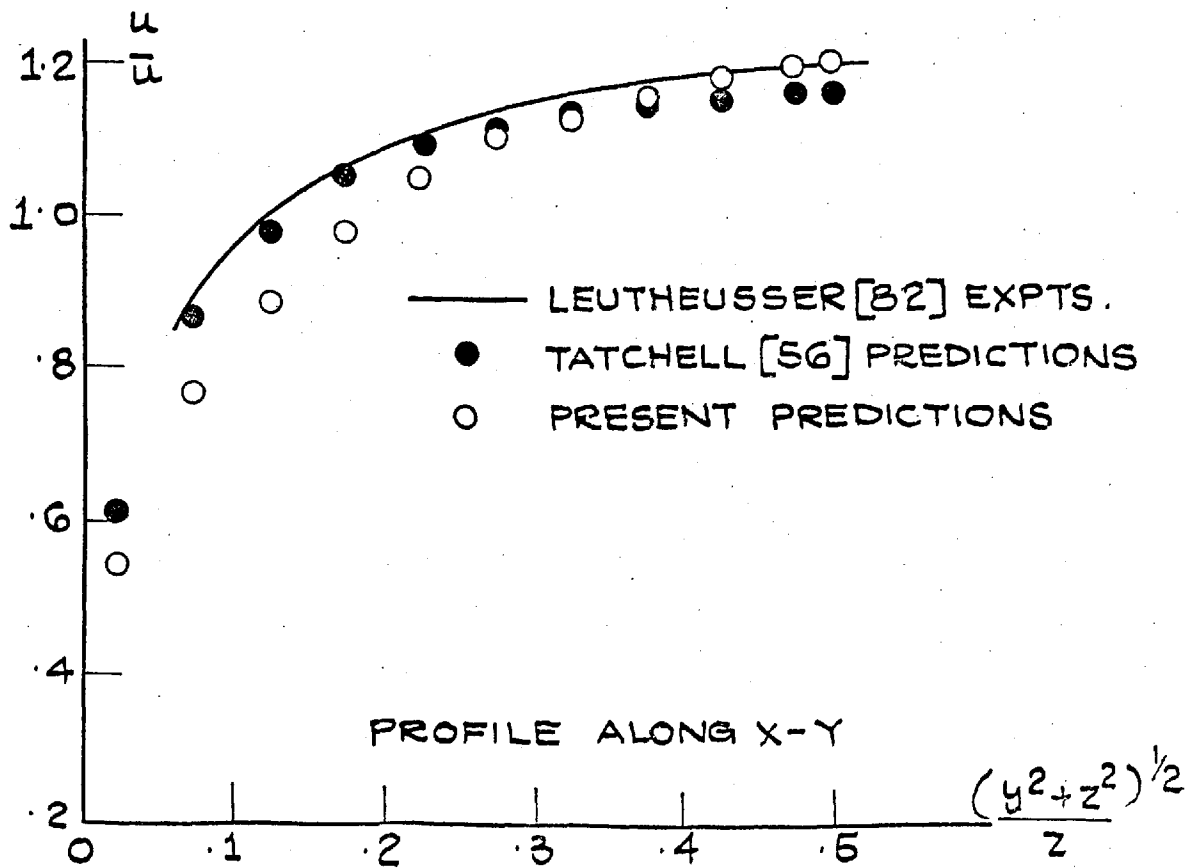
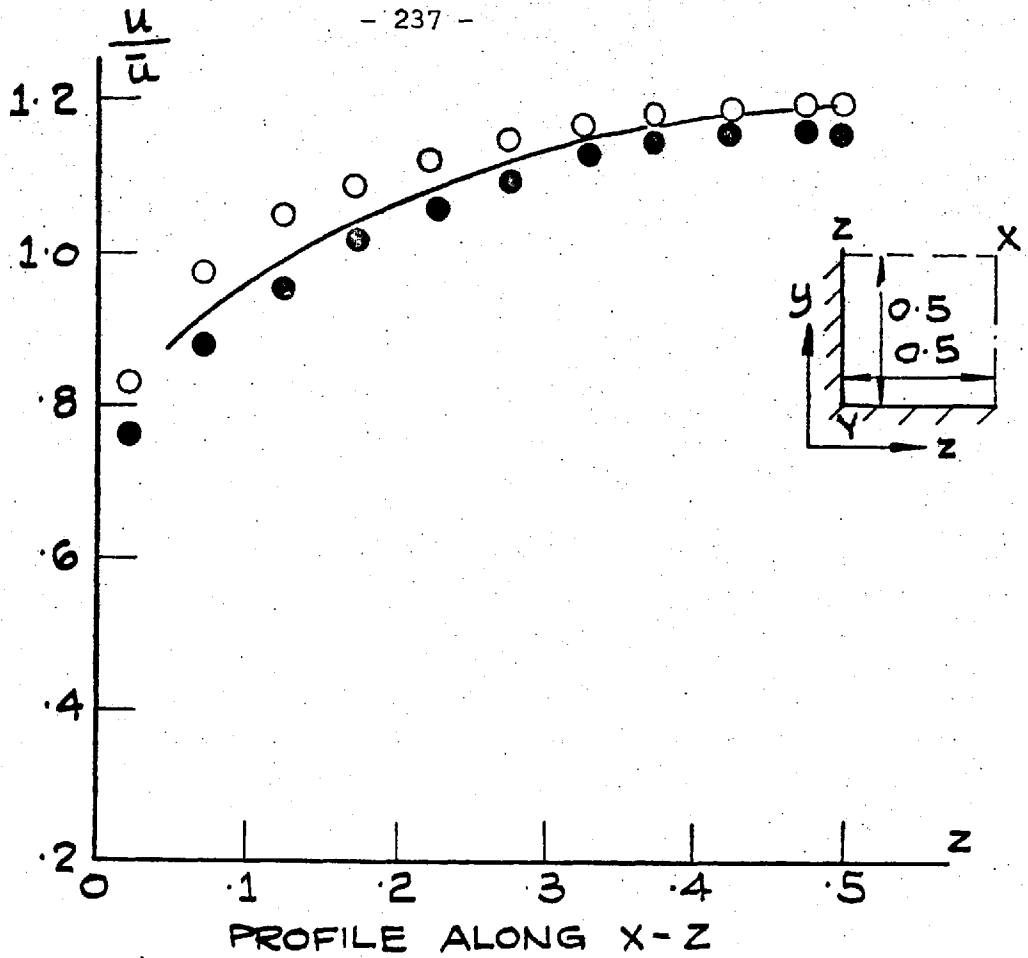


FIG. 6.2.1: MEAN FLOW TURBULENT VELOCITY PROFILES IN A SQUARE DUCT FULLY DEVELOPED FLOW.

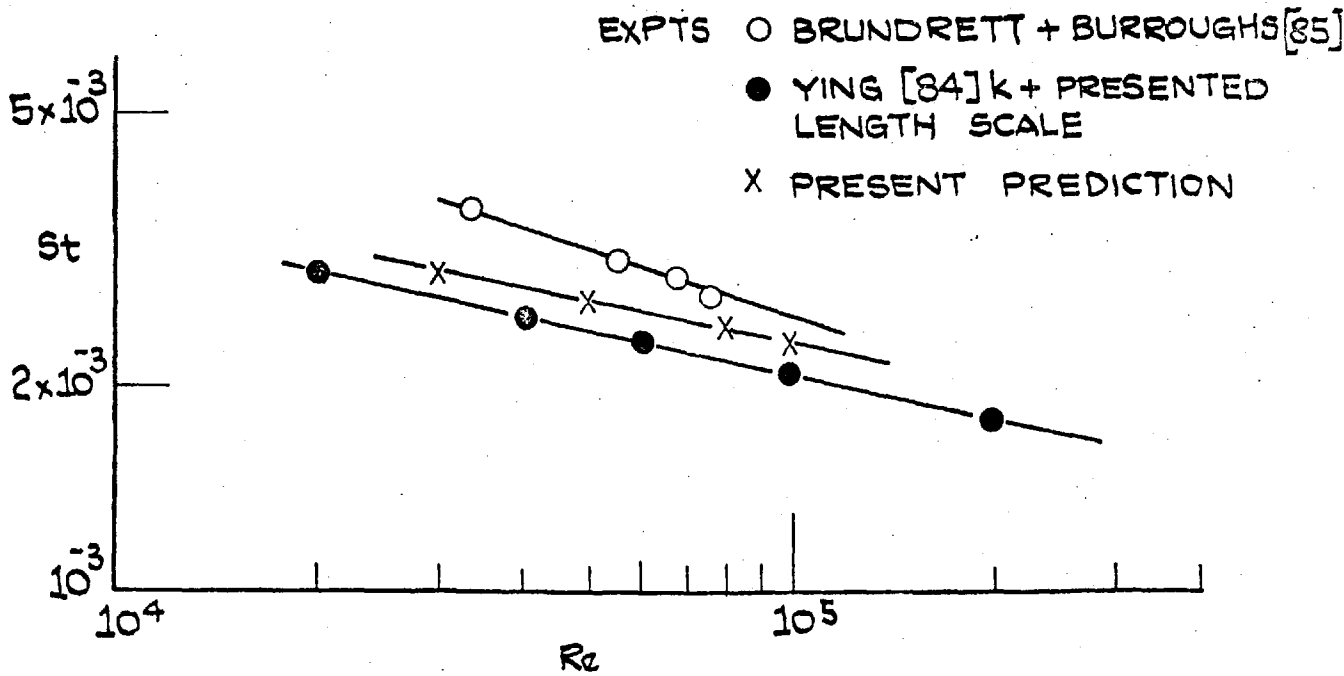
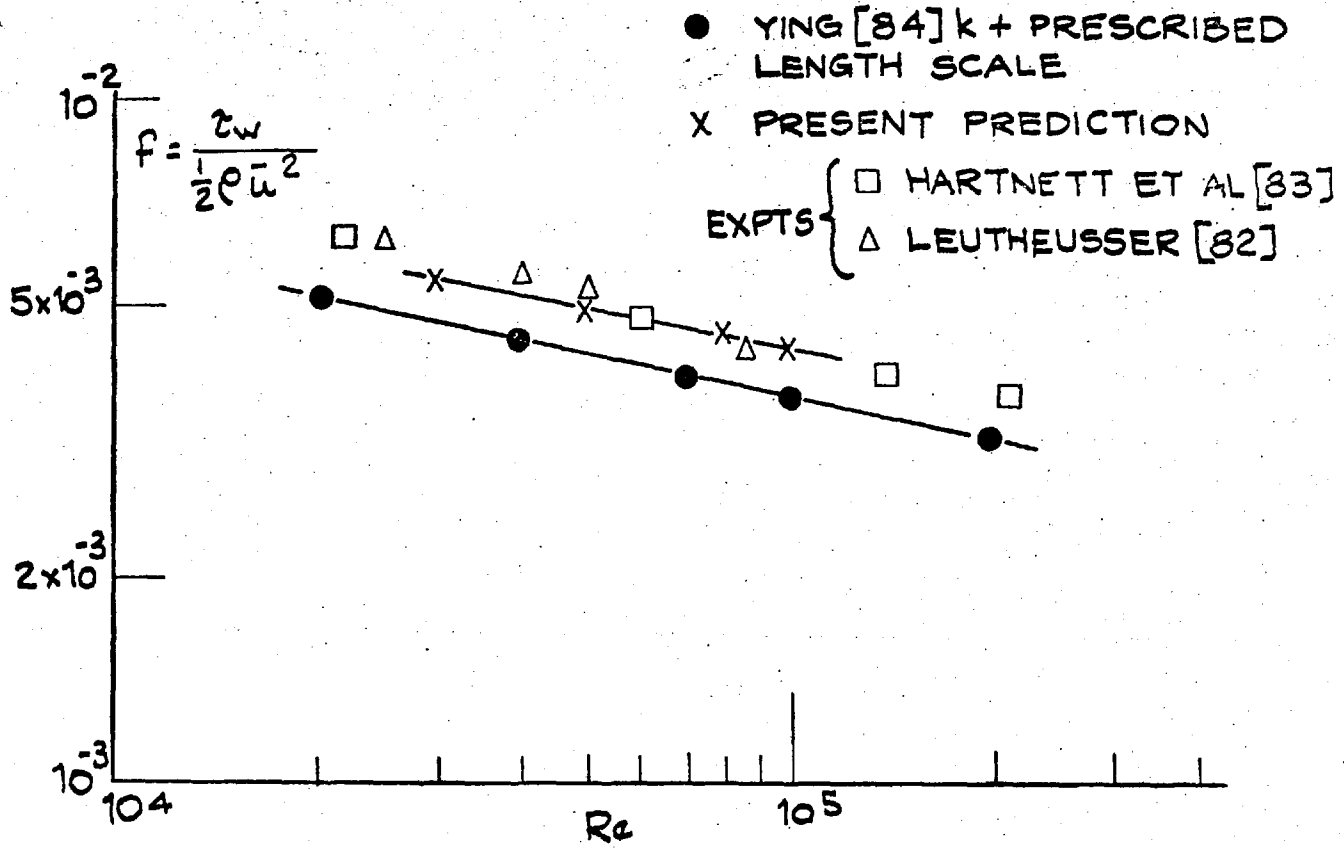


FIG. 6.2.2: FRICTION FACTOR AND STANTON NUMBER RELATIONSHIPS, FULLY-DEVELOPED FLOW IN SQUARE DUCTS.

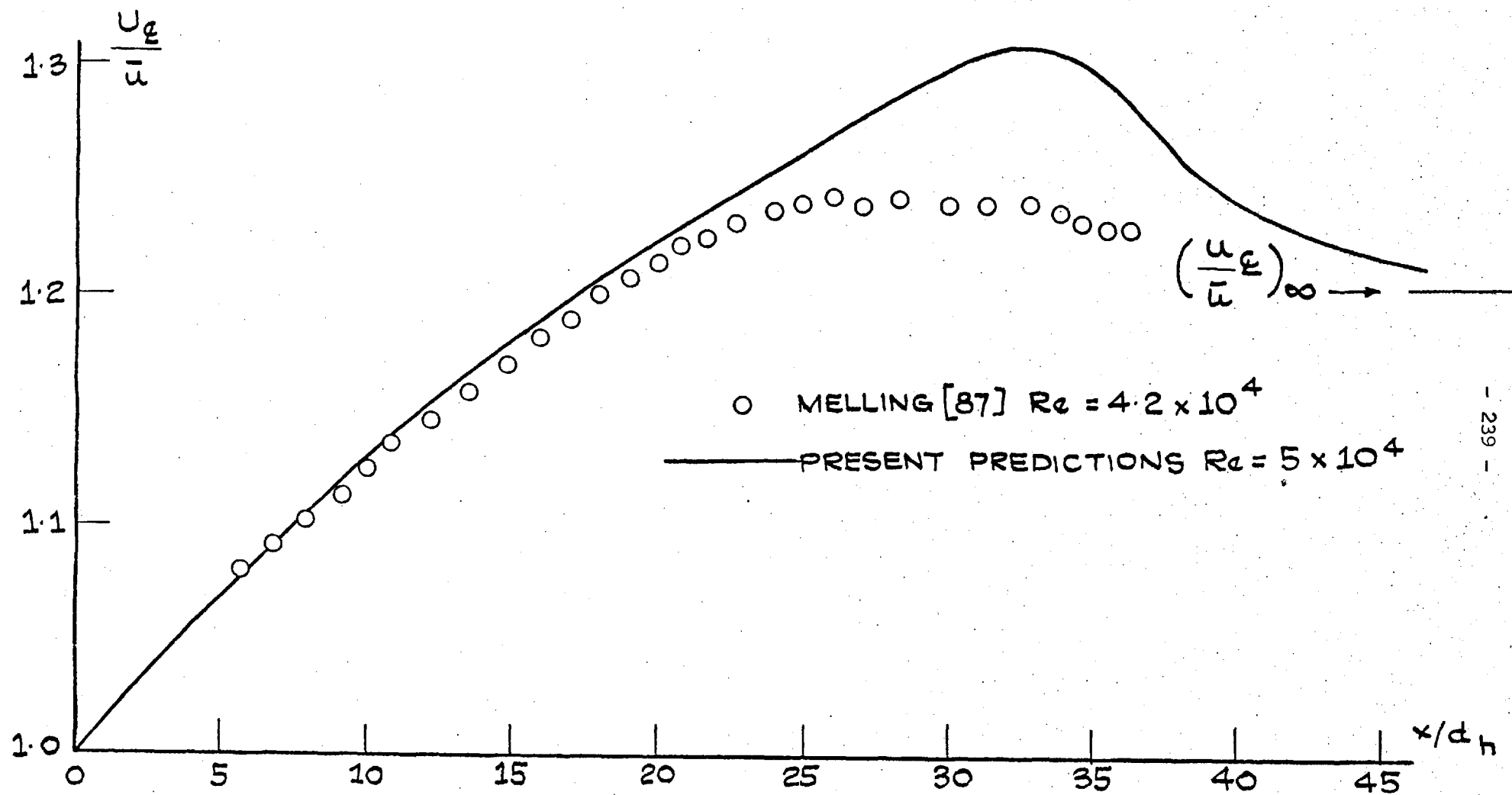


FIG.6.2.3: DEVELOPMENT OF VELOCITY ON AXIS - TURBULENT SQUARE DUCT FLOW.

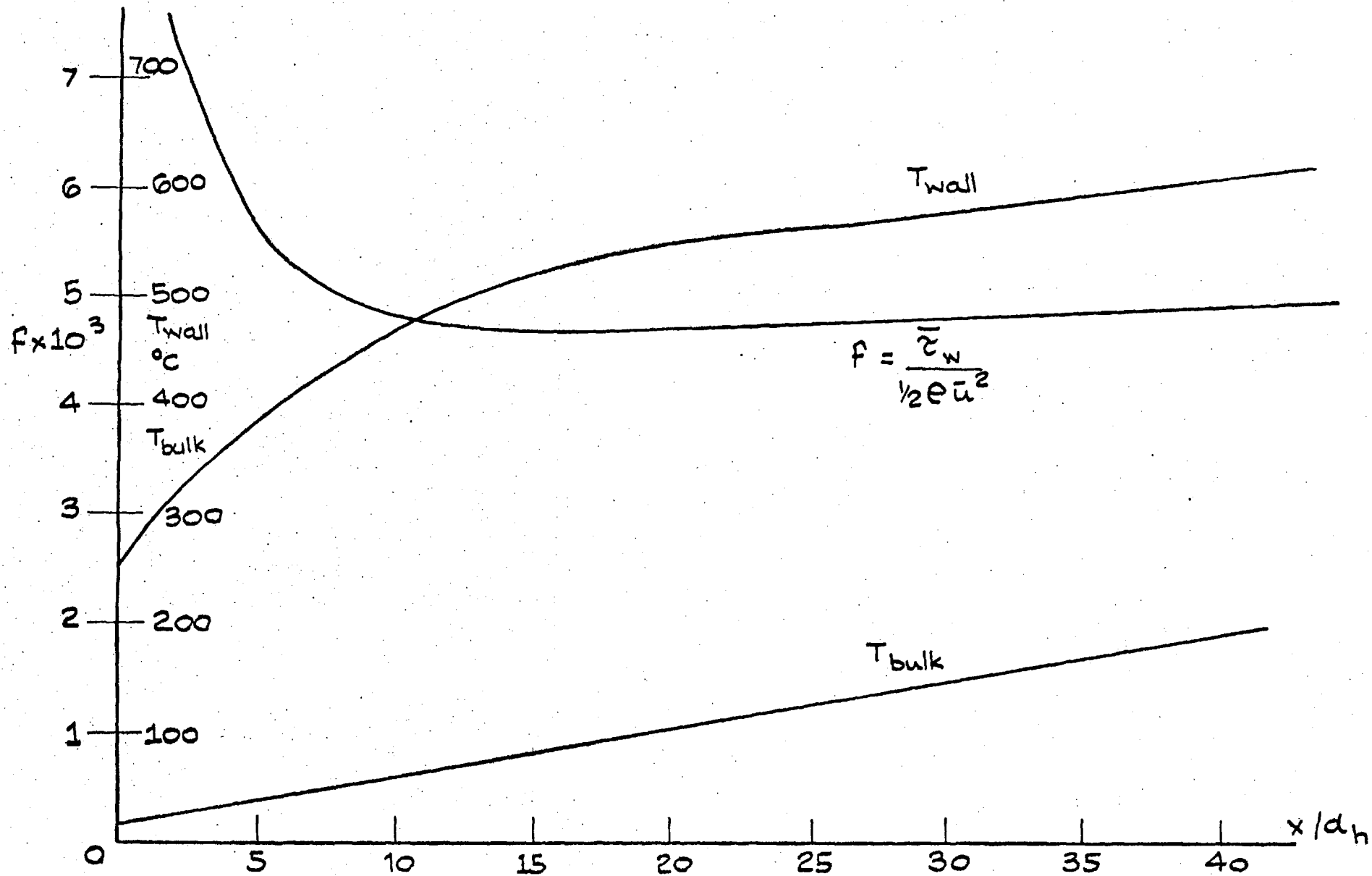


FIG. 6.2.4: DEVELOPING FLOW AND HEAT TRANSFER, TURBULENT SQUARE DUCT FLOW.



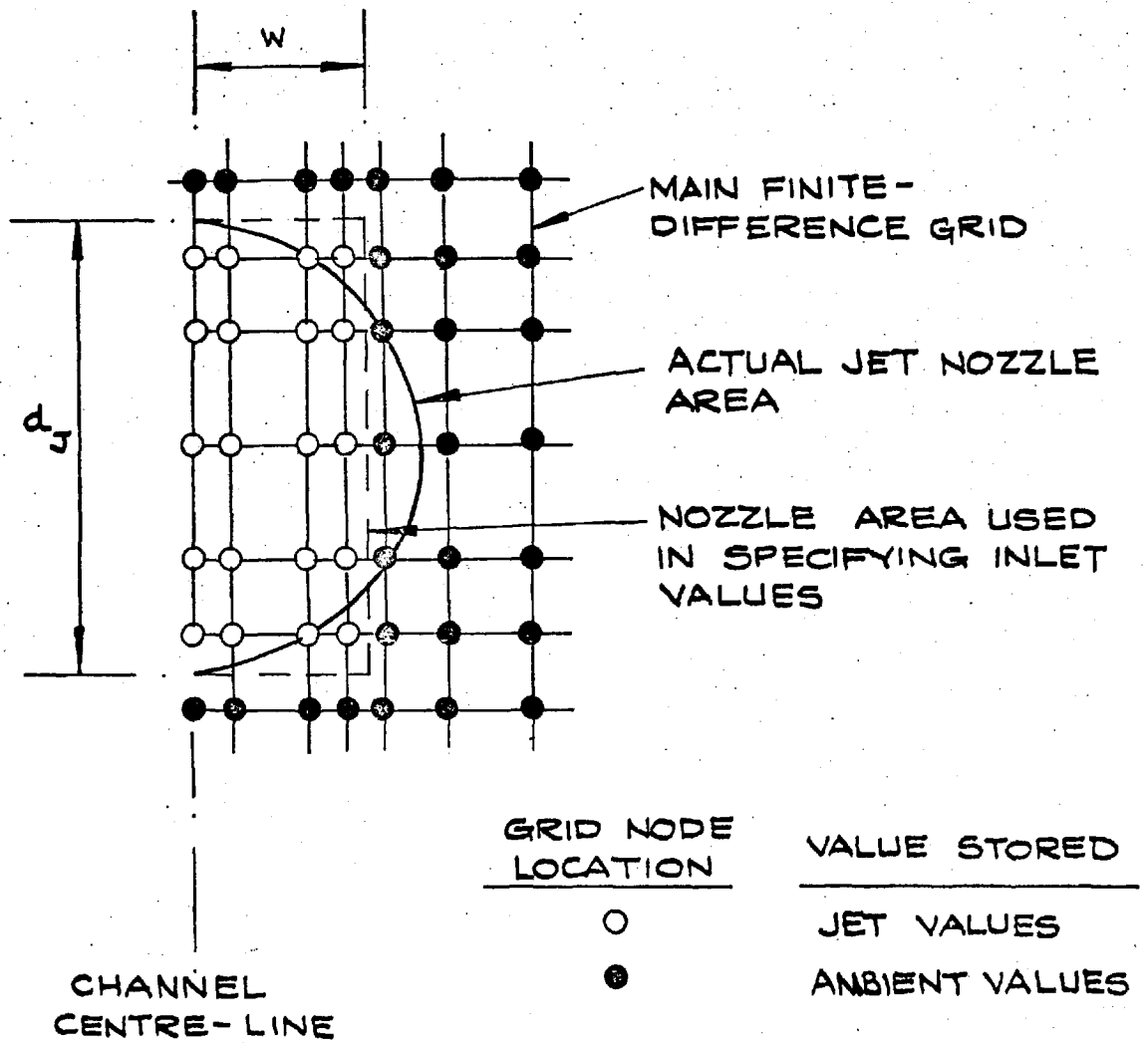


FIG. G.3.1: CLOSE - UP OF JET DISCHARGE AREA.

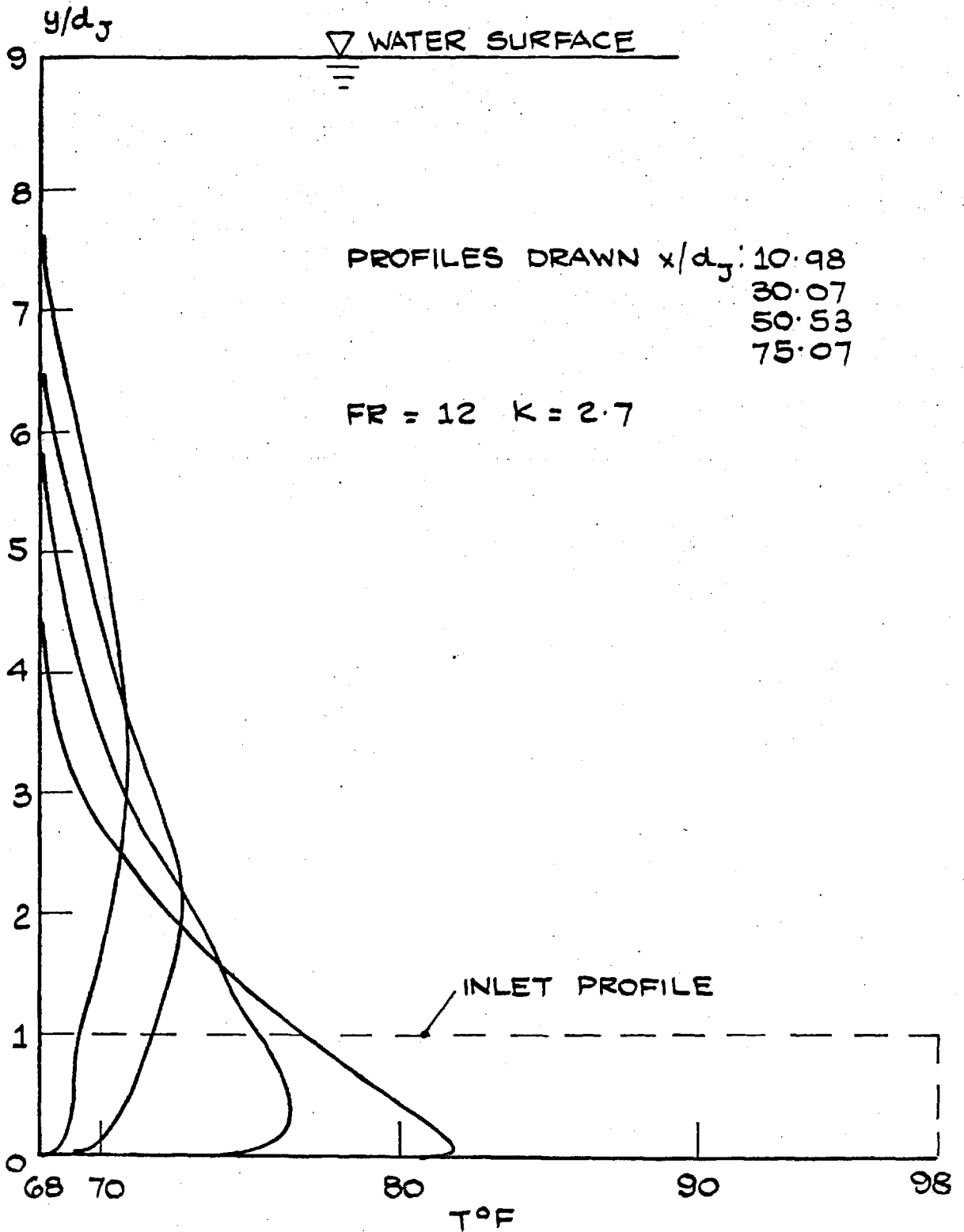


FIG. 6.3.2: VERTICAL TEMPERATURE PROFILES -  
CHANNEL CENTRE-LINE  
WINIARSKI + CHASSE EXPTS.

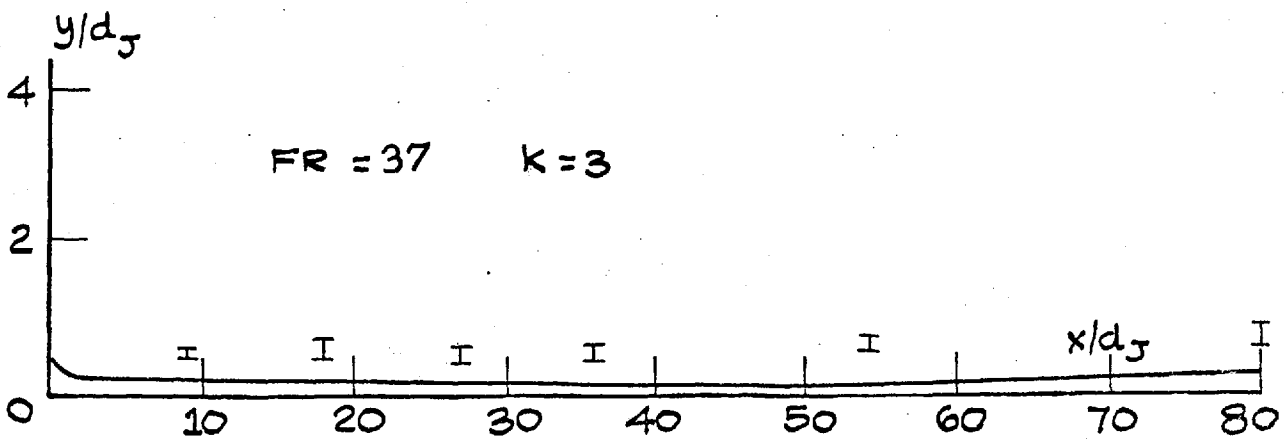
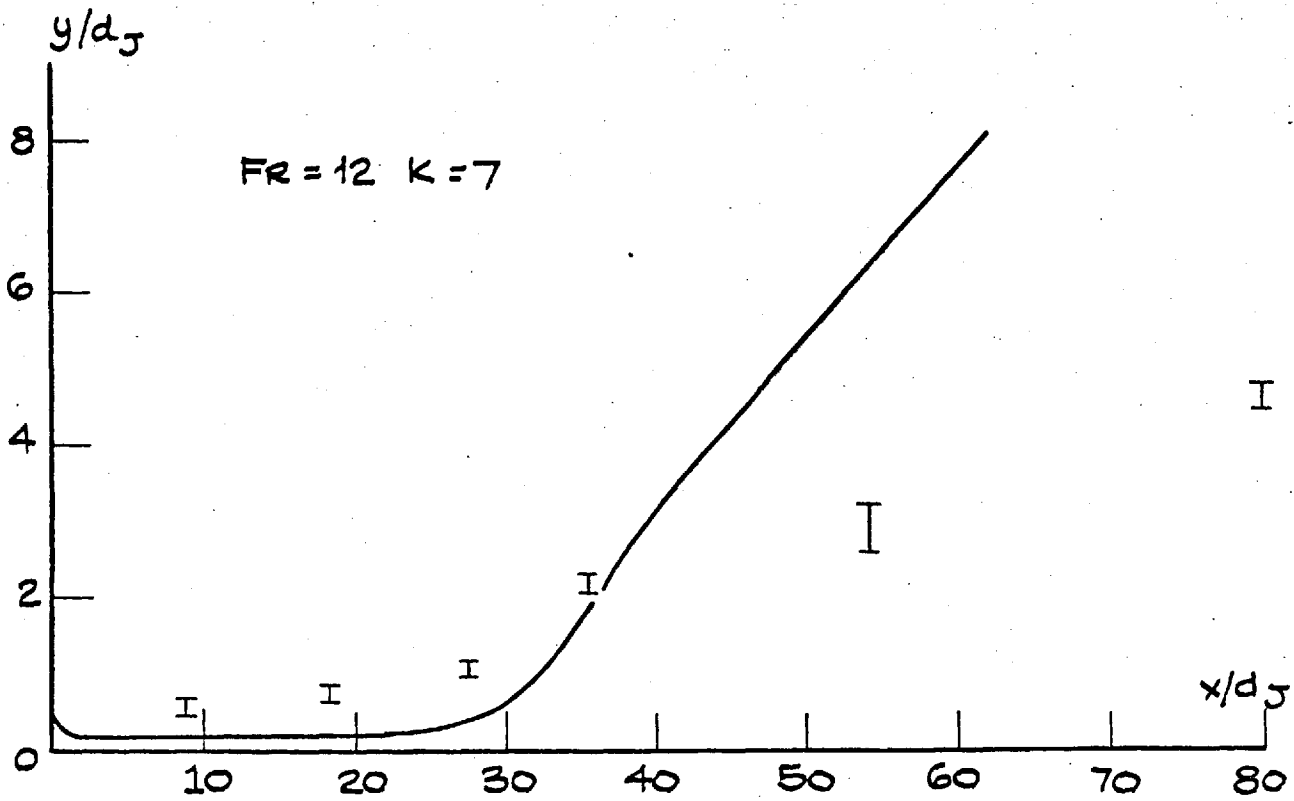
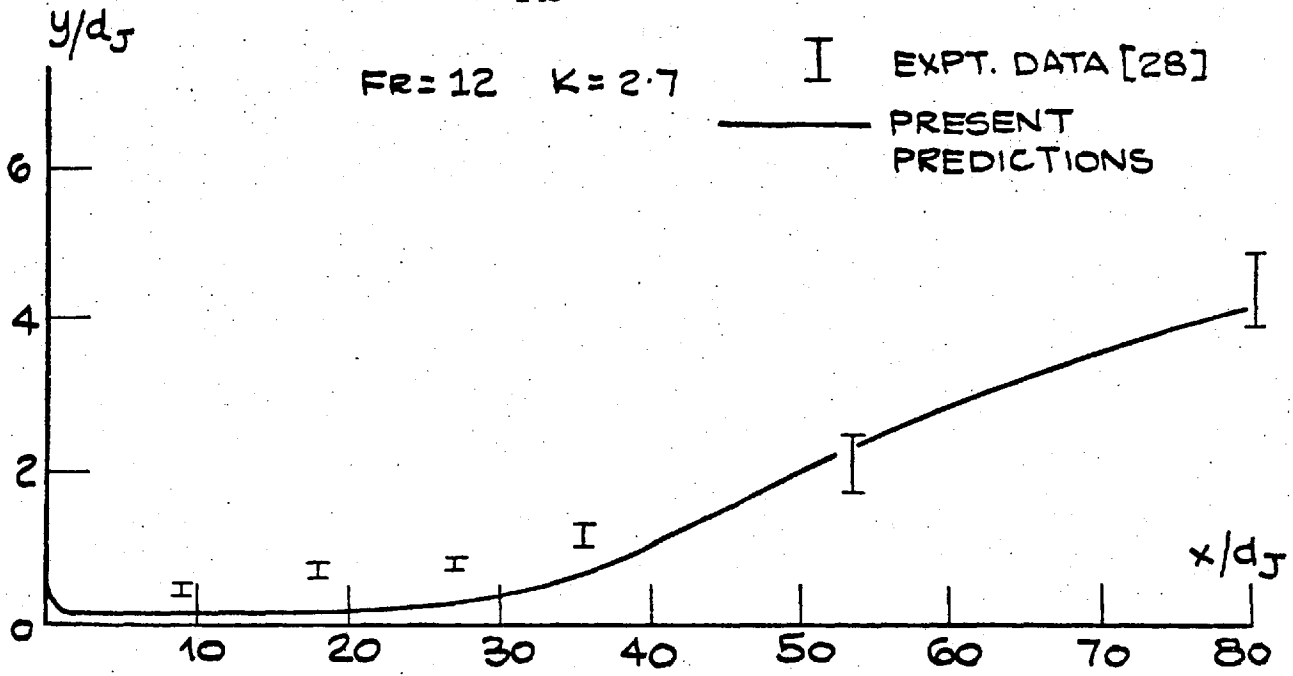


FIG. 6.3.3: PLUME TRAJECTORIES - WINIARSKI + CHASSE EXPTS.

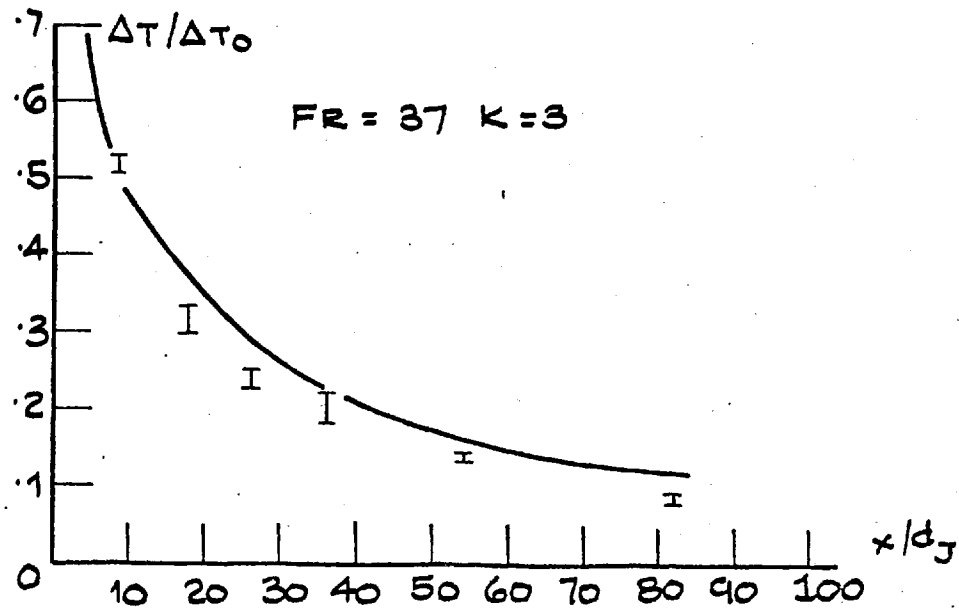
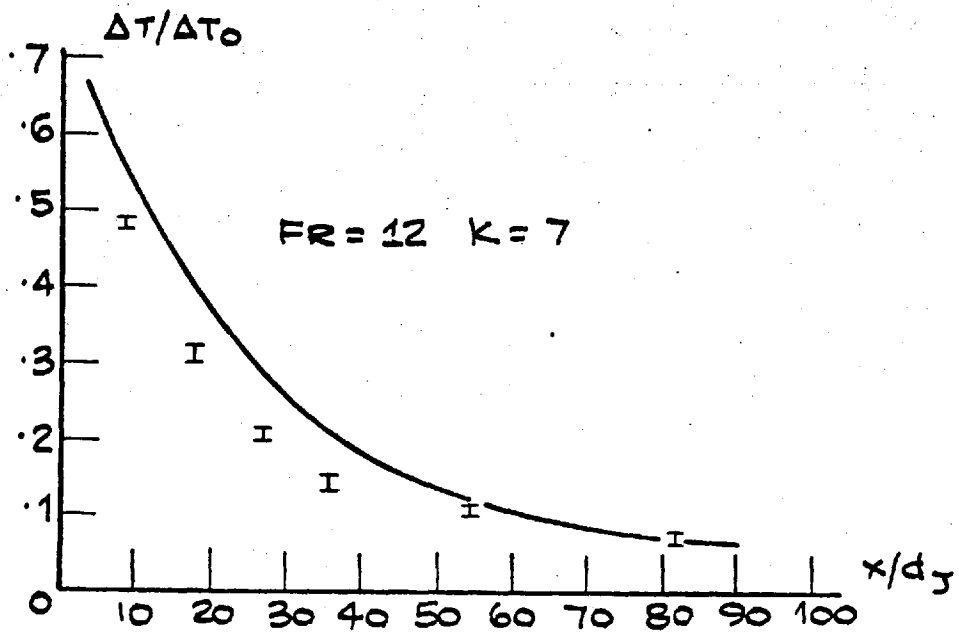
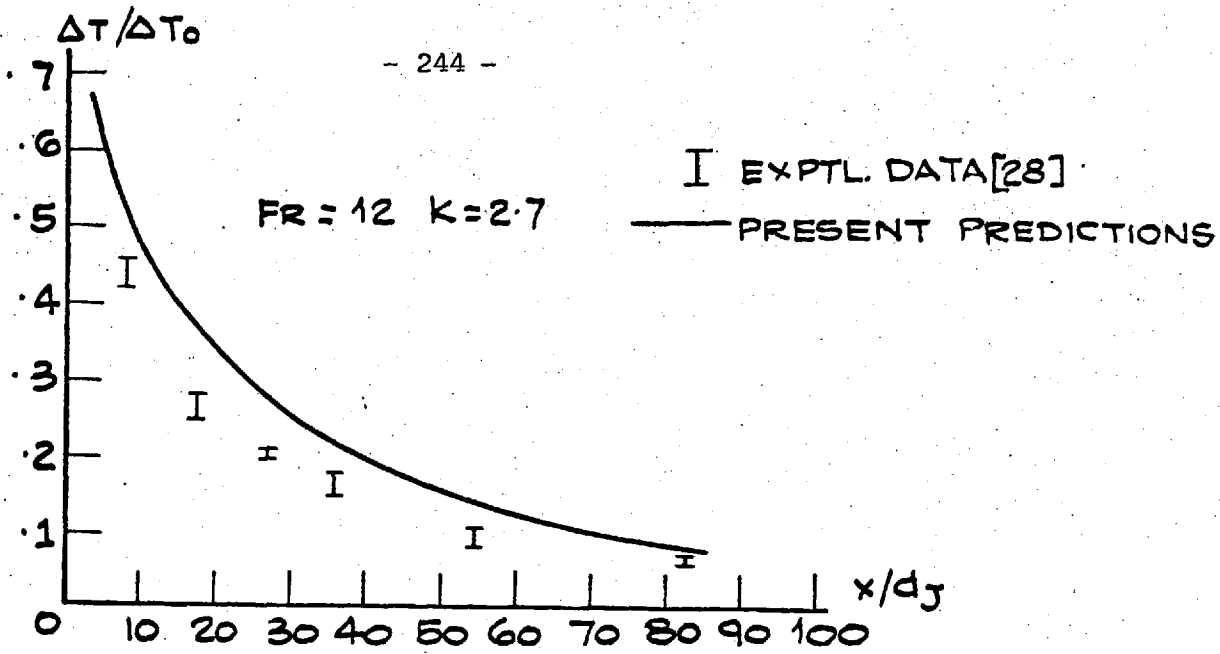


FIG. G.3.4: PLUME DILUTION CURVES -  
WINIARSKI + CHASSE EXPTS.

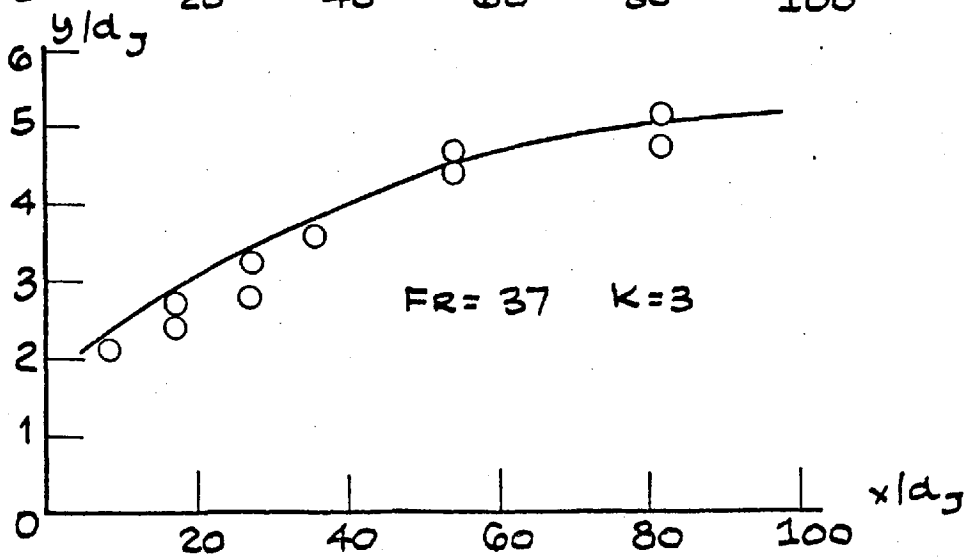
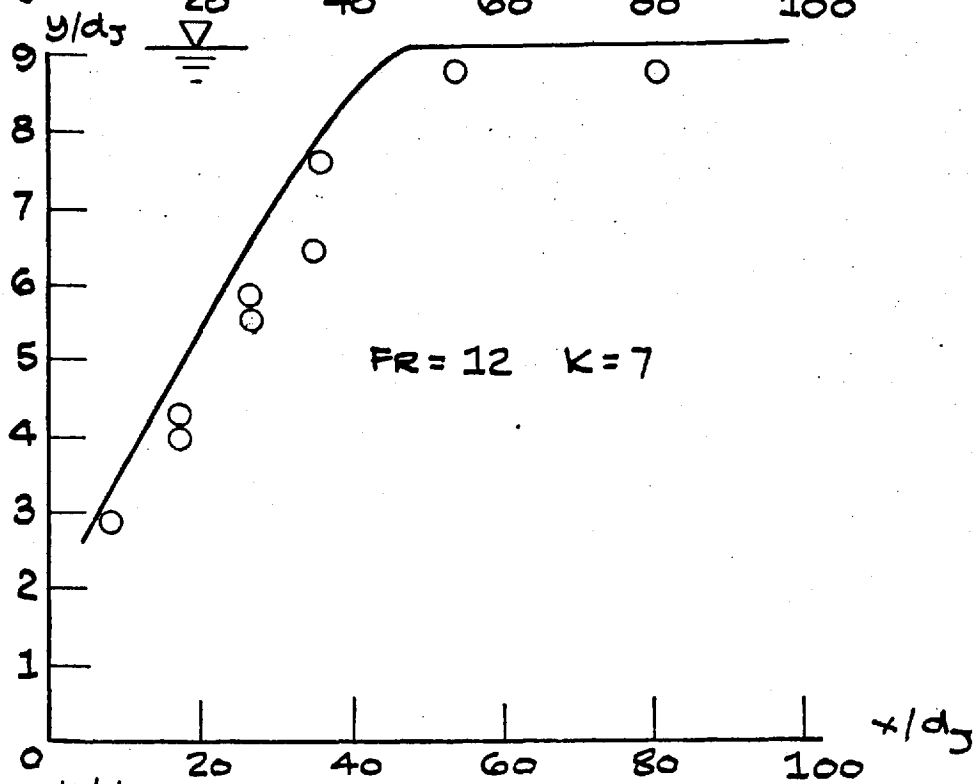
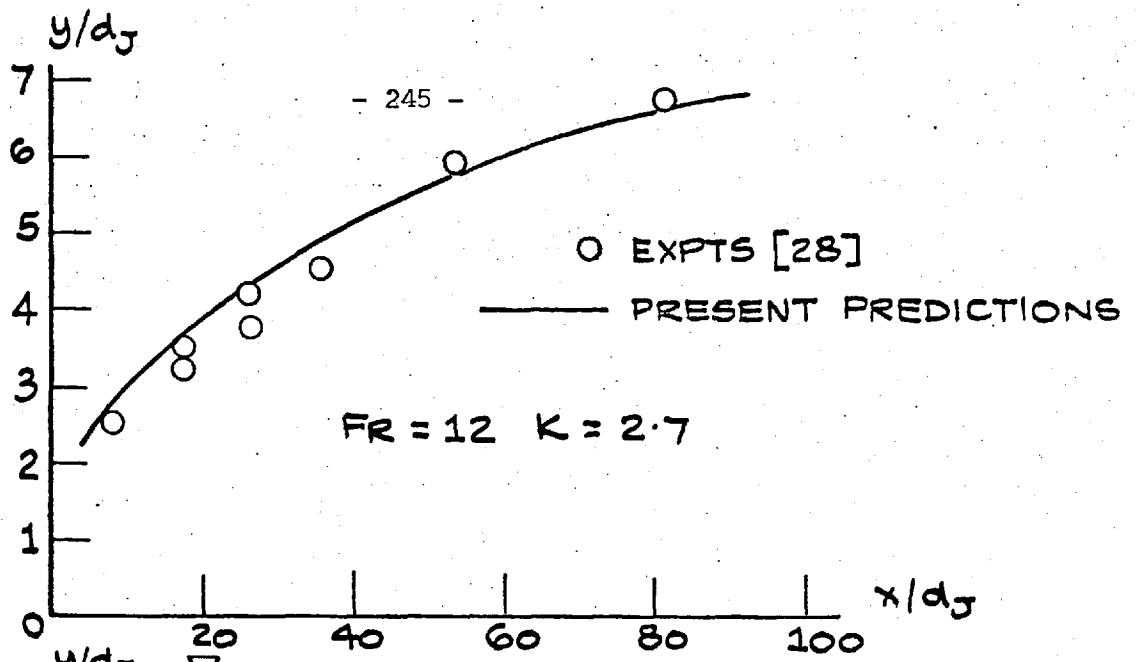


FIG. G.3.5: VERTICAL PLUME WIDTHS -  
WINIARSKI AND CHASSE EXPTS.

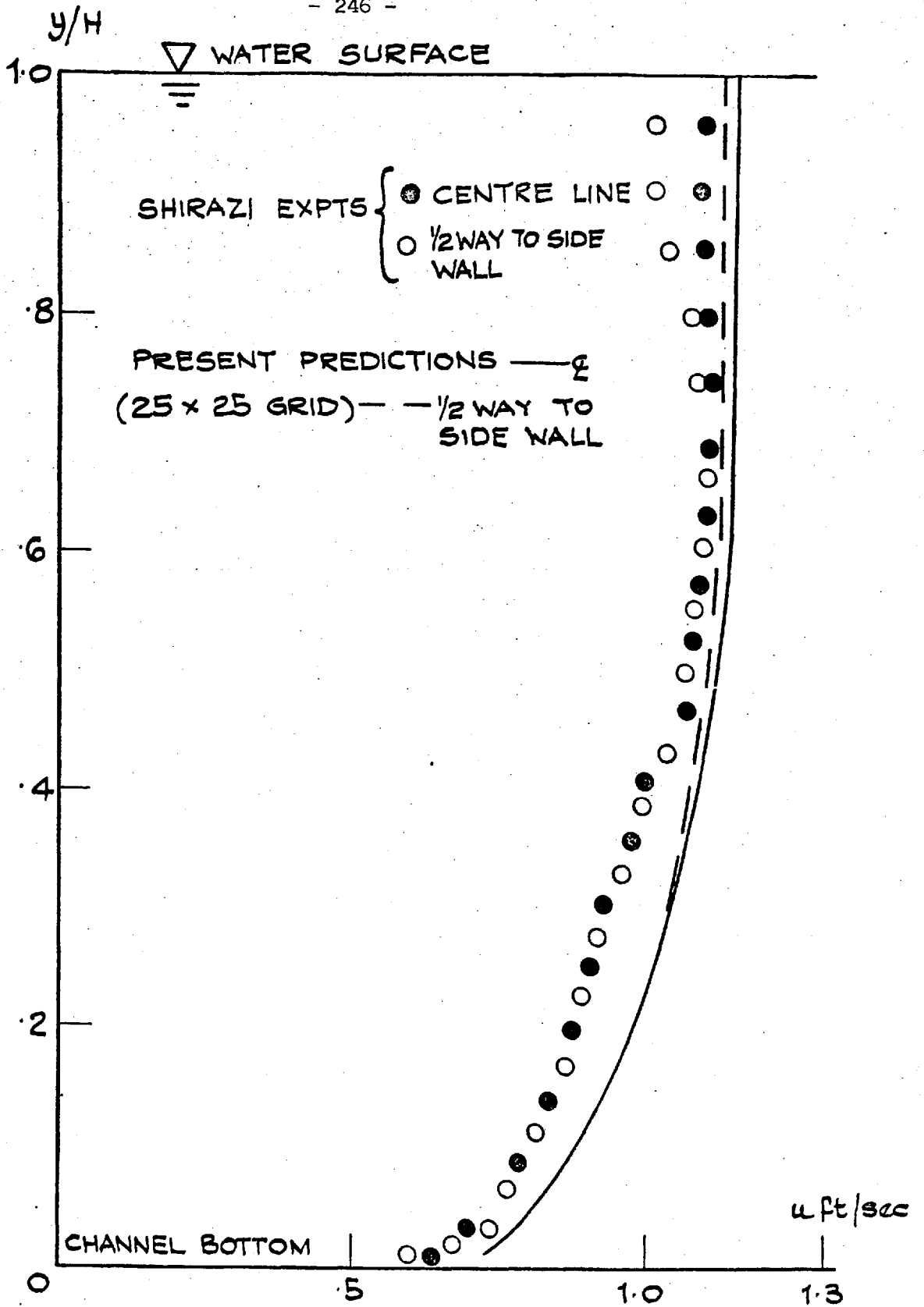
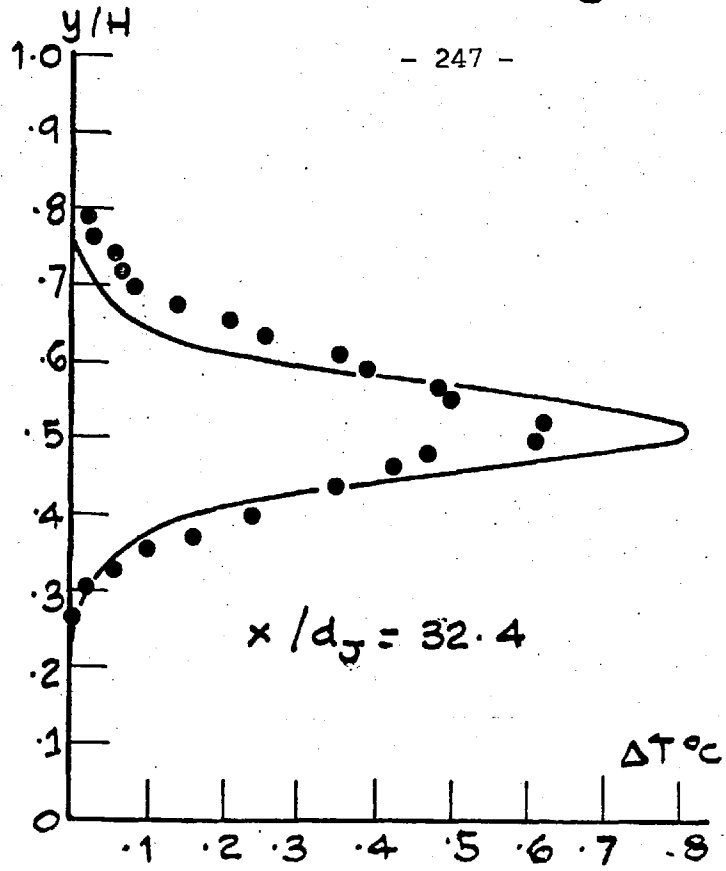
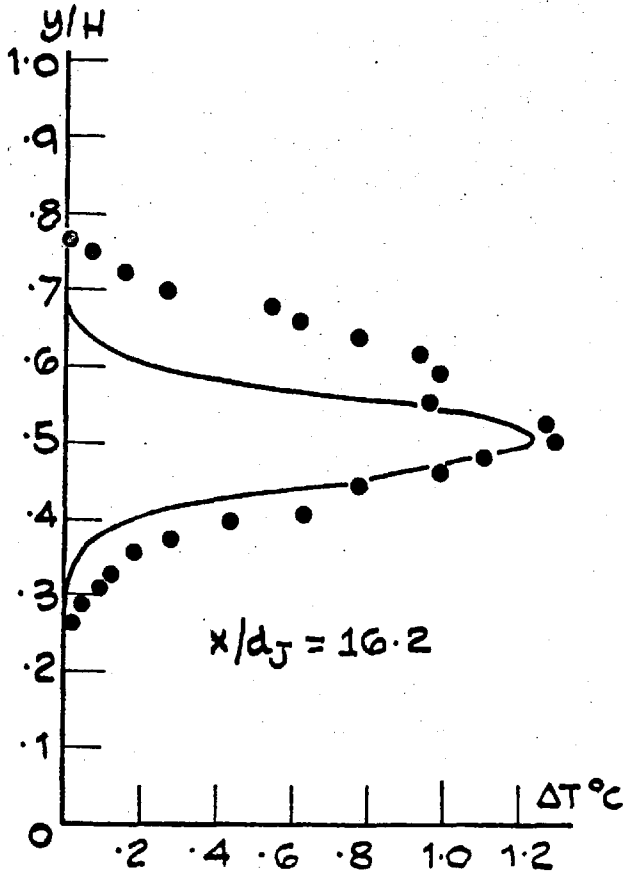


FIG. G.3.6: CHANNEL VELOCITY PROFILES - SHIRAZI ET AL EXPTS.

LARGE NOZZLE ( $d_J = 1.882 \text{ cm}$ )  $K = 0.44$   $FR = 6.3$   $A_E = 10$



● EXPTS [23]

PRESENT PREDICTIONS

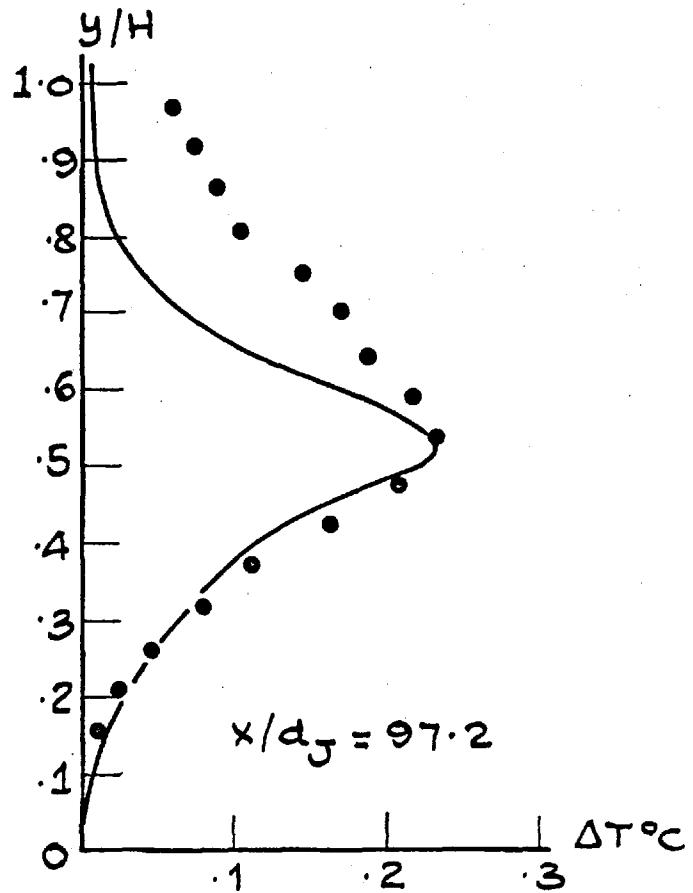
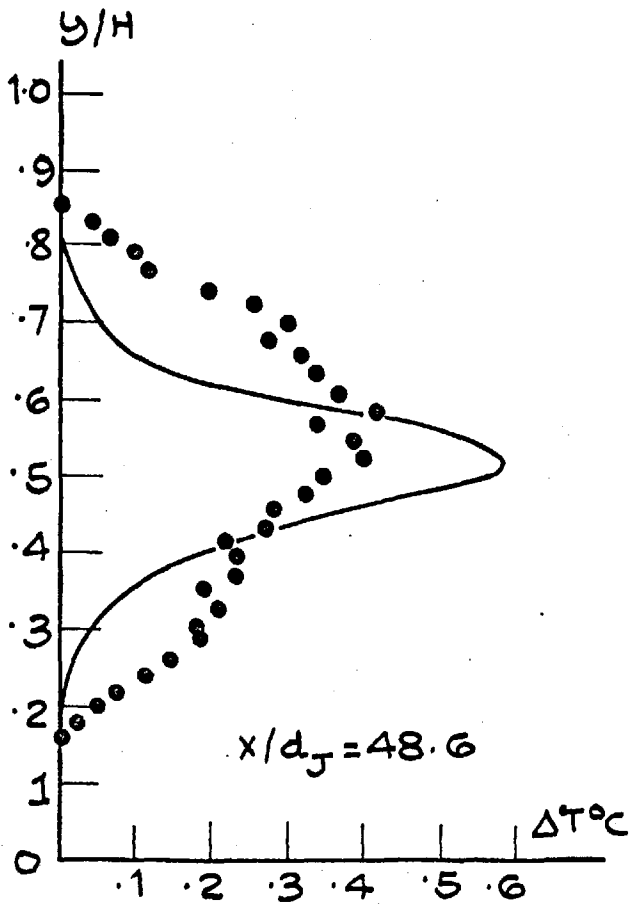


FIG. G.3.7: VERTICAL TEMPERATURE PROFILES - SHIRAZI ET AL EXPTS.

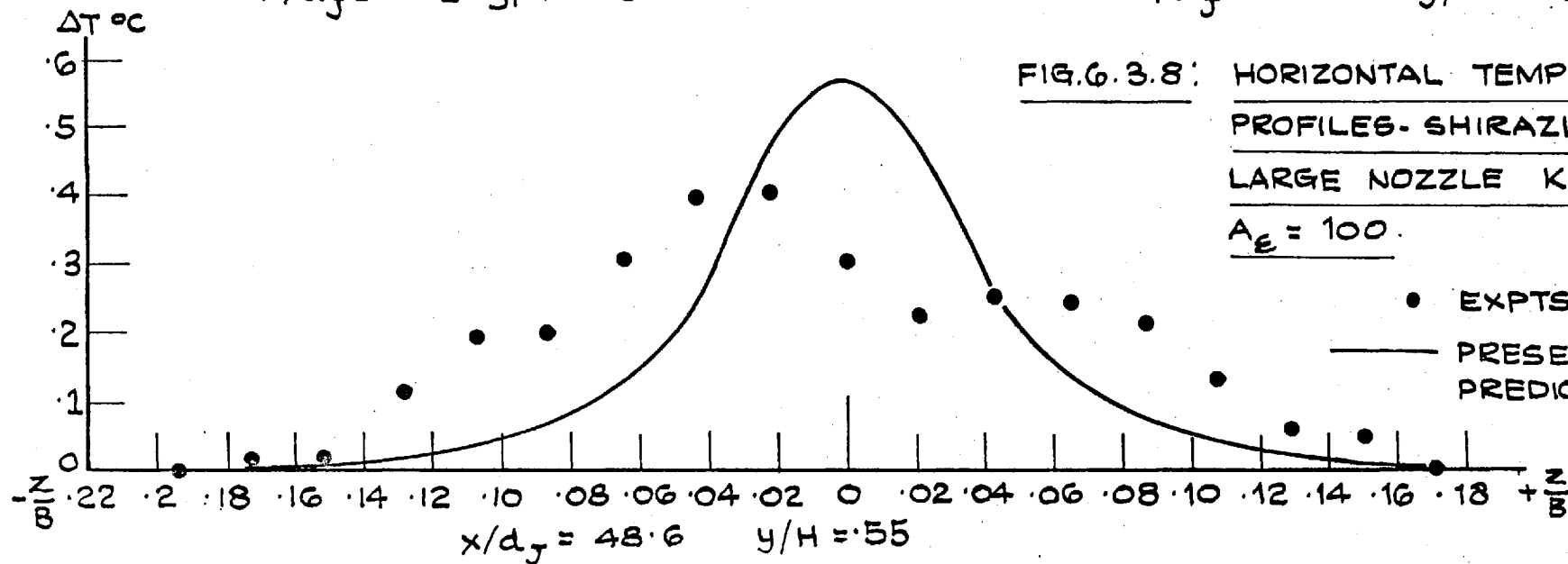
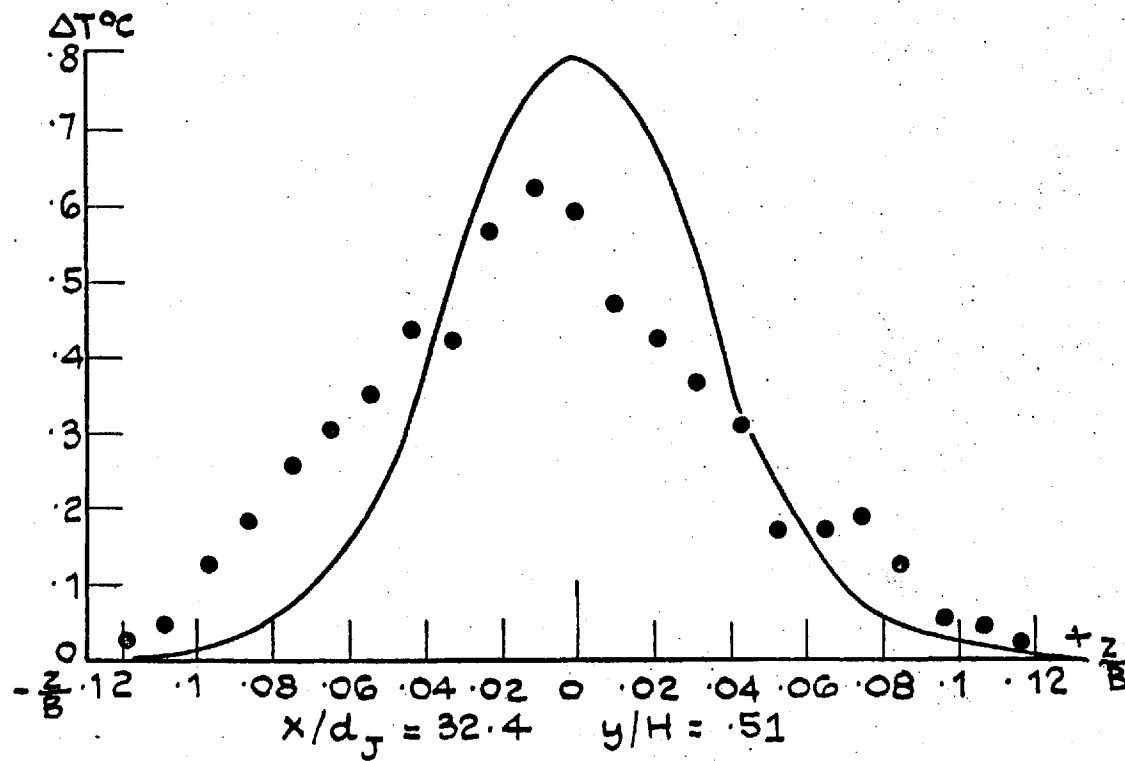
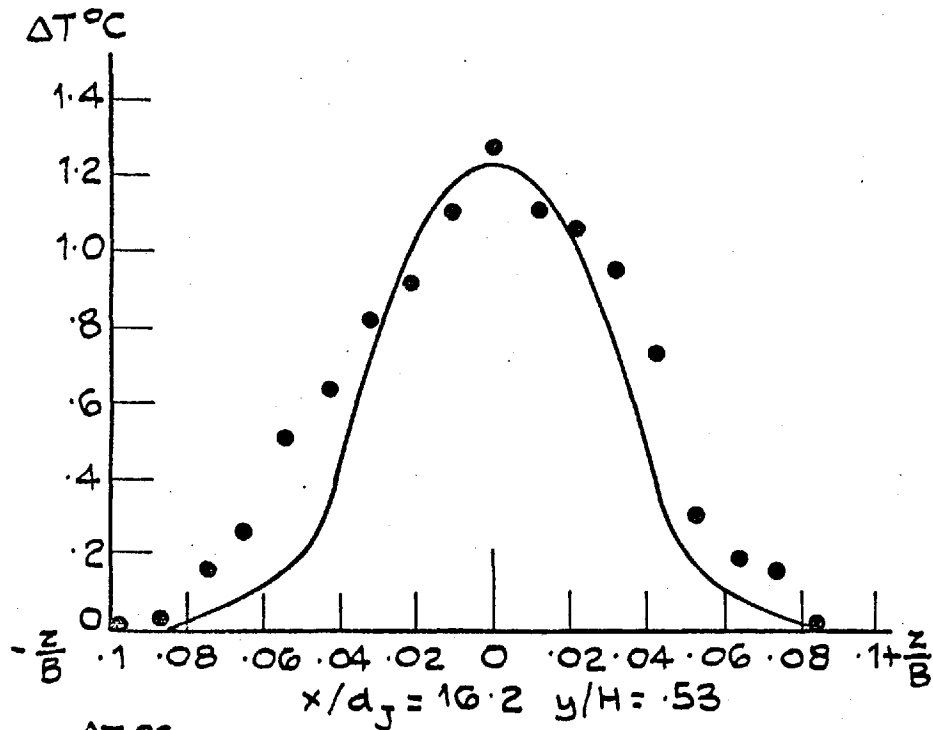
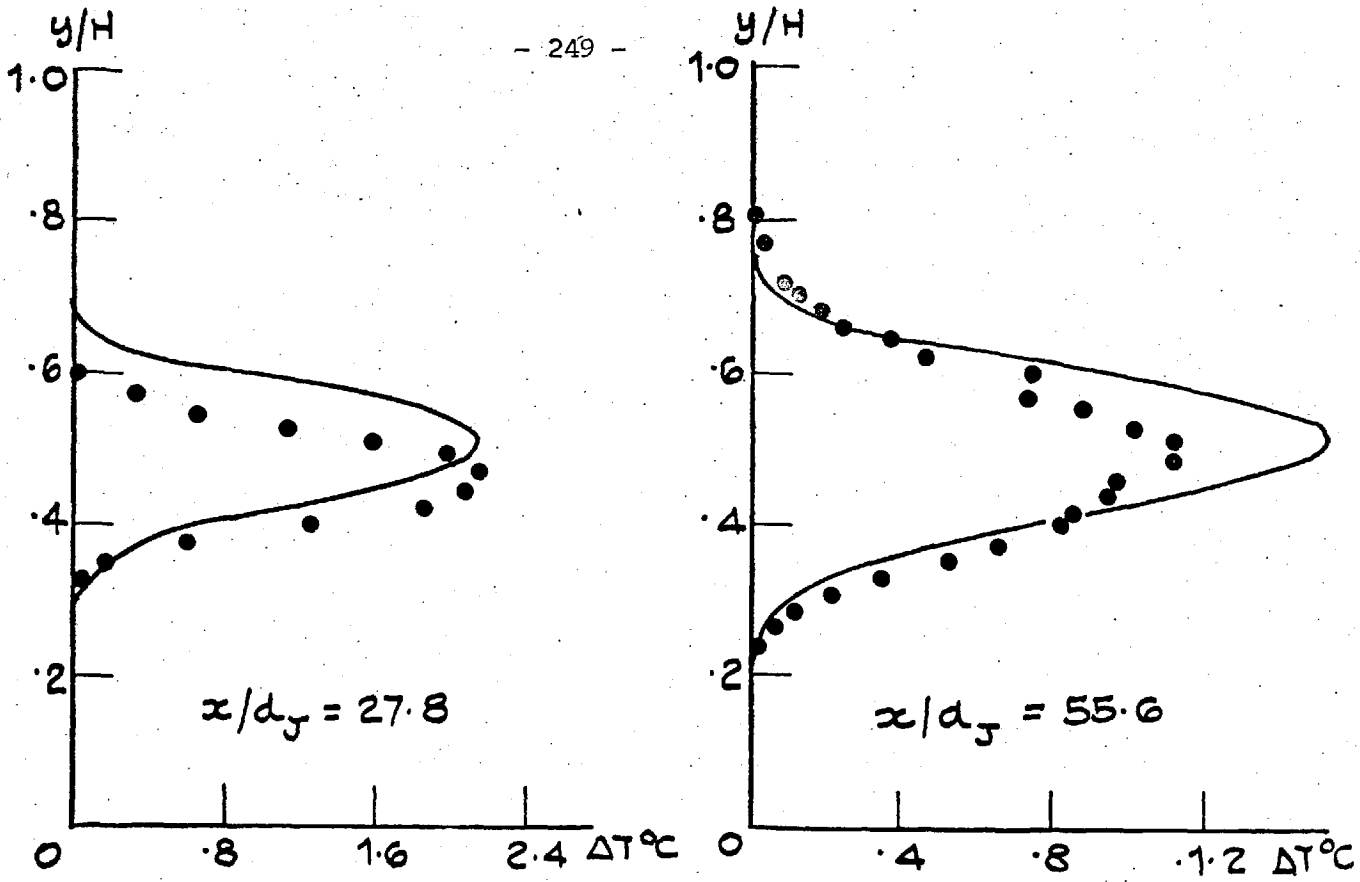


FIG. 6.3.8: HORIZONTAL TEMPERATURE  
 PROFILES - SHIRAZI ET AL EXPTS  
 LARGE NOZZLE  $K = 0.44$   $FR = 6.3$   
 $A_E = 100$ .

• EXPTS [23]  
 — PRESENT  
 PREDICTIONS





MEDIUM NOZZLE ( $d_j = 1.09\text{cm}$ )  $K = 3.82$   $FR = 72$   $A_E = 25$

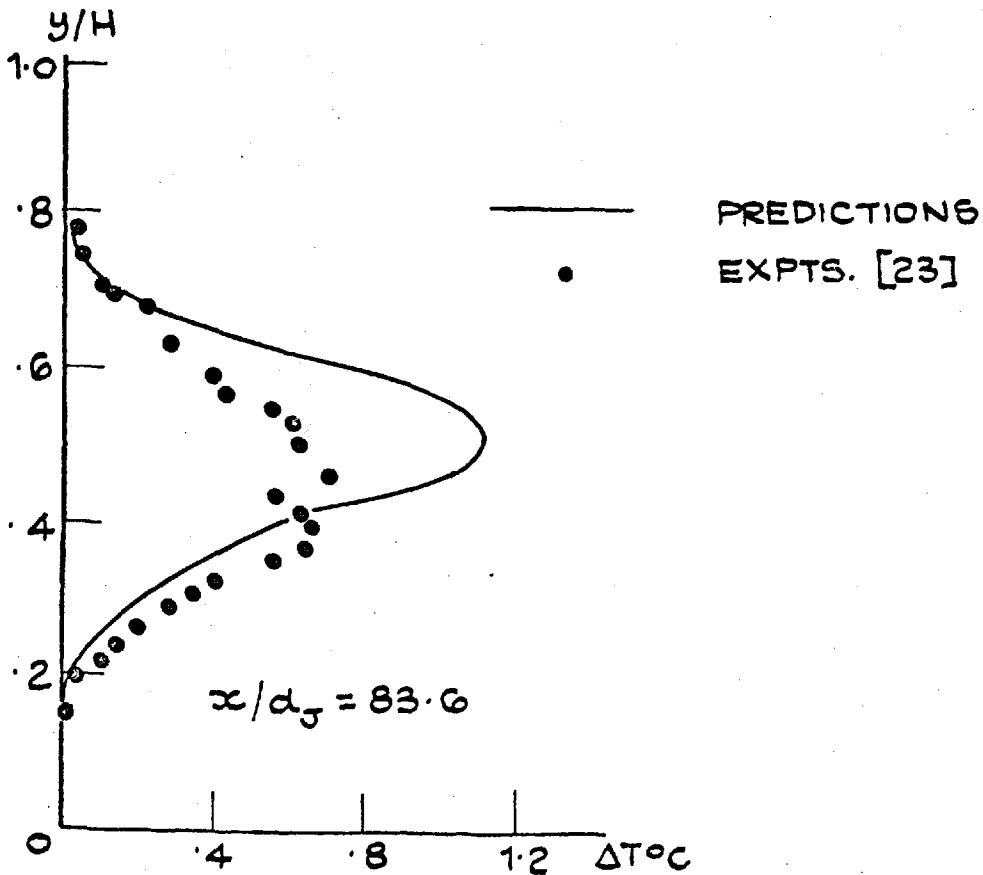
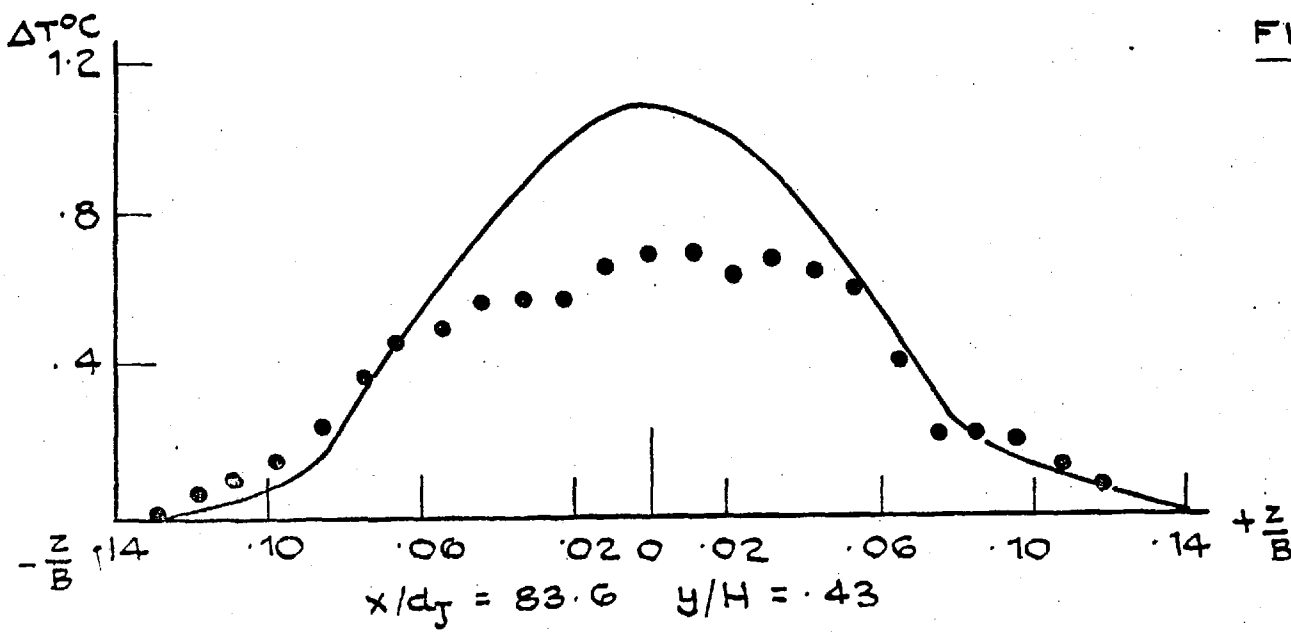
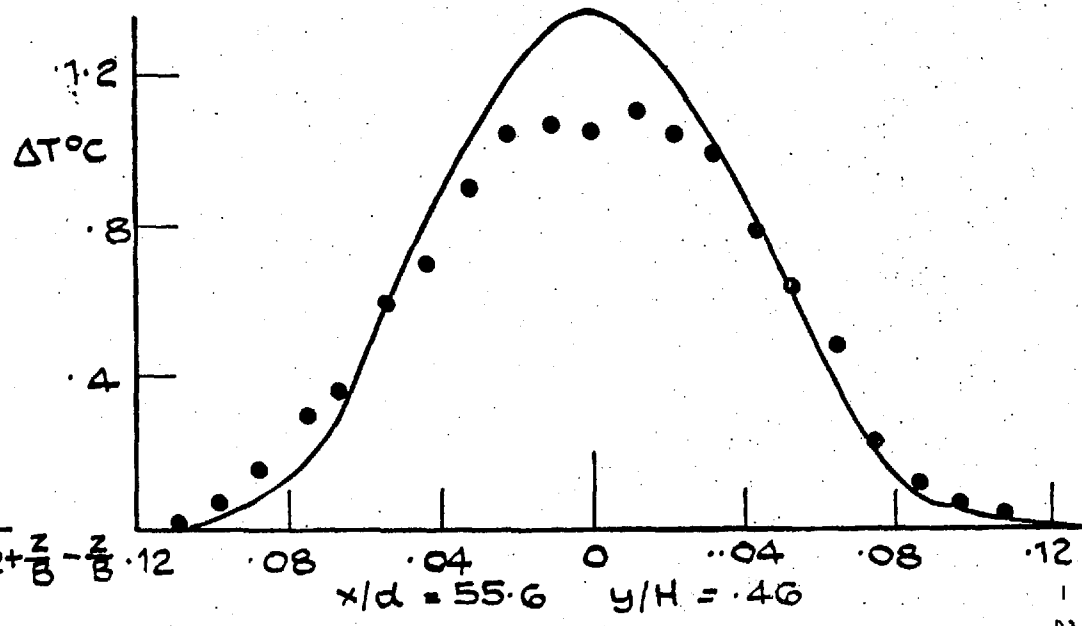
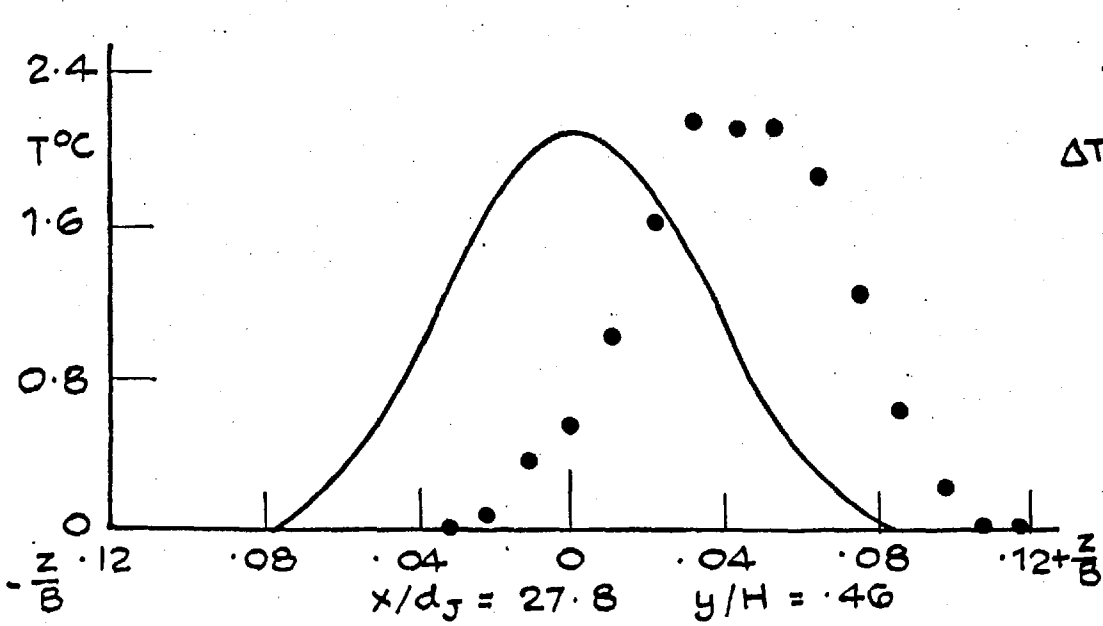
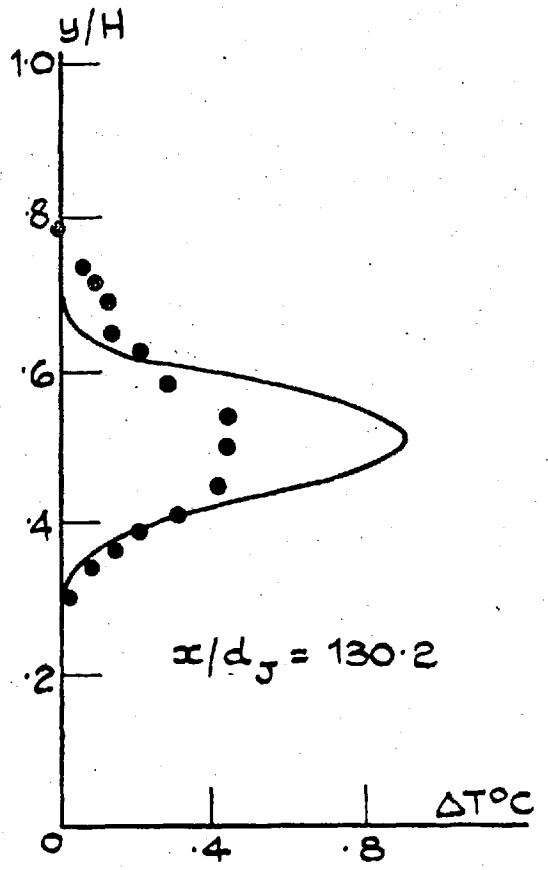
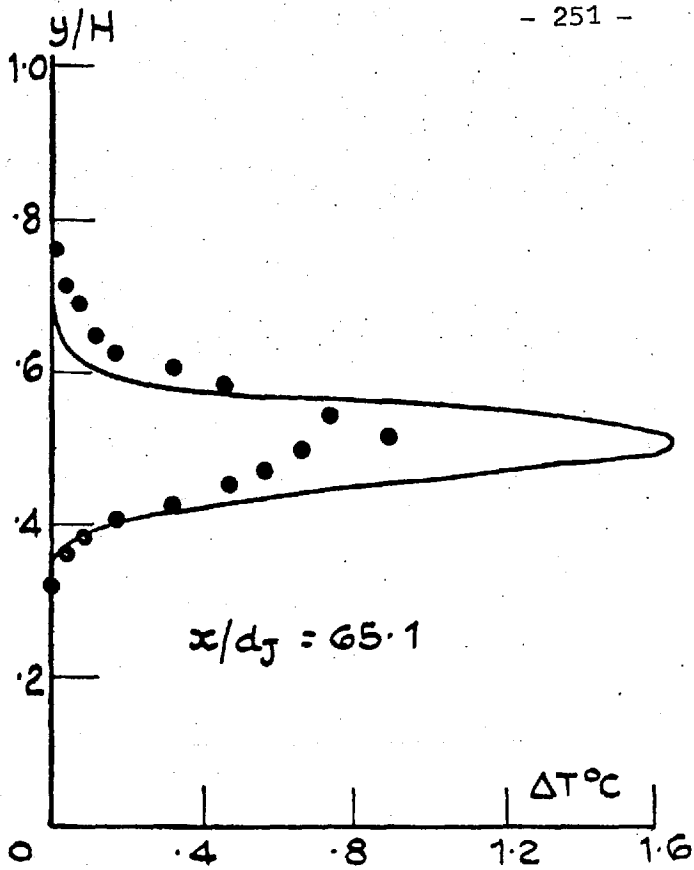


FIG. 6.3.9: VERTICAL TEMPERATURE PROFILES  
SHIRAZI ET AL DATA.



**FIG. G.3.10: HORIZONTAL TEMPERATURE PROFILES - SHIRAZI ET AL EXPTS**  
**MEDIUM NOZZLE  $K = 3.82$**   
 **$FR = 72$   $A_{\epsilon} = 25$**

● EXPTS.  
 — PRESENT PREDICTIONS.



SMALL NOZZLE ( $d_j = .468 \text{ cm}$ )  $K = 7.15$   $Fr = 205$   $A_\varepsilon = 10$

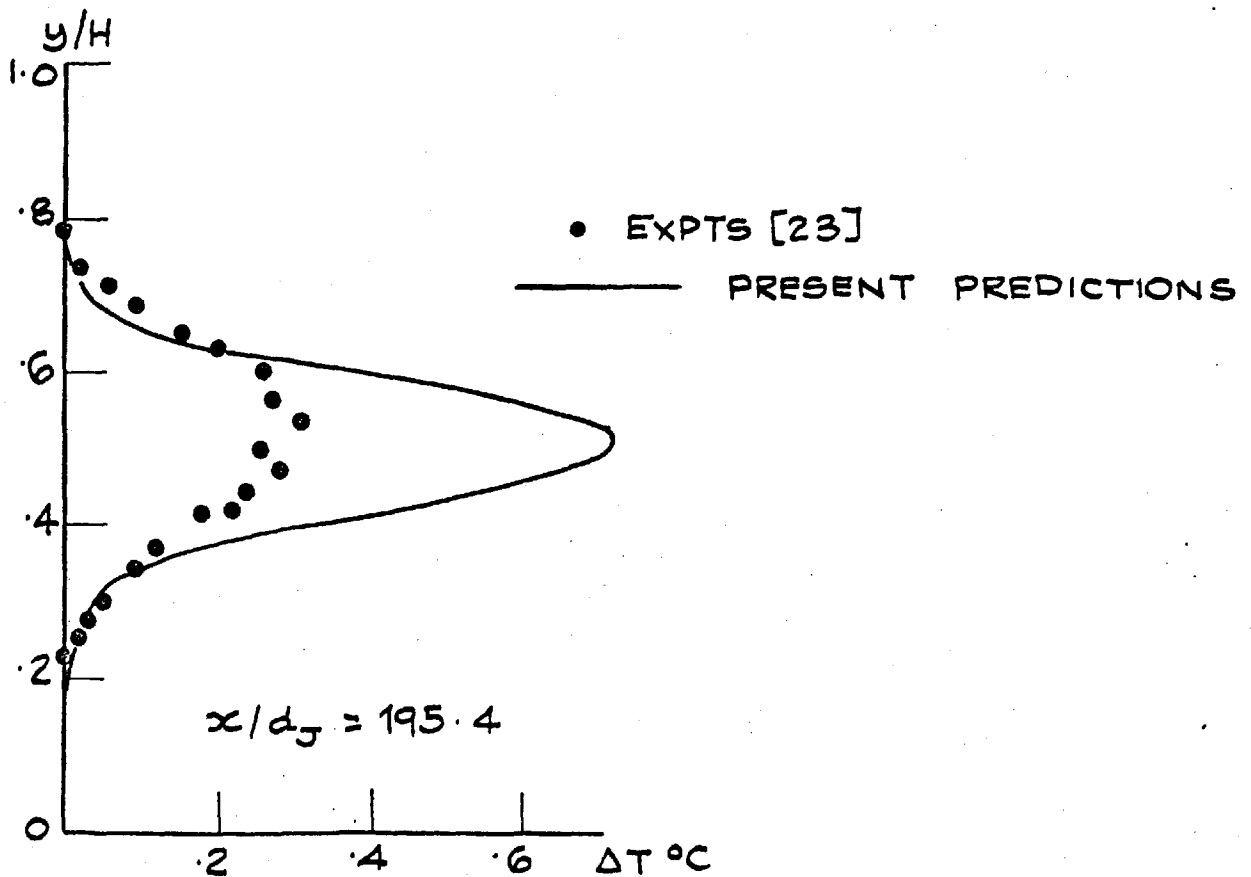


FIG. G. 3.11: VERTICAL TEMPERATURE PROFILES  
SHIRAZI ET AL DATA.

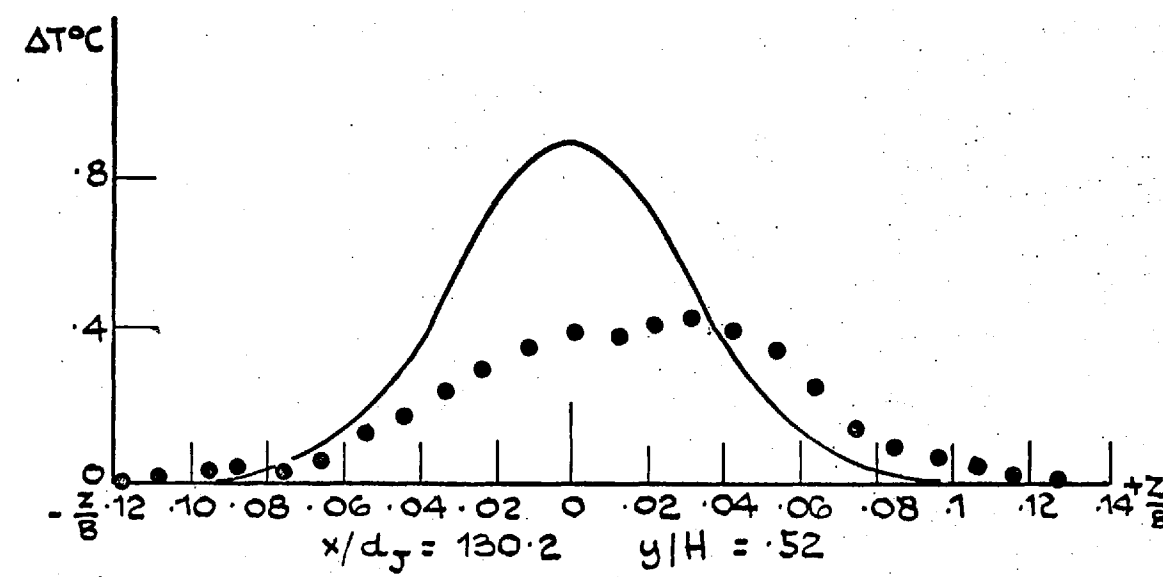
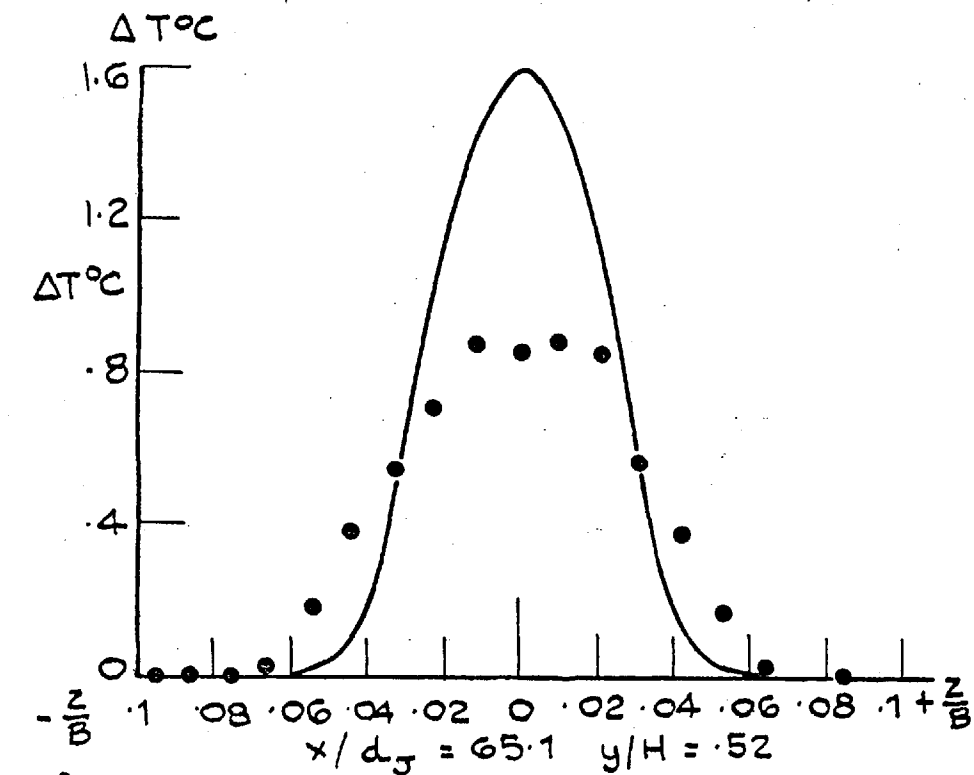
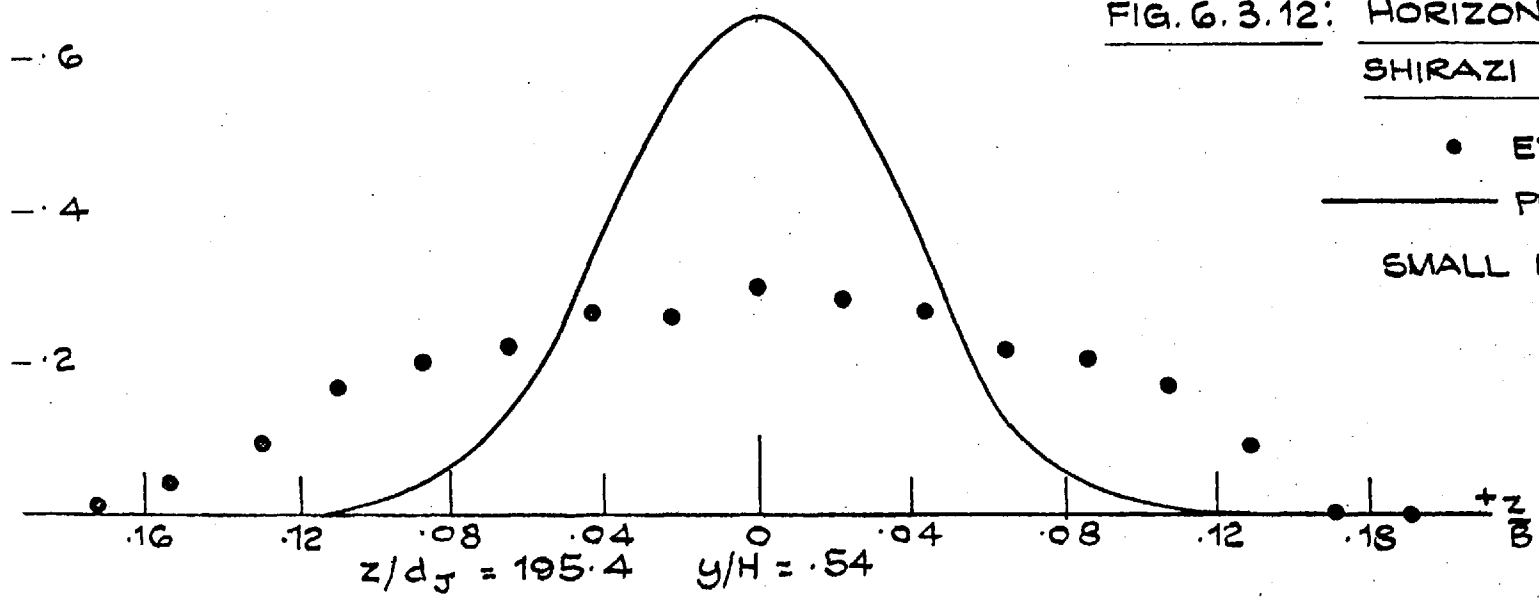


FIG. 6.3.12: HORIZONTAL TEMPERATURE PROFILES  
SHIRAZI ET AL DATA.



• EXPTS [23]  
 — PRESENT PREDICTIONS  
 SMALL NOZZLE  $K = 7.15$   $FR = 205$   
 $A_E = 10$

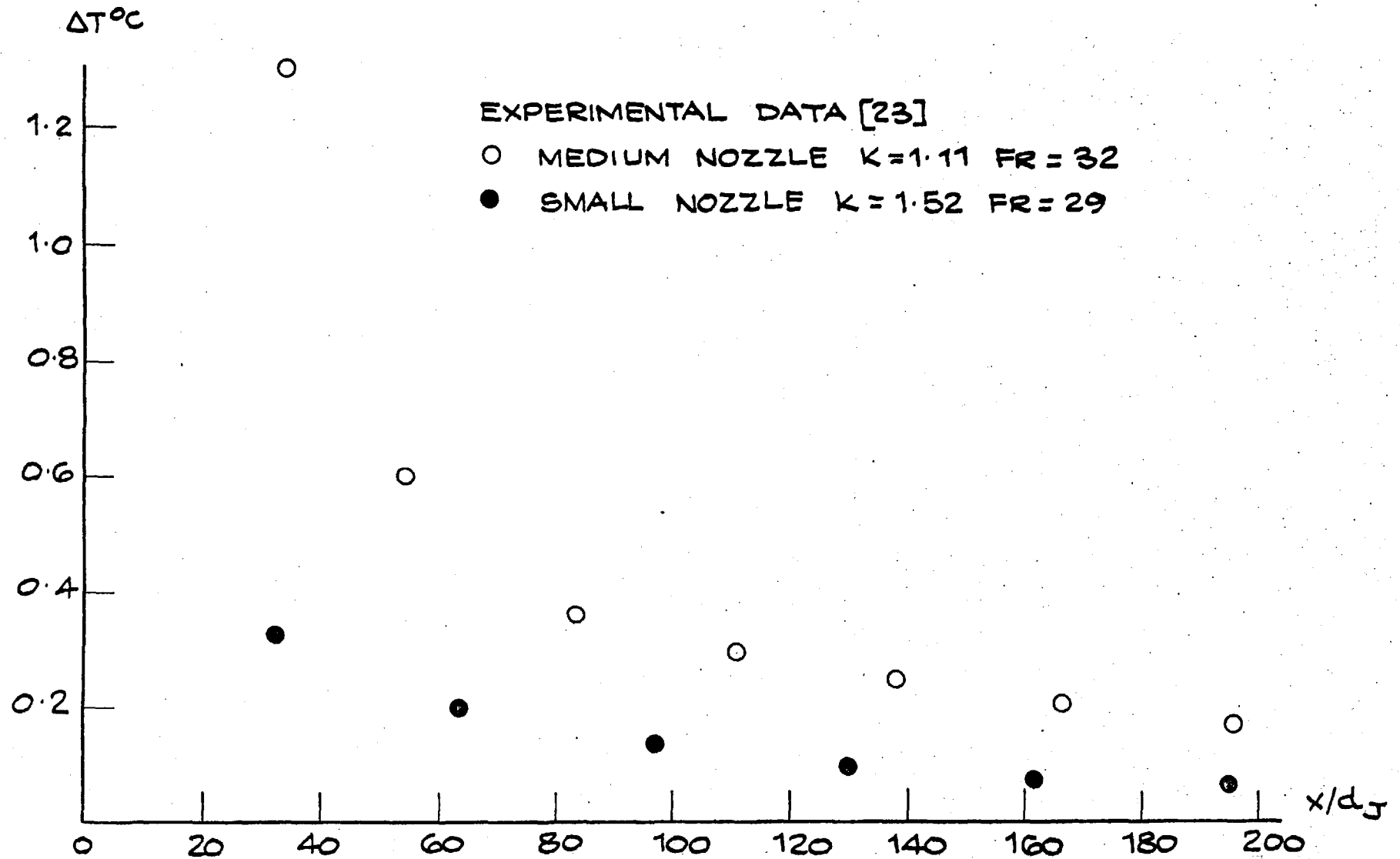


FIG. 6.3.13: PLUME DILUTION CURVES - SHIRAZI ET AL EXPTS.

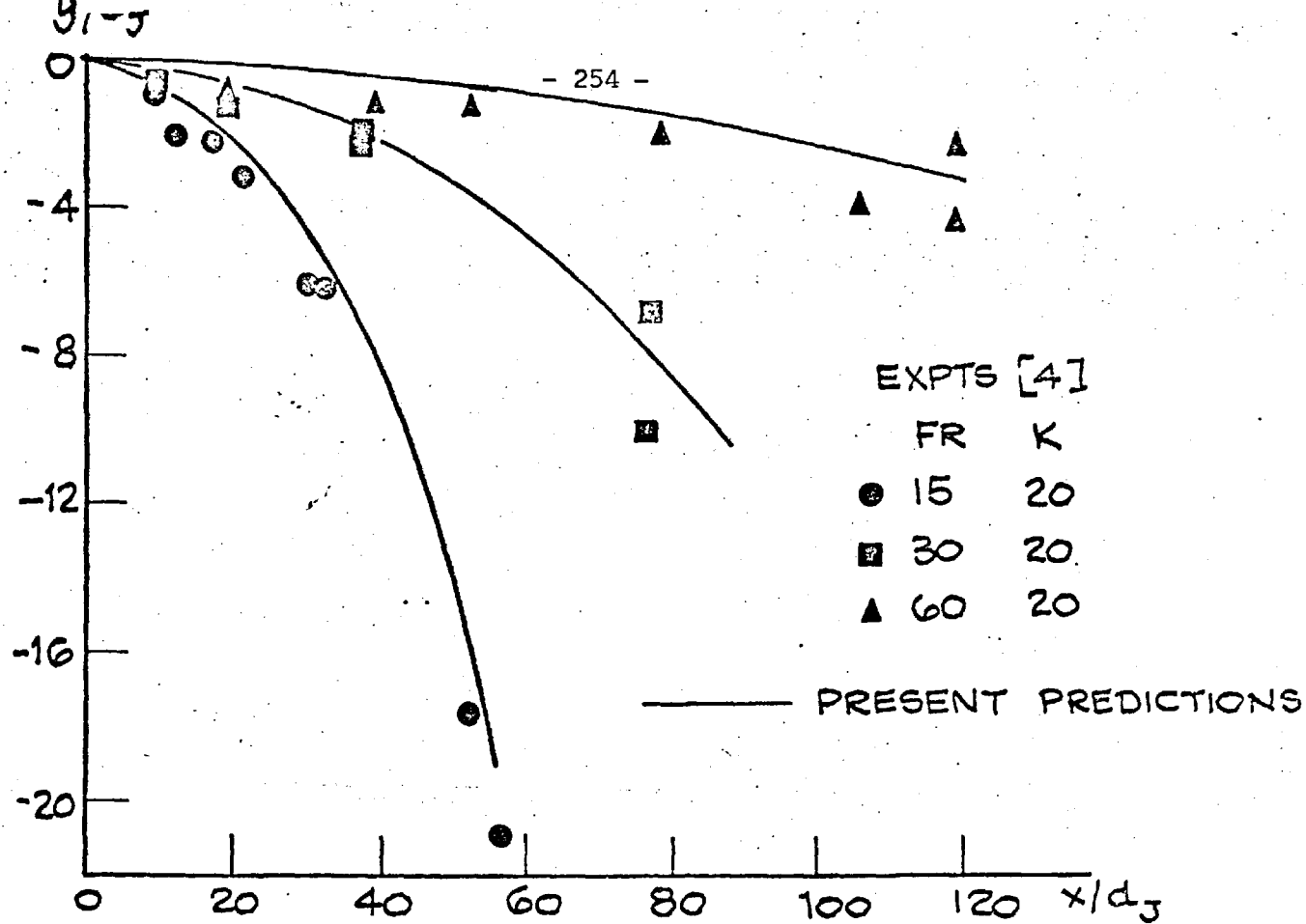


FIG. G. 3. 14: EFFECT OF FROUDE NUMBER ON PLUME TRAJECTORY.

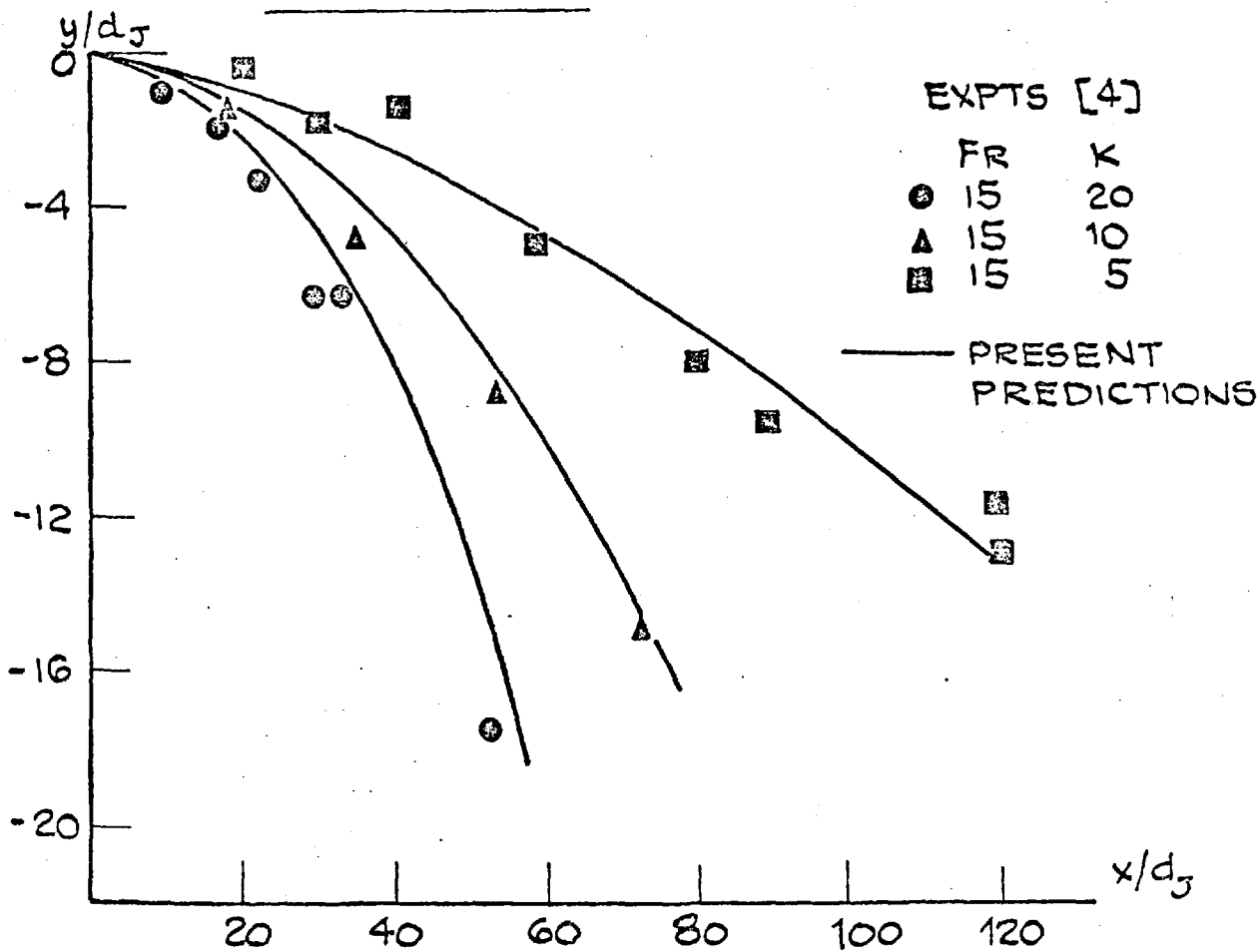


FIG. G. 3. 15: EFFECT OF VELOCITY RATIO ON PLUME TRAJECTORY.

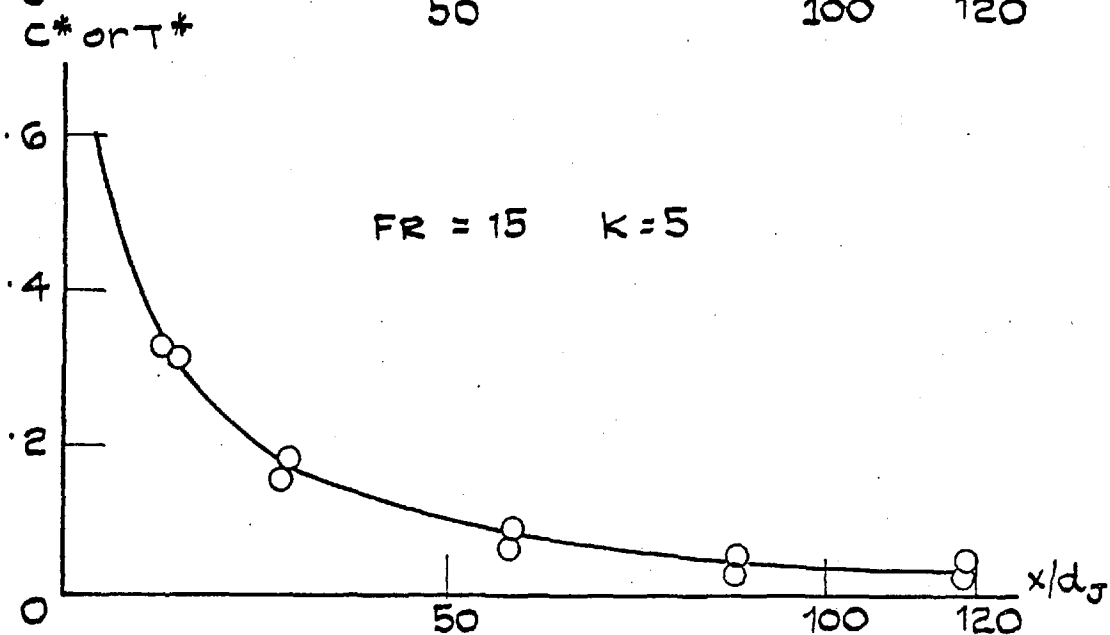
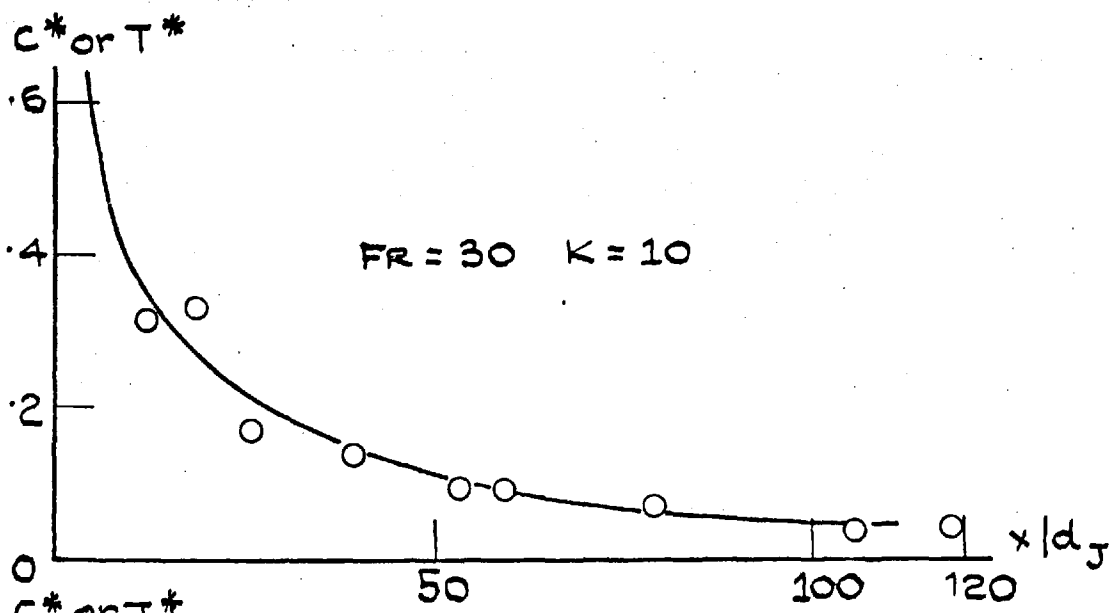
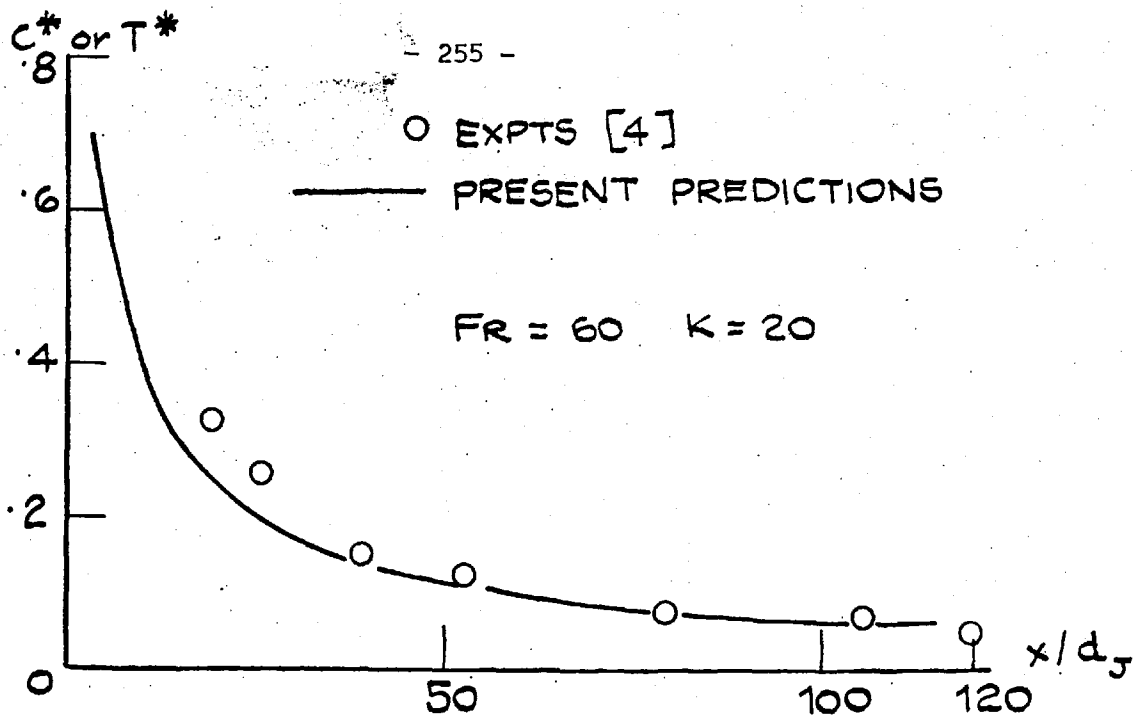


FIG. G.3.16: PLUME DILUTION CURVES AYOUB EXPTS.

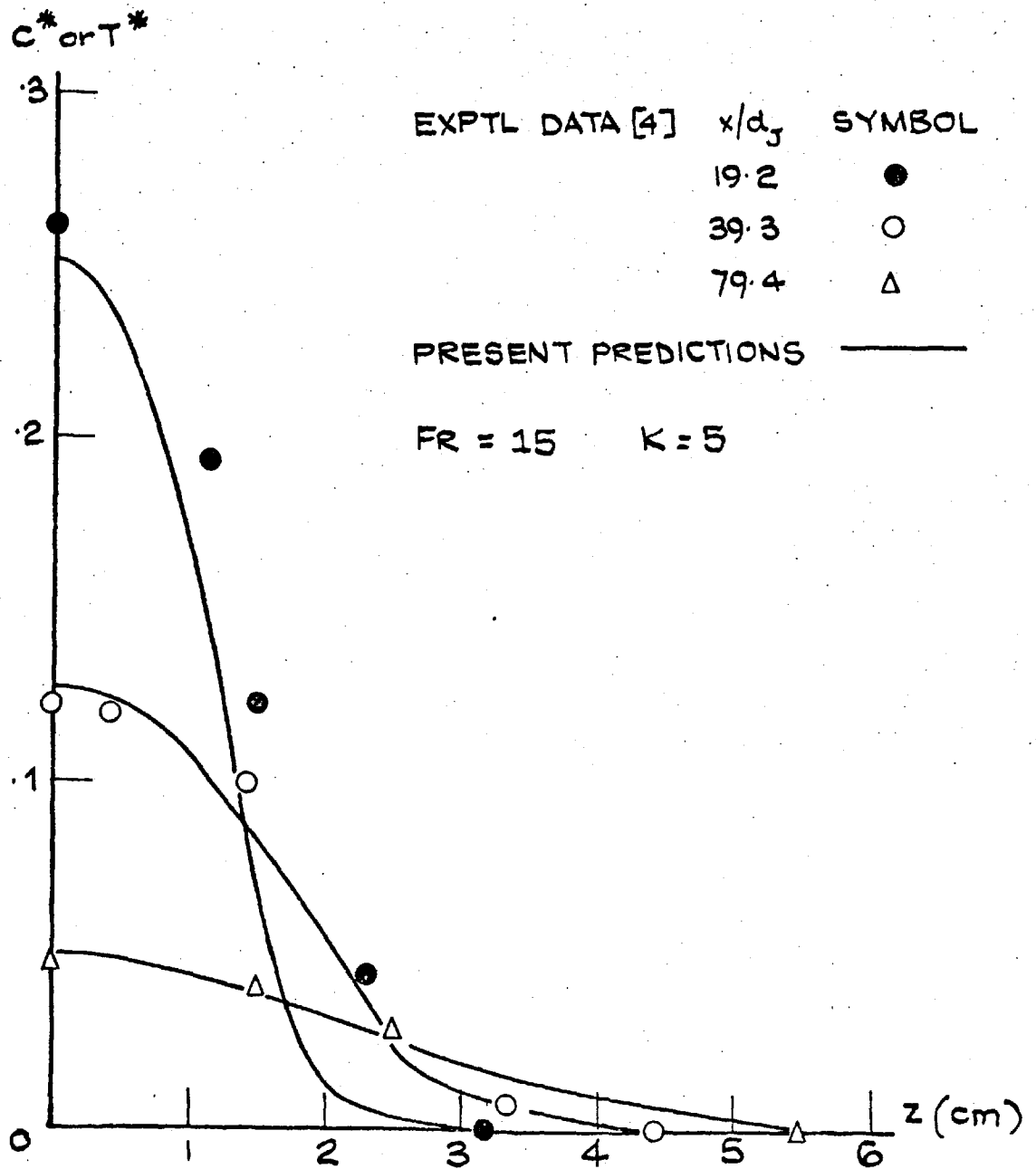


FIG. 6.3.17: NON-DIMENSIONAL CONCENTRATION/  
TEMPERATURE PROFILES.



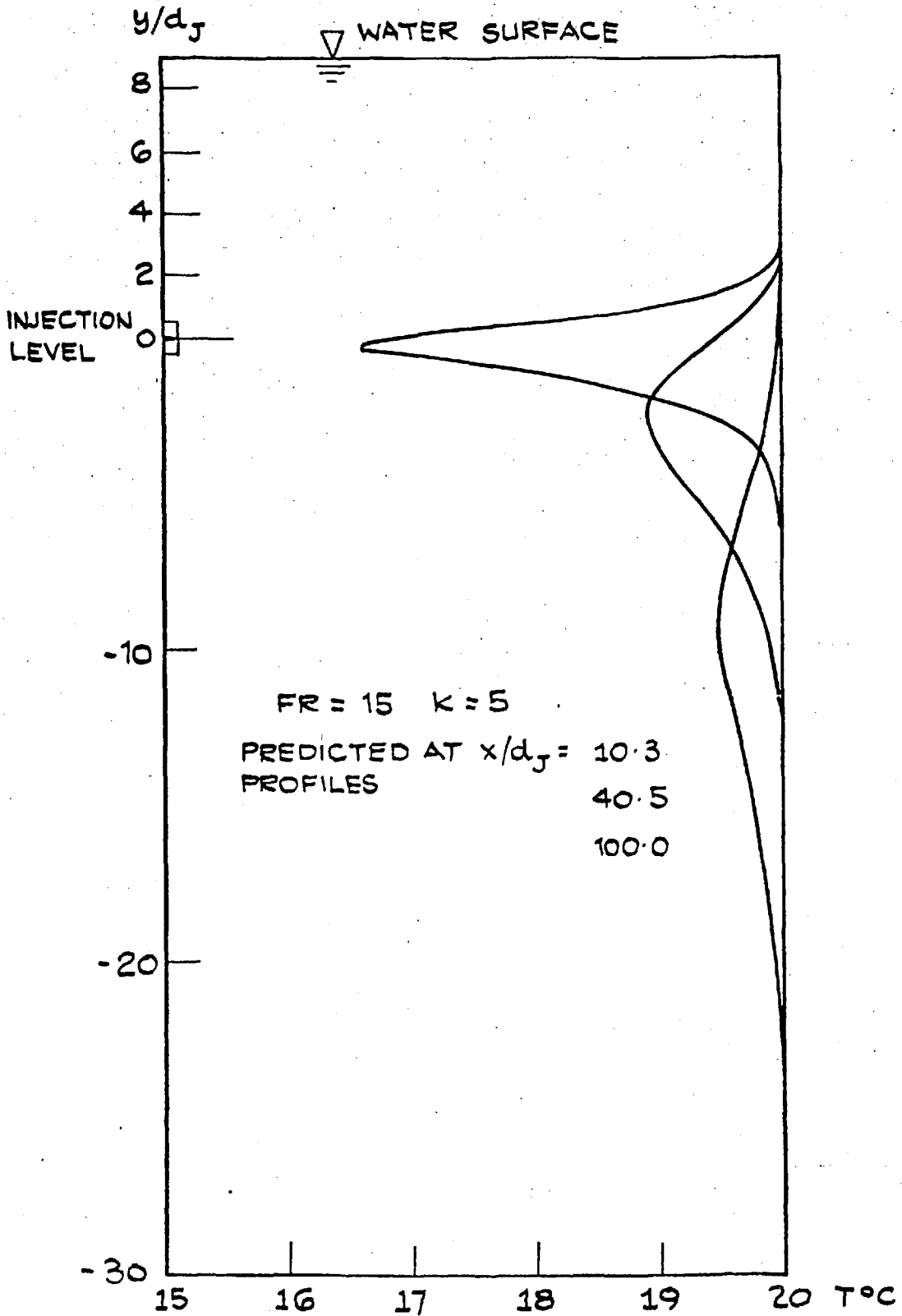


FIG. 6.3.18: VERTICAL PROFILES ON CHANNEL  
CENTRE-LINE PREDICTIONS FOR  
AYOUB EXPTS.

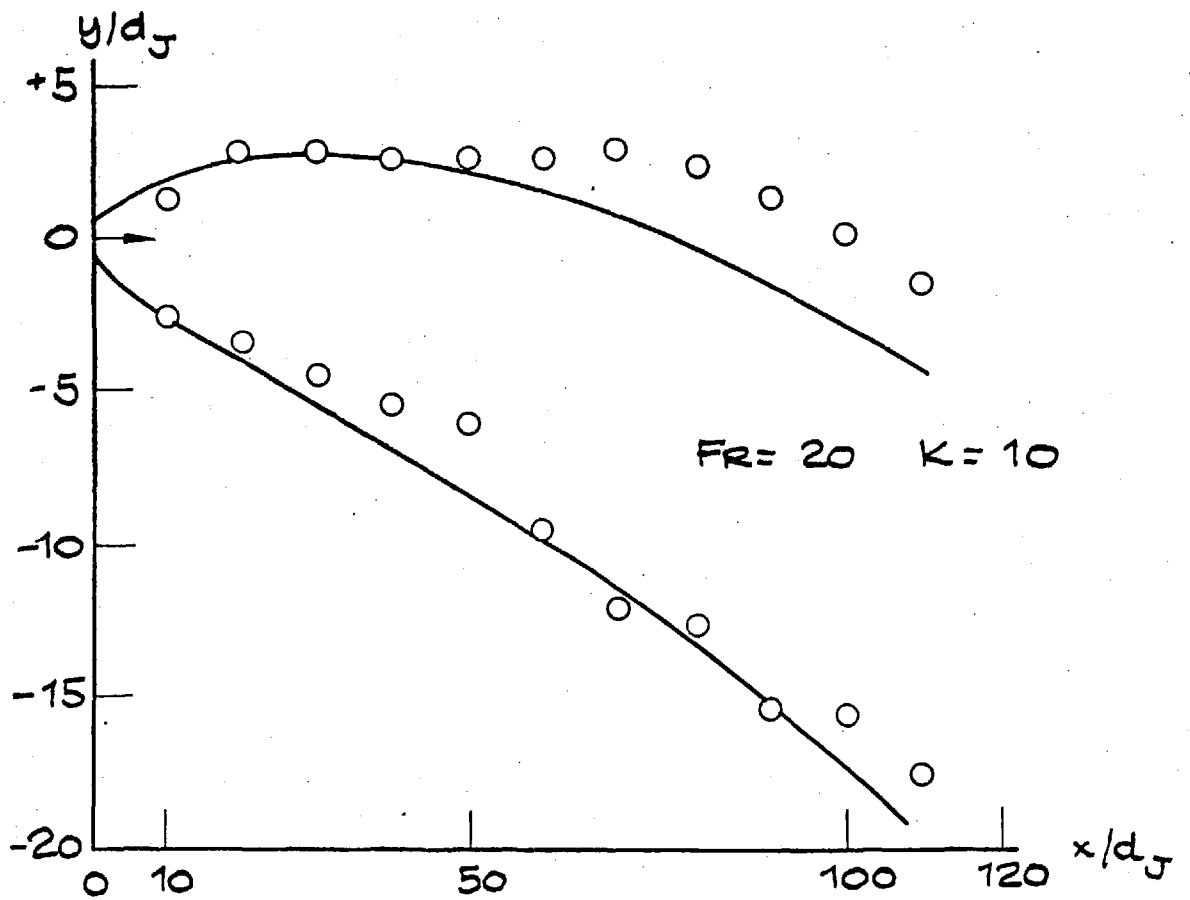
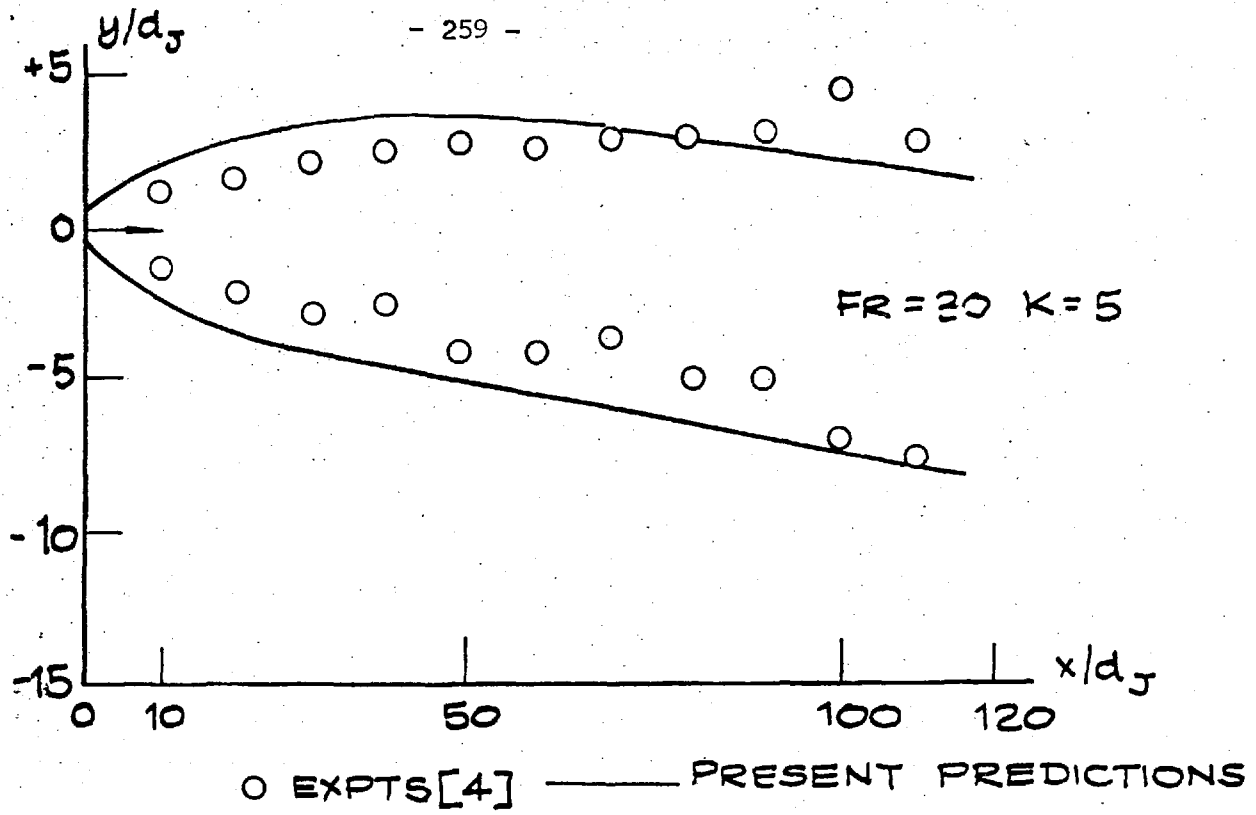


FIG. G. 3. 19: PLUME WIDTH VS DOWNSTREAM DISTANCE AYOUB EXPTS.

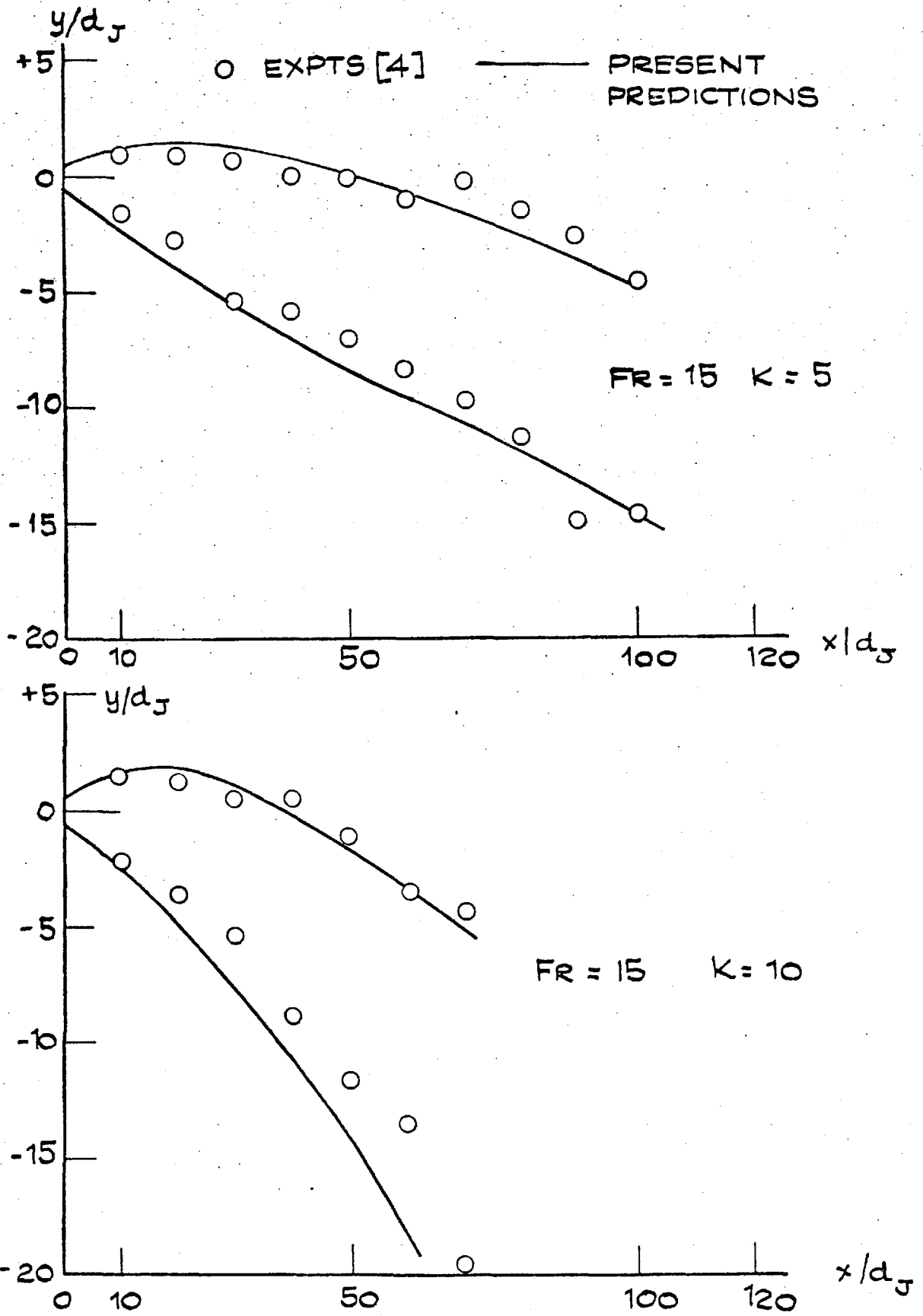


FIG. G. 3.20: PLUME WIDTH vs DOWNSTREAM  
DISTANCE AYOUB EXPTS.

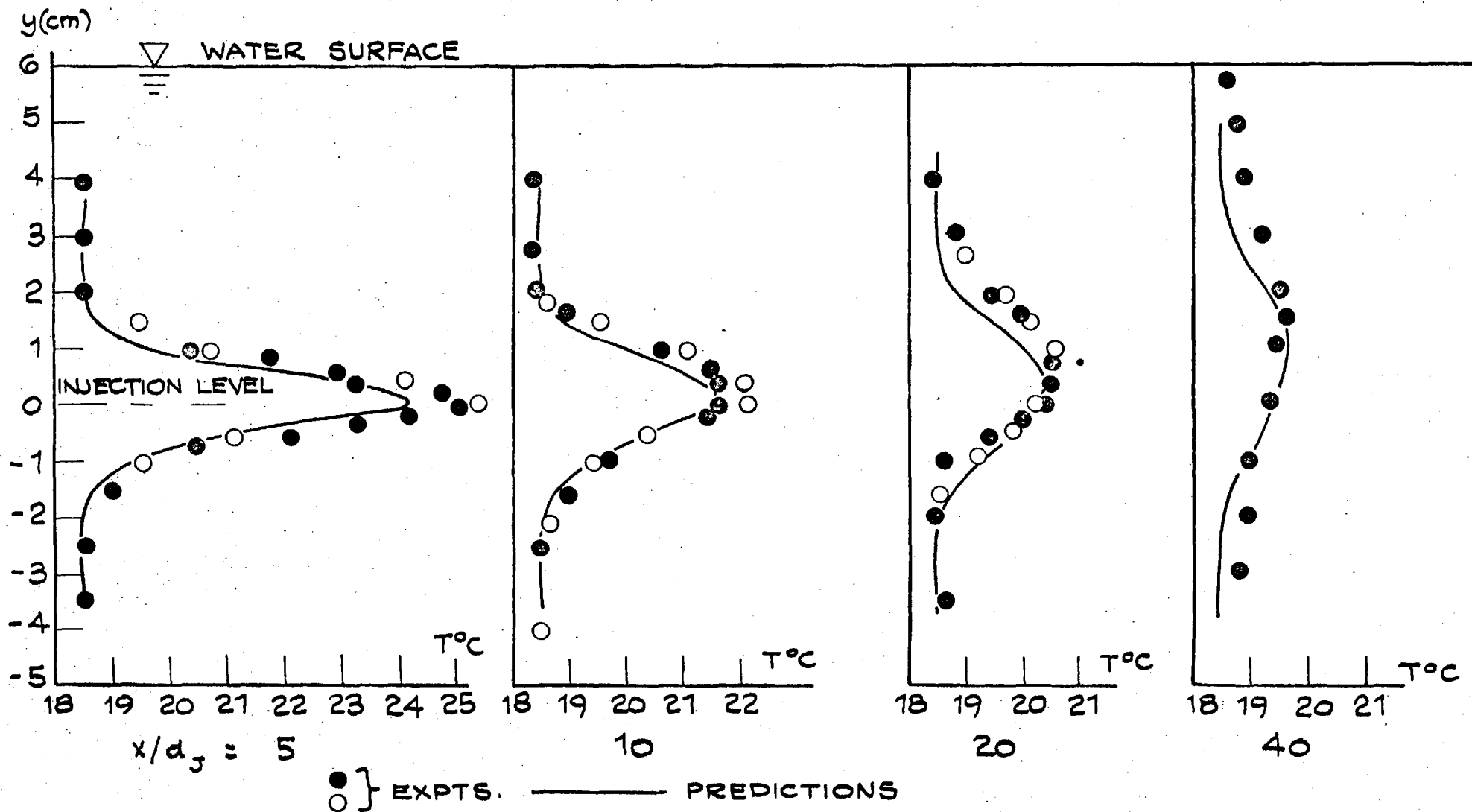


FIG. G. 3. 21: VERTICAL CENTRE - LINE TEMPERATURE PROFILES - PRESENT EXPTS.

FR = 15      K = 2       $T_{\text{Jet}} = 26^{\circ}\text{C}$        $T_{\text{amb}} = 18.5^{\circ}\text{C}$ .

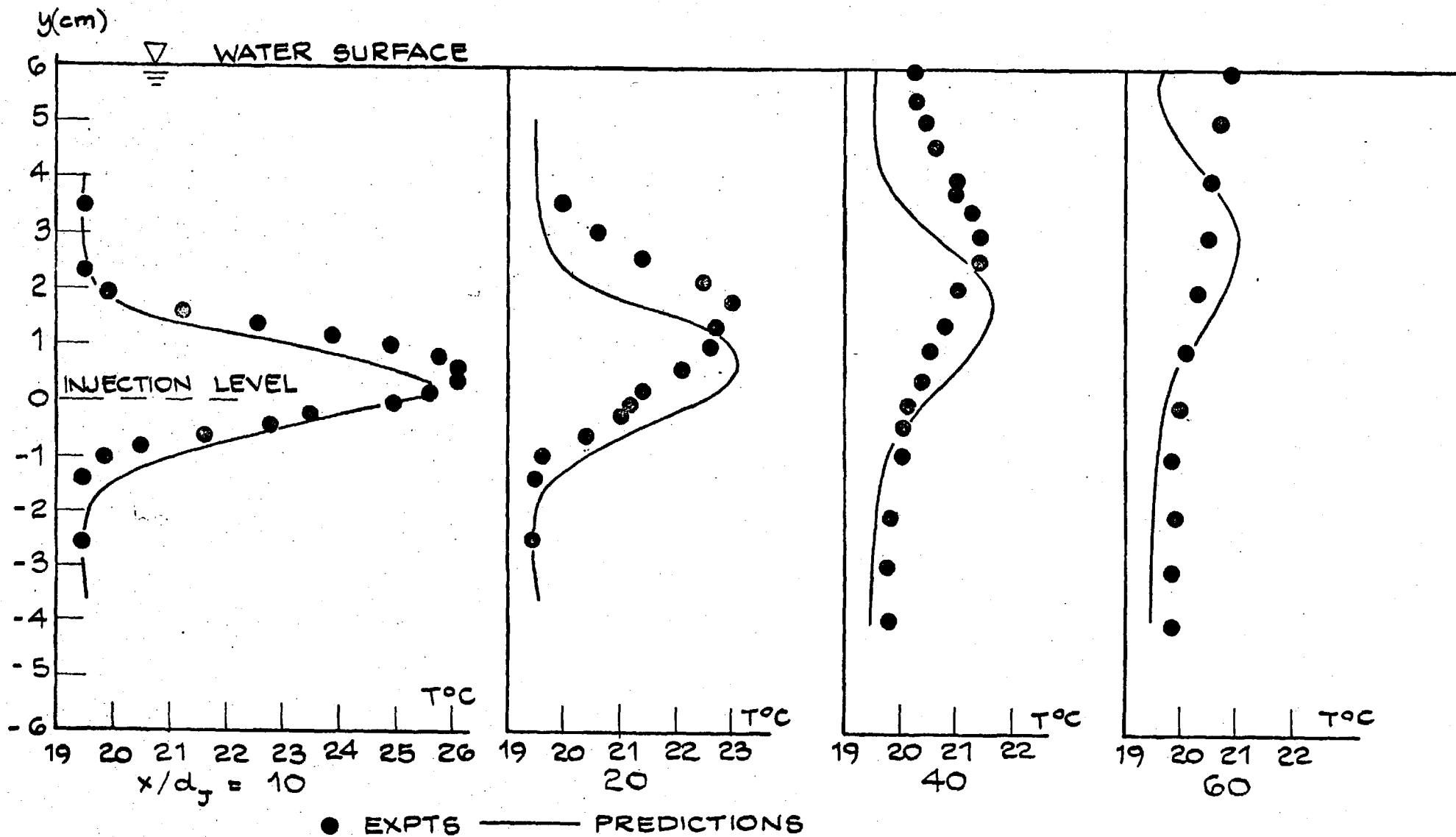
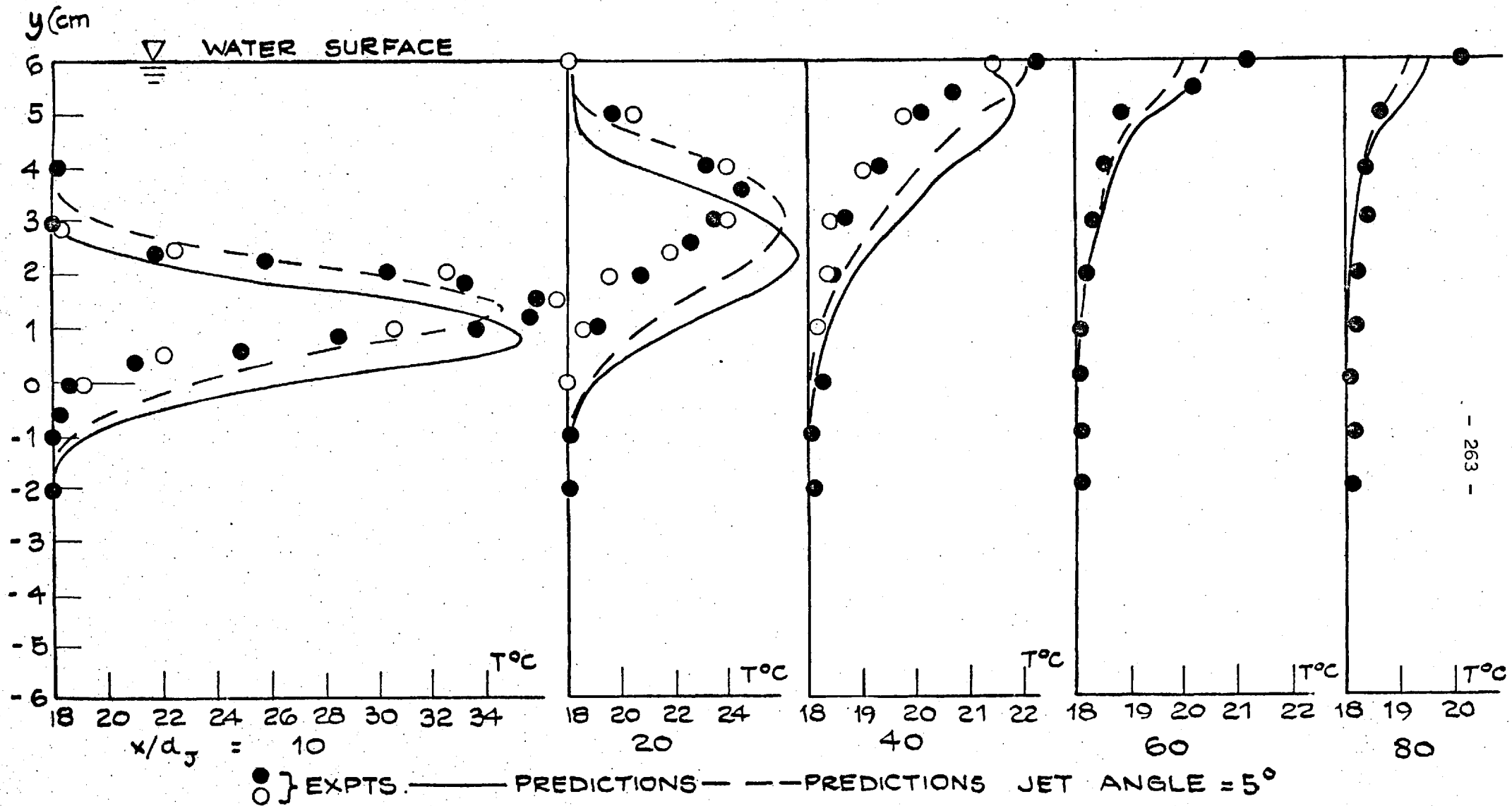


FIG. 6.3.22: VERTICAL CENTRE-LINE TEMPERATURE PROFILES -  
 PRESENT EXPTS.

$FR = 10$     $K = 2$     $T_{\text{jet}} = 34.0^{\circ}\text{C}$     $T_{\text{amb}} = 19.5^{\circ}\text{C}$ .



**FIG. 6.3.23: VERTICAL CENTRE - LINE TEMPERATURE PROFILES - PRESENT EXPTS.**

$FR = 5$     $K = 2$     $T_{JET} = 62.5^{\circ}\text{C}$     $T_{amb} = 18.0^{\circ}\text{C}$

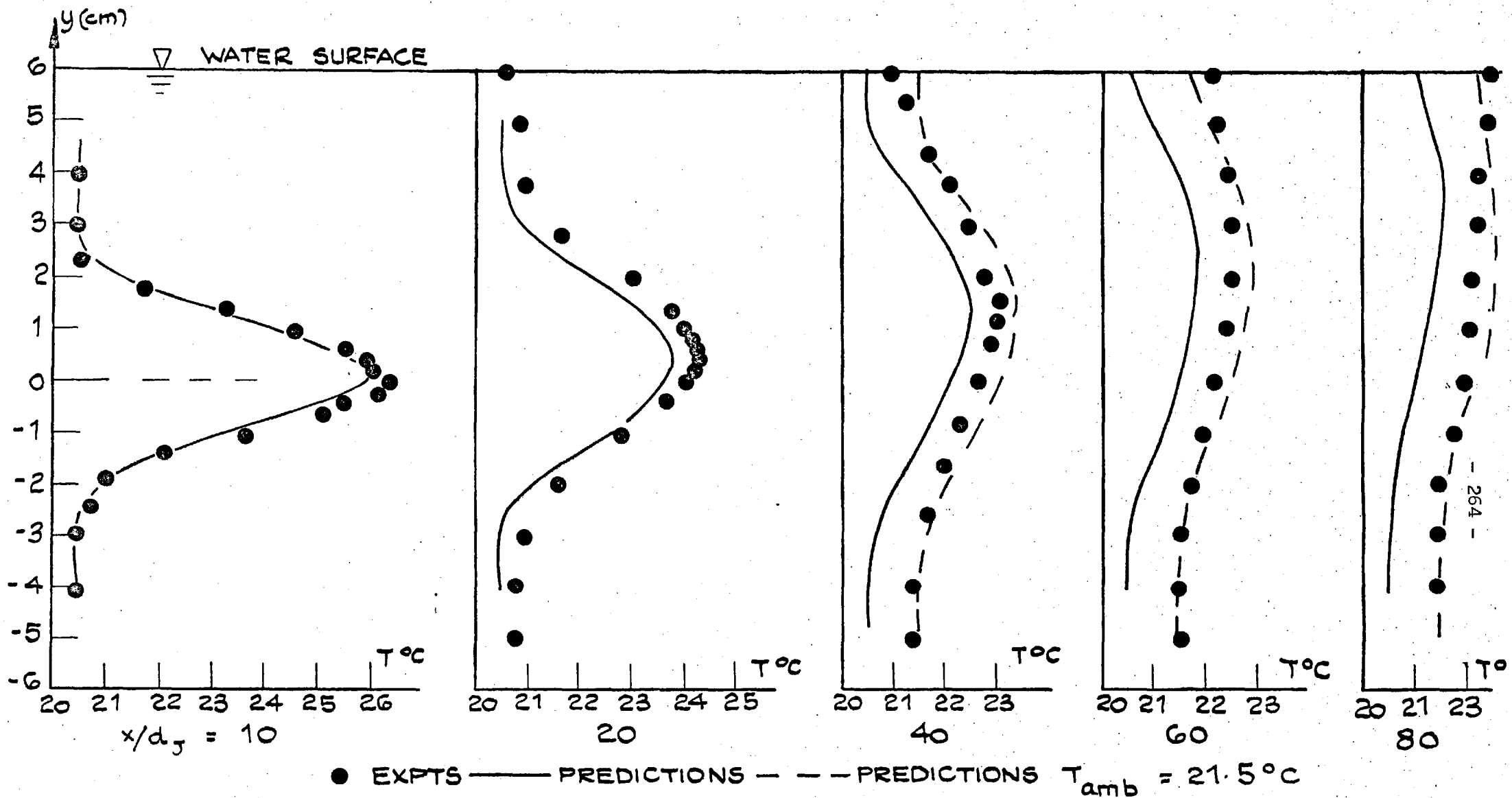


FIG. G. 3. 24: VERTICAL CENTRE-LINE TEMPERATURES PROFILES - PRESENT EXPTS.  
FR = 20 K = 4  $T_{JET} = 35.5^\circ\text{C}$   $T_{amb} = 20.5^\circ\text{C}$





(cm)

WATER SURFACE

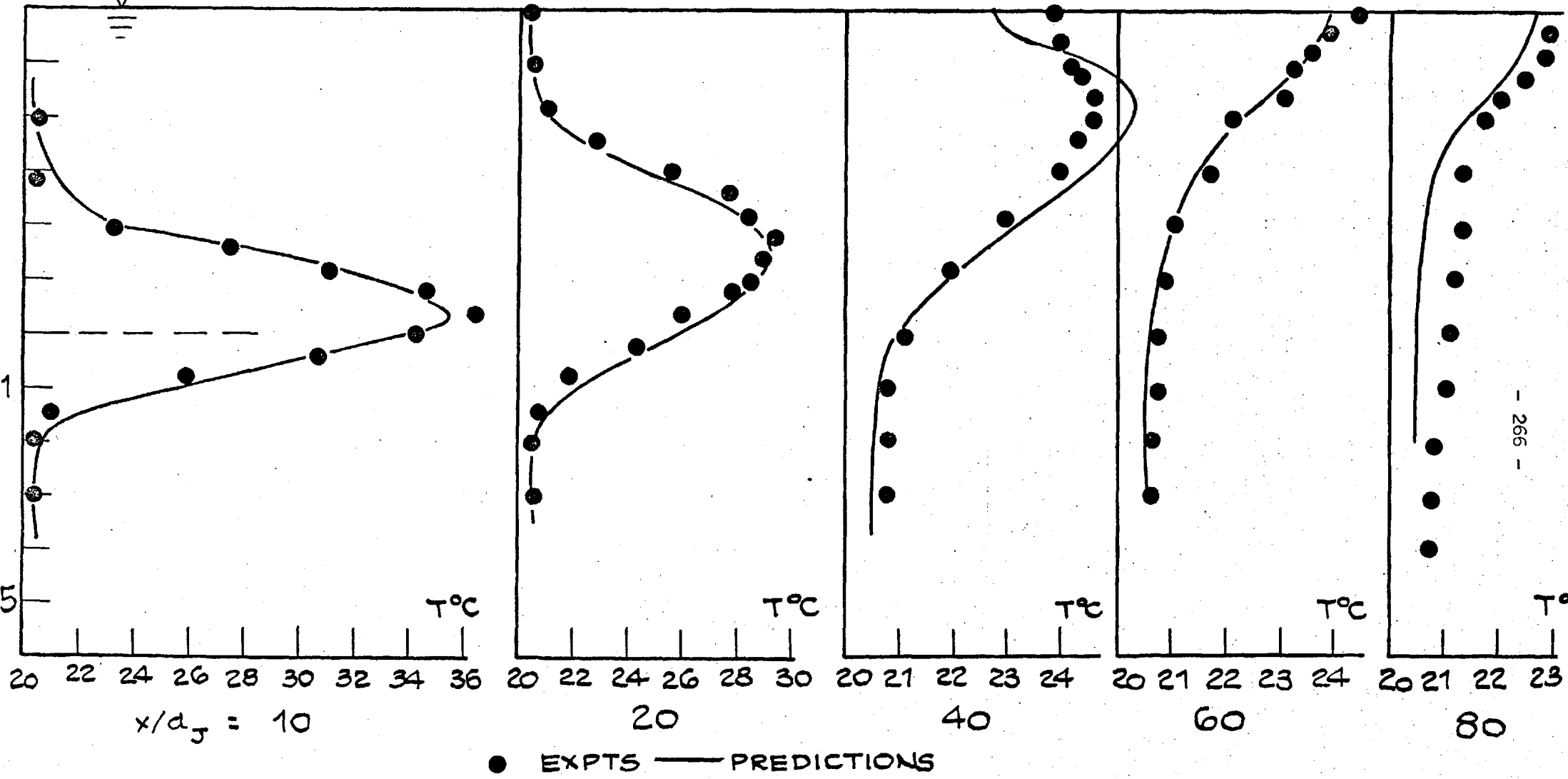


FIG. 6. 3. 26: VERTICAL CENTRE-LINE TEMPERATURE PROFILES -  
 PRESENT EXPTS FR = 10 K = 4  $T_{Jet} = 61.0^{\circ}C$   $T_{amb} = 20.5^{\circ}C$ .

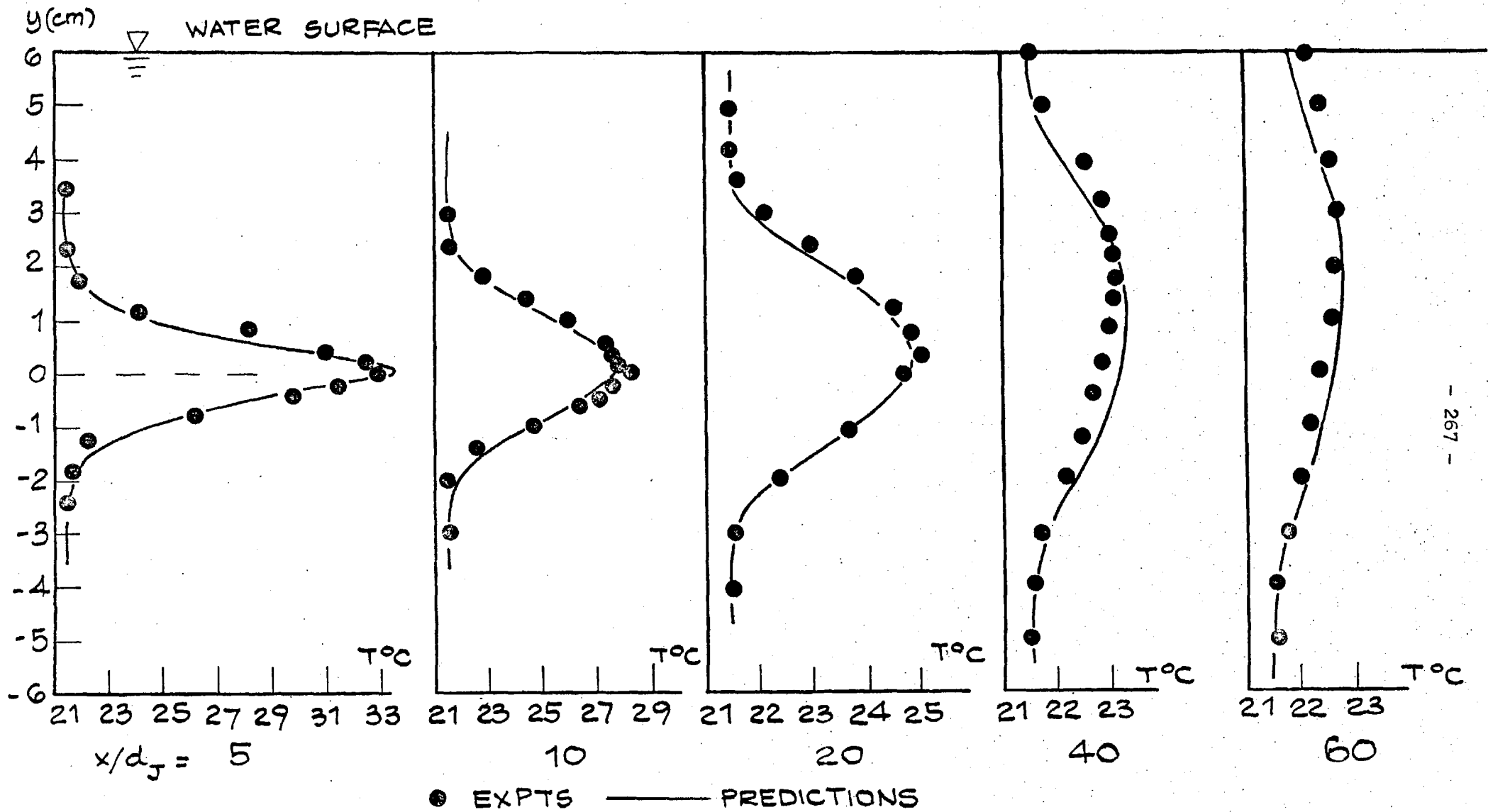


FIG. G. 3. 27: VERTICAL CENTRE - LINE TEMPERATURE PROFILES -  
 PRESENT EXPTS FR= 30 K= 6  $T_{jet} = 35.5^\circ\text{C}$   $T_{amb} = 21.5^\circ\text{C}$ .

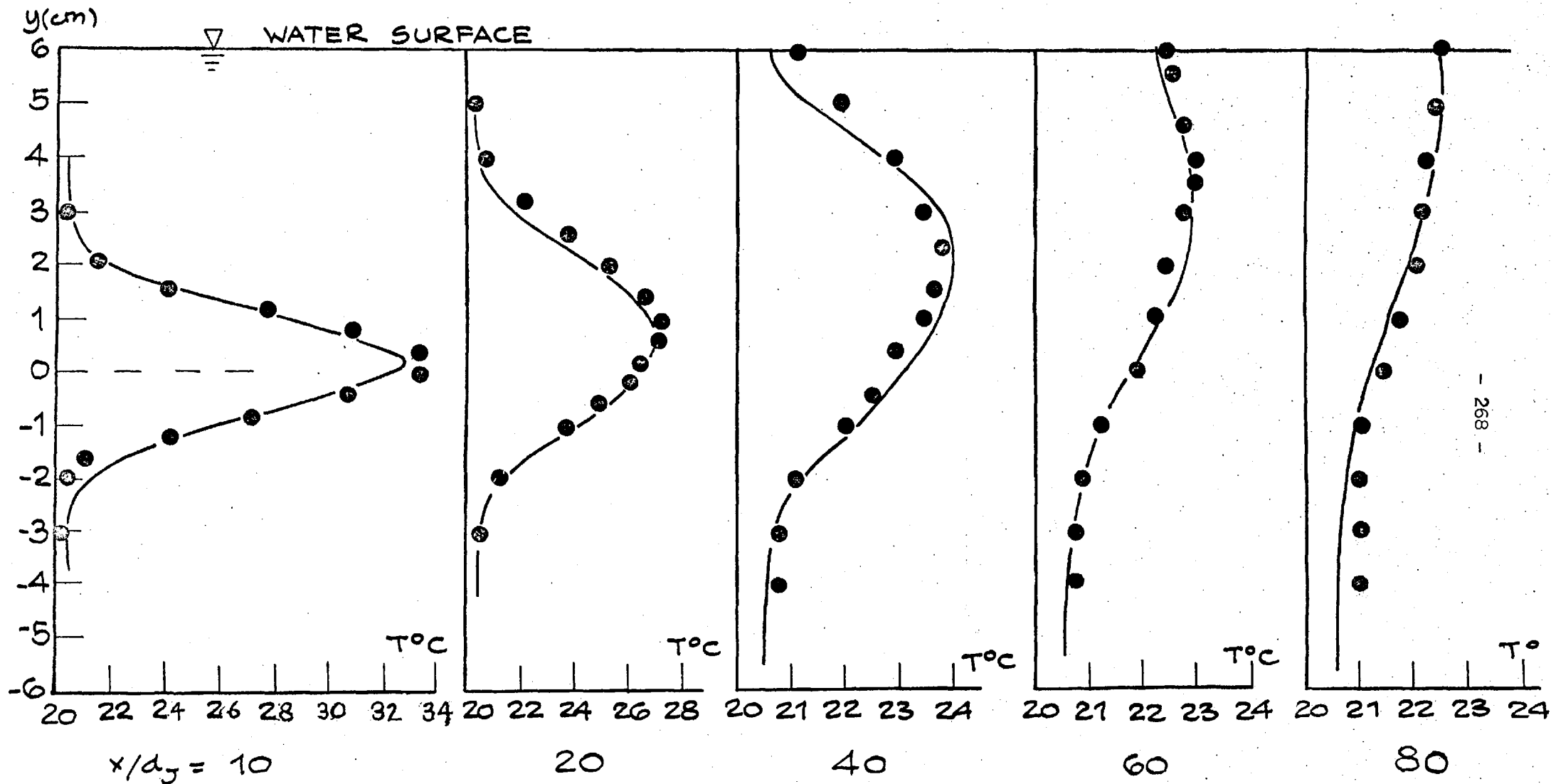


FIG. 6.3.28: VERTICAL CENTRE - LINE TEMPERATURE PROFILES  
 PRESENT EXPTS  $FR = 20$   $K = 0$   $T_{jet} = 47.5^\circ C$   $T_{amb} = 20.5^\circ C$

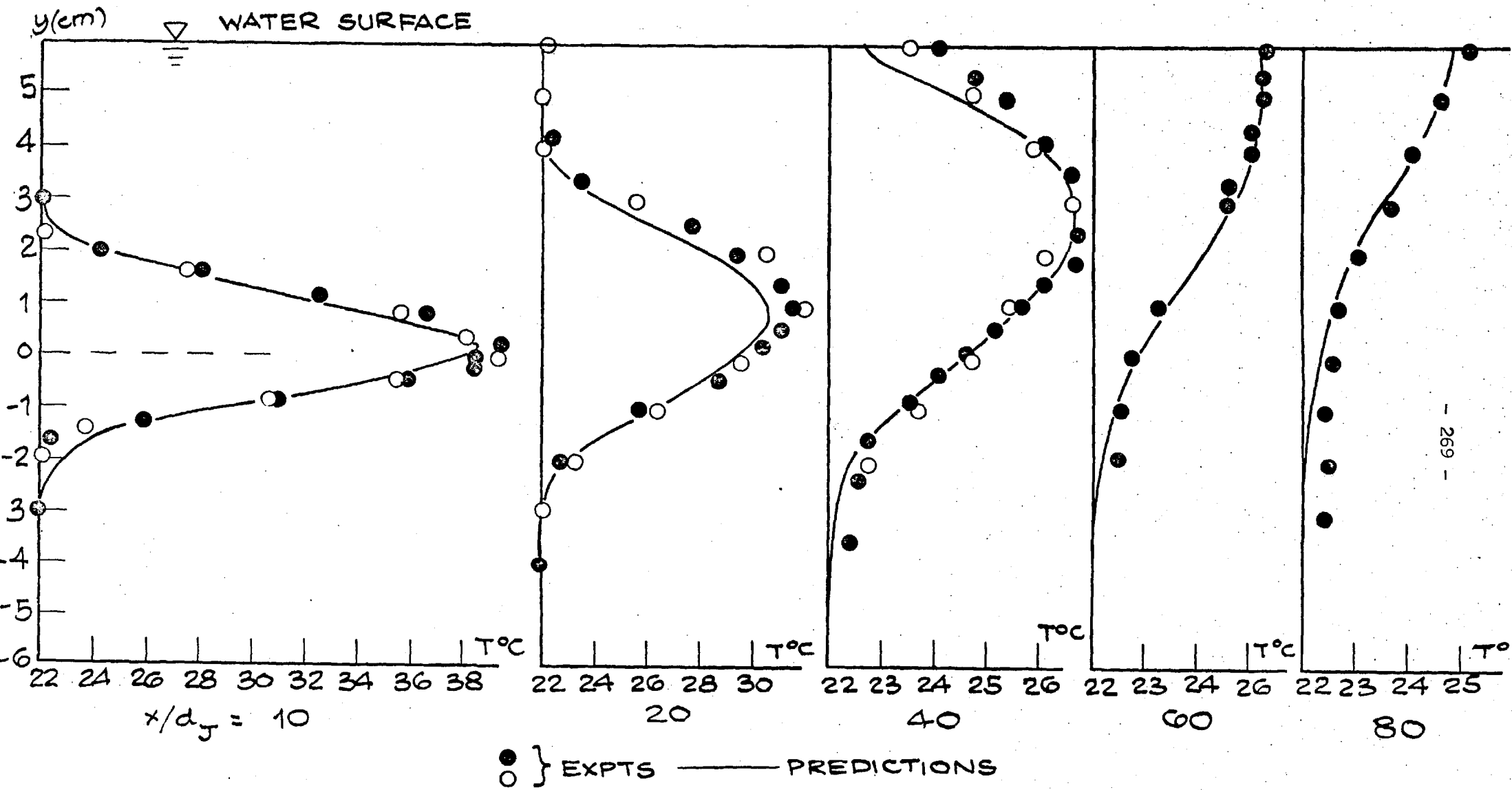
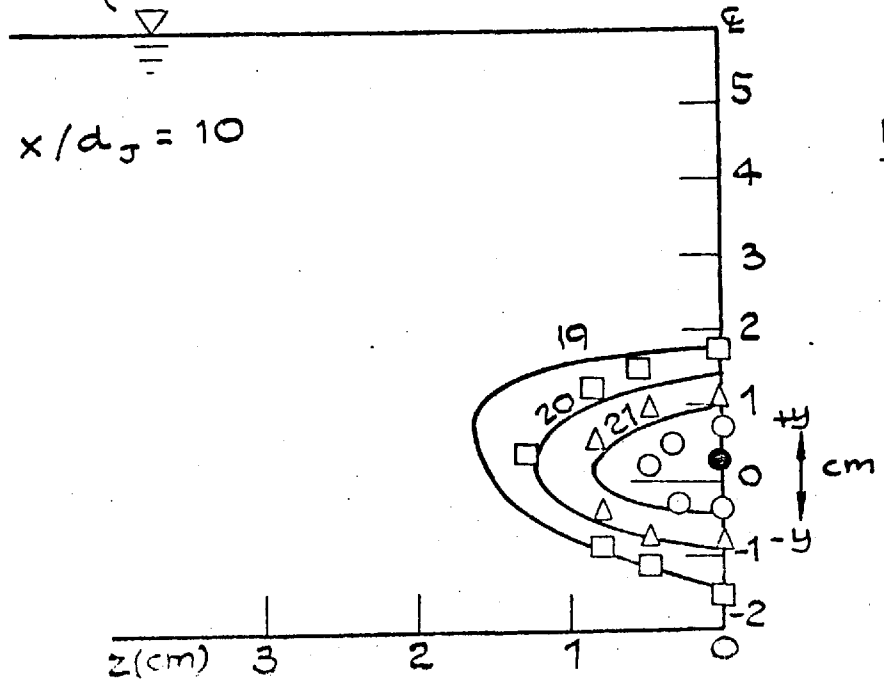
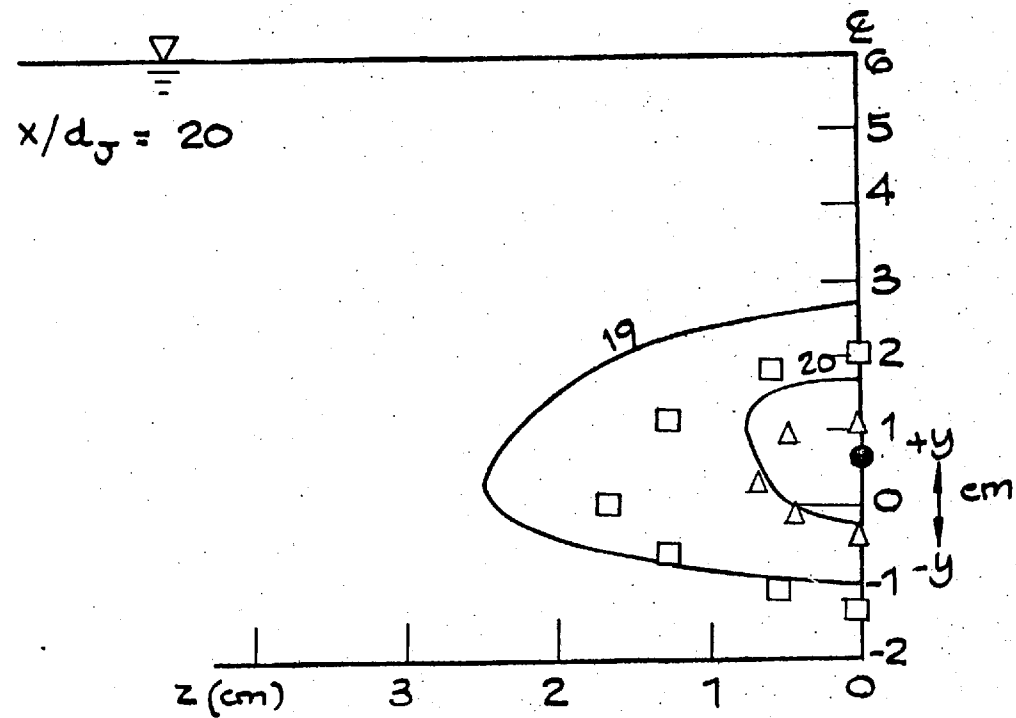
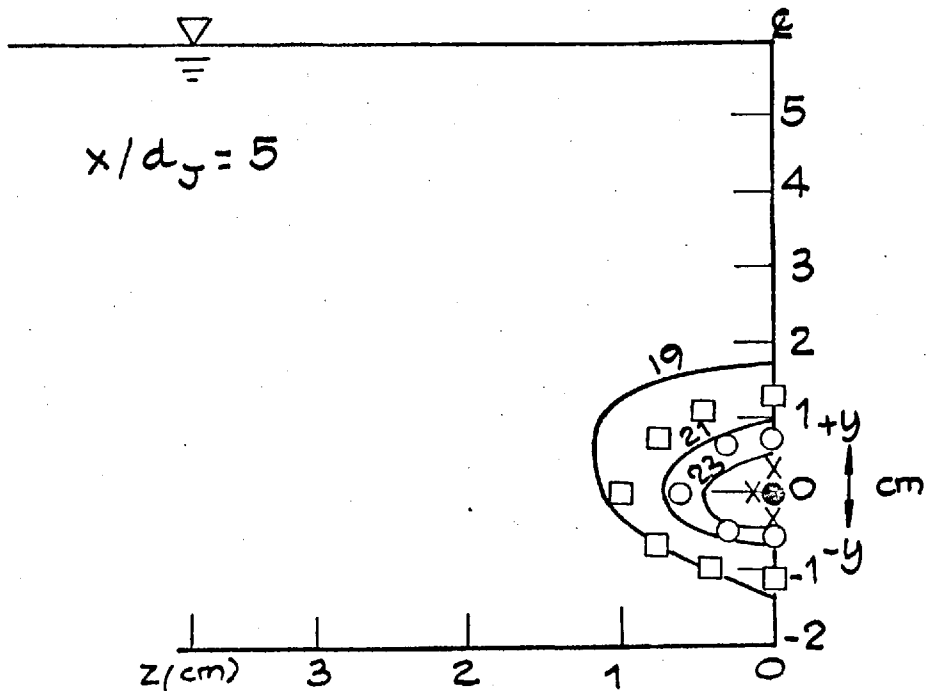
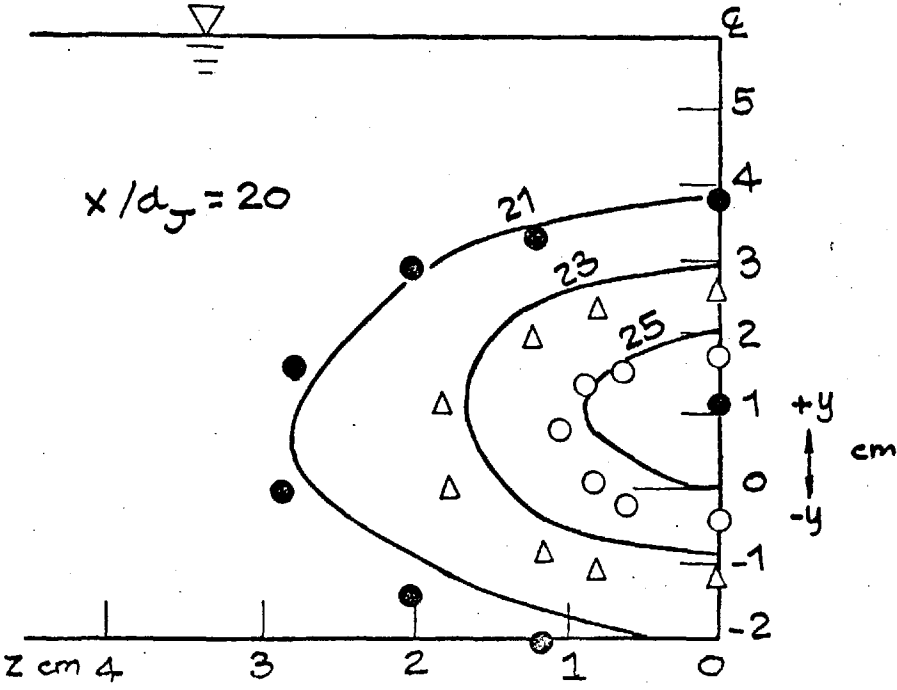
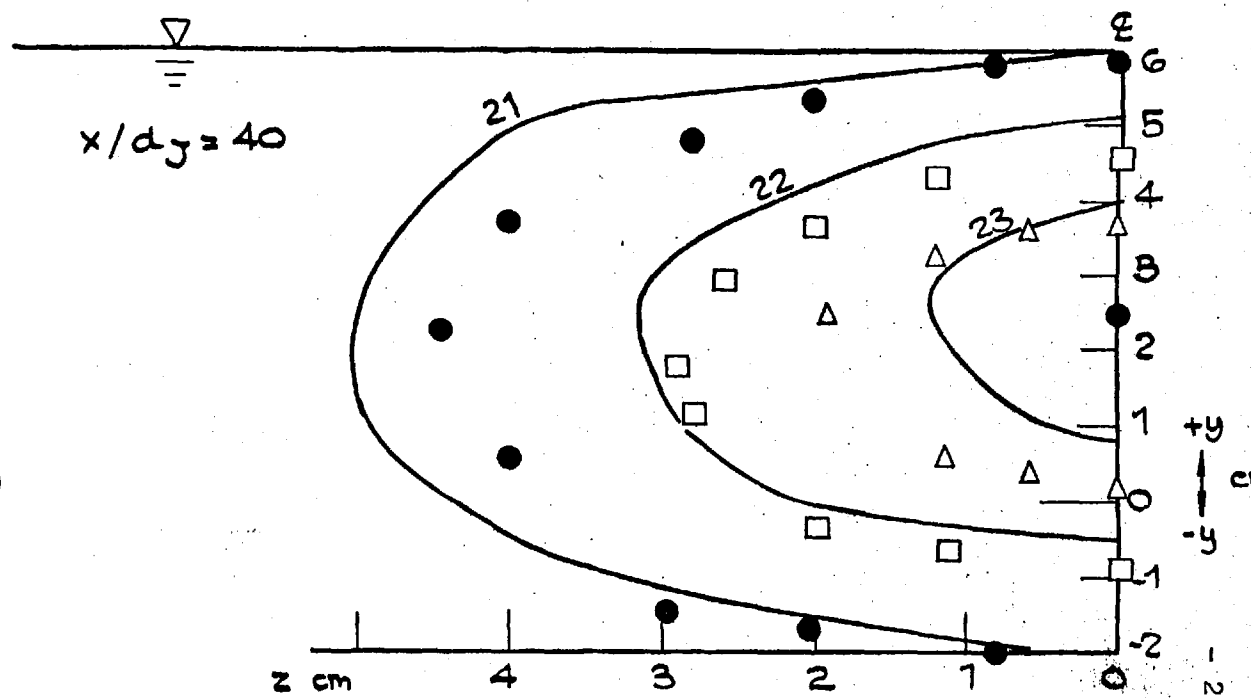
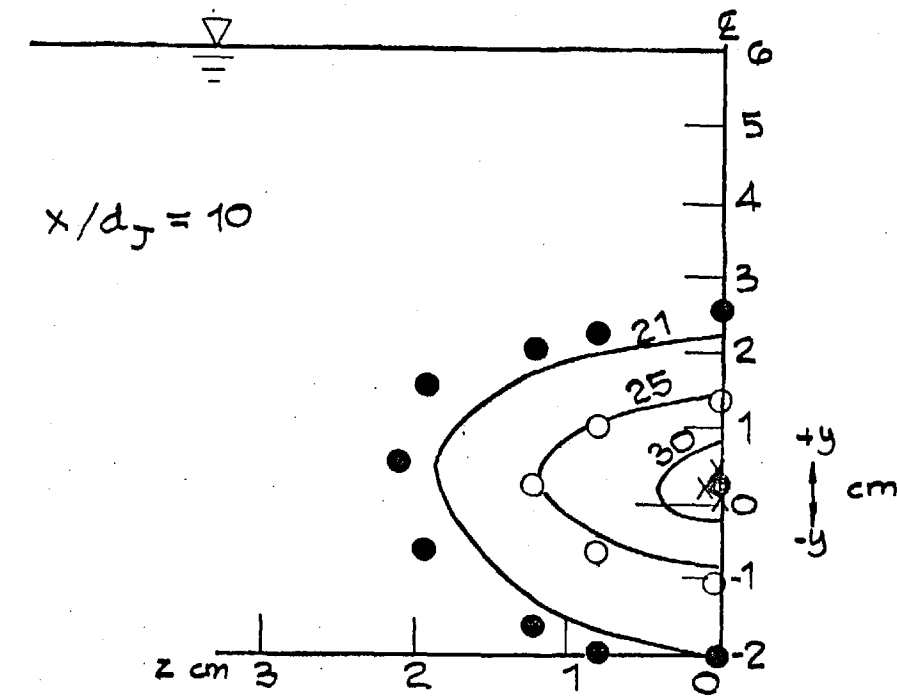


FIG. G. 3. 29: VERTICAL CENTRE-LINE TEMPERATURE PROFILES -  
 PRESENT PREDICTIONS     $FR = 16.5$      $K = 6$      $T_{\text{Jet}} = 58^{\circ}\text{C}$   
 $T_{\text{amb}} = 22.0^{\circ}\text{C}$



**FIG. 6. 3. 30: CROSS-SECTIONAL TEMPERATURE CONTOURS - PRESENT EXPTS**  
**FR = 15 K = 2.**

EXPTS.		PREDICTIONS	
SYMBOL	T°C	SYMBOL	T°C
X	23	X	23
O	21	O	21
Δ	20	Δ	20
□	19	□	19



**FIG. G. 3.31 : CROSS-SECTIONAL TEMPERATURE CONTOURS - PRESENT EXPTS.**  
FR = 15    K = 4.

EXPTS		PREDICTIONS	
SYMBOL	T °C	SYMBOL	T °C
x	30	○	25
○	25	△	23
△	23	□	22
□	22	●	21
●	21		

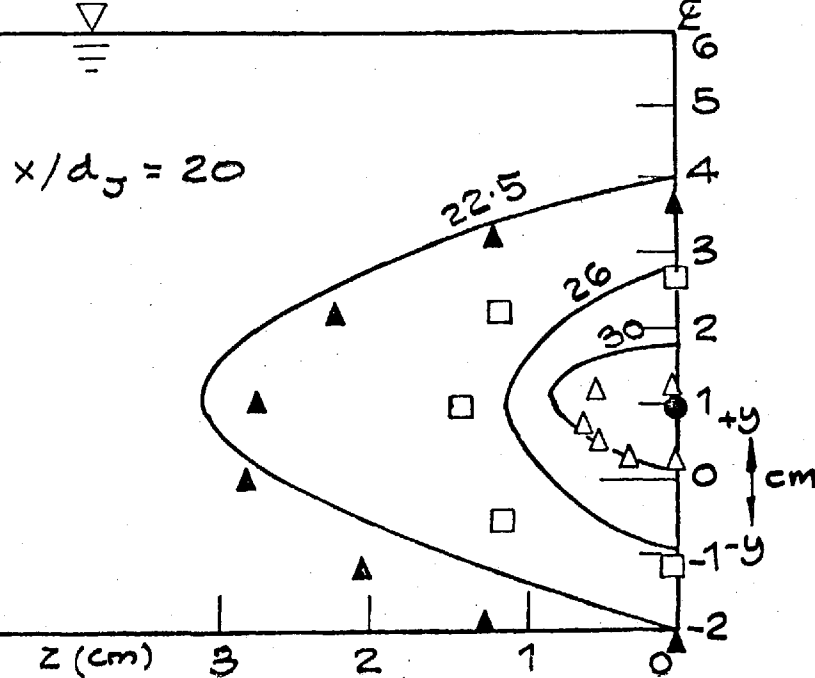
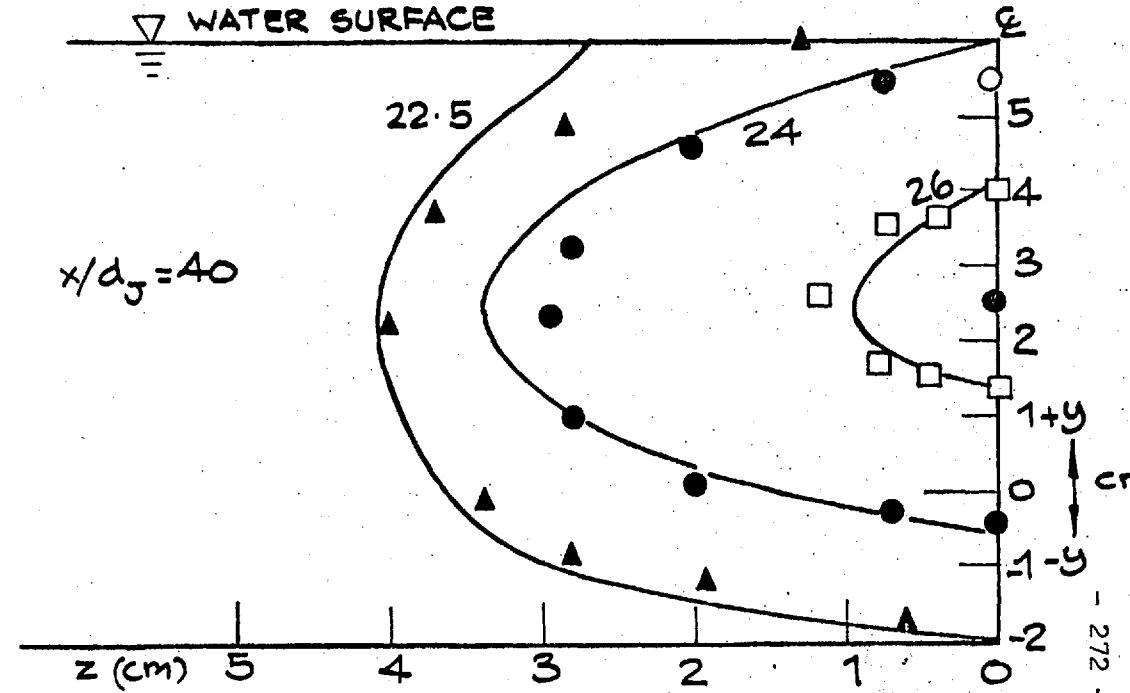
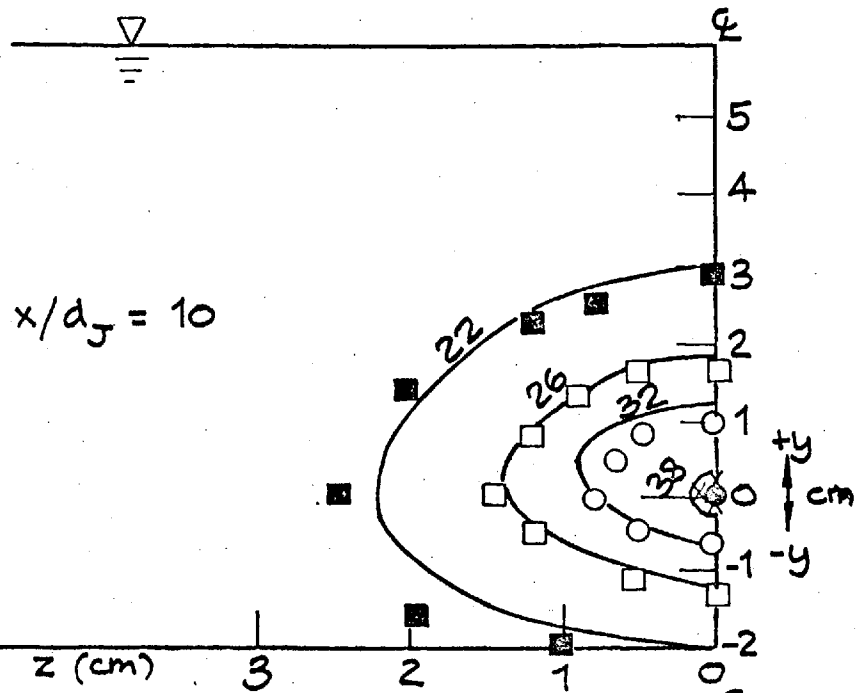


FIG. 6. 3. 32: CROSS-SECTIONAL TEMPERATURE CONTOURS - PRESENT EXPTS.

EXPTS.

PREDICTIONS

FR=16.5 K=6

SYMBOL	T °C
X	38
O	32
△	30
□	26
●	24
▲	22.5
■	22

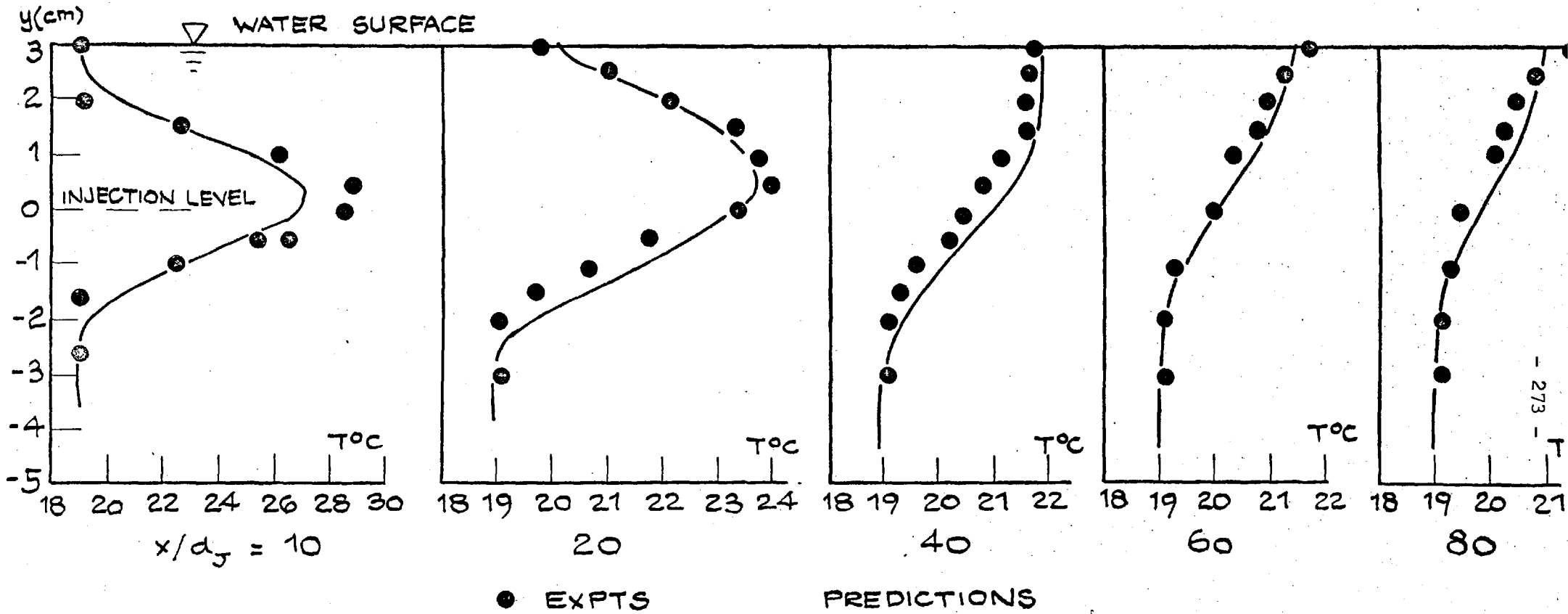


FIG. 6.3.33: VERTICAL CENTRE-LINE TEMPERATURE PROFILES  
PRESENT EXPTS 3cm SUBMERGENCE FR = 15  
 $k = 4$   $T_{jet} = 42^{\circ}\text{C}$   $T_{amb} = 19^{\circ}\text{C}$ .



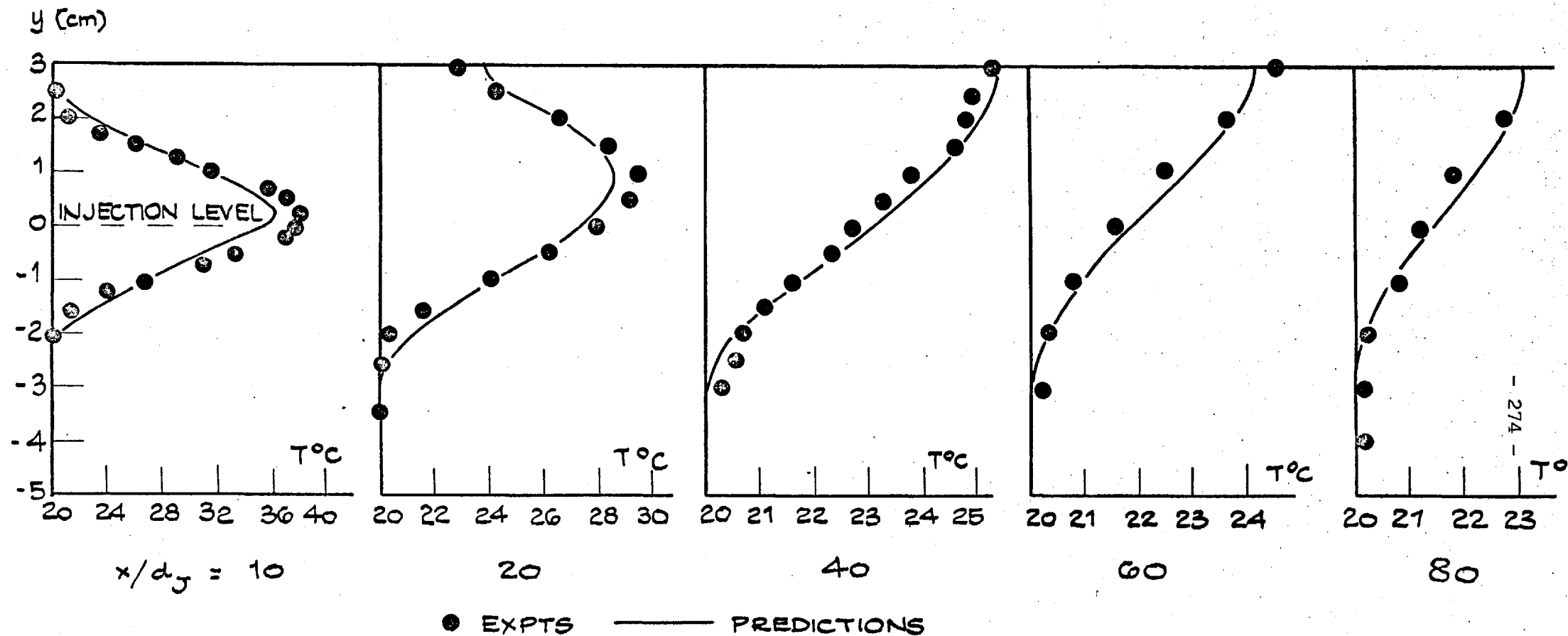


FIG. G. 3. 34: VERTICAL CENTRE - LINE TEMPERATURE PROFILES -  
PRESENT EXPTS. 3cm SUBMERGENCE  $FR = 16.5$   $K = 6$   
 $T_{jet} = 56.5^{\circ}\text{C}$   $T_{amb} = 20^{\circ}\text{C}$ .

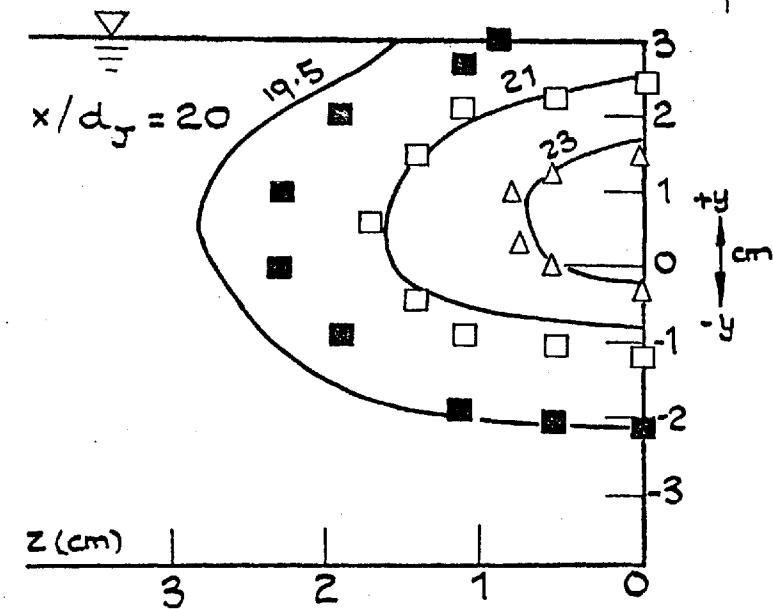
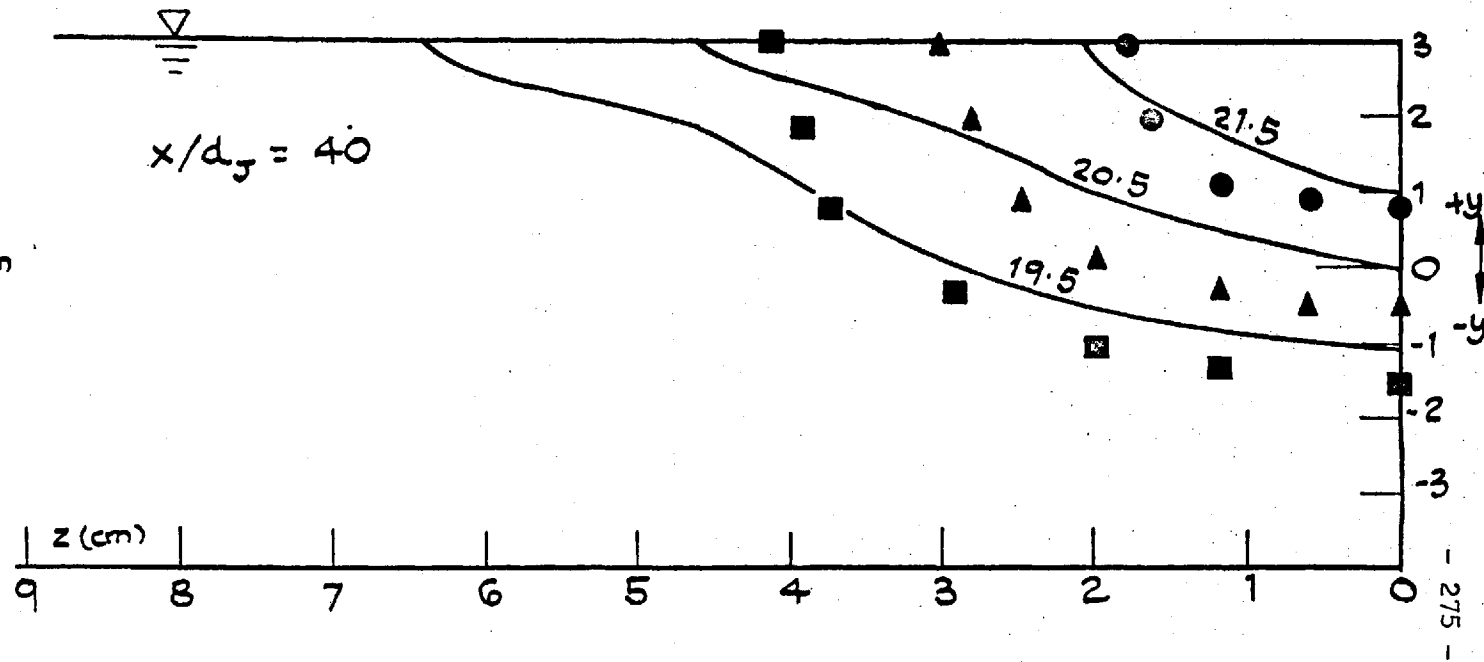
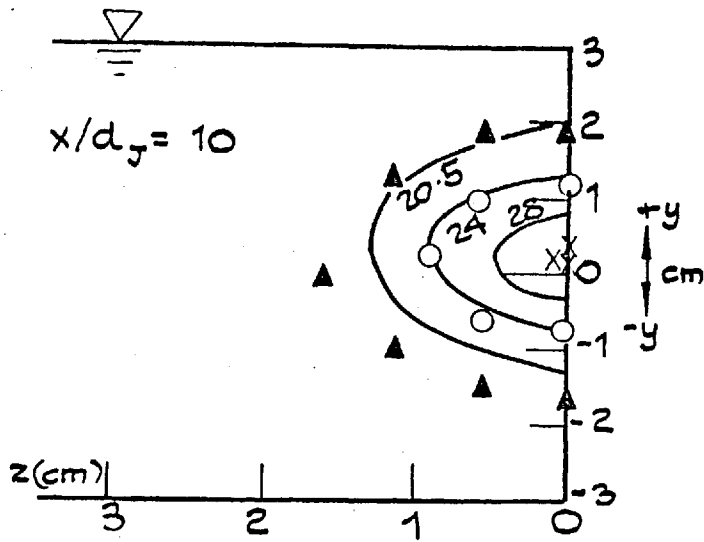
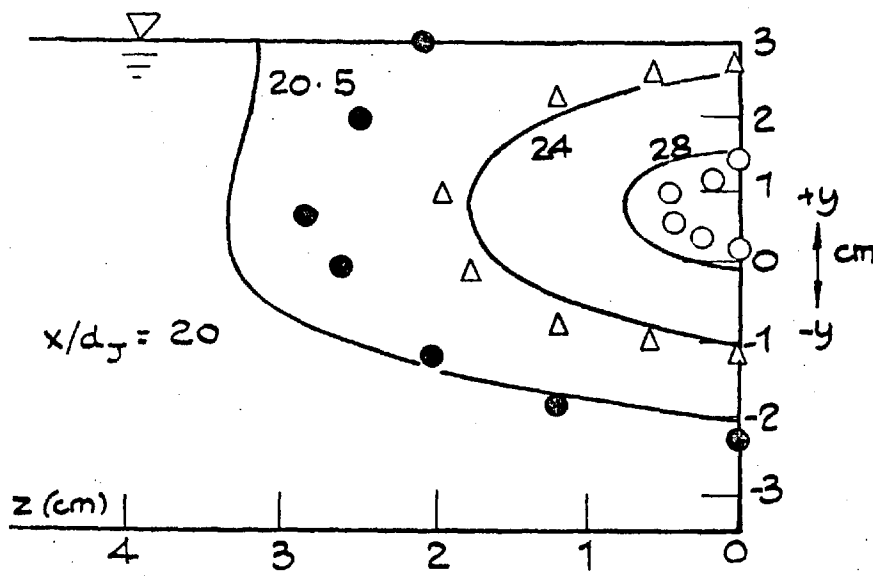
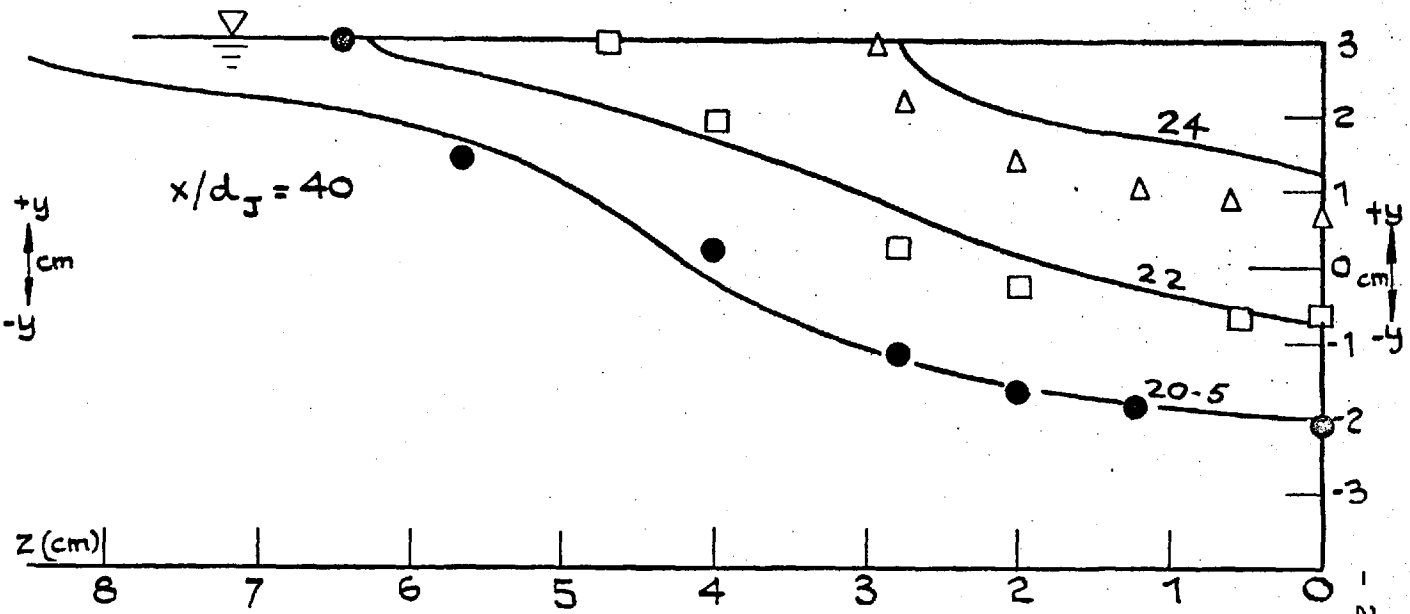
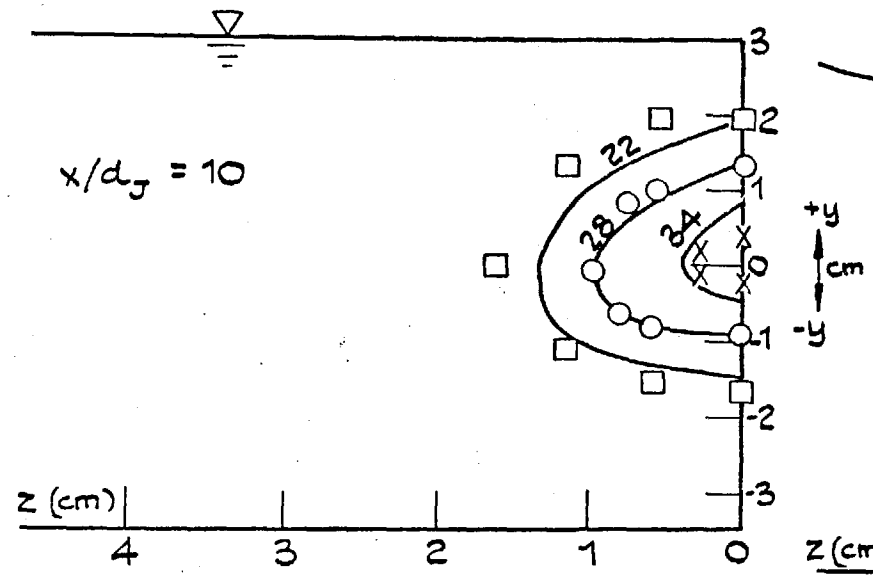


FIG. 6.3.35: CROSS-SECTIONAL TEMPERATURE CONTOURS  
 EXPERIMENTS 3 cm SUBMERGENCE  
 FR = 15 K = 4 — EXPTS PREDICTIONS.

SYMBOL	T°C
X	28
○	24
△	23
□	21
⊙	21.5
▲	20.5
■	19.5



**FIG. 6.3.36: CROSS - SECTIONAL TEMPERATURE CONTOURS - PRESENT EXPTS.**  
 3cm SUBMERGENCE  $FR = 16.5$   $K = 6$

EXPTS.		PREDICTIONS	
SYMBOL	T °C	SYMBOL	T °C
X	34	X	34
O	28	O	28
Δ	24	Δ	24
□	22	□	22
●	20.5	●	20.5

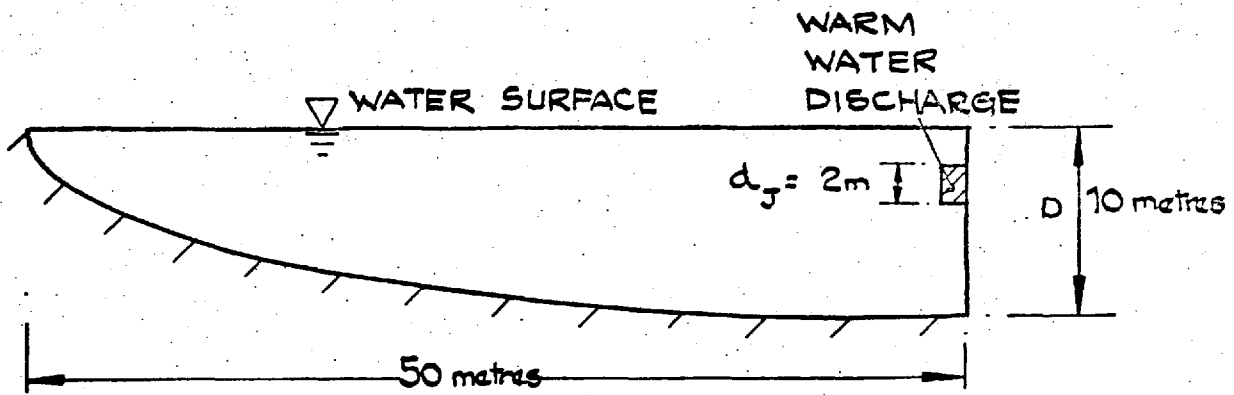


FIG. 7.2.1: RIVER THERMAL DISCHARGE PROBLEM.

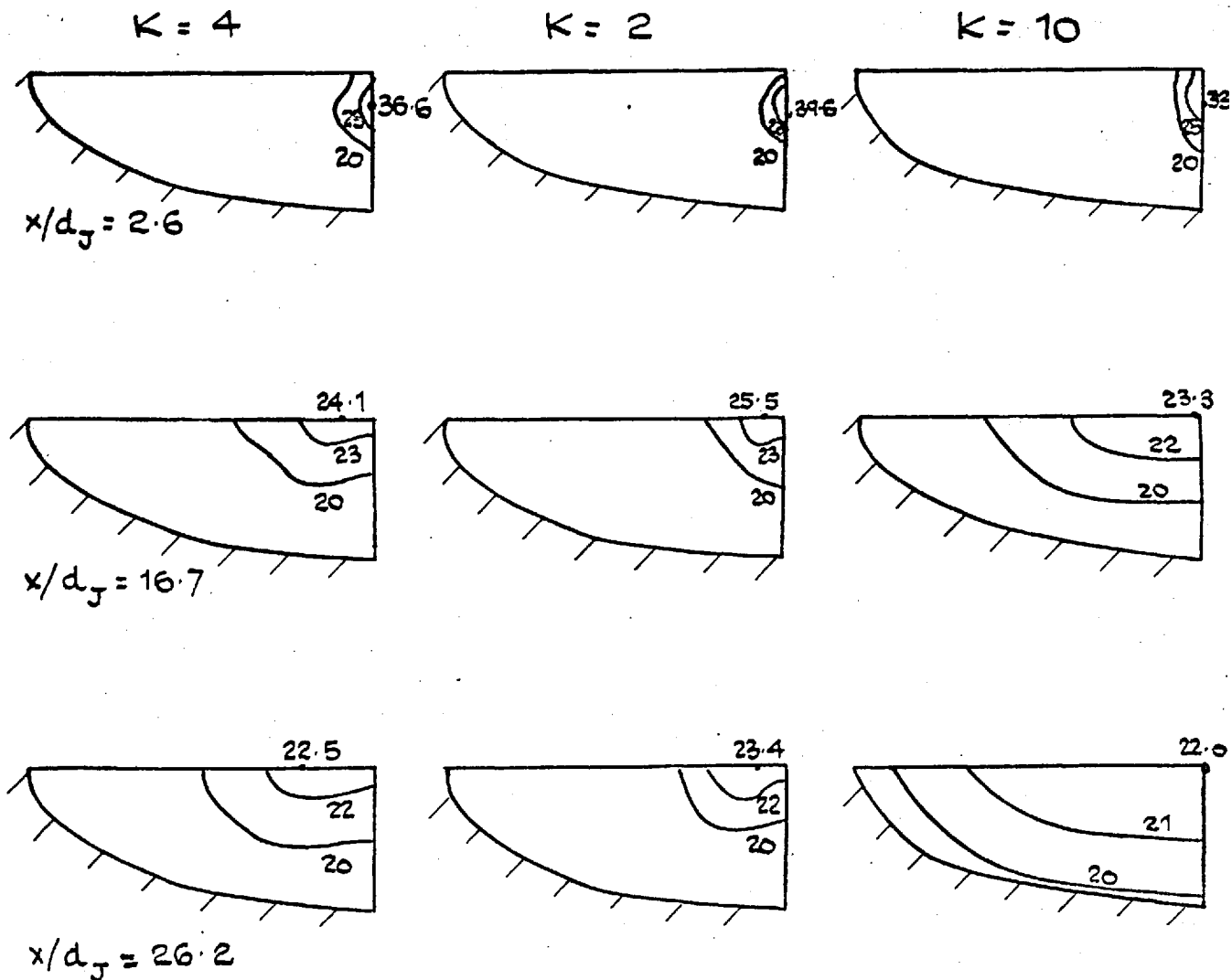


FIG. 7.2.2: EFFECT OF VELOCITY RATIO ON CROSS-SECTIONAL TEMPERATURE CONTOURS ( $^{\circ}\text{C}$ ).

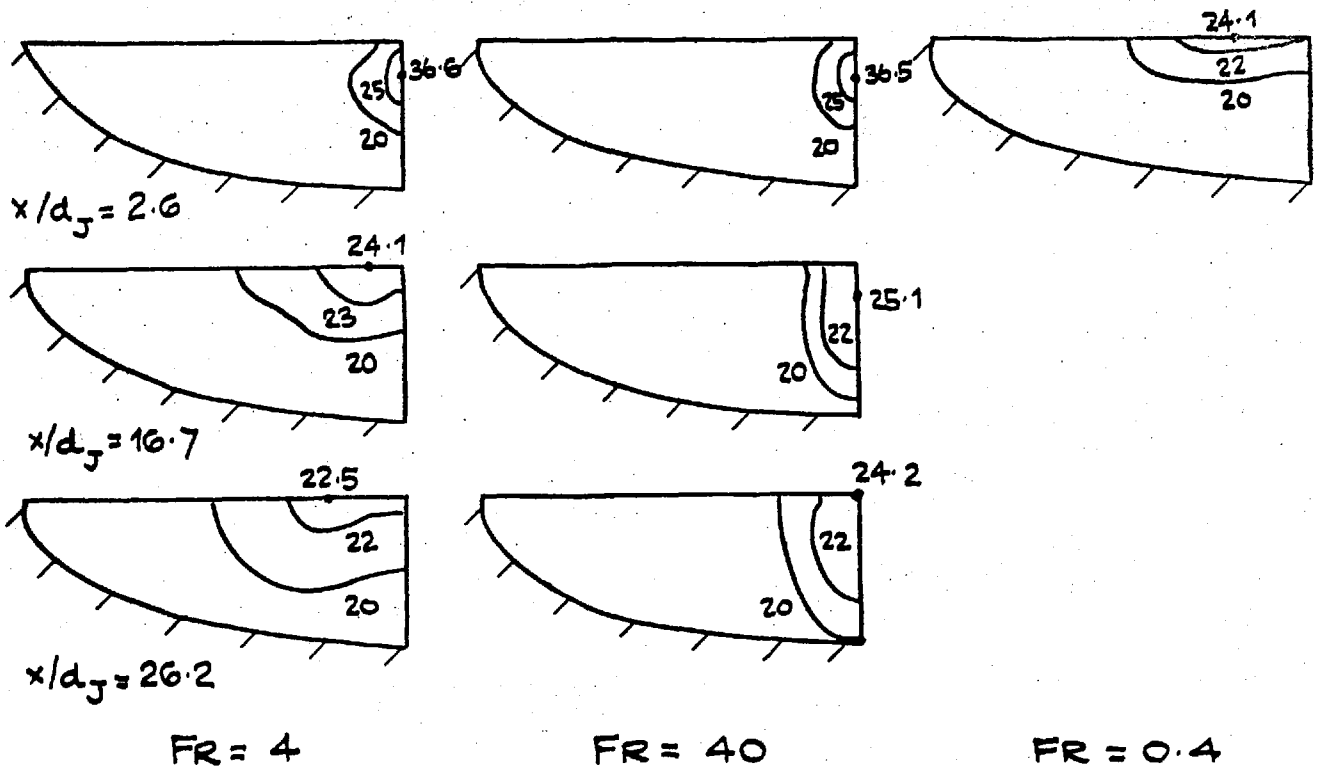


FIG. 7.2.3: EFFECT OF FROUDE NUMBER ON CROSS-SECTIONAL TEMPERATURE CONTOURS ( $^{\circ}\text{C}$ )

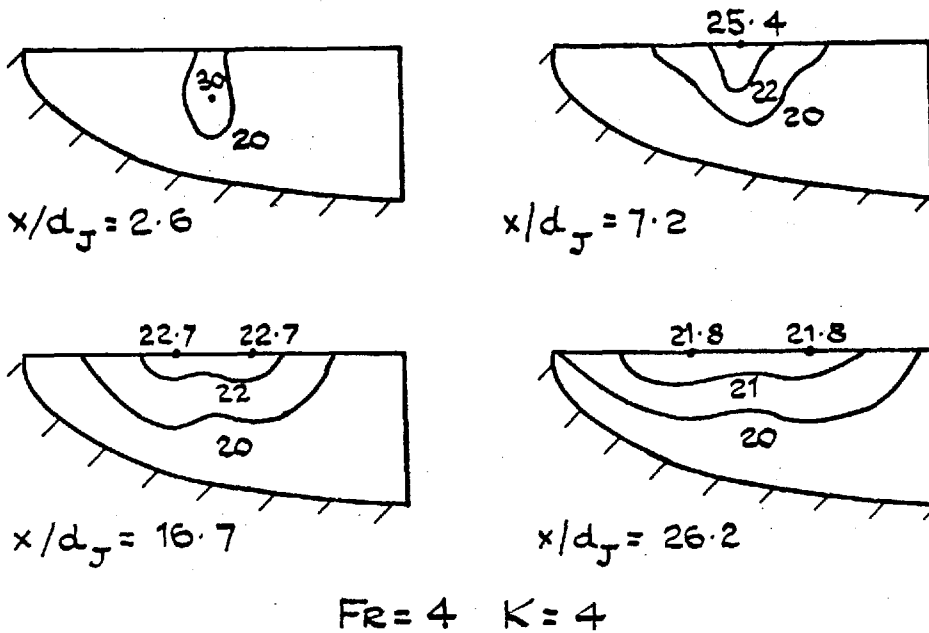


FIG. 7.2.4: EFFECT OF OFF-CENTRE-LINE DISCHARGE.

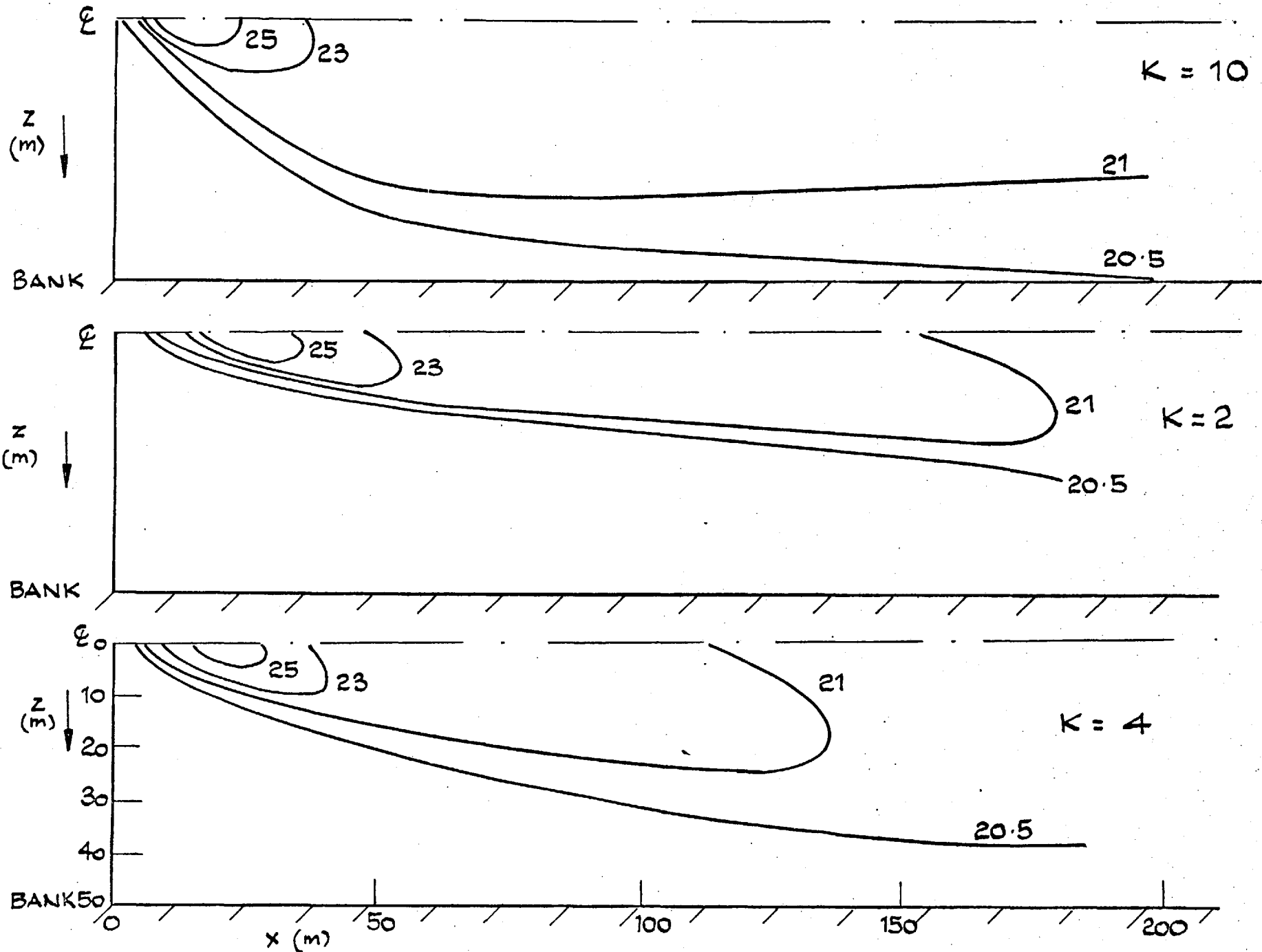


FIG.7.2.5: RIVER DISCHARGE - SURFACE TEMPERATURE CONTOURS EFFECT OF  $K$  AT  $Fr = 4$ .

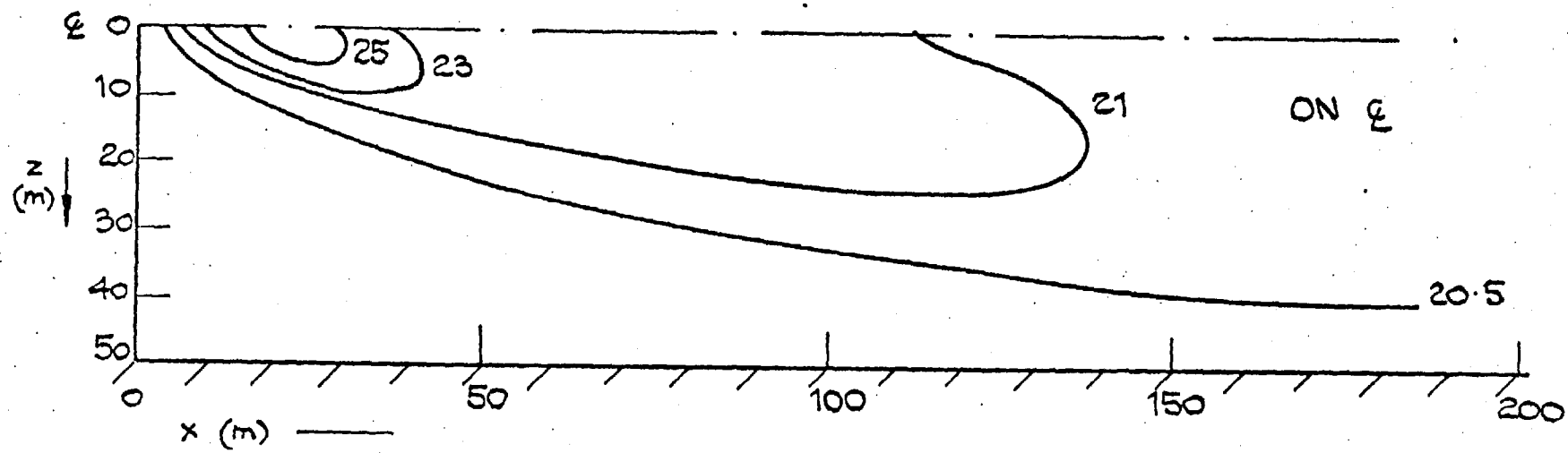
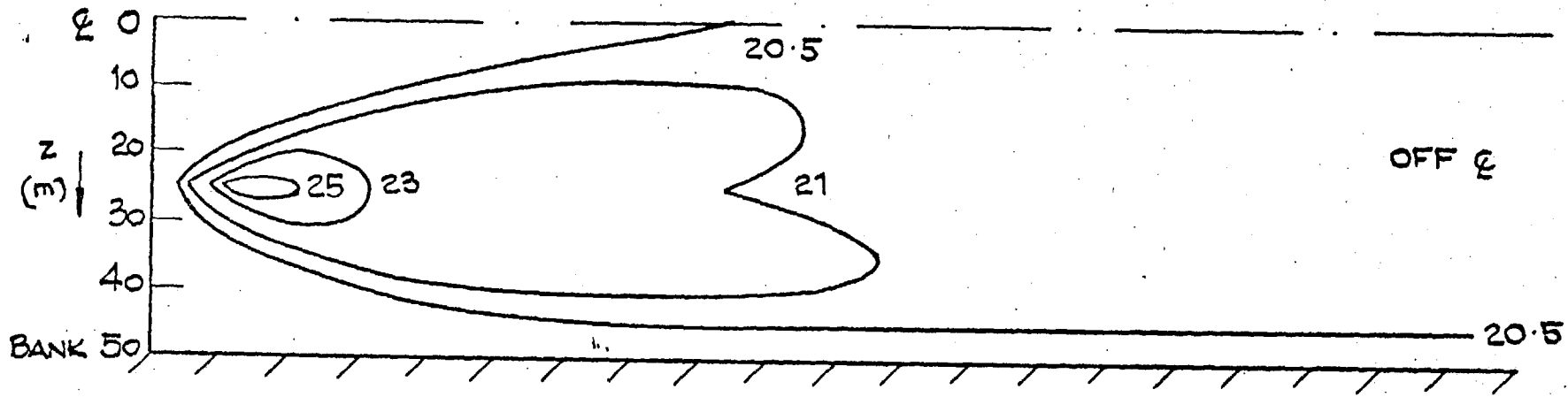


FIG. 7.2.6: RIVER DISCHARGE - SURFACE TEMPERATURE CONTOURS - TWO DISCHARGE LOCATIONS  $FR=4$   $K=4$ .